GRAVITY WAVES AND TURBULENCE IN THE LOWER ATMOSPHERE

By

Florian Zink, M.Sc., M.Sc.

Thesis

submitted for the degree of

DOCTOR OF PHILOSOPHY

at the

UNIVERSITY OF ADELAIDE

(Department of Physics and Mathematical Physics)

March 2000

Contents

Abstract

This thesis describes observations of gravity waves and turbulence in the lower atmosphere and their analysis using theory and modeling studies.

After a short introduction about the importance of gravity waves for the global circulation of the atmosphere, the theory of gravity waves, their saturation, and propagation through the atmosphere is introduced in Chapter 2. In Chapter 3 and 4 we present the development and application of a wavelet-based technique to detect gravity wave packets in routine meteorological radiosonde soundings. The advantages of the wavelet technique over more traditional Fourier techniques are illustrated, and an algorithm to apply wavelet analysis to vertical profiles of horizontal wind and temperature is introduced. After detection of the wave packets the wave parameters can be extracted by hodograph analysis. The technique is applied to twice-daily radiosonde soundings of the lower stratosphere over Macquarie Island between 1993 and 1995. In the interpretation of the results attention is paid to the limited observational bandwidth of the radiosonde method. Wavelet analysis can also provide information about the height extent of the gravity wave packets leading to a definition of source intermittency, i.e the time fraction the gravity wave sources had to be active to produce the observed wave field. Knowledge of source intermittency and wave parameters then allows us to deduce the effects of the observed gravity wave field on the lower and middle atmosphere using a linear ray tracing model.

The remainder of the thesis deals with the application of the University of Adelaide's VHF radar at Buckland Park to measurements of wind and turbulence. The principles of atmospheric radar for measurements of horizontal and vertical wind

speeds are introduced in Chapter 5. Chapter 6 presents radar signal processing algorithms for the removal of intermittent clutter from radar time series and for the analysis of Doppler Beam Steering experiments, which were developed during the course of this thesis. Two common techniques to infer atmospheric turbulence parameters from radar measurements are presented in Chapter 7. In Chapter 8, we compare measurements of wind and turbulence parameters by radar and thermosondes during a six day campaign in August 1998. The two methods agree reasonably well when the turbulence parameters are inferred from the backscattered power. Deduction of turbulence parameters from the spectral width of the radar signals, on the other hand, is shown to be impractible for the available radar height resolution due to large contributions from spatial gravity wave fluctuations. The high-resolution thermosonde data, furthermore, allows us to examine the relationship between the observed turbulence and gravity wave fields by comparison with a theoretical model and Monte Carlo simulations. Characteristics of the observed turbulence layers such as layer thickness and spacing are shown to be well reproduced by the models. Further analysis of the radar data in Chapter 9 reveals the existence of a stratospheric inertio gravity wave. Its parameters are deduced and we discuss its possible generation by geostrophic adjustment of the jet stream. A thesis summary with suggestions for future research is provided in Chapter 10.

This work contains no material which has been accepted for the award of any other degree or diploma in any university or other tertiary institution and, to the best of my knowledge and belief, contains no material previously published or written by another person, except where due reference has been made in the text.

I give consent to this copy of my thesis, when deposited in the University Library, being available for loan and photocopying.

Signed: ..... dated: 21.3.2000

Florian Zink, M.Sc., M.Sc.

Acknowledgements

First of all, I'd like to thank my supervisors Iain Reid and, especially, Bob Vincent for their support and encouragement during my candidature. The discussions with Joan Alexander[1] and Greg Nastrom[2] on gravity waves and turbulence, respectively, are also greatly appreciated. The work on turbulence would not have been possible without the help of Owen Cote[3], who provided the thermosonde data and further insights into atmospheric turbulence.

I'd also like to thank the technical staff of the Atmospheric Physics group, Alex Didenko and Leslie Rutherford, for their support in keeping the Buckland Park VHF radar running after the lightning and water damage in 1998, and also the staff of Tomco Electronics, Genesis Software and ATRAD, especially David Holdsworth. Thanks also to Dallas Kirby and Lyn Byrchby for their support in administrative and all other matters.

The past and present students and members of the Atmospheric Physics Group, Ali Kazempour, Andrew MacKinnon, Andrew Taylor, Bridget Hobbs, Chris Lucas, Daniel Badger, Dorothy Gibson-Wilde, Graham Elford, Jonathan Woithe, Karen Berkefeld, Laurence Campbell, Minh Nguyen, Rupa Vuthaluru, Scott Dullaway, Stephen Grant and Sujata Kovalam provided a great atmosphere to study the atmosphere. Thanks to all of them.

Outside of University, I am especially indebted to Silja, Linda, and Andrew. To a visitor, a city/country/continent is only a few places and people, and it is largely due

[1]Colorado Research Associates, Boulder
[2]St. Cloud State University
[3]Phillips Lab, Hanscom Airforce Base

to you that I enjoyed my stay in Australia as much as I did. Thanks for your love and friendship over the years. Last but not least, I want to thank my parents for their support and understanding over the several years I've spent abroad. The distance can only get smaller now, and I might even get a "real" job one day.

The research in this thesis was supported by an International Postgraduate Research Scholarship.

Chapter 1

Introduction

Gravity waves are wave motions in a stratified fluid arising from the restoring forces of gravity acting downwards and buoyancy acting upwards on vertically displaced fluid parcels. More accurately, they are referred to as buoyancy waves. During propagation to higher altitudes their amplitude generally increases due to the exponential decrease in atmospheric density with height, until the waves encounter their breaking levels. Here, the amplitude is so large that the material deformations due to the wave motion become irreversible and the wave deposits energy and momentum into the mean flow. Gravity waves are, therefore, an important means to redistribute momentum and energy from one region in the atmosphere to another. In addition to the transfer of energy and momentum, gravity wave breaking also results in turbulent mixing and vertical transport of atmospheric constituents. Due to their small spatial scales, gravity waves cannot be explicitly resolved in general circulation models, and their parameterization remains one of the most fundamental problems in these models.

To understand the important role gravity waves play for the general circulation, we give an introduction about the vertical structure of the atmosphere and illustrate why some means of momentum transport is required to explain the significant deviations of the atmosphere from its radiative equilibrium state. We then show how gravity wave parameterization schemes have been applied sucessfully to represent the required momentum transport and relate some open questions in that area to the research

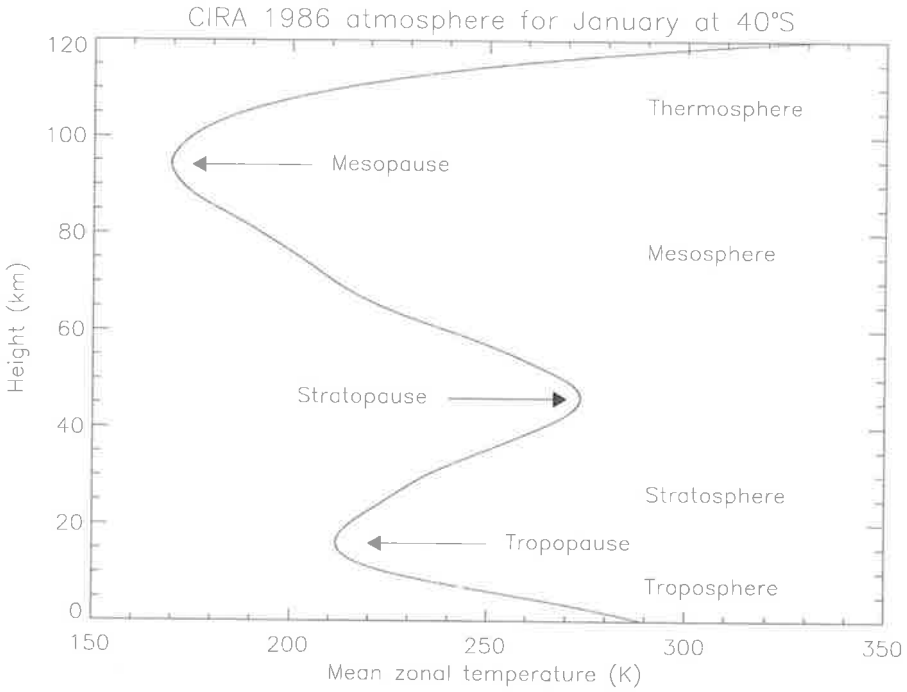

Figure 1.1: Identification of the different regions of the atmosphere using the mean zonal temperature profile for January from the COSPAR International Reference Atmosphere 1986 (CIRA) at a latitude of 40° S.

conducted in this thesis.

1.1 Vertical structure of the atmosphere

Based on the observed vertical temperature structure the Earth's atmosphere can be divided into different height intervals. Figure 1.1 shows the mean zonal temperature profile for January from the COSPAR International Reference Atmosphere 1986 (CIRA) at a latitude of 40° S. From the sign of the vertical temperature gradient one can distinguish four regions called troposphere, stratosphere, mesosphere, and thermosphere. The heights between those regions where the temperature reaches local extrema are identified as the tropopause, the stratopause, and the mesopause.

In principle this temperature structure can be understood by the effects of solar irradiation and atmospheric photochemistry, which lead to heating and cooling processes

at different heights. In the troposphere the thermal structure is mainly determined by the heating of the surface due to the absorption of solar radiation. The surface then reemits this radiation at much longer infra-red wavelengths. Greenhouse gases like water vapour and carbon dioxide can absorb parts of this infra-red radiation and heat the atmosphere. Due to the strong negative temperature gradient, an air parcel that cools adiabatically due to its expansion when slightly moved upwards can still be warmer than the background and, therefore, will continue to rise. Convection leads to an overturning of air masses and strong mixing of constituents in the troposphere.

In the stratosphere, on the other hand, the strong positive temperature gradient inhibits convection, and any constituent mixing is due to turbulence. The reason for the temperature increase with height in the stratosphere is absorption of ultraviolet solar radiation by ozone. At heights below 70 km virtually all the absorbed energy goes into kinetic energy of the molecules. For thermal equilibrium a cooling mechanism is needed as well. This is provided mainly by the emission of infra-red radiation from carbon dioxide molecules. Figure 1.2 shows the vertical distribution of heating and cooling rates due to the absorption of solar radiation and the emission of infra-red radiation, respectively. Above the stratopause, the temperature decreases with height again due to rapidly decreasing ozone concentrations until the coldest atmospheric temperatures are encountered at the mesopause. The remaining part of the atmosphere above the mesopause is called the thermosphere, where photoabsorption by various chemical species leads to a strong increase of temperature with height.

1.2 The requirement for a zonal drag

Problems start to occur when one tries to explain the global atmospheric temperature (and zonal wind) distribution with radiative equilibrium arguments alone [*Geller*, 1983]. Figure 1.3 shows contour plots of the zonal mean temperature (top) and zonal mean winds (bottom) of the CIRA 1986 for January as a function of latitude. As is to be expected by the geometry of incoming solar radiation, the warmest temperatures

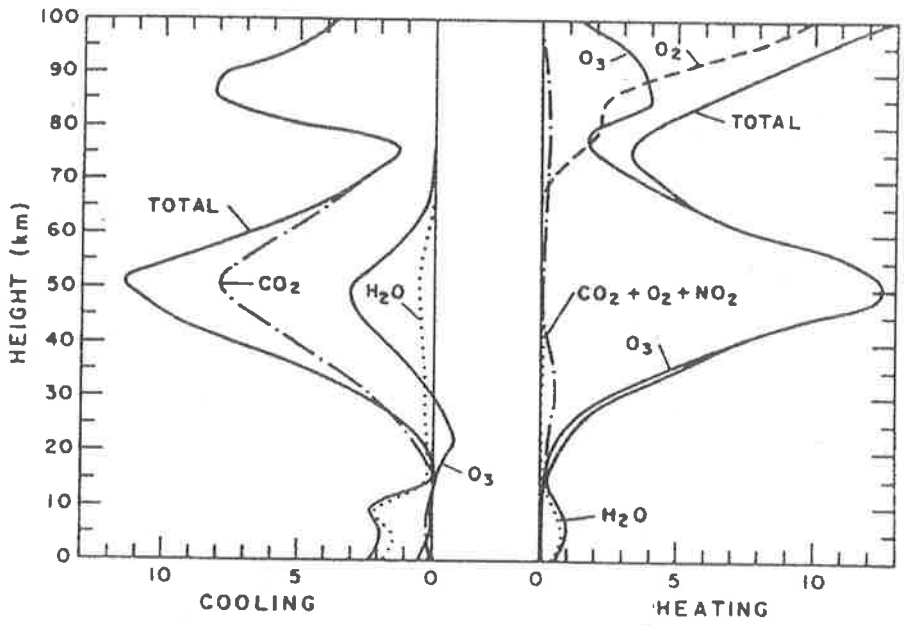

Figure 1.2: Vertical distribution of heating due to absorption of solar radiation (right) and cooling due to emission of infrared radiation (left). Units are K day^{-1}. (From *London* [1980])

at the surface are found in the tropics. At the stratopause, a temperature maximum exists at the summer pole, consistent with a maximum solar ozone heating there. However, the local temperature minimum at the tropical tropopause and the temperature distribution in the mesosphere, with warm temperatures at the winter pole and cold temperatures at the summer pole, cannot be explained in terms of radiative equilibrium. Regarding the mean zonal winds, an eastward jet can be seen around the tropopause height for both winter and summer. In the mesosphere, around 60 to 70 km, there is an eastward jet in the winter and a westward jet in the summer hemisphere.

Figure 1.4 (top) shows the distribution of radiative equilibrium temperatures, i.e. the temperature field for which the local solar heating is exactly balanced by the local infra-red cooling, from a model calculation [*Geller*, 1983]. The temperature field is not only in quantitative but also in qualitative disagreement with the temperatures of the CIRA 1986 in Figure 1.3. Neither the temperature minimum at the tropical tropopause

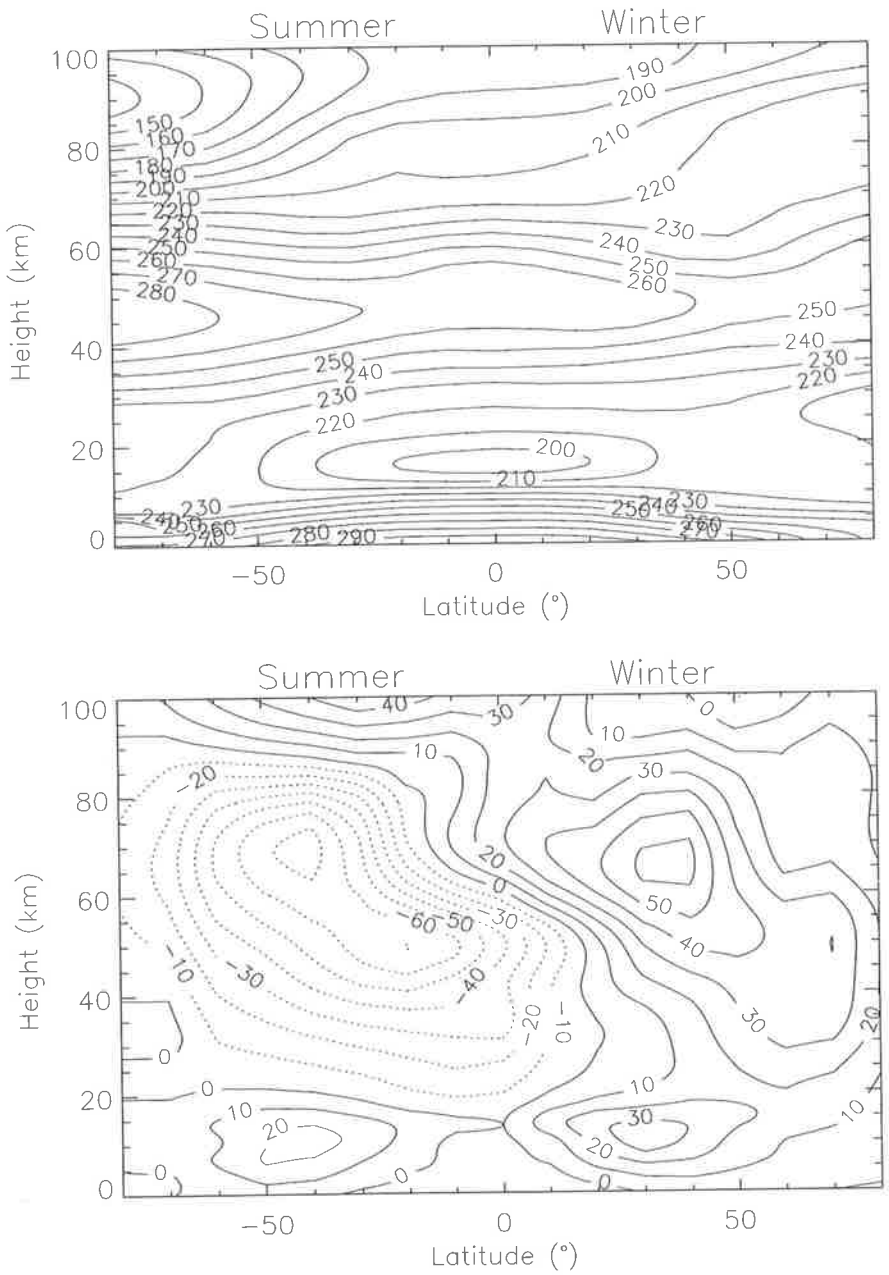

Figure 1.3: Contour plots of zonal mean temperature in K (top) and zonal mean wind in m s^{-1} (bottom) of the COSPAR International Reference Atmosphere 1986 for January as a function of latitude and height.

nor the summer-winter temperature distribution in the mesosphere are reproduced by the model. Figure 1.4 (bottom) presents the corresponding mean zonal wind field. The mean zonal winds are related to the temperature distribution by the thermal wind equation, i.e. they are balanced by the Coriolis force of the rotating Earth and the horizontal pressure gradient forces due to temperature gradients. Because of this exact balance, there is neither meridional nor vertical motion. No values are shown near the equator as the geostrophic approximation is not applicable there. The model winds are quite different from the observed winds of the CIRA 1986 and show that the mean state of the atmosphere departs significantly from radiative equlibrium.

To improve the agreement between model and observations a mechanism for zonal momentum dissipation was suggested [*Leovy*, 1964; *Schoeberl & Strobel*, 1978; *Holton & Wehrbein*, 1980]. This mechanism can be produced mathematically by the introduction of a so-called Rayleigh drag, i.e. a drag that decelerates the mean zonal wind speed linearly. Application of a Rayleigh drag to the model results in temperature and zonal wind distributions in much better agreement with the observations than before (see *Geller* [1983], for an example). For equilibrium conditions, an additional force is needed to counterbalance the Rayleigh drag. This can be provided by the Coriolis force if a mean meridional motion exists from the summer to the winter pole. Mass continuity then requires an upward motion at the summer pole and a compensating downward motion at the winter pole. The circulation also leads to a rising motion at the tropical tropopause and subsidence across the extratropical tropopause. The deviations of the temperature distribution from the radiative equilibrium can thus be explained by expansion cooling and compression heating [*Geller*, 1983].

Houghton [1978] considered the role various types of atmospheric waves could take in balancing the mesospheric momentum budget and proposed gravity waves as the source for the required zonal momentum drag.

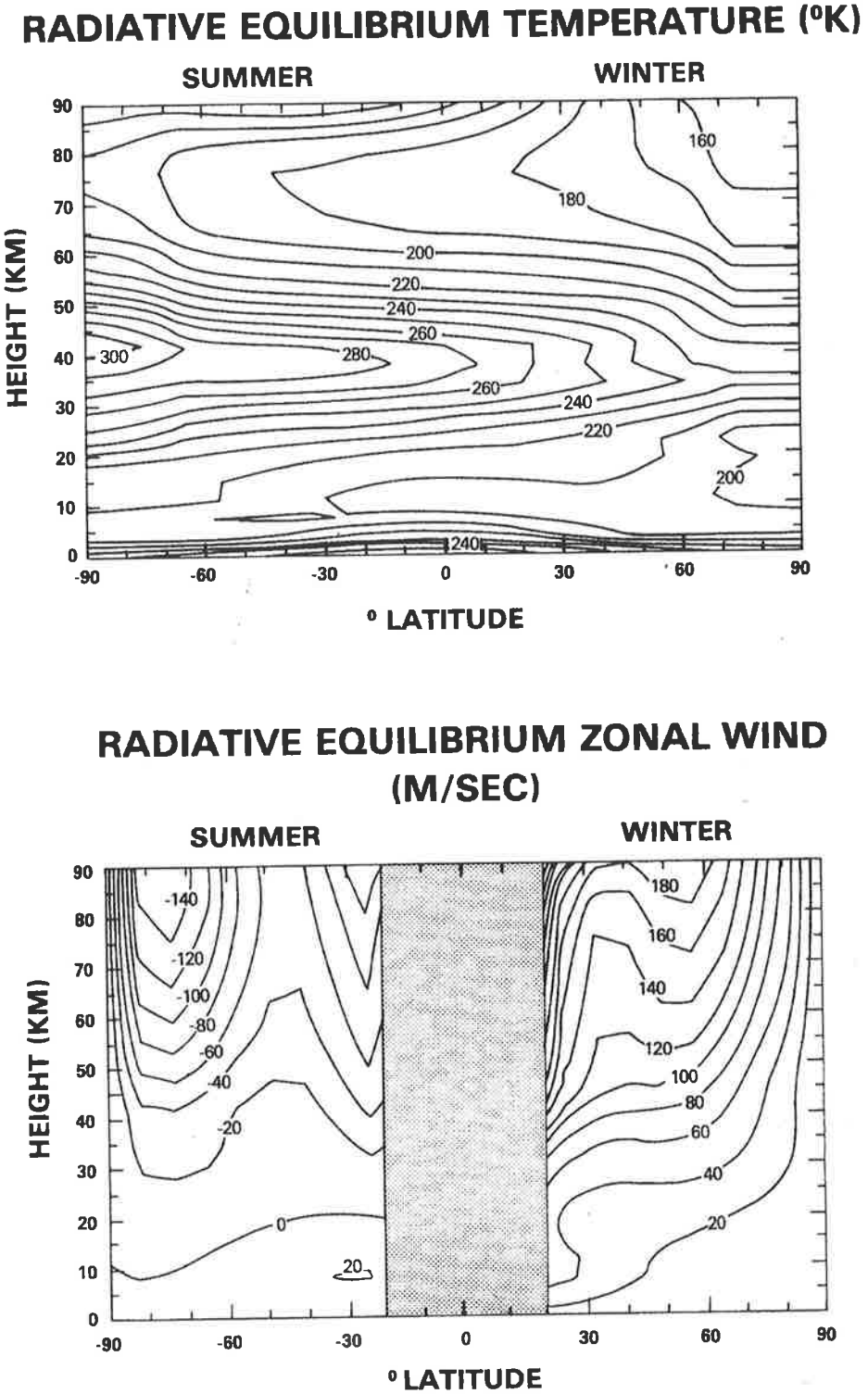

Figure 1.4: Radiative equilibrium temperatures (top) and corresponding geostrophic mean zonal winds (bottom). (From *Geller* [1983])

1.3 Gravity waves

The seminal paper by *Hines* [1960] proposed that gravity waves were the cause of the seemingly irregular appearance of wind profiles in the mesosphere. In his paper, Hines provided a mathematical description of these waves and anticipated many of their important upper atmospheric effects. He could explain the observed fluctuations, which previously had been attributed mainly to turbulence, as a superposition of gravity wave motions.

Due to their small scales, gravity waves cannot usually be resolved in global numerical simulations and the parameterization of their effects poses one of the main difficulties in global circulation models. Although the concept of gravity waves depositing energy and momentum into the mean flow had been discussed before [*Hodges Jr.*, 1967; *Hodges Jr.*, 1969; *Bretherton & Garrett*, 1969; *Hines*, 1972], it was the parameterization of *Lindzen* [1981] that found quick acceptance by modellers, who were then able to include the gravity wave drag into their models of the middle atmosphere to reach far better agreement with observations than had previously been obtained [*Matsuno*, 1982; *Holton*, 1982; *Holton*, 1983; *Dunkerton*, 1982; *Schoeberl et al.*, 1983; *Holton & Zhu*, 1984]. Only after the importance of gravity wave drag for the dynamics of the mesosphere was proven, was the effect of orographically generated gravity waves, i.e. mountain waves, also incorporated into general circulation models of the lower atmosphere, with consequent improvement of the model results [*Boer et al.*, 1984; *Palmer et al.*, 1986; *Tanaka*, 1986; *McFarlane*, 1987].

Several studies try to infer the unresolved wave drag directly from global measurements of temperature, wind, and distributions of photochemically active atmospheric constituents. This was done for the mesosphere by *Gille et al.* [1987] and *Shine* [1989], and more recently for the stratosphere by *Alexander & Rosenlof* [1996]. In contrast to the mesosphere, where the gravity wave driven force on the mean flow is decelerative, the study by *Alexander & Rosenlof* [1996] suggests an accelerative force in the stratosphere.

A multitude of experimental observations and theoretical and modelling studies over the last decades have improved considerably our understanding of gravity waves and their effects on the atmosphere [*Fritts*, 1984*a*; *Fritts*, 1989], and several different parameterization schemes have been developed since that of *Lindzen* [1981] [*Fritts & VanZandt*, 1993; *Hines*, 1997; *Warner & McIntyre*, 1999]. However, a number of fundamental scientific problems remain in formulating realistic parameterizations for the lower and middle atmosphere.

One problem in many of the current schemes is the tendency of the waves to break significantly only at high altitudes, resulting in mean-flow accelerations that are too weak at lower heights [*WMO*, 1998]. The breaking levels can be shifted to lower altitudes by increasing the wave amplitudes. To keep the average wave activity constant, however, the waves cannot be present continuously anymore but only for a certain time fraction [*Hamilton*, 1997; *Alexander*, 1998]. Quantitative information about the degree of intermittency in the real atmosphere is required to implement intermittency in gravity wave parameterization schemes. Another problem is the current lack of detailed observations to characterize the wave spectrum and its relation to possible wave sources [*WMO*, 1998]. While most gravity waves are believed to originate in the troposphere or lower stratosphere by generation mechanisms such as topography [*Smith*, 1985; *McFarlane*, 1987; *Hines*, 1988*b*; *Nastrom & Fritts*, 1992], thunderstorms [*Fovell et al.*, 1992; *Pfister et al.*, 1993; *Alexander et al.*, 1995], fronts [*Fritts & Nastrom*, 1992; *Griffiths & Reeder*, 1996; *Reeder & Griffiths*, 1996], wind shear [*Lalas & Einaudi*, 1976; *Chimonas & Grant*, 1984; *Fritts*, 1982] and geostrophic adjustment [*Schubert et al.*, 1980; *Uccellini & Koch*, 1987; *Duffy*, 1990; *Fritts & Luo*, 1992; *Luo & Fritts*, 1993], the exact shape of the gravity wave source spectrum and the relative importance of the different wave sources are largely unknown. Campaigns to study atmospheric gravity waves and their effects have been performed throughout the world using rockets [*Wu & Widdel*, 1991; *Thrane et al.*, 1994], balloons [*Allen & Vincent*, 1995], aircraft [*Bacmeister et al.*, 1996], radars [*Murayama et al.*, 1994; *Sato*, 1994], airglow imagers [*Hecht et al.*, 1994] and lidars [*Senft & Gardner*, 1991; *Whiteway &*

Carswell, 1994]. The observed geographic and seasonal variability of the gravity wave activity, however, is not necessarily due to a variability of the gravity wave sources, but could also be due to the inherent observational filters of the different methods [*Alexander*, 1998] or interactions of the waves with the background atmosphere [*Eckermann et al.*, 1994; *Eckermann*, 1995*a*; *Whiteway & Duck*, 1996]. Clearly, more detailed observations and comparisons with modeling studies are required to address the issue of variability and relative importance of different source mechanisms. Both wave intermittency and source mechanisms will be dealt with in this thesis.

In addition to the drag breaking gravity waves exert on the mean flow, they are also an important means for the transport and mixing of constituents throughout the atmosphere [*Garcia & Solomon*, 1985; *O'Sullivan & Dunkerton*, 1995; *Holton et al.*, 1995]. This is important for the study of both pollutants and photochemically active constituents, which can heat certain regions of the atmosphere and may be essential to the absorption of biologically harmful radiation from the sun.

1.4 Thesis overview

Chapter 2 gives an introduction to basic gravity wave theory, wave propagation and saturation, as necessary for the understanding of the remainder of this thesis. In Chapter 3, we introduce a wavelet-based algorithm for the extraction of gravity wave packets from operational radiosonde soundings, and apply it to radiosonde soundings of the stratosphere over Macquarie Island in Chapter 4. In the interpretation of the deduced wave parameters, great attention is paid to the observational filter of the radiosonde technique, and the importance of comparisons with modeling studies is emphasized. Wavelet analysis also provides information about the height extent of the wave packets, and can be used to obtain estimates of wave intermittency. Knowledge of wave intermittency then allows us to compute the effects of the detected wave packets on the mean flow in the lower and middle atmosphere using a linear ray-tracing model.

Due to its observational filter, each observation technique can only provide information about a certain part of the wave spectrum. In this thesis, we use radar as an alternative means to study the atmosphere with a relatively high time resolution. The fundamentals of atmospheric radar are presented in Chapter 5, and Chapter 6 introduces some radar signal processing algorithms developed during the course of this thesis. In Chapter 7, we give an overview of atmospheric turbulence theory and the possibilities to infer turbulence parameters from radar observations by measurements of the returned power and the spectral width of the radar signal, respectively.

Chapter 8 and 9 deal with the analysis of data obtained during a six-day campaign to study refractive turbulence in August 1998. Measurements of wind and turbulence parameters were performed simultaneously by radar, thermosondes, and high-altitude aircraft. We compare observations of wind and turbulence parameters by radar and thermosonde and relate the high-resolution thermosonde measurements of turbulence layers to the observed gravity wave field. A detailed analysis of the radar wind field, furthermore, allows us to deduce the parameters of a stratospheric inertio gravity-wave packet and to tentatively identify its source mechanism. A thesis summary with suggestions for future research is provided in Chapter 10.

Chapter 2

Gravity wave theory

2.1 Introduction

In the last chapter we gave a short overview of the importance of gravity waves in the atmosphere. The interpretation of observational data requires detailed knowledge about gravity wave motions and the propagation of waves through the atmosphere. While many derivations of the gravity wave solutions already exist in the literature, we consider it worthwhile to reproduce a derivation of the dispersion relation from first principles, as this will clarify the assumptions inherent in the resulting framework. Only if one is aware of these assumptions can the theory be applied meaningfully to the observations in later chapters of this thesis.

Large parts of this chapter are based on the textbooks of *Gossard & Hooke* [1975], *Gill* [1982], *LeBlond & Mysak* [1978], and *Lighthill* [1978], where more details of gravity wave theory can be found.

2.2 Dispersion relation

The fluid-dynamical equations of motion in an inviscid atmosphere can be written as

$$\frac{\mathrm{D}u}{\mathrm{D}t} - fv = -\frac{1}{\rho}\frac{\partial p}{\partial x}$$

$$\begin{aligned} \frac{\mathrm{D}v}{\mathrm{D}t} + fu &= -\frac{1}{\rho}\frac{\partial p}{\partial y} \\ \frac{\mathrm{D}w}{\mathrm{D}t} &= -\frac{1}{\rho}\frac{\partial p}{\partial z} - g, \end{aligned} \tag{2.1}$$

where: $\mathbf{u} = \begin{pmatrix} u \\ v \\ w \end{pmatrix}$ is the fluid velocity,

$f = 2\Omega \sin\theta$ is the Coriolis parameter,
with Ω the earth's angular rotation rate
and θ the latitude of observation,

ρ is the density,

p is the pressure,

g is the acceleration due to gravity, and

$\frac{\mathrm{D}}{\mathrm{D}t}$ represents differentiation following the motion,i.e.
$\frac{\mathrm{D}}{\mathrm{D}t} = \frac{\partial}{\partial t} + \mathbf{u}\nabla$.

The continuity equation is

$$\frac{\partial \rho}{\partial t} + \mathrm{div}\rho\mathbf{u} = 0. \tag{2.2}$$

If we assume the advection process to be fast enough to not allow any heat exchange of the advected parcel with its environment, the adiabatic ideal gas equation

$$\frac{\mathrm{D}p}{\mathrm{D}\rho} = \gamma \mathrm{R}T \tag{2.3}$$

can be used to close the system of equations, where $\gamma = \frac{c_p}{c_V}$ is the ratio of specific heats for constant pressure and constant volume.

Often the adiabatic ideal gas equation is expressed in terms of the potential temperature

$$\Theta = T\left(\frac{p_r}{p}\right)^{\kappa}, \tag{2.4}$$

where $\kappa = \frac{\gamma - 1}{\gamma}$ and p_r is a reference pressure often chosen as 1000 hPa. The potential temperature is the temperature that a parcel of fixed composition would acquire if

moved adiabatically to a given reference pressure level p_r. The adiabatic ideal gas equation can then be written as

$$\frac{\mathrm{D}\Theta}{\mathrm{D}t} = 0. \tag{2.5}$$

The above system of equations is highly nonlinear (due to terms in $\mathbf{u}$ in $\frac{\mathrm{D}}{\mathrm{D}t}$) and very difficult, if not impossible, to solve analytically. If we restrict ourselves to small perturbations of a zero-order state, however, the equations can be linearized and an analytical solution is much easier to achieve. Using a small ordering parameter ϵ we can write

$$\begin{aligned} u &= u_o + \epsilon u' + \epsilon^2 u'' + \dots \\ v &= v_o + \epsilon v' + \epsilon^2 v'' + \dots \\ w &= w_o + \epsilon w' + \epsilon^2 w'' + \dots \\ p &= p_o + \epsilon p' + \epsilon^2 p'' + \dots \\ \rho &= \rho_o + \epsilon \rho' + \epsilon^2 \rho'' + \dots \end{aligned} \tag{2.6}$$

Substituting Equations 2.6 into Equations 2.1 to 2.3 and assuming a background atmosphere with $\mathbf{u}(\mathbf{z}) = \begin{pmatrix} u_o \\ v_o \\ 0 \end{pmatrix}$ yields the following perturbation equations to first order in ϵ:

$$\begin{aligned} \frac{\mathrm{D}u'}{\mathrm{D}t} - fv' &= -\frac{1}{\rho_o}\frac{\partial p'}{\partial x} \\ \frac{\mathrm{D}v'}{\mathrm{D}t} + fu' &= -\frac{1}{\rho_o}\frac{\partial p'}{\partial y} \\ \frac{\mathrm{D}w'}{\mathrm{D}t} &= -\frac{1}{\rho_o}\frac{\partial p'}{\partial z} - \frac{\rho'}{\rho_o}g \end{aligned} \tag{2.7}$$

$$\frac{\mathrm{D}\rho'}{\mathrm{D}t} + w'\frac{\partial \rho_o}{\partial z} + \rho_o \mathrm{div}\mathbf{u}' = 0 \tag{2.8}$$

$$\frac{\mathrm{D}p'}{\mathrm{D}t} + w'\frac{\partial p_o}{\partial z} - \gamma \mathrm{R} T_o \left(\frac{\mathrm{D}\rho'}{\mathrm{D}t} + w'\frac{\partial \rho_o}{\partial z} \right) = 0 \tag{2.9}$$

Substituting wave-like solutions of the form

$$\begin{pmatrix} u' \\ v' \\ w' \end{pmatrix} = \rho_o^{-1/2} \begin{pmatrix} \hat{u} \\ \hat{v} \\ \hat{w} \end{pmatrix} \exp i(kx + ly + mz - \omega t) \tag{2.10}$$

$$\begin{pmatrix} p' \\ \rho' \end{pmatrix} = \rho_o^{+1/2} \begin{pmatrix} \hat{p} \\ \hat{\rho} \end{pmatrix} \exp i(kx + ly + mz - \omega t) \tag{2.11}$$

we obtain

$$\begin{aligned} -i\hat{\omega}u' - fv' + ikp' &= 0 \\ -i\hat{\omega}v' + fu' + ilp' &= 0 \\ -i\hat{\omega}w' + g\rho' + i(m - \frac{i}{2H_\rho})p' &= 0 \\ -i\hat{\omega} + i(m - \frac{i}{2H_\rho})w' + iku' + ilv' &= 0 \\ -i\hat{\omega}\frac{p'}{c_s^2} + i\hat{\omega}\rho' + \frac{N^2}{g}w' &= 0, \end{aligned} \tag{2.12}$$

where

$$\hat{\omega} = \omega - \mathbf{ku} \tag{2.13}$$

is the intrinsic frequency, i.e. the frequency in a coordinate system moving with the fluid.

$$N^2 = -\frac{g}{\rho_o}\frac{\partial \rho_o}{\partial z} - \frac{g^2}{c_s^2} = \frac{g}{\Theta_o}\frac{\partial \Theta_o}{\partial z} \tag{2.14}$$

is the buoyancy or Brunt-Vaisala frequency,

$$H_\rho = \frac{1}{\rho_o}\frac{\partial \rho_o}{\partial z} \tag{2.15}$$

the density scale height and

$$c_s = \sqrt{\gamma \mathrm{R} T_o} \tag{2.16}$$

the speed of sound. If we take the coefficients c_s, N, and H_ρ to be constant in the layer under consideration we can obtain the dispersion relation by setting the determinant of system 2.12 to zero:

$$m^2 = \frac{N^2 - \hat{\omega}^2}{\hat{\omega}^2 - f^2}(k^2 + l^2) - \frac{1}{4H_\rho^2} + \frac{\hat{\omega}^2}{c_s^2} \tag{2.17}$$

Since we used the adiabatic ideal gas equation 2.3 in our derivation, the dispersion relation 2.17 also includes an acoustic branch. Acoustic waves can be excluded by letting $c_s \to \infty$, leaving us with the dispersion relation for internal buoyancy or gravity waves:

$$m^2 = \frac{N^2 - \hat{\omega}^2}{\hat{\omega}^2 - f^2}(k^2 + l^2) - \frac{1}{4H_\rho^2} \tag{2.18}$$

Another, often invoked, approximation is the so-called Boussinesq approximation. It consists of neglecting the term $\frac{i}{2H_\rho}$ in the third and fourth equation of 2.12 and, consequently, omission of the second term in the dispersion relation 2.18. It is valid for vertical wave numbers $m \gg \frac{1}{2H_\rho}$ and, therefore, a short wavelength approximation. Figure 2.1 shows contours of constant frequency in the wavenumber domain.

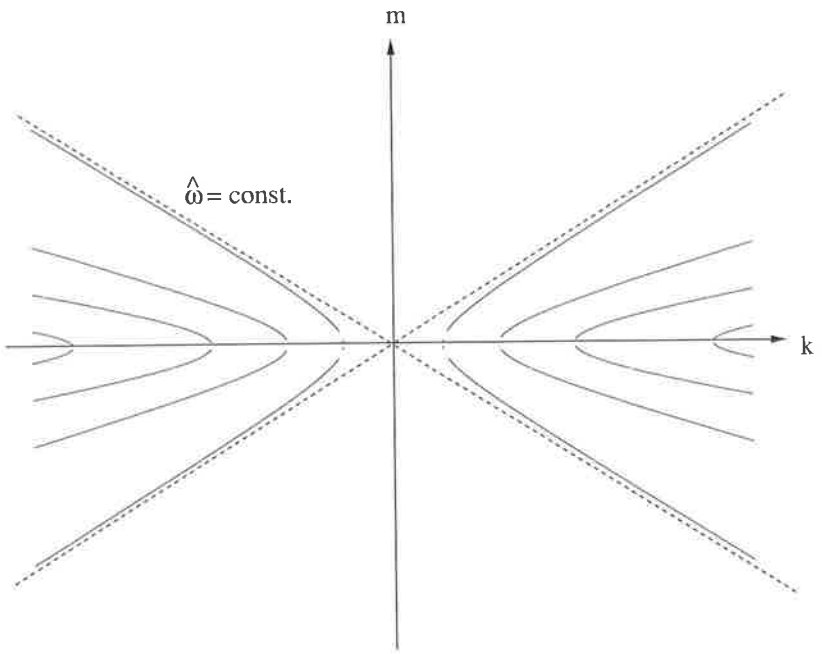

Figure 2.1: Contours of constant intrinsic frequency in the wavenumber domain using the dispersion relation Equation 2.18 (solid lines). For m sufficiently large the influence of the $\frac{1}{4H_\rho^2}$ term becomes negligible and the contour lines approach those of a Boussinesq fluid (dashed line).

A peculiarity of buoyancy waves is that phase fronts and energy move in opposite directions vertically. While the phase fronts move with the vertical phase velocity $\hat{c}_z = \frac{\hat{\omega}}{m}$, the energy is transported with the vertical group velocity

$$\hat{c}_{g,z} = \frac{\partial \hat{\omega}}{\partial m} = -\frac{m(\hat{\omega}^2 - f^2)}{\hat{\omega}(k^2 + l^2 + m^2 + \frac{1}{4H_\rho^2})}. \tag{2.19}$$

It can readily be seen that the intrinsic vertical phase and group velocities have opposite signs. The horizontal propagation direction of phase fronts and energy are both in the direction of the horizontal component of **k**.

2.3 Polarization equations

Having obtained the dispersion relation by setting the determinant of system 2.12 to zero we can now solve the system for the perturbation quantities. The equations relating these perturbation quantities are the so-called polarization equations, and the most important are given below in the Boussinesq approximation.

$$\begin{aligned} v' &= \frac{l\hat{\omega} - ikf}{k\hat{\omega} + ilf} u' \\ w' &= -\frac{\hat{\omega}m}{\hat{\omega}k + ifl} \frac{\hat{\omega}^2 - f^2}{N^2 - \hat{\omega}^2} u' \\ \hat{T}' &= \frac{T'}{T_o} = -i\frac{N^2}{g\hat{\omega}} w' = i\frac{N^2(k^2 + l^2)}{mg} \frac{1}{\hat{\omega}k + ifl} u' \end{aligned} \tag{2.20}$$

2.4 Ray-tracing equations

Up to now we have only considered the rather unrealistic case where the coefficients in system 2.12 are constant, i.e. where the properties of the medium (N, H_ρ, c_s, **u**) do not vary in height or time. It is possible to generalize this treatment to wave propagation in a medium with variable properties. This is the so-called Liouville-Green or WKB approximation, or the eikonal equation of geometric optics. It is applicable if the properties of the medium vary slowly over one wavelength and the equations with constant coefficients hold locally (see *Einaudi & Hines* [1970] for a more detailed

discussion). For a wave

$$\Phi(\mathbf{x},t) = A(\mathbf{x},t)\exp^{iS(\mathbf{x},t)} \tag{2.21}$$

this means that the amplitude $A(\mathbf{x},t)$ has to be slowly varying compared to the phase $S(\mathrm{x},t)$. We then can *define* the (ground-based) frequency ω and wavenumber $\mathbf{k}$ by

$$\omega = -\frac{\partial S(\mathbf{x},t)}{\partial t} \tag{2.22}$$

$$\mathbf{k} = \nabla S(\mathbf{x},t), \tag{2.23}$$

leading to

$$\frac{\partial \mathbf{k}}{\partial t} + \nabla\omega = 0 \tag{2.24}$$

Substituting a dispersion relation

$$\omega(\mathbf{k},\mathbf{u},\Lambda_i) = \hat{\omega}(\mathbf{k},\Lambda_i) + \mathbf{uk}, \tag{2.25}$$

where Λ_i are the parameters describing the medium, i.e. N, H_ρ, and c_s, into Equation 2.24 we obtain

$$\frac{\mathrm{D_g}k_i}{\mathrm{D}t} = -\frac{\partial\hat{\omega}}{\partial\Lambda_j}\frac{\partial\Lambda_j}{\partial x_i} - k_j\frac{\partial u_j}{\partial x_i}, \tag{2.26}$$

with summation over symmetric indices. Here

$$\frac{\mathrm{D_g}}{\mathrm{D}t} = \frac{\partial}{\partial t} + \mathbf{c}_g\cdot\nabla \tag{2.27}$$

is the derivative following a point moving with the (ground-based) group velocity of the wave

$$\mathbf{c}_g = \begin{pmatrix} \frac{\partial\omega}{\partial k} \\ \frac{\partial\omega}{\partial l} \\ \frac{\partial\omega}{\partial m} \end{pmatrix}. \tag{2.28}$$

Solving for $\frac{\mathrm{D_g}\omega}{\mathrm{D}t}$ and substituting Equation 2.26 yields

$$\frac{\mathrm{D_g}\omega}{\mathrm{D}t} = \frac{\partial\hat{\omega}}{\partial\Lambda_j}\frac{\partial\Lambda_j}{\partial t} + k_j\frac{\partial u_j}{\partial t}. \tag{2.29}$$

The ray equations 2.26, 2.28 and 2.29 together with the dispersion relation 2.18 can now be used to study the propagation of waves in a medium with variable properties as

long as the variations are sufficiently slow in space and time. In many studies one can restrict oneself to a background atmosphere that is horizontally homogeneous and independent of time. In that case the ray equations show that the ground-based frequency ω and the horizontal wave numbers k and l are invariants along the ray. Variations of wave parameters with height can then readily be computed using Equation 2.13 and the dispersion relation 2.18.

2.5 Turning and critical levels

Vertical propagation of a wave is only possible for real m, i.e. $0 < m^2 < \infty$. From the dispersion relation 2.18 one can see that this is the case [1] for $|f| < \hat{\omega} < \hat{\omega}_c$, with

$$\hat{\omega}_c^2 = N^2 - \frac{N^2 - f^2}{4H_\rho^2(k^2 + l^2 + \frac{1}{4H_\rho^2})} \tag{2.30}$$

When a wave is propagating through an atmosphere with vertical shear the intrinsic frequency is Doppler-shifted. When the wave encounters a level where the intrinsic frequency $\hat{\omega} \to \hat{\omega}_c$ the wave cannot propagate any further vertically and it will be reflected. Both the vertical wave number m and the vertical group velocity $c_{g,z}$ reach a zero-crossing at such a turning-level. A wave can, thus, be trapped in a certain height interval of the atmosphere.

If the wave approaches a so-called critical level, its intrinsic frequency is Doppler-shifted towards the inertial frequency f and its vertical wavelength approaches zero. Hence, the wave is strongly attenuated by friction. Using the WKB approximation *Bretherton* [1966] showed that an upward propagating internal wave packet would approach the critical level, but that it would not reach it in any finite time. Thus he inferred that it would be effectively absorbed. In the vicinity of the critical level, however, the WKB approximation is not valid and the governing wave equations have to be solved differently. This was done by *Booker & Bretherton* [1967], who derived an attenuation factor for the amplitude of a wave packet that crosses its critical level using linearized wave equations.

[1] We follow the convention that $\hat{\omega} > 0$.

2.6 Wave action

While the ray equations 2.26, 2.28 and 2.29 enable us to calculate the variation of frequency and wavenumber along a ray path, they do not contain any information about the amplitude of the wave. *Bretherton & Garrett* [1969] found that for slowly varying waves of small amplitude the wave-action density

$$A = \frac{E}{\hat{\omega}}, \tag{2.31}$$

where E is the wave energy density and $\hat{\omega}$ the intrinsic frequency, is conserved following a wave,

$$\frac{\partial A}{\partial t} + \nabla(\mathbf{c}_g A) = 0. \tag{2.32}$$

Andrews & McIntyre [1978*b*] gave a generalized derivation of this result. Due to the involvement of spatial derivatives of $\mathbf{c}_g$, Equation 2.32 requires consideration of a bundle of neighbouring rays to include horizontal deformations of the wave packet. As the fine scale geography of wave sources is not known, however, modelers often restrict themselves to quasi-one-dimensional models. In the case of a steady-state atmosphere, Equation 2.32 then simplifies to

$$\frac{\partial}{\partial z}\left(A \cdot c_{g,z}\right) = 0, \tag{2.33}$$

the conservation of vertical wave action flux.

2.7 Wave-mean flow interactions

When a gravity wave propagates through the background atmosphere, air parcels are accelerated and displaced. Yet, when averaged over one wave cycle, the net momentum flux of wave-induced particle motions is zero, and the displaced air parcels are returned to their equilibrium position as long as the processes involved are reversible. When material contours are deformed irreversibly, however, for example by wave breaking, then momentum is transferred to the mean flow. Mathematically, this momentum transfer can be described by the Reynolds stress tensor [*Bretherton*, 1969*a*], whose

divergence appears as a force term in the momentum equations. The most important Reynolds stress term for gravity waves is the vertical flux of horizontal momentum, but there is also a contribution due to the meridional transport of heat, which becomes important for waves of low intrinsic frequency. All these contributions are included in the generalized Eliassen-Palm flux [*Eliassen & Palm*, 1961; *Andrews & McIntyre*, 1976; *Andrews & McIntyre*, 1978*a*]. Often it is easier to work in terms of the wave pseudo-momentum flux given by [*McIntyre*, 1981]

$$\mathbf{F_p} = \mathbf{k}\frac{E}{\hat{\omega}}c_{g,z}. \tag{2.34}$$

The resulting wave induced acceleration is then simply given by

$$\frac{\partial}{\partial t}\mathbf{u} = -\frac{1}{\rho_o}\frac{\partial}{\partial z}(\rho_o \mathbf{F_p}). \tag{2.35}$$

2.8 Dissipative processes

Wave dissipation has to occur in order to transfer momentum to the mean background flow wave. Dissipative processes include wave-breaking (dynamic and convective instability), non-linear wave-wave interactions, and radiative or turbulent damping.

Dynamic instability can occur if the wave-induced shear is large enough that the kinetic energy extracted from the mean-flow is sufficient to overcome the buoyancy forces to overturn the wave. The Richardson number

$$\mathrm{Ri} = \frac{N^2}{\left(\frac{\partial u}{\partial z}\right)^2} \tag{2.36}$$

represents the ratio of work required to interchange vertically adjacent air parcels against buoyancy to the kinetic energy available to do this work. *Miles* [1961] established a stability criterion for plane parallel shear flows in an incompressible fluid. His criterion states that $\mathrm{Ri} \geq \frac{1}{4}$ everywhere in the flow is a sufficient condition for stability in a stratified shear flow. An extension to compressible fluids was provided by *Chimonas* [1970]. A very simplified reasoning to understand the number of $\frac{1}{4}$ as a critical value was given by *Ludlam* [1967]. He considered the exchange of two air parcels

with vertical separation Δz in a stratified medium with plane parallel shear flow. To exchange the two air parcels each parcel has to be removed a distance Δz from its equilibrium position. The gain in potential energy per unit volume is, therefore,

$$\Delta E_{\text{pot}} = 2 \cdot \frac{1}{2}\overline{\rho} N^2 \Delta z^2, \tag{2.37}$$

where $\overline{\rho}$ is the average density. Ludlam furthermore assumed this parcel interchange to be the result of a momentum equalizing disturbance [2]. The kinetic energy difference between the initial and final state is, therefore,

$$\begin{aligned} \Delta E_{\text{kin}} &= \frac{1}{2}\overline{\rho}\left(u(z)^2 + \left(u(z) + \frac{\partial u}{\partial z}\Delta z\right)^2 - 2\left(\frac{u(z) + u(z) + \frac{\partial u}{\partial z}\Delta z}{2}\right)^2\right) \\ &= \frac{1}{4}\overline{\rho}\left(\frac{\partial u}{\partial z}\right)^2 \Delta z^2. \end{aligned} \tag{2.38}$$

To enable this air parcel interchange from an energetic point of view the released kinetic energy has to be at least the gained potential energy:

$$\text{Ri} = \frac{N^2}{\left(\frac{\partial u}{\partial z}\right)^2} \leq \frac{1}{4} \tag{2.39}$$

In the case of convective (static) stability, the wave modifies the local buoyancy frequency in such a way, that the buoyancy forces amplify small perturbations, i.e. the buoyancy force (per unit mass) on an air parcel a vertical distance ξ from its equilibrium position, $F_b = -N^2\xi$, tries to increase ξ. This implies $N^2 < 0$ and, therefore,

$$\text{Ri} = \frac{N^2}{\left(\frac{\partial u}{\partial z}\right)^2} < 0. \tag{2.40}$$

Hodges Jr. [1967] used linear gravity wave theory to calculate a threshold for wave instability. He found that a wave becomes convectively unstable if its perturbation amplitude (in direction of horizontal wave propagation) $u'_{||}$ exceeds its intrinsic horizontal phase speed $\hat{c}_{phase}$,

$$u'_{||} \geq \hat{c}_{phase} = \frac{\hat{\omega}}{\sqrt{k^2 + l^2}}. \tag{2.41}$$

[2] As shown by *Hines* [1988*a*] this is equivalent to a release of maximum kinetic energy.

He also showed that for a monochromatic gravity wave of frequency $\hat{\omega} \gg f$ (i.e. essentially two-dimensional) the criterion for convective instability (Ri < 0) requires only a small fractional increase in wave amplitude once the dynamic instability criterion (Ri $< \frac{1}{4}$) is fulfilled. As the e-folding time of the instability shortens dramatically as Ri changes from positive to negative values [*Hines*, 1988*a*] convective stability is assumed to dominate the saturation process for $\hat{\omega} \gg f$. Surprisingly, the minimum of the Richardson number Ri is reached near that phase of the wave motion where the amplitude is maximum, that is the region where the shear of the horizontal velocity is near zero [*Hodges Jr.*, 1967; *Fritts & Rastogi*, 1985].

For frequencies $\hat{\omega} \approx f$, where rotational effects are important, the wave induced shear also includes a transverse component. This leads to an amplitude required for dynamic instability much less than that for static instability [*Fritts & Rastogi*, 1985; *Fritts*, 1989]:

$$u'_{\parallel} \geq \frac{2\sqrt{1-\frac{f^2}{\hat{\omega}^2}}}{1+\sqrt{1-\frac{f^2}{\hat{\omega}^2}}}\hat{c}_{phase} \tag{2.42}$$

As a generalization of the above scheme, Hines argued that the gradients introduced by the gravity wave motions are not necessarily vertical [*Hines*, 1971; *Hines*, 1988*a*]. He considered energetics of air parcels which are interchanged along an arbitrary axis s, inclined at an angle α to the vertical. Such a slantwise interchange is energetically feasible, if, for dynamic instability [*Hines*, 1971]

$$\frac{\frac{g}{\Theta}\frac{\partial\Theta}{\partial s}\cos\alpha}{\left(\frac{\partial u}{\partial s}\right)^2} \leq \frac{1}{4}, \tag{2.43}$$

and, for static instability, [*Hines*, 1988*a*]

$$\frac{g}{\Theta}\frac{\partial\Theta}{\partial s}\cos\alpha < 0. \tag{2.44}$$

His equations reduce to the criteria given above when the s axis is chosen to be vertical, i.e. $\alpha = 0$.

Energetic feasibility at a certain time, however, does not ensure that an instability actually develops. *Hines* [1988*a*] argued that the condition for instability should have to last for a sufficiently long time to allow perturbations to grow. In the case of gravity

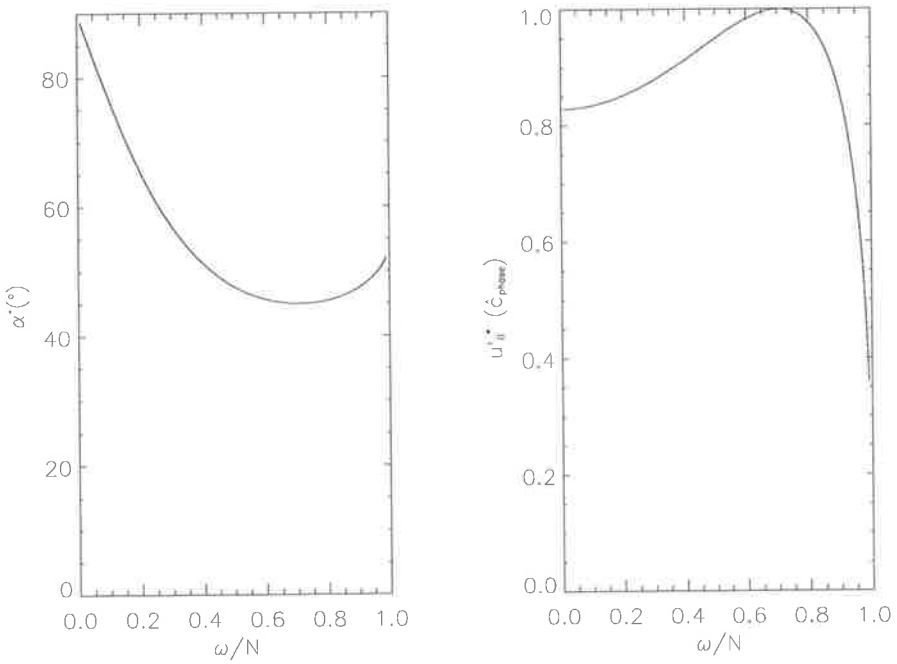

Figure 2.2: Zenith angle α^* most favourable for the development of turbulence from slantwise static instability and required normalized horizontal perturbation velocity as a function of normalized frequency. The horizontal perturbation velocity is given in units of $\hat{c}_{phase}$, i.e. as fraction of the horizontal perturbation velocity required for vertical static instability.

waves, he proposed that the e-folding time for the growth of the instabilities, τ, has to be smaller than some fraction $(2\pi\beta)^{-1}$ of the intrinsic wave period for the instabilities to develop. Figure 2.2 shows the zenith angle α^* which requires the smallest horizontal perturbation velocity $u'^*_{||}$ to develop turbulence via static instability. A value of $\beta = 1$ was used as recommended by *Hines* [1988*a*]. The figure shows that slantwise static instability occurs for smaller perturbation velocities than vertical static instability and that the axis along which the parcel interchange occurs is closer to the horizontal than to the vertical. *Marks & Eckermann* [1995] extended the scheme to include dynamic instability. This leads to saturation amplitudes around 10 percent smaller than those given by Equation 2.42 for $\hat{\omega} \approx f$ if $\beta = 1$ is used.

Equations 2.1 to 2.3 were linearized under the assumption that the perturbation

amplitudes were small enough to neglect higher-order terms. Even though these non-linear terms do not affect the linear solution considerably over time spans of a wave period, the cumulative effect of the non-linear interactions over many periods (or between several waves) might be important. Consider two plane waves with wave numbers $\mathbf{k_1}$ and $\mathbf{k_2}$ and intrinsic frequencies $\hat{\omega}(\mathbf{k_1})$ and $\hat{\omega}(\mathbf{k_2})$. Products of perturbation quantities in the governing equations lead to terms in

$$e^{i(\mathbf{k_1}\mathbf{x}-\hat{\omega}(\mathbf{k_1})t)} \cdot e^{i(\mathbf{k_2}\mathbf{x}-\hat{\omega}(\mathbf{k_2})t)} = e^{i((\mathbf{k_1}+\mathbf{k_2})\mathbf{x}-(\hat{\omega}(\mathbf{k_1})+\hat{\omega}(\mathbf{k_2}))t)}, \tag{2.45}$$

i.e. they describe a forcing of a wave with wavenumber $\mathbf{k_1}+\mathbf{k_2}$ and frequency $\hat{\omega}(\mathbf{k_1})+\hat{\omega}(\mathbf{k_2})$. If the wave number and frequency of the forced wave fulfill the dispersion relation,

$$\hat{\omega}(\mathbf{k_1})+\hat{\omega}(\mathbf{k_2}) = \hat{\omega}(\mathbf{k_1}+\mathbf{k_2}), \tag{2.46}$$

then resonance occurs and the three waves are said to form a resonant triad. Generally, a whole spectrum of wave exists, and the amplitude of a wave of wavenumber $\mathbf{k}$ and frequency $\hat{\omega}$ is affected by many possible resonant triads. However, *McComas & Bretherton* [1977] showed that the transfer of energy in an internal wave spectrum is dominated by three classes of nonlinearly interacting triads (Figure 2.3):

1. Induced diffusion: Here the triad consists of one low-frequency wave and two nearly identical waves of much larger wave number and frequency. The shear of the former wave acts as a slowly-changing background flow to the latter waves. This will affect the spectrum primarily as a diffusion of wave action in vertical wavenumber in the region of small-scale large-frequency waves.

2. Elastic scattering: The triad contains two waves which are nearly vertical reflections of each other and a third low-frequency nearly vertical wave with twice the vertical wave number of the first two waves. The third wave, thus, acts in a way similar to that of a crystal lattice in Bragg scattering and equalizes the intensity of upwards and downwards propagating waves. Most of the energy exchange is between the two high-frequency waves.

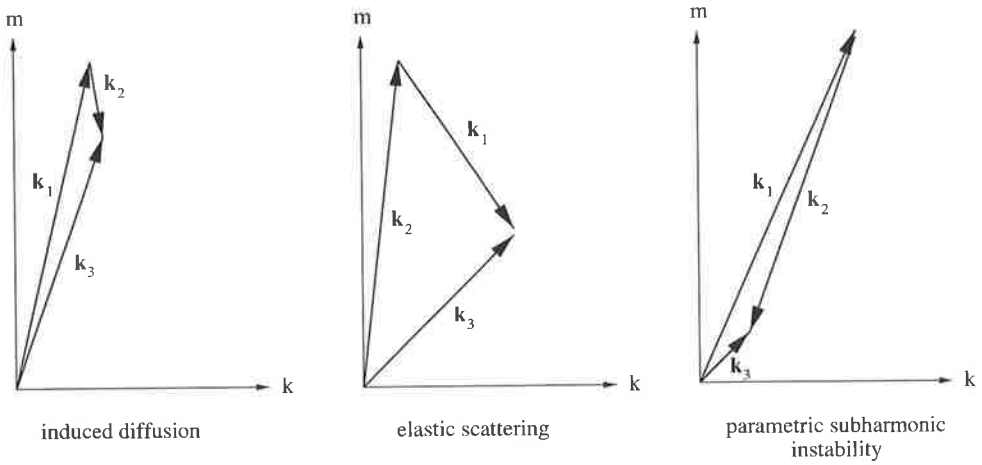

Figure 2.3: Representation of the three resonant triad classes (after *McComas & Bretherton* [1977]).

3. Parametric subharmonic instability: Here two waves of nearly opposite wave numbers interact with a wave of much smaller wave number and twice the frequency. Energy is lost from the large-scale wave to the waves at half its frequency. *Hasselmann* [1967] has shown that a wave is unstable, if two members of a resonant trio with lower frequency can be found. In the case of internal gravity wave this means that any wave with a frequency $\hat{\omega} > f$ is unstable, as one should always be able to find two waves of frequency $\hat{\omega} > f$ to make up a resonant triad. This suggests that the inertial peak of the internal wave spectrum may be due to parametric subharmonic instability.

In contrast to the static and dynamic instabilities, these non-linear effects do not require a certain amplitude of the wave motion to be invoked but act on waves of all amplitudes. Thus, they might keep the wave amplitudes low enough to prevent the occurrence of static and convective instabilities [*Fritts & Rastogi*, 1985].

2.9 Gravity wave spectra

2.9.1 Universality

Wind and temperature fluctuations due to gravity waves are conveniently described in terms of power spectra versus frequency or vertical wavenumber. These spectra were observed to be independent of season, meteorological conditions and geographical location, and *VanZandt* [1982] pointed out that they can be described in terms of a universal spectrum of internal gravity waves. *VanZandt* [1985] compiled gravity wave spectra from different sources and compared them with the universal spectrum. He noted that the vertical wavenumber spectra of horizontal wind speed fluctuations increased negligibly with altitude compared to the frequency spectra, at least for the large vertical wave numbers that were considered. The spectra seemed to be saturated for large enough vertical wave numbers m and were of the form m^{-t} with t somewhere around 3.

Since then, several theories have been suggested to explain the observed spectrum by means of gravity wave saturation [*Dewan & Good*, 1986; *Smith et al.*, 1987; *Weinstock*, 1990; *Hines*, 1991*b*; *Dewan*, 1994; *Gardner*, 1994; *Zhu*, 1994; *Medvedev & Klaassen*, 1995]. Each theory proposes physical processes responsible for limiting wave amplitude growth and predicts a saturated vertical wavenumber spectrum for horizontal wind fluctuations approximately proportional to N^2/m^3 for large m. According to *Hines* [1993], these theories can be divided into three main classes. In the first class, the spectral amplitudes at high vertical wave numbers are limited by linear instability of either individual waves or the wave field as a whole [*Dewan & Good*, 1986; *Smith et al.*, 1987; *Dewan*, 1994]. The second is based on the idea that the saturation is caused by some form of wave dissipation due to non-linear, off-resonant wave-wave interactions [*Weinstock*, 1990; *Gardner*, 1994; *Zhu*, 1994; *Medvedev & Klaassen*, 1995], while in the third class individual waves are Doppler-spread by the whole spectrum to large wave numbers and dissipated once a threshold wavenumber is reached [*Hines*, 1991*b*].

2.9.2 Spectral parameterization

Even though there is no consensus about which physical mechanism is causing the saturation of the vertical wavenumber spectra at large vertical wave numbers, parameterizations of the gravity wave spectrum are a useful means to describe the observed spectra. One commonly applied spectral parameterization was provided by *Fritts & VanZandt* [1993]. They assume an upwards propagating spectrum of total energy per unit mass, that is separable in vertical wavenumber m, intrinsic frequency $\hat{\omega}$, and azimuthal propagation direction ϕ,

$$E(\mu, \hat{\omega}, \phi) = E_o A(\mu) B(\hat{\omega}) \Phi(\phi), \tag{2.47}$$

where

$$A(\mu) = A_o \frac{\mu^s}{1 + \mu^{s+t}} \tag{2.48}$$

$$B(\hat{\omega}) = B_o \hat{\omega}^{-p} \tag{2.49}$$

and where $\mu = m/m_*$, m_* is the characteristic vertical wavenumber, and (s, t, p) are chosen by comparison with observed power spectra as $(1, 3, \frac{5}{3})$. The functions $A(\mu)$, $B(\hat{\omega})$, and $\Phi(\phi)$ are normalized to unity when integrated over all possible μ, $\hat{\omega}$, and ϕ, respectively. Assuming the polarization relations in Boussinesq approximation, but allowing for non-hydrostatic ($\hat{\omega} \sim N$) and rotational ($\hat{\omega} \sim f$) effects, the variance spectra for the horizontal and vertical perturbation velocities u', v', and w' can be expressed as

$$E_u(\mu, \hat{\omega}, \phi) = E(\mu, \hat{\omega}, \phi) \left[\cos^2 \phi + \left(\frac{f}{\hat{\omega}} \right)^2 \sin^2 \phi \right] \gamma \tag{2.50}$$

$$E_v(\mu, \hat{\omega}, \phi) = E(\mu, \hat{\omega}, \phi) \left[\sin^2 \phi + \left(\frac{f}{\hat{\omega}} \right)^2 \cos^2 \phi \right] \gamma \tag{2.51}$$

$$E_w(\mu, \hat{\omega}, \phi) = \left(\frac{\hat{\omega}}{N} \right)^2 E(\mu, \hat{\omega}, \phi), \tag{2.52}$$

where $\delta_\pm = 1 \pm (f/\hat{\omega})^2$ and $\gamma = 1 - (\hat{\omega}/N)^2$.

Chapter 3

Wavelet algorithm

3.1 Introduction

Gravity waves play an important role in driving the circulation of the atmosphere as demonstrated in numerical modeling studies [*Lindzen*, 1981; *Holton*, 1982; *Dunkerton*, 1982; *Garcia & Solomon*, 1985]. Since the resolution of general circulation models is usually too coarse to adequately resolve gravity waves, several gravity wave parameterization schemes have been developed to take these unresolved wave effects into account [*Lindzen*, 1981; *Fritts & VanZandt*, 1993; *Hines*, 1997; *Warner & McIntyre*, 1999]. These models generally require information about the gravity wave spectrum at a certain source level which is then propagated through the atmosphere. In a physically realistic model the choice of this source spectrum is influenced by experimental observations of the gravity wave field at the source height and by the agreement of the parameterized effects with measurements throughout the atmosphere.

Many experimental campaigns have been conducted to study characteristics and effects of gravity waves in the lower, middle, and upper atmosphere over the last decades. While some methods aim to directly measure the momentum fluxes associated with the gravity wave field [*Vincent & Reid*, 1983; *Fritts et al.*, 1990; *Sato*, 1994; *Alexander & Pfister*, 1995], others try to obtain information about the gravity wave activity from gravity wave induced perturbations of the wind and temperature fields. Radar winds

have been analyzed in the lower and middle atmosphere at several locations, but the geographical coverage of these campaigns is rather sparse. The increasing use of high resolution radiosondes for operational soundings of the lower atmosphere, on the other hand, has the potential to compile a global climatology of gravity wave activity around the world [*Hamilton & Vincent*, 1995]. As each method can only observe a part of the gravity wave spectrum, however, different methods have to be used together to enable a better understanding of the processes involved [*Alexander*, 1998].

In this chapter we develop a wavelet-based method to decompose vertical profiles of horizontal wind into gravity wave packets. While wavelet analysis has been applied to wind and temperature fluctuations in the atmosphere previously [*Sato & Yamada*, 1994; *Chen et al.*, 1995; *Shimomai et al.*, 1996], these studies mainly concentrated on the changes of the wavelet spectrum with time or height, and less on the packet structure of the gravity wave field.

3.2 Hodograph analysis

Hodograph analysis is a well known means of extracting gravity wave parameters from vertical wind profiles. The horizontal perturbation velocity vector as a function of height, the so called hodograph, of a single plane gravity wave traces out an ellipse (Figure 3.1). Using the polarization and dispersion relations it is possible to infer important parameters of this gravity wave from its hodograph.

To facilitate the algebra we rotate the coordinate system so that the horizontal wavenumber vector coincides with the new x-axis. The wind profile is taken at $x = y = 0$, and if we assume that the measurements are taken within a time t much smaller than the wave period, we can also set $t = 0$. The polarization equations 2.20 can then be written as

$$u'_{||} = \rho_o^{-1/2} \hat{u}_{||} \exp(imz) \tag{3.1}$$

$$v'_{\perp} = -i \frac{f}{\hat{\omega}} u'_{||} \tag{3.2}$$

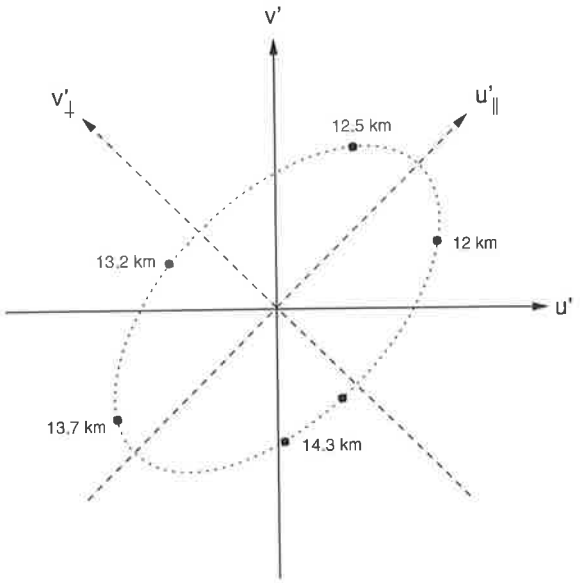

Figure 3.1: Hodograph of a single gravity wave. The horizontal perturbation velocity vector traces an ellipse as a function of height. The horizontal propagation direction of the gravity wave is parallel to the major axis. The anti-clockwise rotation indicates an upward propagating wave (southern hemisphere).

$$\hat{T}' = i\frac{N^2}{g\hat{\omega}}\frac{k}{m}u'_{\|}, \tag{3.3}$$

where $u'_{\|}$ and $v'_{\perp}$, respectively, are the horizontal perturbation velocities parallel and perpendicular to the horizontal wave propagation direction.

Inspection of Equations 3.1 and 3.2 shows that the horizontal perturbation velocity vector (as a function of height) traces an ellipse with the major axis parallel to the horizontal propagation direction and the axial ratio equal to the ratio of Coriolis parameter f and intrinsic frequency $\hat{\omega}$. The sense of rotation is given by the signs of m and f and indicates the vertical propagation direction of the wave (anti-clockwise for upwards propagating waves in the southern hemisphere). The ambiguity in the horizontal propagation direction can be resolved by obtaining the sign of k from the phase shift between $\hat{T}'$ and $u'_{\|}$ and Equation 3.3. Finally, the dispersion relation yields the magnitude of k.

In the case of non-negligible wind shear in the background wind, equation (3.2) and the dispersion relation (2.18) are coupled by a term in $\frac{dv_{\perp}}{dz}$ [*Hines*, 1988*c*]. Then these

two equations have to be solved simultaneously for $\hat{\omega}$ and the magnitude of k. Thus, if the wind profile is determined by a single coherent wave, it is possible to deduce the wave parameters from the hodograph of the perturbation velocities. In practice, however, the wind profile often contains a superposition of different gravity waves. In order to get meaningful results, these waves have to be detected and isolated in vertical wavenumber and/or height prior to hodograph analysis. The aim of the next section is to demonstrate the advantages wavelet analysis can have in this process compared to more established Fourier methods.

3.3 Isolation of wave packets in the wind profile

Fourier transformation can be used to separate waves according to their vertical wavelength. For each wavelength, a single sine wave is fitted over the whole considered height range (to u' and v' profiles separately). Its amplitude and phase give the average contribution of all waves of the respective wavelength present anywhere within the whole height range. In wavenumber-height space, this can be represented as a tiling with excellent wavenumber resolution, but no height resolution (Figure 3.2).

Different methods exist, which perform the hodograph analysis directly in Fourier space, e.g. rotary spectra [*Gonella*, 1972], Stokes parameters [*Eckermann & Vincent*, 1989; *Vincent & Fritts*, 1987] and cross spectral methods [*Cho*, 1995]. In a recent paper *Eckermann* [1996] has shown how exactly these methods are related to each other and how all of them can be expressed in terms of Stokes parameter analysis.
Due to the averaging process over the whole height range several problems can arise: Two gravity wave packets, separated in height, but with the same sense of rotation and the same mean vertical wavelength, will contribute to the same wavelength bin. If the wave packets have different horizontal propagation directions or frequencies, then the parameters obtained from the hodograph analysis of their common wavelength bin might yield erroneous results.
Another problem is due to irregularities, such as sharp peaks at temperature inversions.

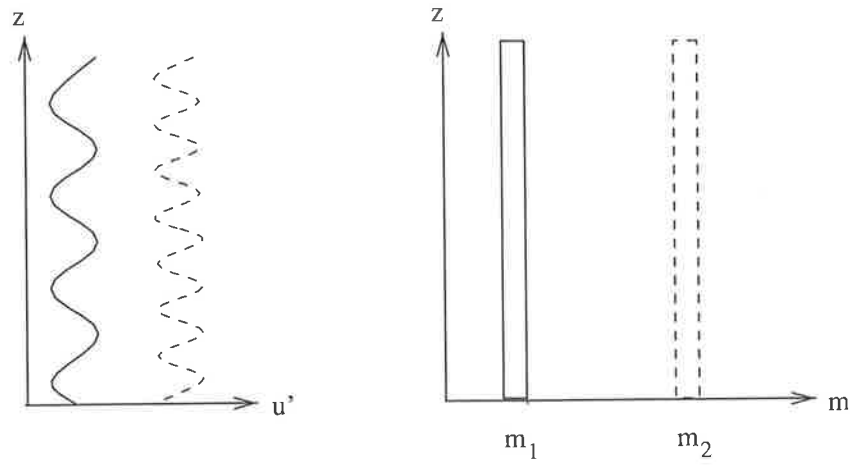

Figure 3.2: Schematic representation of the Fourier transform. For each wavelength a sine wave extending over the whole height range is fitted to the wind profile. In wavenumber-height space this corresponds to a tiling with good wavenumber resolution but no height resolution.

Because the Fourier transform averages over the whole height range these irregularities will contaminate the whole profile. It is clear that a separation in both vertical wavenumber and height is necessary.

In the windowed Fourier transform, a window of a certain height Δz is slid along the wind profile, and the Fourier transform is applied only within this window. The gain in height resolution Δz causes a loss in wavenumber resolution Δm, such that $\Delta z \cdot \Delta m = \text{const.}$. While it is now possible to locate a wave packet within the analyzed height range, the uncertainty in the estimation of its wavelength is increased. The method is illustrated in Figure 3.3.

The (subjective) choice of a window height or height resolution Δz fixes the wavenumber resolution Δm and, therefore, emphasizes certain wavelengths. For $\Delta z \ll \lambda$, only a fraction of the wave packet will lie within the window and the relative error in wavenumber, $\frac{\Delta m}{m}$, will be quite large. For $\Delta z \gg \lambda$, on the other hand, this relative error will be favourably small, but the wave packet cannot be located properly. The window might even contain two different wave packets separated in height, and the same considerations as made for the Fourier transform apply.

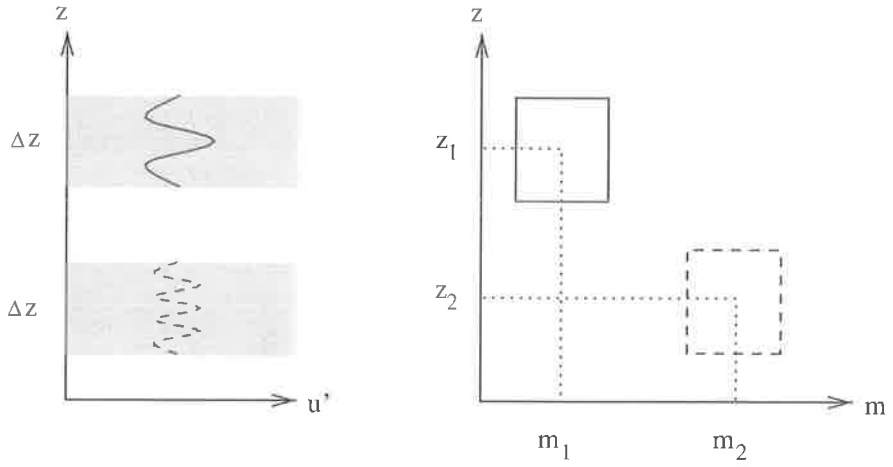

Figure 3.3: Schematic representation of the windowed Fourier transform. Here the functions that are fitted to the wind profile extend only over a small window of height Δz, which is slid along the data series. The increased height resolution leads to a decreased wavenumber resolution, as shown in the tiling of the wavenumber-height space.

A method is desirable that does not favour any particular scale or wavelength, but treats all of them equally. This is achieved by the wavelet transform. Here the window size Δz is adjusted depending on the considered wavelength λ (Figure 3.4). For large λ, a large Δz is used, while for small λ a small Δz is chosen, such that $\Delta z = \text{const.} \cdot \lambda$. In keeping the number of oscillations within the window constant, all wave packets can be adequately located and the relative wavenumber resolution $\frac{\Delta m}{m}$ is independent of m.

For wave packets which extend over a large height range, the restriction to a window of size Δz results in a wavenumber resolution worse than what could be achieved with a Fourier transform of the whole wave packet. To overcome this problem, the wavelet transform will only be used as a means to detect wave packets objectively. Once detected, it is possible to reconstruct the wave packet from its wavelet coefficients and analyze it separately with the method of choice.[1]

[1] As the background atmosphere probably changes over the extent of the wave packet so will the wavenumber of the wave packet. An increase in nominal wavenumber resolution much in excess of the bandwidth of the physical wave packet does not, therefore, yield any new information.

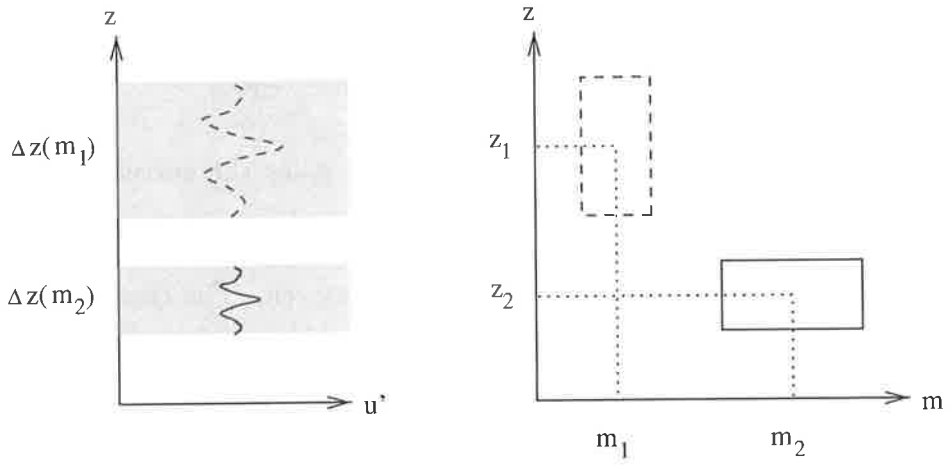

Figure 3.4: Schematic representation of the wavelet transform. Here the height range Δz of the fitted functions is adjusted to keep the number of oscillations within the window constant. The relative height and wavenumber resolutions, $\frac{\Delta z}{\lambda}$ and $\frac{\Delta m}{m}$, respectively, are independent of m.

3.4 The Wavelet Transform

3.4.1 Basic Formalism

In this section we give the definitions necessary to implement the wavelet algorithm described in this chapter. For a more detailed description and a review of wavelet applications in geophysics see [*Kumar & Foufoula-Georgiou*, 1997] and references therein.

The term wavelets refers to a family of small waves generated from a single function $g(z)$, the so-called mother wavelet, by a series of dilations and translations. A sufficient condition for a function $g(z)$, real or complex, to qualify as a mother wavelet is admissibility,

$$c_g = \int_{-\infty}^{+\infty} \frac{|G(m)|^2}{|m|} \mathrm{d}m < \infty, \tag{3.4}$$

where $G(m)$ is the Fourier transform of $g(z)$.[2] If $g(z)$ is an integrable function, it only has to be oscillatory, of finite energy and with an average value of zero to fulfill this criterion.

The continuous wavelet transform of a real function $f(z)$ with respect to a given

[2]This admissibility condition is a sufficient, but not necessary condition for $g(z)$.

admissible mother wavelet $g(z)$ at scale a and dilation b is then defined as[3]

$$W_f(a,b) = \frac{1}{a}\int_{-\infty}^{+\infty} f(z)g^*(\frac{z-b}{a})\mathrm{d}z, \tag{3.5}$$

where $a > 0$ and $b \in \mathbf{R}$. The wavelet transform gives the correlation between the original function $f(z)$ and the scaled and translated version of the mother wavelet, $g(\frac{z-b}{a})$, i.e. it measures how well the two signals match. The transform can also be expressed in Fourier space as

$$W_f(a,b) = \frac{1}{2\pi}\int_{-\infty}^{+\infty} G^*(am)F(m)\exp(imb)\mathrm{d}m, \tag{3.6}$$

which shows that the wavelet transform is basically a bandpass filtered version of the original function $f(z)$. If $G(m)$ is centered at $\hat{m}$ with width Δm, then the scaled wavelet $G(am)$ is centered at $\frac{\hat{m}}{a}$ with width $\frac{\Delta m}{a}$. The relative wavenumber resolution is, therefore, given by the choice of the mother wavelet and independent of scale. In the general case, however, the mother wavelet can show holes and spikes in its Fourier spectrum, and the bandpass interpretation should not be taken too literally. After all, the great flexibility of the wavelet transform originates in the choice of an almost arbitrary mother wavelet.

Admissibility is required to make sure that the original function $f(z)$ can be reconstructed from its wavelet transform without any loss of information. This reconstruction can be accomplished by summing scaled and translated versions of the mother wavelet appropriately weighted with the wavelet coefficients $W_f(a,b)$:

$$f(z) = \frac{1}{c_g}\int_0^{+\infty}\int_{-\infty}^{+\infty} W_f(a,b)g(\frac{z-b}{a})\frac{\mathrm{d}b\mathrm{d}a}{a^2}. \tag{3.7}$$

The continuous wavelet transform (3.5) is calculated for all points of the $a > 0 - b \in \mathbf{R}$-plane and shows a high degree of redundancy. Due to this redundancy it is possible to reconstruct the original function using a completely different mother wavelet, e.g. the delta function [*Farge*, 1992]:

$$f(z) = \frac{1}{c_\delta}\int_0^{+\infty} W_f(a,z)\frac{\mathrm{d}a}{a}, \tag{3.8}$$

[3]For convenience we chose a different normalization of the wavelet coefficients than is commonly applied.

where

$$c_\delta = \int_0^{+\infty} W_\delta(a,0)\frac{\mathrm{d}a}{a}. \tag{3.9}$$

With the normalization chosen above, the modulus square of the wavelet coefficients, $E(a,b) = |W_f(a,b)|^2$, can be interpreted as an energy density, at least for bandfilter-like mother wavelets. The total energy of the signal is given by[4]

$$E_{tot} = \frac{1}{c_g}\int_0^{+\infty}\int_{-\infty}^{+\infty} E(a,b)\mathrm{d}b\frac{\mathrm{d}a}{a}. \tag{3.10}$$

It is possible to reduce the redundancy inherent in the continuous wavelet transform and to calculate the wavelet coefficients for a discrete subset of the a-b plane only, but restrictions in addition to the admissibility (3.4) have to be applied. A commonly used subset for the discrete wavelet transform is the dyadic grid,$a = \frac{1}{2^j}, b = \frac{k}{2^j}, \quad j,k \in \mathbf{Z}$, for which fast algorithms exist.

3.4.2 Selection of a Mother wavelet

Having introduced the basic wavelet formalism, the next step is to choose the wavelet best suited for our purposes.

As mentioned above, a discrete wavelet transform works only on certain discrete scales, with the corresponding bandpass filters centered at discrete wave numbers. Consider two gravity wave packets as represented by the shaded regions in Figure 3.5. To reconstruct the packet at small wavenumber m, information from Scale 1 and Scale 2 of the discrete transform is required. But Scale 2 contains a significant part of the wave packet at large m, so that the two wave packets cannot be easily separated. With the continuous wavelet transform, on the other hand, the scale is adjusted quasi-continuously, corresponding to a bandpass filter that slides along the wavenumber axis. The central wavenumber of the filter can therefore be adjusted to contain each of the wave packets alone, enabling an easy separation.

[4]Note that total energy conservations holds for all wavelet transforms irrespectively of their orthogonality.

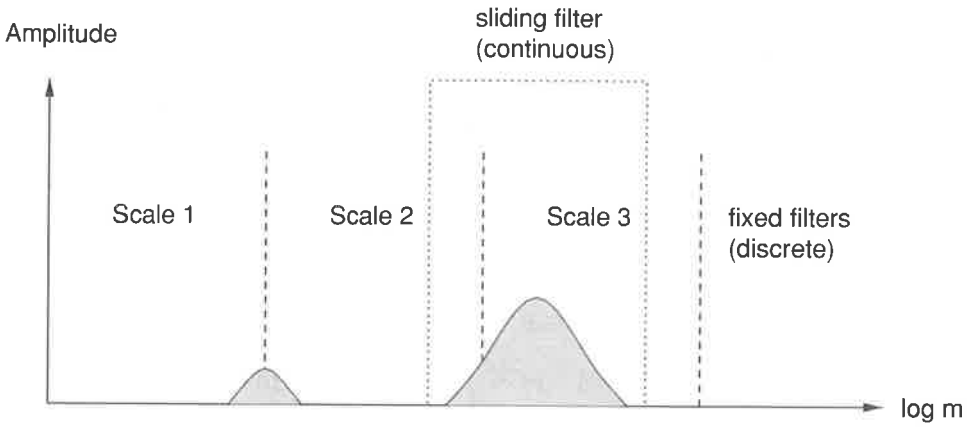

Figure 3.5: The scales of a discrete wavelet transform corresponds to bandpass filters centered at discrete wave numbers. If one scale contains contributions from two wave packets (illustrated by the shaded regions), the wave packets cannot be easily separated. The continuous wavelet transform corresponds to a sliding bandpass filter. The center wavelength can be adjusted to the center wavelength of each wave packet.

According to Equation 3.6 the transformation of a real signal (e.g. wind component) with a real wavelet yields a bandpass filtered version of the signal, with the Fourier transform of the wavelet as the filter function. If we want to detect wave packets, however, it is more instructive to look at the envelope of the bandpass filtered signal rather than at the bandpass filtered signal itself. This envelope is readily obtained as the modulus of a wavelet transform with a progressive wavelet. A progressive wavelet is a complex wavelet, where the real and imaginary part are 90° out of phase. It therefore yields the in-phase and in-quadrature components of the bandpass filtered signal as the real and imaginary part of the transform, respectively.

As the horizontal wind perturbations u' and v' of a gravity wave packet are essentially amplitude modulated sine waves, the Morlet wavelet (Figure 3.6) seems to be an obvious choice. It has the representations

$$g(z) = e^{i \cdot 5.4 \cdot z} e^{-\frac{z^2}{2}} \tag{3.11}$$

$$G(m) = \sqrt{2\pi} e^{-\frac{(m-5.4)^2}{2}} \tag{3.12}$$

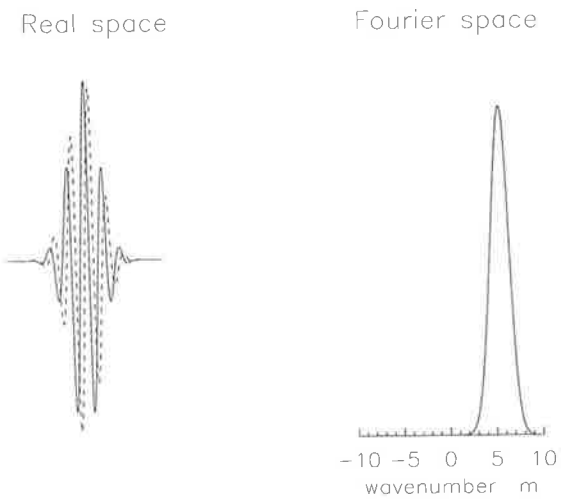

Figure 3.6: The Morlet wavelet in real space and Fourier space. The solid line in the real space diagram depicts the real part, the dashed line the imaginary part.

in real and Fourier space, respectively. As a progressive wavelet it has non-zero contributions only for $m > 0$. The relation between equivalent Fourier wavelength λ and wavelet scale a of a certain mother wavelet can be derived by wavelet transforming a sine wave of given wavelength λ [*Meyers et al.*, 1993]. In our case of the Morlet wavelet (3.11) it is given by $\lambda = 1.14a$.

The Morlet wavelet is not orthogonal and the wavelet coefficients are not independent. This means that the total energy of a superposition of different wavelets is not necessarily equal to the sum of the energies of each of the wavelets. The choice of an orthogonal wavelet would resolve this problem, but one has to keep in mind that the propagation of gravity waves through the atmosphere includes nonlinear saturation effects. The proper treatment of these nonlinear effects requires knowledge about the peak amplitudes of the gravity wave packets as physical entities. While the wavelet coefficients of an orthogonal wavelet transform are independent in the mathematical sense, several of these coefficients have to be used together to represent an actual physical wave packet and to reconstruct its peak amplitude. We, therefore, find it more convenient to use a mother-wavelet with a strong resemblance to the gravity wave packets to be analyzed, and to renormalize the energy if necessary.

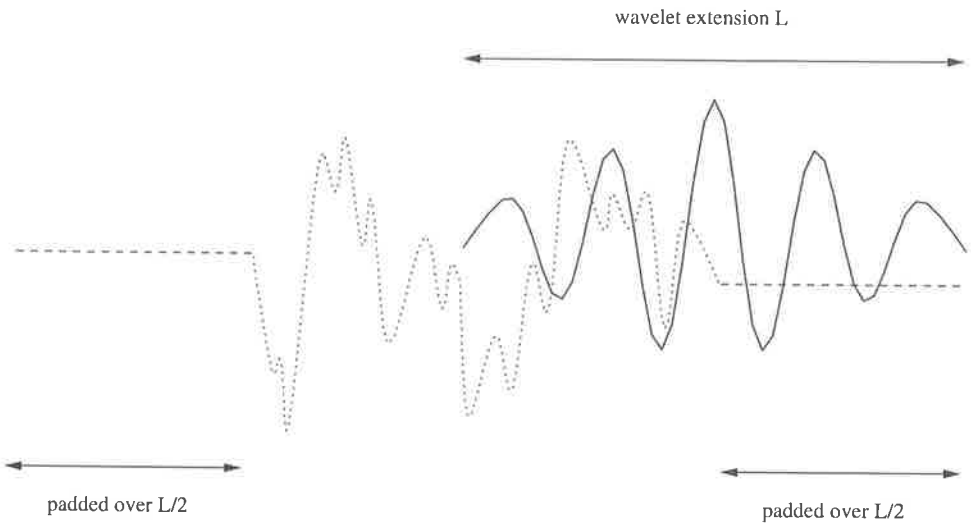

Figure 3.7: The wavelet centered at the end of the data series overlaps it by a length of $L/2$. As the Fourier transform assumes periodicity, this overlap would be wrapped around to the beginning of the data series. To avoid wrap-around effects, the data series has to be padded over this length.

3.4.3 Practical implementation of the continuous wavelet transform

The calculation of the wavelet transform was performed in Fourier space using Equation 3.6 and implemented as follows:

First, the real data series $f(z)$ is padded on both sides to avoid wrap-around effects. The number of points to be added depends on the largest wavelength to be considered. Equation 3.5 states, that the wavelet transform for a scale a at position b is given by integrating over the product of the data series $f(z)$ and the wavelet of scale a with its center at b. As the Fourier transform assumes periodicity of the transformed data series, any overhang of the wavelet at the end of the data series is wrapped around to the start of the data series, leading to undesirable contributions to the integral. If we assume the largest scale wavelet to extend over a length of approximately $L/2$ on each side of its center, the data series has to be padded with this length to avoid any wrap-around effects (Figure 3.7).

This padded data series is then Fourier transformed and, for each scale a of interest, multiplied by the Fourier transform $G(am)$ of the scaled mother wavelet. Inverse Fourier transforming and unpadding then yields the complex wavelet transform $W_f(a, b)$. Its real part contains the data series $f(z)$ bandpass filtered according to scale a, and its imaginary part a 90° phase-shifted version thereof. Its modulus corresponds to the envelope of the bandpass-filtered signal. Figure 3.8 gives an example of the wavelet transform of a hypothetical wind profile using the Morlet wavelet.

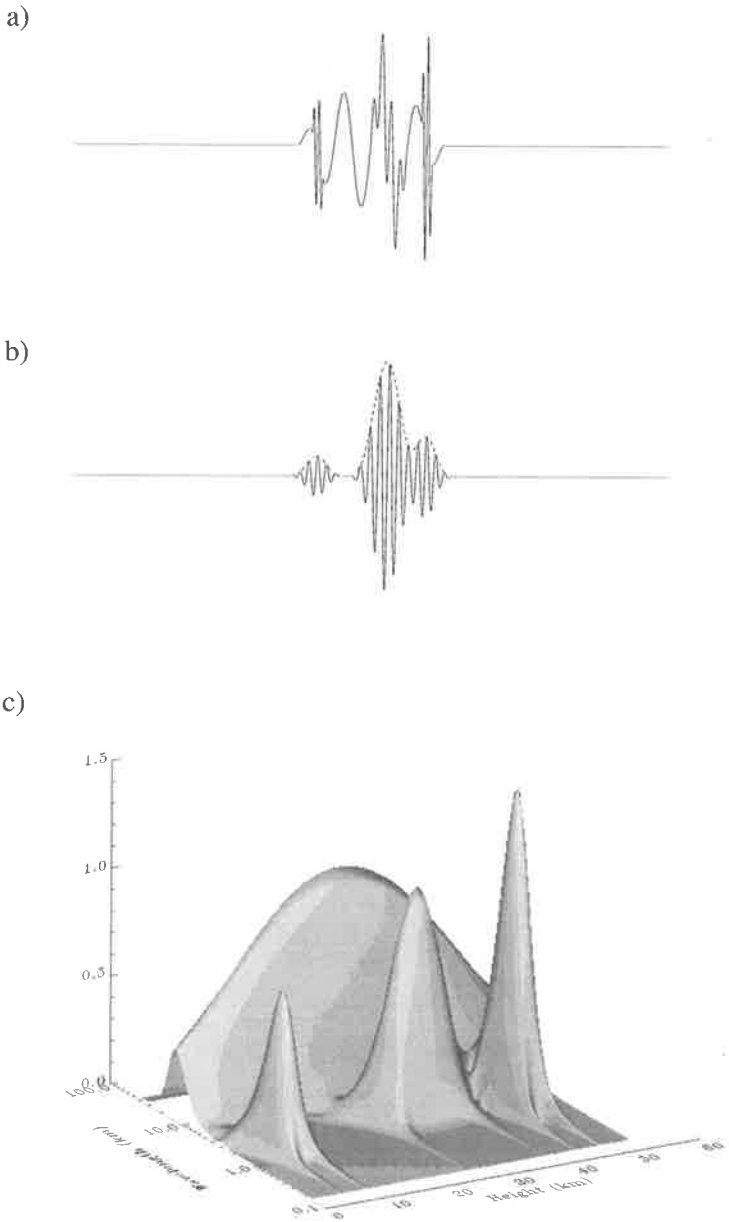

Figure 3.8: Example of the wavelet transform of a hypothetical wind profile using the Morlet wavelet. a) The hypothetical wind profile, padded to avoid wrap-around effects. b) Wavelet transform of the profile in a) for a certain scale a. The solid line represents the real part, the dashed line the modulus of the transform. c) Surface plot of the modulus of the wavelet transform as a function of wavelength and height. The four wave packets are clearly resolved.

3.5 Application to radiosonde data

Using the algorithm described above, we now can apply the wavelet transform to radiosonde data, i.e. vertical profiles of horizontal wind velocity u and v and temperature T. In order to detect wave packets in the horizontal wind data, we first calculate the wavelet coefficients $W_u(a,z)$ and $W_v(a,z)$ of the zonal and meridional wind components, respectively. Then we scan the surface $S(a,z) = |W_u(a,z)|^2 + |W_v(a,z)|^2$ for local maxima (cf. Figure 3.8c). Only maxima exceeding a certain threshold S_{thresh} are retained in the further analysis. For each of these maxima the extension of the corresponding wave packet is recorded. The boundaries (z_1, z_2 and a_1, a_2 for height and scale, respectively) are determined by scanning the surface $S(a,z)$ descending from the maximum at (a_{max}, z_{max}) until it drops to a value $\frac{1}{4}S(a_{max}, z_{max})$ or starts rising again.

The wave packets can now be reconstructed by adding up the complex wavelet coefficients of all contributing scales $a_1 \ldots a_2$ at each height $z_1 \ldots z_2$ for u, v, and T (Equation 3.8). The resulting profiles, designated by $\widetilde{u}$, $\widetilde{v}$, and $\widetilde{T}$, respectively, now contain the isolated wave packet as their real part, and its 90° phase-shifted (i.e. Hilbert transformed) version as their imaginary part. To avoid effects of the convolution with the wavelet, the wave packet extent has to be determined from the reconstructed wave packet.[5] We use the full-width half-maximum of the horizontal wind variance as the vertical wave packet extent. To extract wave parameters of a packet we applied Stokes parameter analysis [*Vincent & Fritts*, 1987; *Eckermann & Vincent*, 1989]. Let u_o and v_o designate the peak amplitudes of the horizontal wind perturbations and ϵ their phase difference, then the Stokes parameters to be calculated are:

$$D = \langle u_o^2 - v_o^2 \rangle$$

[5]The bandwidth of the wave packet might be larger than the bandwidth of each of the constructing wavelets. The extent of the wave packet can therefore be smaller than the extent of any of the constructing wavelets.

$$
\begin{aligned}
 & = \langle \widetilde{u}_R^2 + \widetilde{u}_I^2 - \widetilde{v}_R^2 - \widetilde{v}_I^2 \rangle \\
P & = 2\langle u_o v_o \cos\epsilon \rangle \\
 & = 2\langle \widetilde{u}_R \widetilde{v}_R + \widetilde{u}_I \widetilde{v}_I \rangle \\
Q & = 2\langle u_o v_o \sin\epsilon \rangle \\
 & = 2\langle \widetilde{u}_R \widetilde{v}_I - \widetilde{u}_I \widetilde{v}_R \rangle
\end{aligned}
\tag{3.13}
$$

where $\langle\rangle$ denotes spatial average and the indices I and R the real and imaginary part, respectively. The Stokes parameter D gives the contribution of linear polarized waves along the x- or y-axis, while P indicates linear polarized waves along axes at 45° and 135° azimuth. Circular polarized waves are represented by Q. (For a more detailed discussion see *Born & Wolf* [1970] and *Hecht* [1987].)

The vertical propagation direction of the gravity wave packet is given by the sign of Q, the dominant horizontal alignment by

$$\phi = \frac{1}{2}\arctan(\frac{P}{D}), \tag{3.14}$$

where ϕ is given in the mathematical sense, i.e. in degrees anti-clockwise from east.

The horizontal perturbation velocities parallel and perpendicular to the horizontal alignment direction are given by the transformation

$$\begin{pmatrix} u'_{\|} \\ v'_{\perp} \end{pmatrix} = \begin{pmatrix} \cos\phi & \sin\phi \\ -\sin\phi & \cos\phi \end{pmatrix} \begin{pmatrix} u' \\ v' \end{pmatrix}. \tag{3.15}$$

The intrinsic frequency $\hat{\omega}$ is now readily obtained as

$$\hat{\omega} = \frac{\langle u'_{\|} \rangle}{\langle v'_{\perp} \rangle} \|f\| \tag{3.16}$$

The horizontal propagation direction of the gravity wave is parallel to the direction specified by ϕ (Equation 3.14). The phase difference between $\widetilde{u}_{\|}$ and $\widetilde{T'}$ then resolves the directional ambiguity: From Equations (3.1) and (3.3) one can see that $\widetilde{u}_{\|}$ and $\widetilde{T'}$ should be $\pm 90°$ out of phase, depending on the sign of k. For $k > 0$ the wave propagation direction is given by ϕ, for $k < 0$ by $\phi + 180°$. The phase difference can

be calculated via the phase of the coherence function

$$\gamma = \frac{\langle \widetilde{u}_{\parallel} \widetilde{T'}^{*} \rangle}{\sqrt{\langle |\widetilde{u}_{\parallel}|^2 \rangle \langle |\widetilde{T'}|^2 \rangle}}, \tag{3.17}$$

where $\widetilde{u}_{\parallel} = \widetilde{u}_{\parallel,R} + i\widetilde{u}_{\parallel,I}$, $\widetilde{T'} = \widetilde{T'}_R + i\widetilde{T'}_I$, and * denotes the complex conjugate. Finally, the horizontal wavenumber can be calculated from the dispersion relation (2.18).

The hodograph analysis described above uses polarization relations for a single monochromatic gravity wave to infer the intrinsic frequency and orientation of the analyzed wave packet. *Eckermann & Hocking* [1989] demonstrated that in the case of multiple wave packets the inferred intrinsic frequency can be an effect of wave superposition and might indicate azimuthal directionality in wave propagation rather than mean frequency. The wavelet based method described here, however, isolates wave packets in wavenumber and height. Therefore, the possibility of multiple wave packets in the hodograph analysis is much reduced compared to more traditional Fourier methods, where the whole height range is analyzed as a single wave. The analysis of a individual radiosonde sounding, however, does not allow filtering of the observations in frequency. It is, therefore, important to keep in mind, that it is not possible to distinguish different wave packets in a hodograph if they agree in vertical wavenumber.

If two wave packets are close in height-scale space, the boxes used to reconstruct the wave packets might overlap, i.e. certain wavelet coefficients might be used for the reconstruction of more than one wave packet. In these cases the horizontal wind variance corresponding to these wavelet coefficients is divided between the reconstructed wave packets in equal parts to conserve the total wind variance.

3.6 Summary

A method to extract gravity wave packets from vertical profiles of horizontal wind and temperature was presented. Using wavelet analysis we are able to separate the wave field in height and wavelength and, therefore, to reduce the presence of multiple waves

in the hodograph analysis. Furthermore, we get information about the height extent of the wave packets. The Morlet wavelet was chosen to decompose the wave field into basis functions that are similar to the assumed physical gravity wave packets. This allows a simple reconstruction of the actual wave packet amplitude, an important issue when non-linear saturation effects are considered.

Chapter 4

Macquarie Island: A case study

In this chapter we apply the wavelet technique described in Chapter 3 to twice-daily radiosonde soundings of the lower stratosphere over Macquarie Island between 1993 and 1995. In addition to the propagation characteristics, we also obtain information about the height extent of the wave packets which leads to an expression for the intermittency of the observed wave field. Knowledge about the wave intermittency then allows us to compute mean-flow accelerations in the lower and middle atmosphere using a linear ray-tracing model.

4.1 Radiosonde Data and Background Atmosphere

Macquarie Island (55°S, 159°E) is situated approximately 1500 km south of Tasmania in the sub-antarctic storm track. It is aligned in north-south direction with a length of 34 km and a maximum width of 5.5 km. Its maximum height is 433 m above sea level [*Crohn*, 1986]. The winds at Macquarie Island are predominantly eastward with a high frequency of gales. A front or depression center passes the island every 5 or 6 days [*Streten*, 1988].

The Australian Bureau of Meteorology has a weather station on the north part of the island. Operational radiosonde soundings are usually performed twice daily, and the sondes reach typical heights of about 25 to 30 km. Every two seconds the

radiosondes (Vaisala RS 80-15) measure the current values of pressure, temperature and humidity. After filtering and smoothing they are recorded at 10 s intervals at the ground station. With an average balloon ascent rate of 5 m/s this results in a height resolution for the temperature profile of about 50 m. The finite response time of the temperature sensor attenuates high wavenumber fluctuations to a certain extent. Although it is possible to compensate for this effect [*Allen & Vincent*, 1995], no attempts were made in the present study. The accuracy of the temperature measurements is specified as $\pm 0.1°$ C rms. The zonal and meridional wind components, calculated from the radiosonde position over time, are reported every 10 s. After outlier removal a cubic spline is fitted over a running window of 130 s, corresponding to a height range of about 650 m.[1] Wind fluctuations at scales smaller than this will, therefore, be attenuated in some way. The rms random errors in each wind component are believed to be about 0.5 ms^{-1}. It is important to keep in mind that the different treatment of temperature and wind data can distort amplitude and phase relations between these data sets.

Due to the finite ascent rate of the balloon, the gravity wave field undergoes changes while the profiles of wind and temperature are gathered (with an ascent rate of 5 ms^{-1} a launch to a final height of 30 km takes about 100 min), and the sonde itself experiences a horizontal drift. However, these deviations from an instantaneous, vertical profile are assumed to be generally insignificant if the mean winds are less than about 50 ms^{-1} [*Gardner & Gardner*, 1993].[2]

In this study we analyze radiosonde data from between April 1993 and March 1995. The same data set was analyzed previously using a windowed Fourier technique [*Vincent et al.*, 1997; *Allen*, 1996], and the results will be compared where appropriate.[3]

Figure 4.1 presents the monthly mean horizontal winds and temperature over the analyzed time period. The monthly mean profiles were calculated as the average over

[1] The fitting interval was changed to 250 s (1250 m) at the end of January 1994.

[2] We only require that the time taken to sample a certain coherent wave packet is small compared to its period. As we are not interested in the phase relation between packets in different height regions, we do not require different packets to be sampled simultaneously.

[3] As those studies concentrated on different height ranges, a direct comparison is difficult.

all radiosonde launches within that particular month. The zonal winds are particularly strong during winter and reverse sign above 22 km during summer. The mean meridional winds are much weaker with an amplitude of less than about 5 ms^{-1}. The variations in background temperature are most significant in the stratosphere and the tropopause is at a height of about 10 km throughout the whole year.

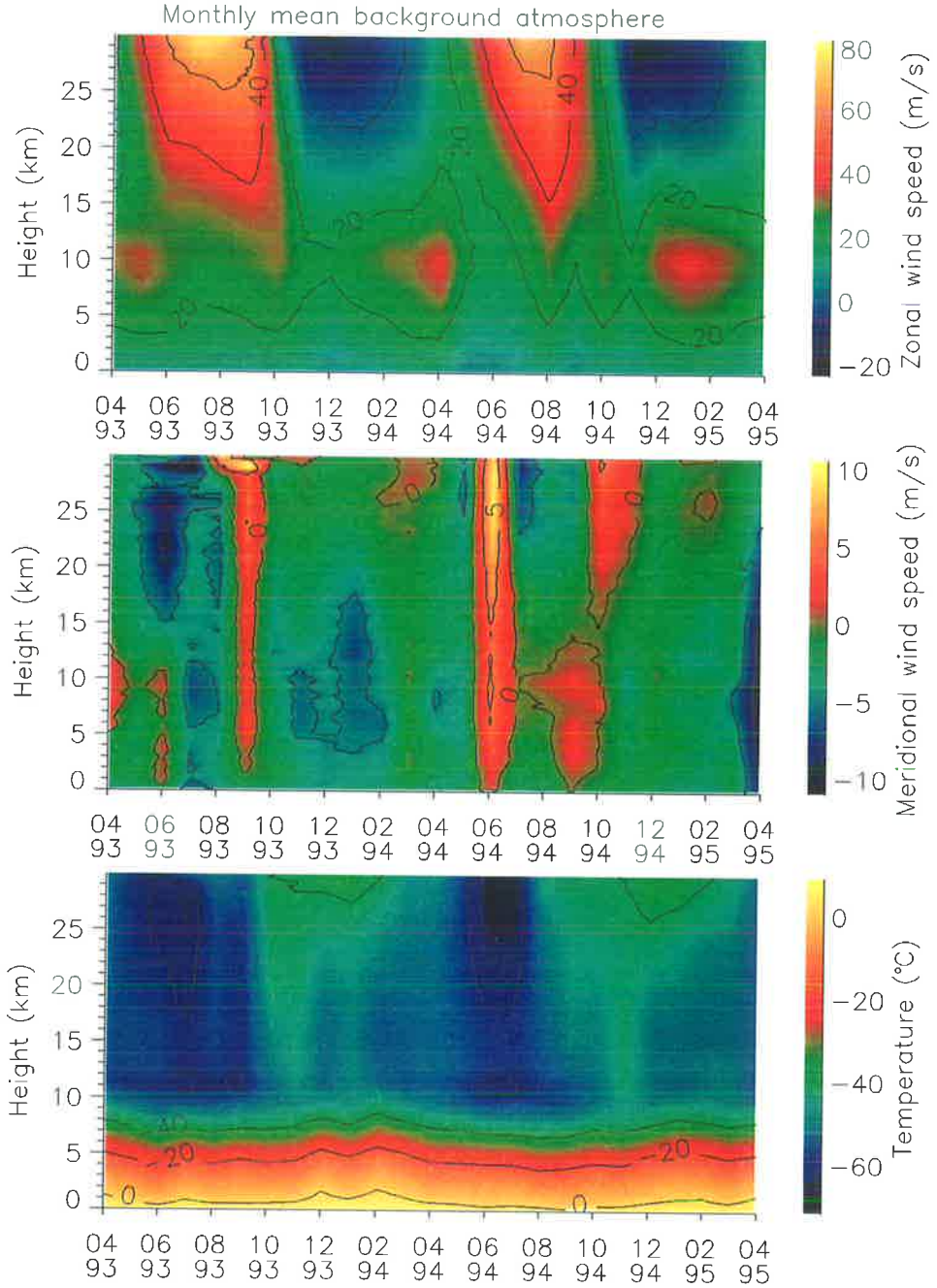

Figure 4.1: Monthly mean profiles of horizontal winds and temperature over Macquarie Island.

4.2 Gravity Wave Parameters

The wavelet analysis of the gravity wave field was performed starting at a height of 12000 m MSL using wavelengths $\lambda_i = 450. \cdot 2^{i/8}, i = 0 \ldots 39$. The profiles of u, v, and T were prefiltered with a fifth order Butterworth filter with half-power points at 450 m and 11000 m or the height extent of the radiosonde data, whatever less. The parameter S_{thresh} was selected as 0.01 m^2/s^2. Many results in this chapter are given as averages per radiosonde flight and function of wavelength or height. In forming these averages the height (and, therefore, wavelength) coverage of the contributing radiosonde flights was taken into account.

Figure 4.2 shows the average monthly horizontal wind variance $\langle u'^2 + v'^2 \rangle$ as a function of height for upwards and downwards propagating gravity wave packets. The decrease in variance from January 1994 on is probably due to the increased phase fitting length (cf. Footnote 1). Note that we here present the gravity wave activity in terms of horizontal wind variance since this variable is directly accessible by measurement and does not depend on other inferred gravity wave parameters like, for example, wave action does.

In our analysis we will mainly concentrate on the height region from 20 to 28 km, as the waves in this region are important for the wave-mean wind interactions in the middle and upper atmosphere.[4] The two phases to be considered are summer (November to March) and winter (April to October). Figure 4.3 presents the number of radiosonde soundings reaching above 20 km and the fraction of horizontal wind variance in the height region 20 ... 28 km used for the reconstruction of the wave packets as functions of time.

Figures 4.4 to 4.6 summarize the parameters of the gravity waves detected in the height range 20 to 28 km for upwards propagating gravity waves in summer and upwards and downwards propagating gravity waves in winter, respectively. The statistics for downwards propagating gravity waves during summer are too poor to form reliable

[4] As will be seen later, waves detected below this region are filtered to a certain extent during their upward propagation.

parameter estimates. The panels on the left-handside of Figures 4.4 to 4.6 present the horizontal wind variance as a function of intrinsic horizontal propagation direction, i.e. direction of horizontal intrinsic phase speed, and histograms of ground-based zonal phase speed

$$c_{\text{phase,zonal}} = \frac{\omega}{k_h \cos(\phi)}, \tag{4.1}$$

where ϕ is the propagation direction in the mathematical sense, i.e. in degrees anticlockwise from east. The intrinsic propagation direction of the wave packets is predominantly south-southwest-wards during winter and nearly isotropic in summer. The horizontal group velocity

$$c_g = \frac{\partial \omega}{\partial \mathbf{k}_h} \tag{4.2}$$

of each wave packet is represented by a point in the lower left diagram and is given relative to the ground-based reference frame. The group velocity is important for ray-tracing studies to find the origin of the observed wave packets. The right-hand panels of Figures 4.4 to 4.6 show the horizontal wind variance of the wave field in histogram form as a function of intrinsic frequency and vertical and horizontal wavelength, respectively. The vertical and horizontal wavelengths are binned logarithmically to take the proportionality $\Delta m \propto m$ of the wavelet analysis into account. The observed wave field is clearly dominated by low-frequency (inertio) gravity waves with an average horizontal wavelength of several hundred kilometers. A shift to higher intrinsic frequencies is evident in winter, when large zonal wind speeds occur. The horizontal wind variance peaks at vertical wavelengths around 4 km. Keep in mind, however, the choice of our high wavelength cutoff of 11 km and that the filtering performed by the radiosonde equipment attenuates wavelengths less than about 1 km. The mean values of intrinsic frequency, horizontal and vertical wavelength, and ground-based zonal phase speed are given in Table 4.1.

		$\langle c_{\text{phase,zonal}} \rangle$	$\langle \hat{\omega} \rangle$	$2\pi/\langle m \rangle$	$2\pi/\langle k_h \rangle$
winter	upwards	15.3 m/s	3.1 f	4.2 km	431 km
	downwards	27.1 m/s	3.7 f	4.1 km	319 km
summer	upwards	6.4 m/s	2.3 f	3.9 km	547 km

Table 4.1: Mean values of gravity wave parameters for the height range 20 . . . 28 km over Macquare Island.

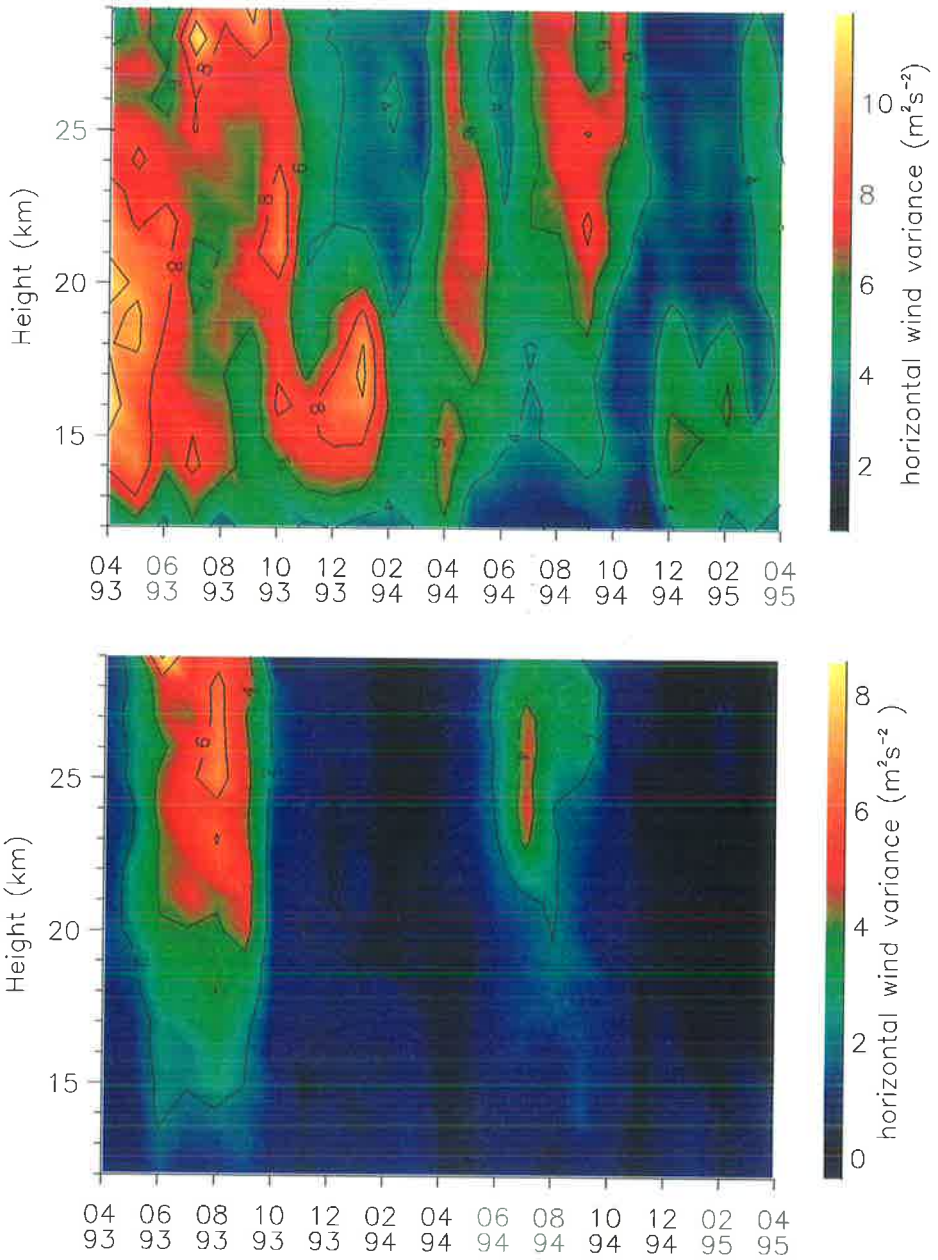

Figure 4.2: Monthly averaged horizontal wind variance $\langle u'^2 + v'^2 \rangle$ as a function of height and time for upwards (top) and downwards propagating gravity wave packets (bottom).

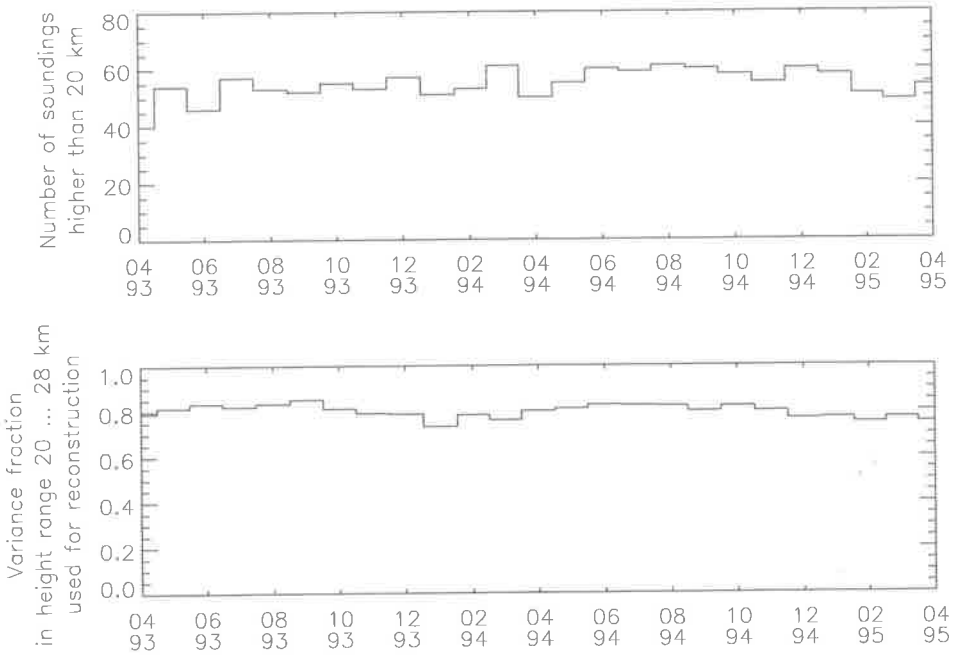

Figure 4.3: Number of radiosonde soundings reaching above 20 km (top) and fraction of horizontal gravity wave wind variance in the height region 20...28 km used for the reconstruction of the wave packets (bottom).

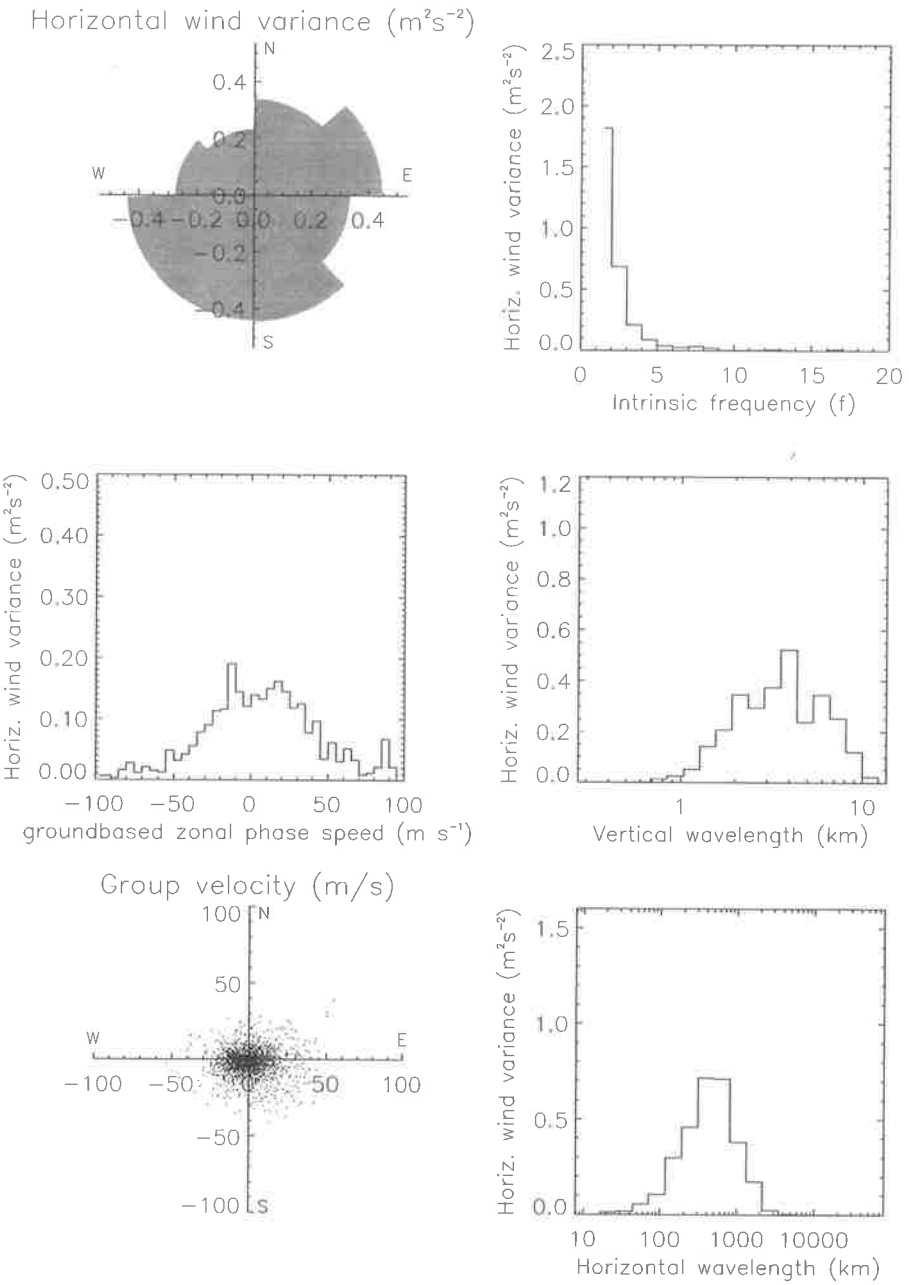

Figure 4.4: Parameters of upwards propagating gravity waves in the height range 20 to 28 km during summer.

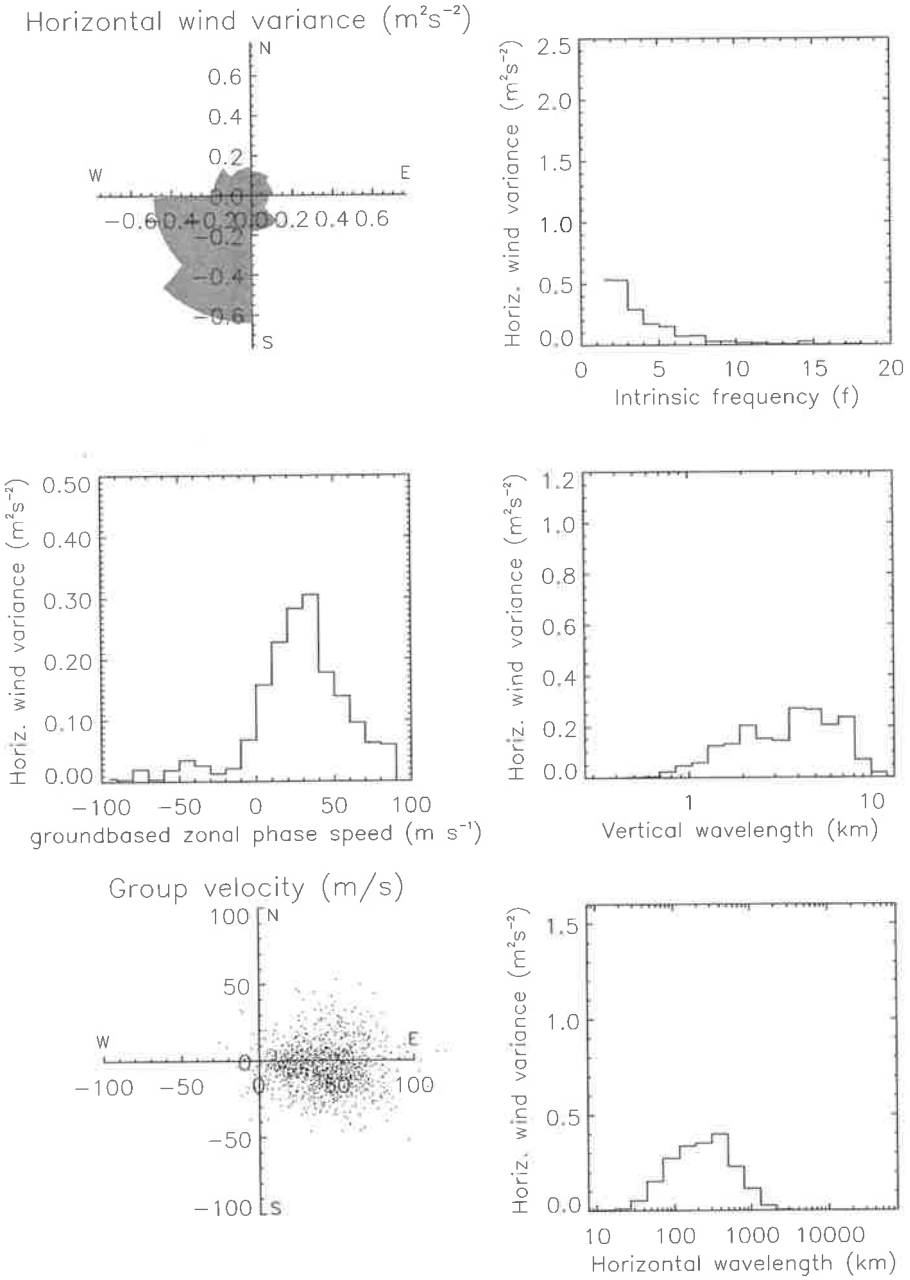

Figure 4.5: Parameters of downwards propagating gravity waves in the height range 20 to 28 km during winter.

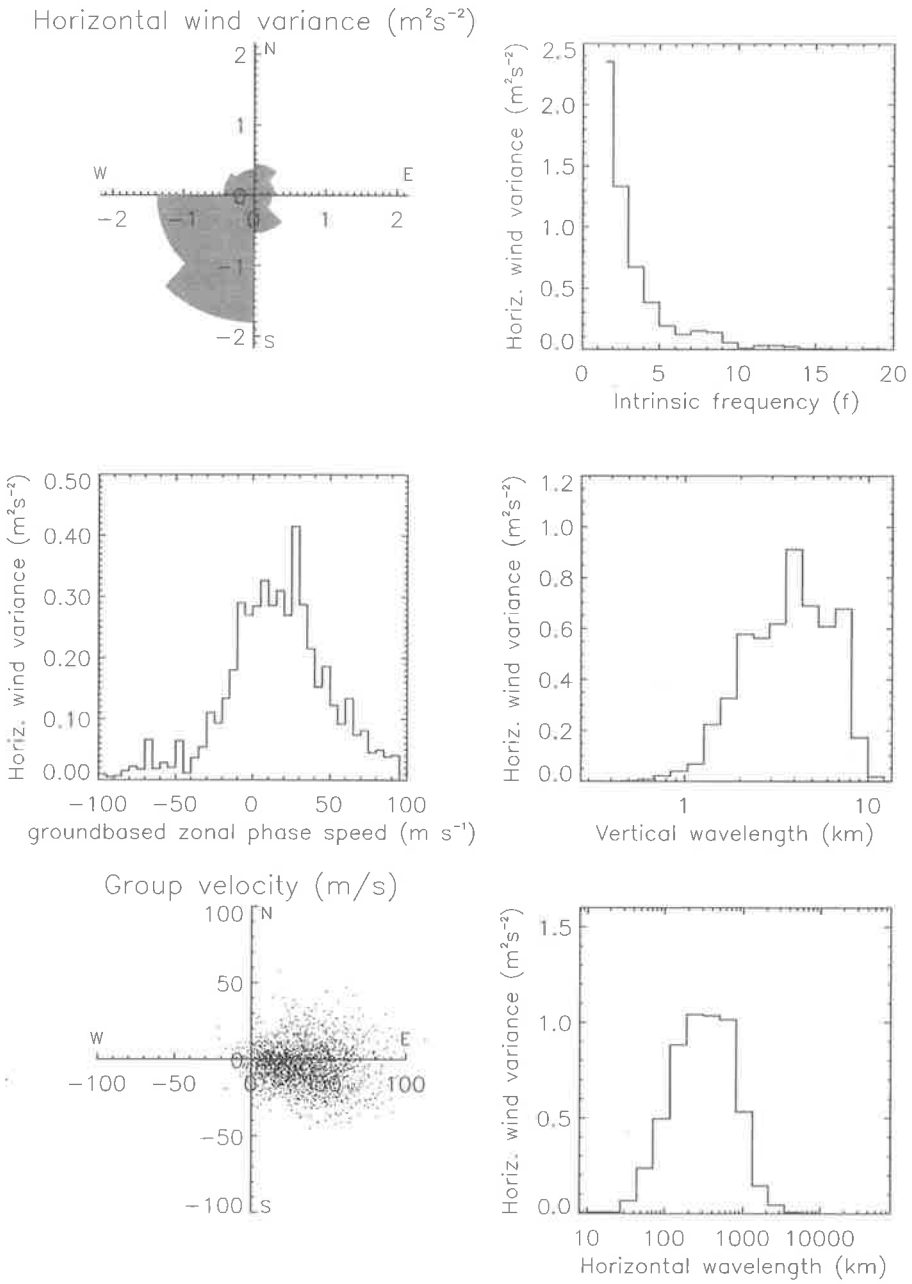

Figure 4.6: Parameters of upwards propagating gravity waves in the height range 20 to 28 km during winter.

4.3 Discussion

4.3.1 Seasonal variation of total gravity wave variance

A closer look at the total gravity wave horizontal wind variance and the zonal background wind speed as a function of time reveals a good correlation between these two variables (Figure 4.7). Both show a clear annual cycle with maximum values of about 9 m^2/s^2 and 60 m/s, respectively, in July/August and minima of about 3 m^2/s^2 and -5 m/s, respectively, around January. A similar annual cycle of gravity wave activity has been observed at a multitude of sites in the mid- and high-latitudes in both hemispheres [*Allen & Vincent*, 1995; *Eckermann et al.*, 1994]. Different mechanisms exist to explain this seasonal variability:

Source strength: Changes in wave generation at the source level will lead to variability in wave activity at higher altitudes. Well-known sources of gravity waves in the lower atmosphere are topography [*Smith*, 1985; *McFarlane*, 1987; *Hines*, 1988*b*; *Nastrom & Fritts*, 1992], thunderstorms [*Fovell et al.*, 1992; *Pfister et al.*, 1993; *Alexander et al.*, 1995], fronts [*Fritts & Nastrom*, 1992; *Griffiths & Reeder*, 1996; *Reeder & Griffiths*, 1996], wind shear [*Lalas & Einaudi*, 1976; *Chimonas & Grant*, 1984; *Fritts*, 1982] and geostrophic adjustment [*Schubert et al.*, 1980; *Uccellini & Koch*, 1987; *Duffy*, 1990; *Fritts & Luo*, 1992; *Luo & Fritts*, 1993]. While topography, convection and wind shear are believed to generate mainly high-frequency waves [*Fritts & Luo*, 1992], the most energetic gravity waves in our case study are those with frequencies close to the inertial frequency f. This is in good agreement with many other observations [*Vincent*, 1984; *Sato*, 1994; *Nastrom et al.*, 1997]. Even though the predominance of inertia-gravity waves might be an observational selection effect of the radiosonde equipment [*Alexander*, 1998], the observed waves could have been generated by geostrophic adjustment and frontogenesis, both of which excite waves with near-inertial frequencies [*Fritts & Luo*, 1992; *Griffiths & Reeder*, 1996; *O'Sullivan & Dunkerton*, 1995]. In the simulations of *Griffiths & Reeder* [1996] the inertio-gravity waves generated by the frontogenesis had vertical wavelengths between 2 and 10 km and horizontal wavelengths

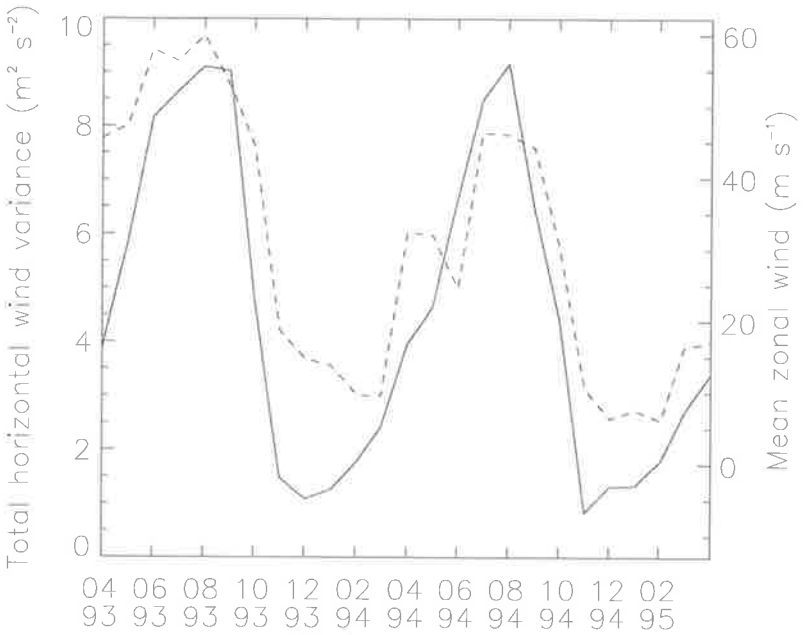

Figure 4.7: Total horizontal gravity wave wind variance (dashed) and zonal background wind speed (solid) averaged over the height range from 20 to 28 km as a function of time

of several hundred kilometers, in good agreement with our observations.[5] Evidence supporting geostrophic adjustment as a generation mechanism for stratospheric waves over Macquarie Island was given by *Guest et al.* [2000], who could ray-trace gravity waves observed during a campaign in October 1994 backwards in time to their origins near the polar jet.

Background atmosphere: If we assume no explicit dependence of the background atmosphere on horizontal position x and y and time t, then the horizontal wave numbers k and l and the ground-based frequency ω are constant along the ray of each wave packet (cf. Section 2.4). The intrinsic frequency $\hat{\omega}$ as a function of height is then

$$\hat{\omega}(z) = \omega - u(z)k - v(z)l \tag{4.3}$$

and the vertical wavenumber $m(z)$ is given via the dispersion relation Equation 2.18. In summer $\frac{du}{dz} < 0$ and waves propagating westwards ($k < 0$) are Doppler-shifted to

[5] Again, keep the imposed wavelength filter of our analysis method in mind.

lower intrinsic frequencies. Their vertical wavelength, therefore, decreases with height. If their intrinsic frequencies drops below the inertial frequency f these waves will be critically filtered. In winter, on the other hand, $\frac{du}{dz} > 0$ and westwards propagating waves are Doppler-shifted to higher intrinsic frequencies and wavelengths. If their intrinsic frequency reaches the turning frequency these waves will be reflected. Due to the limited bandwidth of our analysis methods, however, waves will be shifted out of the observable vertical wavelength range before they encounter critical or turning levels. Nevertheless, the effect of critical level filtering can be observed in the horizontal wind variance for upwards propagating waves during summer at a height of approximately 20 km, where the zonal wind reverses sign (Figure 4.2 top). Observations of similar modulation of gravity wave variance by the background wind were made by *Whiteway & Duck* [1996] and *Whiteway & Duck* [1999].

The wind variance of a wave packet will change even if it is shifted within the observable vertical wavelength range. In the absence of dissipation, the amplitude of a wave packet along its ray is determined by the conservation of wave action flux [*Lighthill*, 1978]

$$A_f = c_{g,z}\frac{E}{\hat{\omega}} = \text{const.}, \tag{4.4}$$

where $c_{g,z}$ is the vertical group velocity and E the total energy density,

$$E = \frac{1}{2}\rho(\overline{u'^2} + \overline{v'^2} + \overline{w'^2} + N^2\overline{\zeta'^2}). \tag{4.5}$$

Here ζ' is the wave-induced vertical displacement of the air parcel from its equilibrium. Due to the density decreasing exponentially with height, the horizontal perturbation velocity of a wave with constant intrinsic frequency grows exponentially in amplitude. If the intrinsic frequency is increasing with height, however, the (horizontal) wave amplitude will grow less than exponentially; if it is decreasing with height, it will grow more than exponentially. *Eckermann* [1995*a*] used this effect of background winds on vertical wavenumber spectra to explain the occurrence of attenuated spectra in several experimental observations. He was also able to model seasonal changes in wave activity due to variability in background temperature and, hence, density [*Eckermann*, 1995*b*].

Similarly, *Alexander* [1998] could explain the variations in gravity wave activity at mid-latitudes with effects of the background atmosphere on a constant source spectrum.

The observed seasonal dependence of gravity wave activity is, therefore, not necessarily indicative of source variability and might be largely explained by the propagation of a constant source spectrum through a variable background atmosphere.

4.3.2 Seasonal variation of downwards propagating gravity wave variance

As mentioned above, increasing wind speed will shift the intrinsic frequency of gravity waves propagating against the wind to larger values. Such a shift of the intrinsic frequency distribution to higher values is evident in winter from Figures 4.4 to 4.6. If the wind speed and, hence, the frequency shift is large enough some waves will reach their turning frequencies and be reflected. Figure 4.8 reveals a good correlation between the absolute background wind speed and the horizontal wind variance of the downwards propagating waves as a function of time. For background wind speeds of about 50 ms^{-1} during the stratospheric winter jet, the horizontal wind variance reaches values of up to 4 m^2s^{-2}, while the wave activity almost ceases during summer, when the atmosphere in the analyzed height range is basically at rest.

Allen [1996] found a similar increase in the fraction of clockwise rotating wind component during winter, when strong mean winds prevail in the stratosphere over Macquarie Island. Following *Eckermann et al.* [1994], the author, however, attributed this increase to a change in frequency distribution rather than in ratio of downwards to upwards propagating gravity wave energy. He argued that the intrinsic frequency of an upwards propagating, zonally aligned gravity wave is Doppler-shifted by the zonal mean winds. This Doppler-shifting to higher frequencies reduces the axial ratio of the hodograph ellipse and results in an increased fraction of anti-clockwise rotation. Even though the wave packet is upwards propagating, rotary spectral analysis would regard that fraction of its horizontal wind variance as downwards propagating. In our

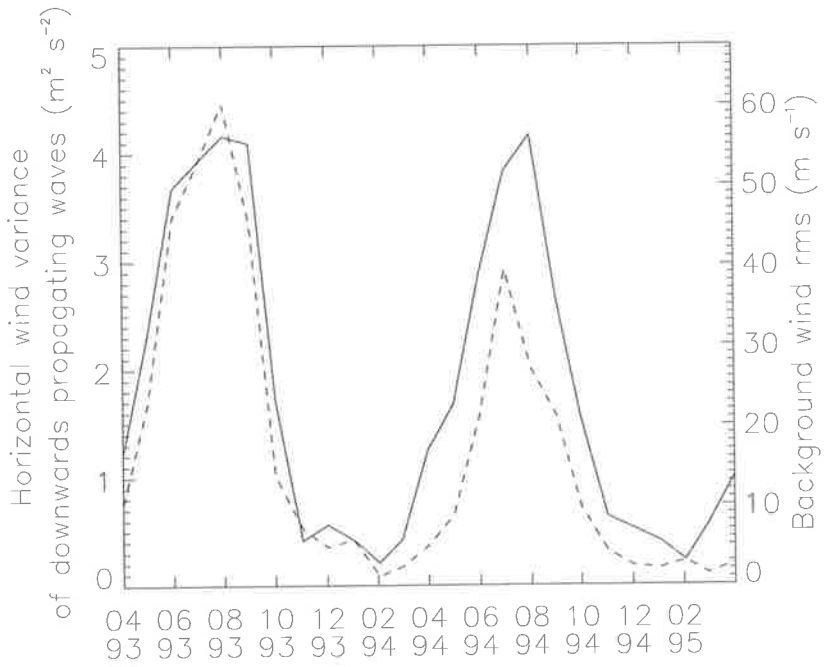

Figure 4.8: Horizontal wind variance of downwards propagating gravity waves (dashed) and absolute background wind speed (solid) as functions of time.

analysis, however, the total horizontal wind variance is counted as either upwards or downwards propagating, depending on the anti-clockwise or clockwise sense of rotation of the hodograph, i.e. the sign of the Stokes parameter Q (equation 3.13). Therefore, the argument of *Eckermann et al.* [1994] can no longer be applied and we believe that in our case we really deal with downwards propagating gravity waves. It is important to note that wave reflection can occur at frequencies much lower than the buoyancy frequency N if the density height terms are retained in the dispersion relation Equation 2.18, i.e. if the Boussinesq approximation is not applied [*Marks & Eckermann*, 1995]. Figure 4.9 shows the turning frequency as a function of horizontal wavelength for a density scale height of 6500 m and a buoyancy frequency of 0.02 rad s^{-1} at Macquarie Island for a compressible (dashed) and incompressible (solid) atmosphere (Equation 2.30). The turning frequency at horizontal wavelengths of several hundred km as observed in this study is reduced to as little as one tenth of the buoyancy frequency N. The local buoyancy frequency encountered by a wave propagating through the

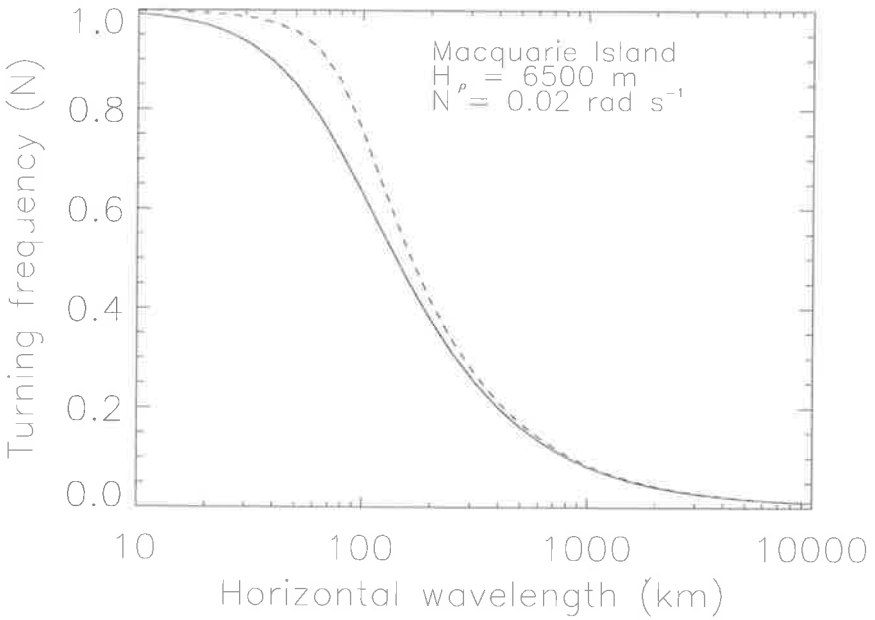

Figure 4.9: Turning frequency as a function of horizontal wavelength for a density scale height of 6500 m and a buoyancy frequency of $0.02\frac{rad}{s}$ at Macquarie Island for a compressible (dashed, $c_s = 300$ m/s) and incompressible (solid) atmosphere.

atmosphere can be substantially reduced compared to the mean background value by waves of large vertical wavelength. These large vertical wavelength waves can act as a background atmosphere for waves of smaller vertical wavelength, in a manner similar to that described by *Hines* [1991*b*]. The observed variation in wind variance of downwards propagating waves might thus be explained by reflection of waves from levels of high background wind speed and low local buoyancy frequency. Generation of downwards propagating waves by geostrophic adjustment of the stratospheric jet could also explain our data.

4.3.3 Preponderance of low-frequency gravity waves

As seen above, inclusion of the density height terms in the dispersion relation can significantly reduce the range of intrinsic frequencies over which wave propagation is possible. If we furthermore consider the imposed wavelength cutoff at a vertical

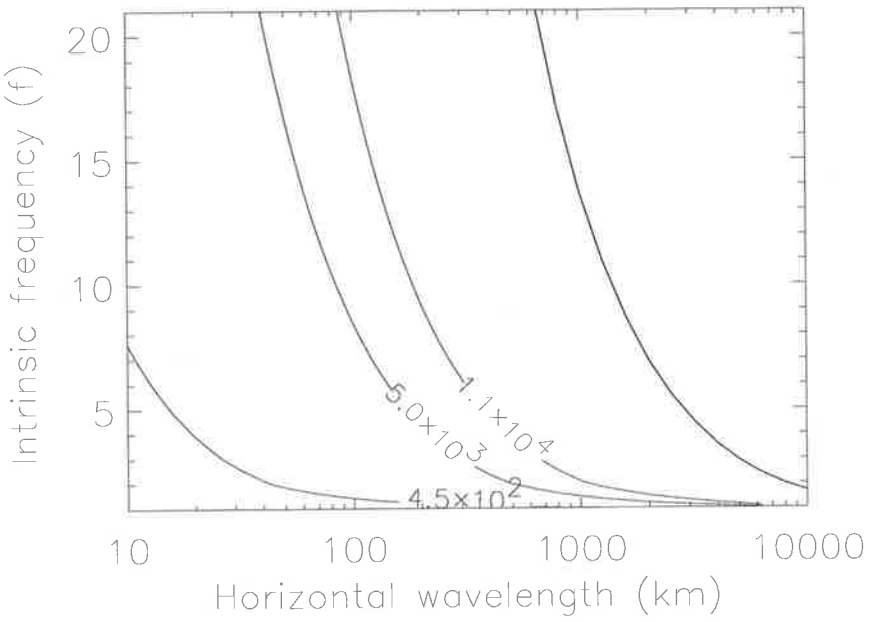

Figure 4.10: Contour plot of vertical wavelength as a function of horizontal wavelength and intrinsic frequency. The numbers on the contour lines are the vertical wavelength in meters. The thick line corresponds to the turning frequency.

wavelength of 11000 m, the maximum observable intrinsic frequency as a function of horizontal wavelength is again drastically reduced (Figure 4.10). The preponderance of inertio gravity waves in our data could, therefore, be an observational selection effect. On the other hand, it could be understood if the main generation mechanisms are frontogenesis and geostrophic adjustment, as indicated above.

Topography, however, is another possible generation mechanism at Macquarie Island, that may generate high frequency waves: When the air stream is deflected by topographical obstacles gravity waves with horizontal wavelengths similar to the scale of the obstacles can be generated. Due to their small horizontal wavelengths these waves can be Doppler-shifted to large intrinsic frequencies when they propagate to regions of large background wind speed. Evidence for the generation of gravity waves by topography is given by *Mitchell et al.* [1990], who report the common occurrence of lee-wave clouds in satellite images of Macquarie Island, which can extend hundreds

of kilometers to the east of the island under favourable conditions. *Schoeberl* [1985] calculated the dominant horizontal wavelength of the gravity wave spectrum forced by a bell shaped mountain ridge of equivalent mountain half width a as $2\pi a$. Considering the prevailing eastwards winds at ground level at Macquarie Island and a half width of the island between 1 and 2 km, the dominant horizontal wavelength lies between about 6 and 13 km. The minimum horizontal wavelength of zonally aligned, stationary (i.e. $\omega = 0$) gravity waves that can propagate through a gradually changing background atmosphere is given by Equation 4.3 with $\omega = l = 0$, i.e.

$$\lambda_{h,min} = 2\pi u/N \tag{4.6}$$

The corresponding time-height contours in Figure 4.11 illustrate that the minimum horizontal wavelengths of mountain waves in the lower stratosphere are around 15 km. A significant portion of the generated mountain waves is, therefore, likely to be trapped in the troposphere and unlikely to contribute to our studies.

4.3.4 Propagation directions

The variance-weighted intrinsic propagation direction of the observed gravity wave packets is predominantly south-southwest-wards during winter and nearly isotropic during summer, as illustrated in Figures 4.4 to 4.6. In interpreting these observations, one has to take the effects of the background atmosphere into account. For the strong zonal winds in winter, zonally propagating gravity waves experience large shifts in intrinsic frequency and vertical wavenumber and can be shifted into and out of the observable vertical wavenumber range. Thus, we anticipate some anisotropy in the zonal direction even for an isotropic source spectrum. Due to the low prevailing meridional winds it is hard to explain the meridional anisotropy by conditions of the background atmosphere or as an observational selection effect. The observed anisotropy could, therefore, be due to an anisotropic source or due to a latitudinally confined source located north of Macquarie Island.

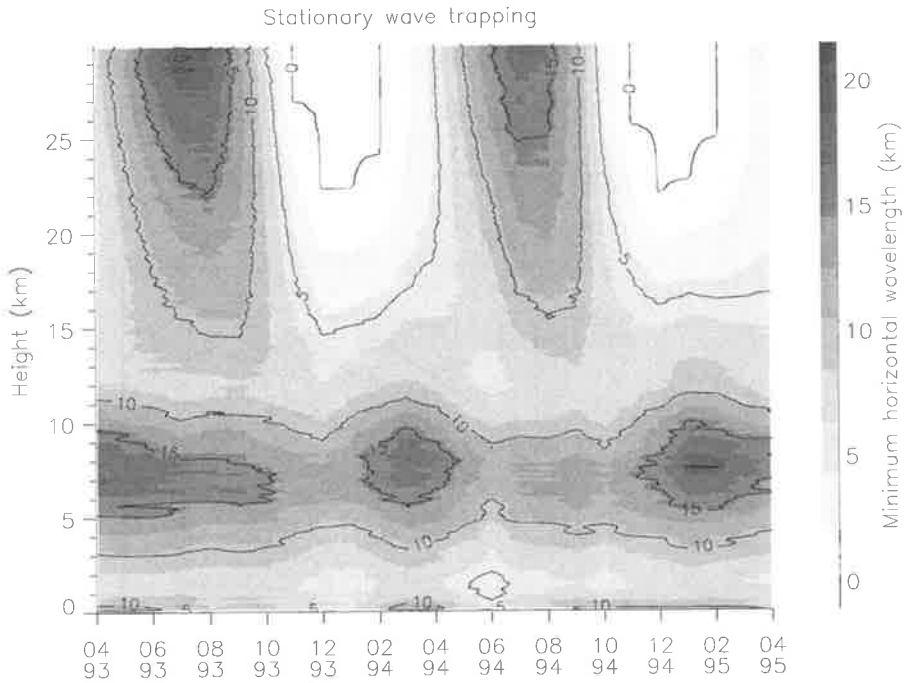

Figure 4.11: Time-height contours for minimum horizontal wavelength of zonally aligned, stationary gravity waves that can propagate through the background atmosphere. The stationary gravity waves encounter their critical level at the zero horizontal wavelength contour.

4.3.5 Wave amplitudes and saturation

Gravity waves will only affect the background flow or lead to mixing of constituents in the atmosphere if wave dissipation occurs. Dynamical and convective instability are thought to be the main dissipation processes [*Fritts & Rastogi*, 1985], although other mechanisms do exist (molecular diffusion, radiative damping, nonlinear interactions). Convective and dynamic instability lead to breaking of a wave if its amplitude exceeds a certain threshold. Due to the transverse shear in the velocity field of low-frequency gravity waves, the wave amplitude required for dynamic instability falls well below that necessary for convective instability as $\frac{f}{\hat{\omega}} \rightarrow 1$ [*Fritts & Rastogi*, 1985]. The threshold amplitude for dynamical instability is [*Fritts*, 1989]

$$u'_{\parallel,\mathrm{sat}} = \frac{2\sqrt{1-\frac{f^2}{\hat{\omega}^2}}}{1+\sqrt{1-\frac{f^2}{\hat{\omega}^2}}} c_{\mathrm{phase,intrinsic}}. \tag{4.7}$$

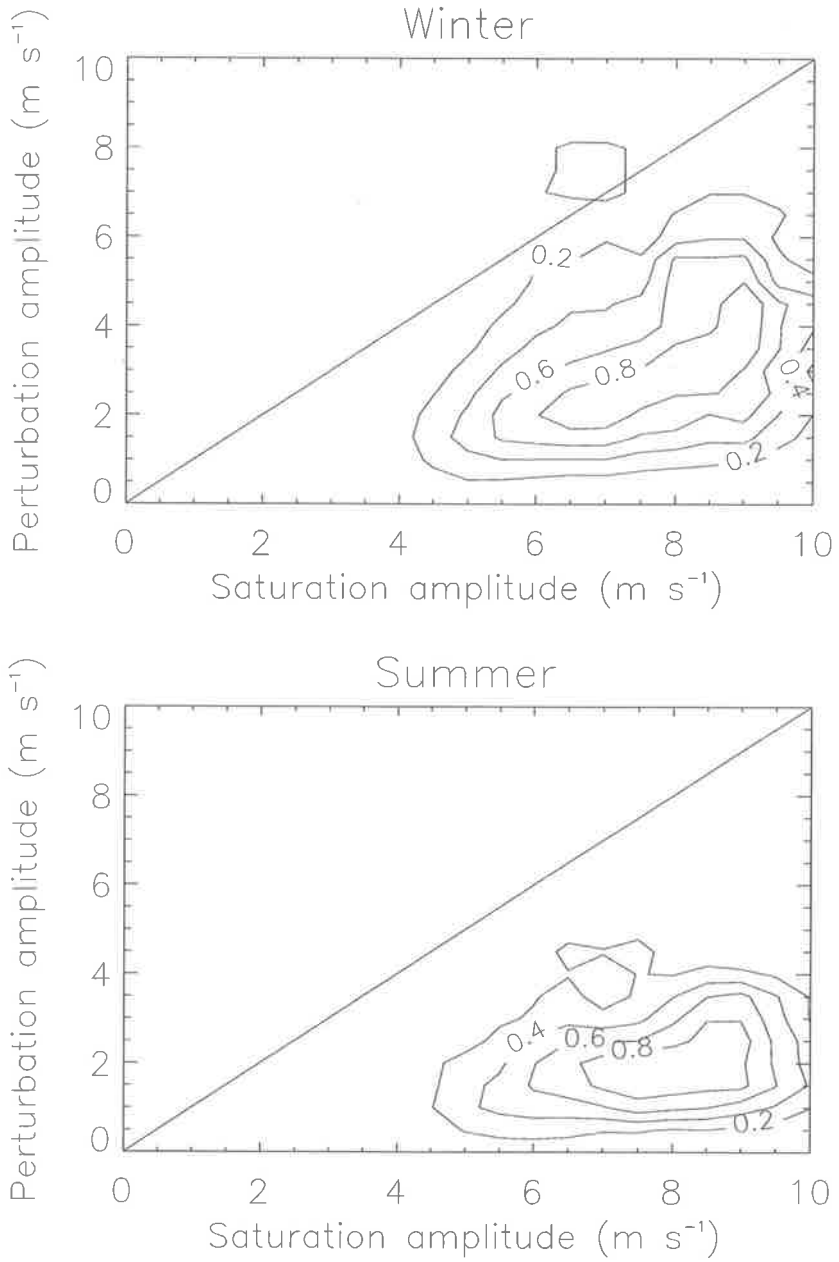

Figure 4.12: Normalized horizontal wind variance as function of perturbation amplitude $u'_{||}$ and saturation amplitude $u'_{||,\mathrm{sat}}$ for summer and winter between heights of 20 and 28 km.

Due to the existence of threshold amplitudes these saturation mechanisms are nonlinear, and the knowledge of actual wave amplitudes is important when the effect of gravity waves on the background atmosphere is to be assessed. Figure 4.12 shows a contour plot of normalized horizontal wind variance as a function of the perturbation amplitude parallel to the intrinsic propagation direction of the wave, $u'_{||}$, and the saturation amplitude $u'_{||,\mathrm{sat}}$ for gravity waves observed at Macquarie Island during summer and winter between heights of 20 and 28 km. Only soundings after February 1994 were considered to ensure identical filtering of the radiosonde data. In both summer and winter, the vast majority of the observed waves have perturbation amplitudes less than the saturation amplitude computed according to Equation 4.7. The amplitudes of these waves are, therefore, either too small to reach the threshold for dynamic instability within the analyzed height range, or have already been dissipated.[6] It is interesting to note, however, that the observed increase in gravity wave variance in winter coincides with an extension of the amplitude distribution to larger values.

[6]This neglects the effects of wave superposition.

4.4 Wave-mean flow interactions

Gravity waves can transport energy and momentum from the troposphere to the middle and upper atmosphere (see *Fritts* [1984*a*] for a review) and influence large-scale temperature and circulation patterns [*Geller*, 1983]. Using the gravity wave parameterization of *Lindzen* [1981] the importance of wave drag and diffusion in the middle atmosphere was demonstrated in numerical simulations [*Holton*, 1982; *Holton*, 1983; *Dunkerton*, 1982; *Garcia & Solomon*, 1985]. For low-frequency gravity waves both the vertical flux of horizontal momentum and the horizontal transport of heat are important to describe the wave mean-flow interactions. Both contributions are contained in the so-called Eliassen-Palm flux, which can be expressed as $\rho\overline{u'w'}\delta_-$, where $\delta_- = 1 - \frac{f^2}{\hat{\omega}^2}$ [*Fritts & Vincent*, 1987]. The resulting zonal acceleration of the mean background flow can then be expressed as

$$\langle A_{zonal} \rangle = -\frac{1}{\rho}\frac{\partial}{\partial z}\langle \rho\overline{u'w'}\delta_- \rangle, \tag{4.8}$$

where $\langle\rangle$ denotes temporal average. Profiles of momentum flux can either be computed directly from measurements at the respective height levels, or they can be inferred from modeling studies where a given gravity wave source spectrum is propagated through the atmosphere.

In this section, we use the gravity wave parameters inferred in Section 4.2 to assess the effect the observed waves have on the mean-flow in the lower and middle atmosphere. As the signal processing parameters of the radiosonde equipment were altered in January 1994, only soundings after that date were included in our analysis.

4.4.1 Momentum flux estimates in the lower stratosphere

Different observational techniques have been used to estimate momentum fluxes in the lower atmosphere. *Lilly & Kennedy* [1973] and *Alexander & Pfister* [1995] used aircraft-mounted systems to measure momentum fluxes associated with orographically and convectively generated gravity waves, respectively. *Vincent & Reid* [1983]

developed a radar method to infer momentum fluxes from symmetric-beam Doppler measurements, which has been applied in the lower and middle atmosphere [*Fritts et al.*, 1990; *Sato*, 1994; *Murayama et al.*, 1994; *Worthington & Thomas*, 1996; *Reid & Vincent*, 1987; *Tsuda et al.*, 1990]. Furthermore, different authors have used radiosonde data for the estimation of momentum fluxes. *Shutts et al.* [1988] calculated the momentum flux of a single gravity wave from fluctuations in balloon ascent rate and horizontal perturbation velocities. *Mobbs & Rees* [1989] made use of the same variables to compute momentum flux profiles over the whole sounding range. The estimation of the vertical perturbation velocity from fluctuations in balloon ascent rate, however, are only reliable for large-amplitude waves. Smaller fluctuations can be due to measurement errors of radiosonde altitude or changed drag coefficients of the balloon. It can, therefore, be advantageous to calculate the vertical perturbation velocity from observed temperature fluctuations, which are measurable with a much higher accuracy. If the intrinsic frequency of the contributing waves is known, the momentum flux can be expressed using the polarization relations as

$$\rho\overline{u'w'} = -\rho\frac{\hat{\omega}g}{N^2}\overline{u'\hat{T}'_{+90}}. \tag{4.9}$$

Here $\hat{T}'_{+90}$ is the 90 degree phase-shifted (i.e. Hilbert transformed) normalized temperature fluctuation $\hat{T}'$ and the overbar denotes spatial average. *Sato & Dunkerton* [1997] analyzed ten years of twice daily radiosonde data at Singapore. They calculated quadrature spectra from time series of horizontal wind speeds and temperature and used Equation 4.9 to compute the corresponding momentum fluxes. Since the mean wind in the considered height range was weak, they ignored the Doppler shift between intrinsic and ground-based frequency and used the ground-based frequency in their computations. *Vincent et al.* [1997] and *Allen* [1996] fitted observed mean spectra to the gravity wave spectrum parameterization of *Fritts & VanZandt* [1993] and integrated over the model spectrum to find an intrinsic mean frequency $\overline{\hat{\omega}}$, which was then used in Equation 4.9 to compute the momentum flux from measured values of $\overline{u'\hat{T}'_{+90}}$. Their method, therefore, assumes similar propagation characteristics

for all waves independent of frequency, even though mainly low frequency waves were resolved.

The wavelet analysis described above provides all required gravity wave parameters to compute the momentum flux of each detected wave packet. We computed the height profiles of momentum flux by assuming a Gaussian shape of the wave packets with a full width half maximum as determined by the wavelet analysis. We used Equation 4.9 to compute the momentum flux from values of $\overline{u'\hat{T}'_{+90}}$ calculated from the perturbation amplitudes of the detected wave packets. The density at the height of the wave packet was obtained from monthly averaged temperature profiles using the hydrostatic approximation, i.e.

$$\rho(z) = \rho(z_o) \exp^{-\int_{z_o}^{z} \frac{\mathrm{d}z'}{H_\rho(z')}}, \tag{4.10}$$

where

$$H_\rho = \frac{1}{\frac{g}{RT} + \frac{1}{T}\frac{\mathrm{d}T}{\mathrm{d}z}} \tag{4.11}$$

is the density scale height.

Figure 4.13 shows contour plots of monthly averages of $\rho\overline{u'w'}\delta_-$ and $\rho\overline{v'w'}\delta_-$ calculated for all detected waves with intrinsic frequencies less than 10 f. This cutoff was chosen as the majority of the detected waves have frequencies less than 10 f, and the determination of intrinsic frequencies from hodograph analysis is prone to large uncertainties for high intrinsic frequencies. The mean values of the momentum fluxes at heights of 20 and 28 km are given in Table 4.2 for summer and winter.

The shape of the momentum flux profiles agrees with *Allen* [1996], although our values are up to an order of magnitude smaller than the ones reported by *Allen* [1996] and *Vincent et al.* [1997]. This, however, can be explained by the restriction of our analysis to waves with intrinsic frequencies less than 10 f, while *Allen* [1996] and *Vincent et al.* [1997] used the full spectrum of waves in their calculations.

In comparison with other experimental observations and in assessing the importance of the observed gravity waves for the mean circulation, the limited frequency range and our vertical wavelength bandwidth of about 1.2 to 11 km has to be kept

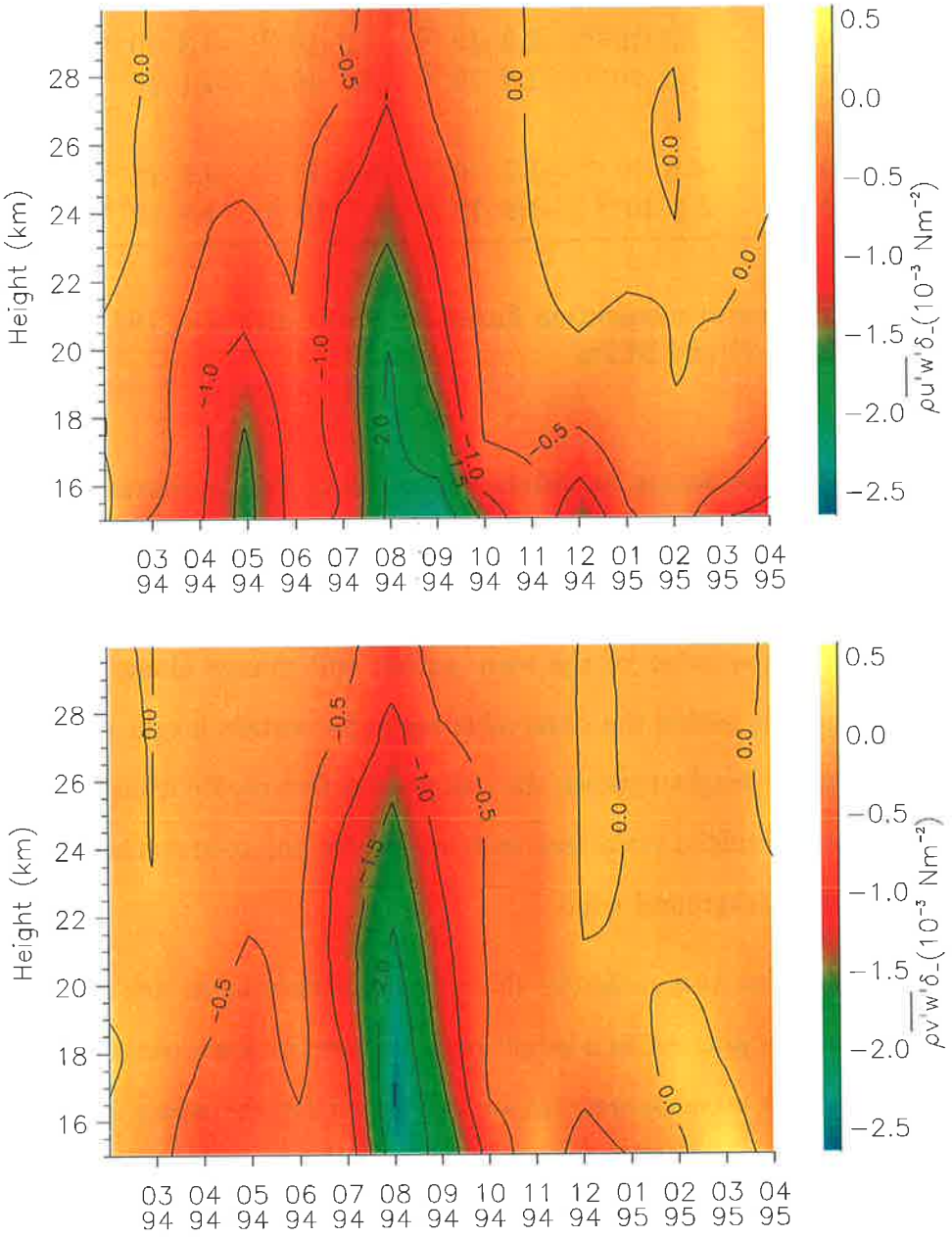

Figure 4.13: Contour plots of monthly averages of $\rho u'w'\delta_-$ (top) and $\rho v'w'\delta_-$ (bottom) for waves with intrinsic frequencies less than 10 f.

	$\langle\overline{u'w'}\delta_-\rangle$ (m^2s^{-2})	$\langle\overline{v'w'}\delta_-\rangle$ (m^2s^{-2})	$\langle\rho\overline{u'w'}\delta_-\rangle$ (Nm^{-2})	$\langle\rho\overline{v'w'}\delta_-\rangle$ (Nm^{-2})
winter				
20 km	$-1.3 \cdot 10^{-2}$	$-1.2 \cdot 10^{-2}$	$-1.0 \cdot 10^{-3}$	$-9.3 \cdot 10^{-4}$
28 km	$-1.6 \cdot 10^{-2}$	$-1.8 \cdot 10^{-2}$	$-3.7 \cdot 10^{-4}$	$-4.1 \cdot 10^{-4}$
summer				
20 km	$-6.6 \cdot 10^{-4}$	$-1.2 \cdot 10^{-3}$	$-5.6 \cdot 10^{-5}$	$-9.9 \cdot 10^{-5}$
28 km	$2.1 \cdot 10^{-3}$	$-1.8 \cdot 10^{-3}$	$5.1 \cdot 10^{-5}$	$-4.5 \cdot 10^{-5}$

Table 4.2: Mean values of momentum fluxes for waves with $\hat{\omega} < 10f$ for winter and summer at heights of 20 and 28 km.

in mind. For the same reason an estimation of mean flow acceleration from these momentum flux profiles is prone to large errors: Consider a wave packet propagating dissipationless through the background atmosphere. Due to changes in background wind the vertical wavenumber of the wave packet will change along its way. If the vertical wavenumber is within the observable range for certain height regions and out of this range for other height regions, the momentum flux profile from radiosonde observations will show artificial variations with height, leading to errors in the calculated accelerations of the background wind.

One can circumvent this difficulty if ray tracing techniques are applied. After extracting the wave parameters in a height region where the wave packet is observable, the parameters of the wave packet can be calculated for the whole height range of interest. It is then possible to compute the momentum flux even for those height regions, where the vertical wavenumber of the wave packet is not within the observable range, avoiding variations in the momentum flux estimates due to the observational filter. Ray tracing, furthermore, enables us to propagate the gravity wave spectrum to higher regions of the atmosphere which are inaccessible to direct measurements with radiosondes.

4.4.2 Mean-flow accelerations and intermittency

4.4.2.1 A linear ray-tracing model

For our modeling studies we applied a simple linear ray tracing model similar to *Eckermann* [1992], *Marks & Eckermann* [1995], *Alexander* [1996] and *Warner & McIntyre* [1996]. If one assumes no explicit dependence of the background atmosphere on horizontal position x and y and time t, then the horizontal wave numbers k and l and the ground-based frequency ω of a wave packet are constant along its ray (cf. Section 2.4). The intrinsic frequency $\hat{\omega}$ as a function of height is then given by

$$\hat{\omega}(z) = \omega - u(z)k - v(z)l \tag{4.12}$$

and the vertical wavenumber $m(z)$ can be obtained from the dispersion relation.

The integration along the ray path is taken from the source level until a turning or critical level is encountered, i.e. $m \to 0$ or $\hat{\omega} \to f$, respectively. In the absence of dissipation, the amplitude of the wave packet along the ray is determined by the conservation of wave action flux [*Lighthill*, 1978], which, in a single-column model, can be written as

$$A_f = \frac{c_{g,z}E}{\hat{\omega}} = \text{const.}, \tag{4.13}$$

where $c_{g,z}$ is the vertical group velocity and E the total energy density. Using the polarization equations in the Boussinesq approximation this can be expressed as

$$A_f = \frac{1}{2m}\rho\hat{u'_{\|}}^2(1 - \frac{f^2}{\hat{\omega}^2}) = \text{const.}, \tag{4.14}$$

where $\hat{u'_{\|}}$ is the horizontal peak perturbation amplitude parallel to the intrinsic propagation direction of the wave packet. The assumption of a single-column model is justified by our lack of knowledge about the fine scale geography of wave sources [*Warner & McIntyre*, 1996]. Equation 4.14 is used to calculate the amplitude of the wave packet from one level to the next when dissipation is negligible. Radiative damping, however, can severely attenuate the amplitude of slowly propagating gravity waves. We, therefore, included this dissipative process in our model using the parameterization of *Zhu*

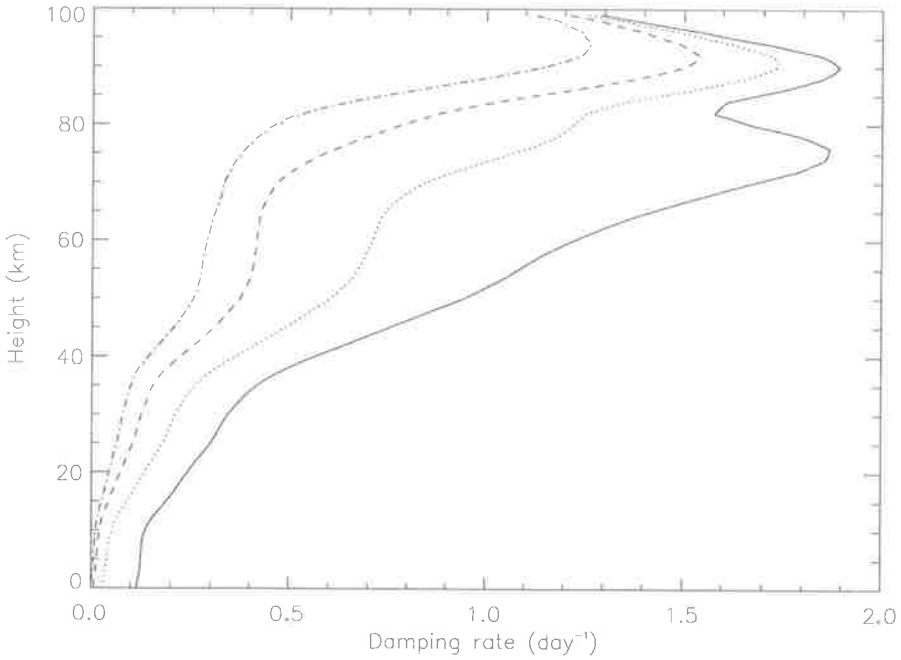

Figure 4.14: Radiative damping rates for the CIRA atmosphere in June at 50° S for vertical wavelengths of 2 (solid), 5 (dotted), 10 (dashed), and 20 (dot-dashed) km.

[1993]. His scheme allows the calculation of the scale-dependent radiative damping rate τ_{rad} as a function of altitude for a given temperature profile. Radiative damping attenuates the amplitude of a wave packet by a factor $\exp(-\tau_{\mathrm{rad}}(z)\frac{\Delta z}{c_{g,z}(z)})$ during its propagation through a height interval Δz at height z. Figure 4.14 shows examples of damping rates for the CIRA atmosphere in June at 50° S.

If the resulting amplitude exceeds the critical amplitude for dynamical instability (Equation 4.7), it is thresholded to this value. This corresponds to a dissipation mechanism that acts instantaneously once the critical amplitude is reached and stops as soon as the amplitude is restored to a sub-critical value. The existence of a threshold amplitude for instability renders the saturation mechanism non-linear. Hence, it is important to use actual wave packet amplitudes, and not averages over space or time.

4.4.2.2 Intermittency and gravity wave source spectrum

While the non-linear saturation mechanism requires the knowledge of actual wave packet amplitudes to correctly identify the heights where saturation becomes important, the mean zonal acceleration (Equation 4.8) depends on the temporally averaged momentum flux. The observation of wave packets in the radiosonde data indicates a degree of intermittency in the gravity wave production, that is, the wave packets will only be present for a certain amount of time at each height level. Hence, a correction factor has to be applied to the momentum flux profile of each wave packet to obtain the required temporal average. Due to the lack of information about wave intermittency, this correction factor was chosen arbitrarily in previous modeling studies to give reasonable magnitudes of acceleration at the required levels in the atmosphere [*Alexander & Rosenlof*, 1996; *Hamilton*, 1997]. The use of wavelet analysis, however, gives us information about the vertical extent of the gravity wave packets and can shed some light on the gravity wave intermittency.

We define the residence time τ of a wave packet as the time it takes to completely traverse an arbitrary height level

$$\tau = \int_{z_{\text{lower}}}^{z_{\text{upper}}} \frac{\mathrm{d}z}{c_{g,z}(z)}, \tag{4.15}$$

where z_{lower} and z_{upper} are the lower and upper boundary of the wave packet at the time of detection and $c_{g,z}(z)$ the vertical group velocity as a function of height. Monthly averaged values of $u(z)$, $v(z)$, and $T(z)$ were used for the calculation of $c_{g,z}(z)$. It is important to realize that the residence time τ is independent of the chosen height level: Consider an upwards propagating wave packet extending from z_{lower} to z_{upper}. It will take the upper end of the wave packet a certain time to reach an arbitrary height level above z_{upper}. The lower end of the wave packet will take the same time plus the time it takes to propagate from z_{lower} to z_{upper}. Thus, the wave packet will be present at the arbitrary height level for the residence time τ, independent of the choice of the height level. Any change in group velocity $c_{g,z}$ along the propagation path is compensated by a stretching or shrinking of the wave packet. The residence time is, therefore, an

invariant of the gravity wave propagation and equals the time the gravity wave source was turned on for the generation of the observed wave packet. Note that our definition of the residence time differs from that in *Alexander* [1998], who defined the residence time as the ratio of a *constant* height interval to the vertical group velocity of the wave packet. Her residence time is, therefore, a function of height, as she did not take the shrinking and stretching of the wave packet into account.

We can then define the intermittency of the wave packet as

$$\epsilon = \frac{\tau}{T_{\max}}, \tag{4.16}$$

where $T_{\max}$ is the residence time of a hypothetical wave packet extending over all those height regions where it could have been observed with the applied analysis method. The intermittency, therefore, equals the fraction of time during the time interval $T_{\max}$ the source had to be active to generate the observed gravity wave packet. $T_{\max}$ can be calculated as

$$T_{\max} = \int_{z_{min}}^{z_{max}'} \frac{\mathrm{d}z}{c_{g,z}(z)}, \tag{4.17}$$

where the prime indicates integration over only those height intervals where the vertical wavenumber $m(z)$ is within the observable range. The method is illustrated in Figure 4.15.

The horizontal wavenumber vector $\mathbf{k_h}$, the ground-based frequency ω, the wave action flux A_f, and the wave intermittency τ, all invariants of the dissipationless wave propagation through a horizontally isotropic steady-state atmosphere, fully characterize the wave packet and its effect on the atmosphere in our model. The applied observation method, however, cannot provide information about the full $(\mathbf{k_h}, \omega)$ spectrum. As indicated above, the radiosonde technique can only observe gravity waves with vertical wavelengths between about 1.2 km and 11 km. Due to this observational filter, only certain parts of the $(\mathbf{k_h}, \omega)$ spectrum are observable at each height. Changes in background wind with height Doppler-shift different parts of the $(\mathbf{k_h}, \omega)$ spectrum into the observable wavenumber range, so that different parts of the spectrum can be observed at different heights. Because of the invariance of $\mathbf{k_h}$, ω, A_f, and τ, however,

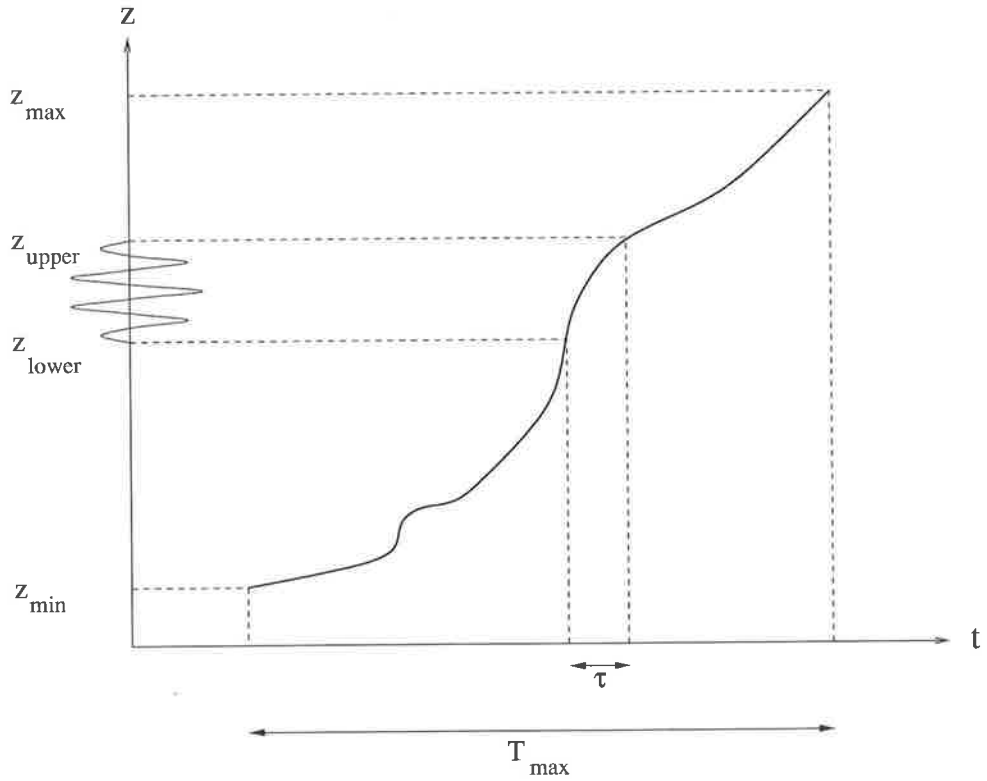

Figure 4.15: Trajectory of a wave packet observed between z_{lower} and z_{upper}. The residence time τ is the time the gravity wave source had to be switched on to produce the observed wave packet. If the wave packet extended over the whole observed height interval $[z_{\text{min}}, z_{\text{max}}]$ the gravity wave source would have had to be active for the whole time T_{max}.

these wave parameters are independent of height and a larger part of the gravity wave spectrum can be reconstructed. By using different observation techniques together, one can obtain more detailed information about the spectrum.

Figures 4.16 and 4.17 illustrate the source spectra reconstructed from our observations for summer and winter, respectively. They are not necessarily the spectra emitted by a physical source somewhere in the lower atmosphere, as the source spectra might not be completely observable by the applied technique. To obtain better statistics, all information about wave propagation directions was discarded in our spectra and only the magnitudes of the horizontal wavenumber vector $\mathbf{k_h}$ and the ground-based frequency ω were utilized. The figures show slightly smoothed contour plots of time-averaged wave action flux

$$\overline{A_f}(k_h,\omega) = \frac{1}{N}\sum_{i=1}^{N} \|A_f(k_h,\omega,i)\| \frac{\tau(k_h,\omega,i)}{T_{\max}(k_h,\omega,i)} \tag{4.18}$$

and source intermittency

$$\overline{\epsilon}(k_h,\omega) = \frac{1}{N}\sum_{i=1}^{N} \frac{\tau(k_h,\omega,i)}{T_{\max}(k_h,\omega,i)}, \tag{4.19}$$

where i is an index over the different radiosonde soundings. The analyzed height range was from 15 km to the maximum height of the soundings, often reaching up to 30 km. The horizontal wavenumber k_h and the ground-based frequency ω were binned logarithmically into 25 bins for the ranges $k_h = \frac{2\pi}{10^7\mathrm{m}} \ldots \frac{2\pi}{10^3\mathrm{m}}$ and $\omega = 0.1f \ldots 300f$, respectively. For a better comparison of source strength between the two seasons, the average source strength is shown as a one-dimensional function of horizontal wavelength and ground-based frequency, respectively, in Figure 4.18. It is evident that the total wave action flux in the observed vertical wavenumber range is very similar in magnitude for winter and summer. This corroborates the argument that the differences in horizontal wind variance as presented in Figure 4.7 can be largely due to seasonal changes in the background atmosphere. It is also noteworthy, that, while the gravity wave field is clearly dominated by low intrinsic frequency, inertio gravity waves, the Doppler-shifting by the background wind leads to tails in the ground-based

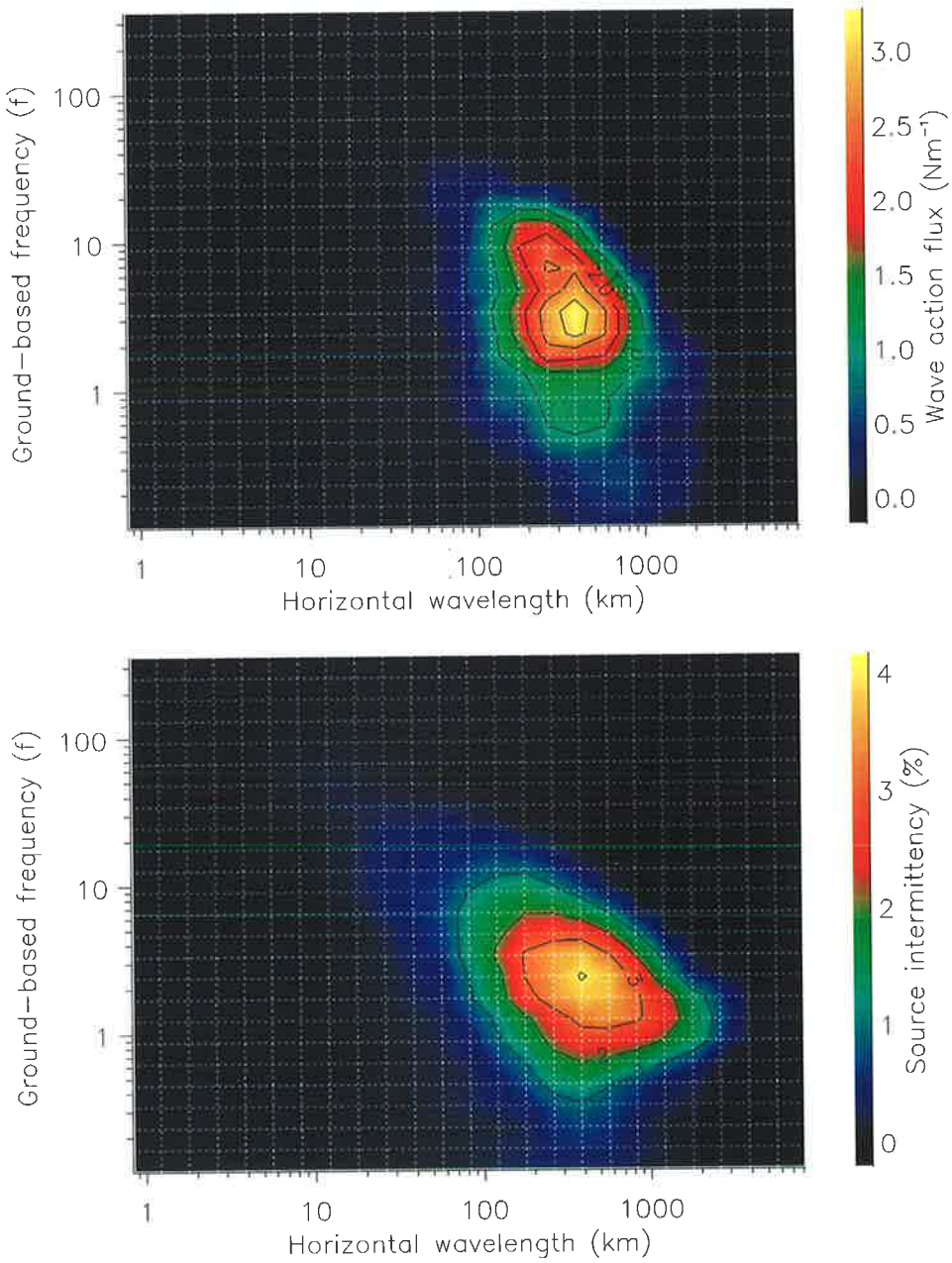

Figure 4.16: Contour plot of average wave action flux (top) and source intermittency (bottom) as a function of horizontal wavelength and ground-based frequency for summer. The dashed lines show the intervals over which the data have been binned.

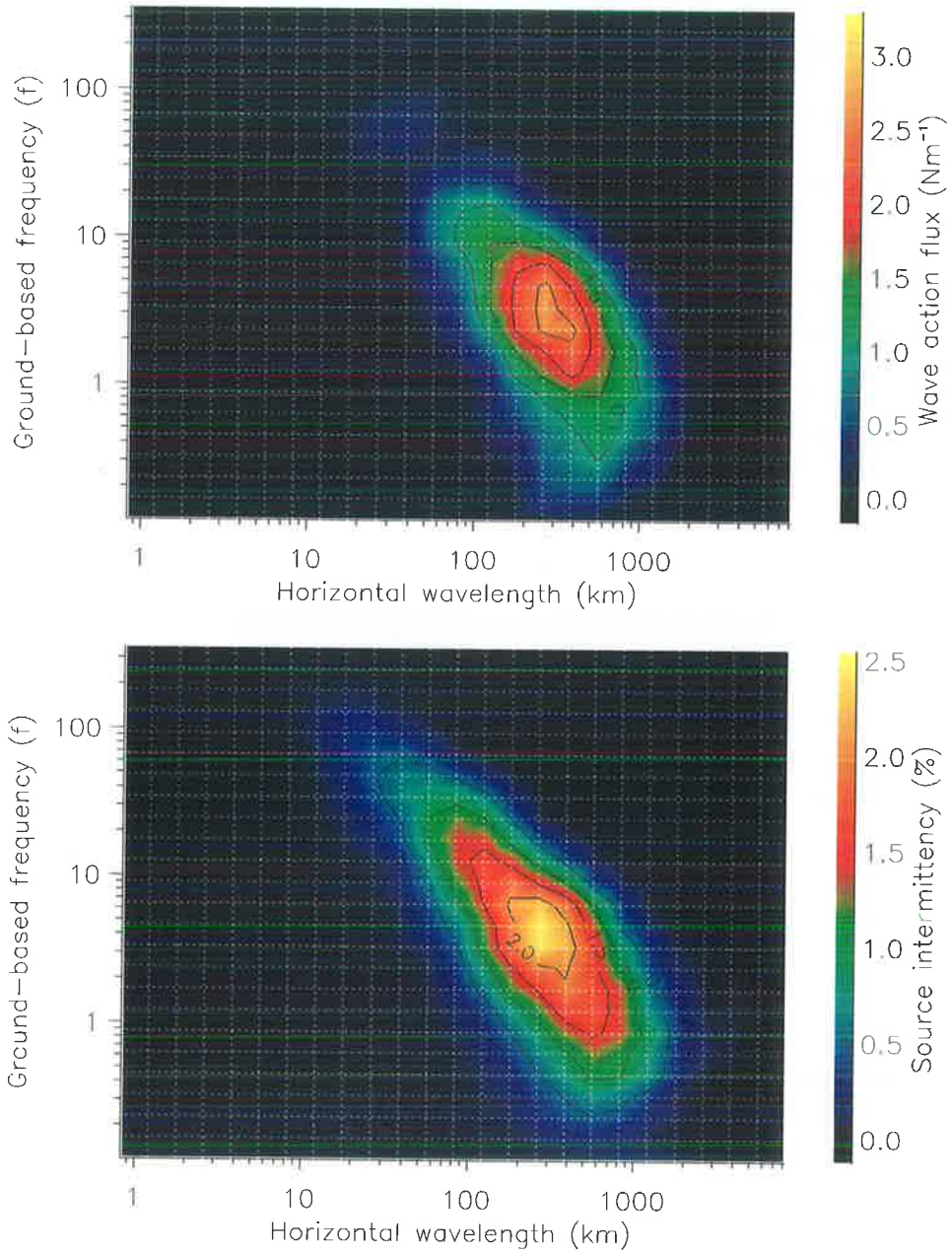

Figure 4.17: Same as Figure 4.16 but for winter.

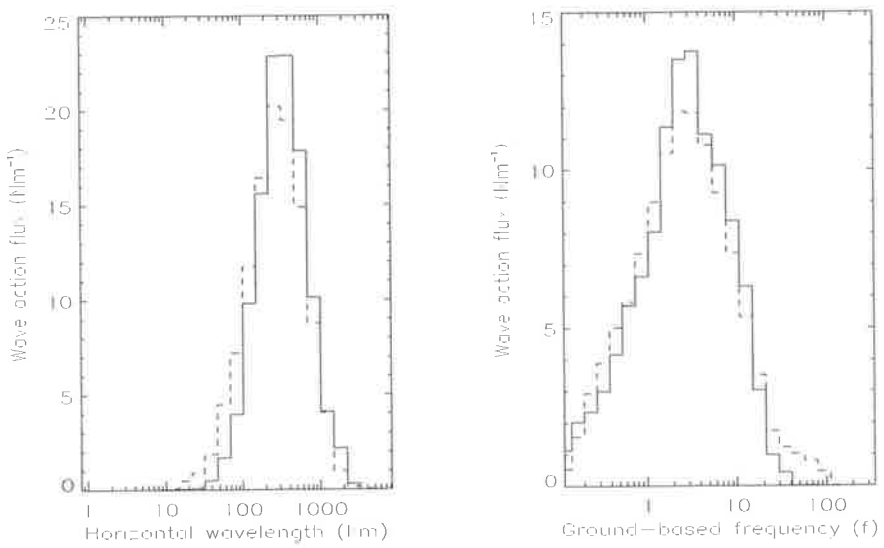

Figure 4.18: Average wave action flux as a function of horizontal wavelength and ground-based frequency for winter (dashed) and summer (solid).

frequency distribution to both low and high frequencies. Figure 4.19 shows the average wave action flux as a function of intrinsic horizontal propagation direction for winter and summer. In both cases the observed wave action flux is distributed anisotropically. This observed anisotropy does not necessarily imply an anisotropic wave field, but may again be due to the observational filter of the radiosonde method. If the dominant background wind is confined to certain azimuths, then only certain regions of the $(\mathbf{k_h}, \omega)$ spectrum contribute to our observations, and what might be an isotropic wave field, can appear anisotropic in observations.

4.4.2.3 Mean-flow accelerations

In our model we ray-traced all upwards propagating gravity wave packets detected above 15 km for each month of the year to a maximum height of 100 km. As a starting level we chose the lowest height above $z_{\text{start}} = 15$ km from where a propagation of a wave packet to its level of detection was possible in the given background atmosphere (Figure 4.20). The wave action flux of the wave packet at the starting level was adjusted to reach agreement between model and observation at the detection level and

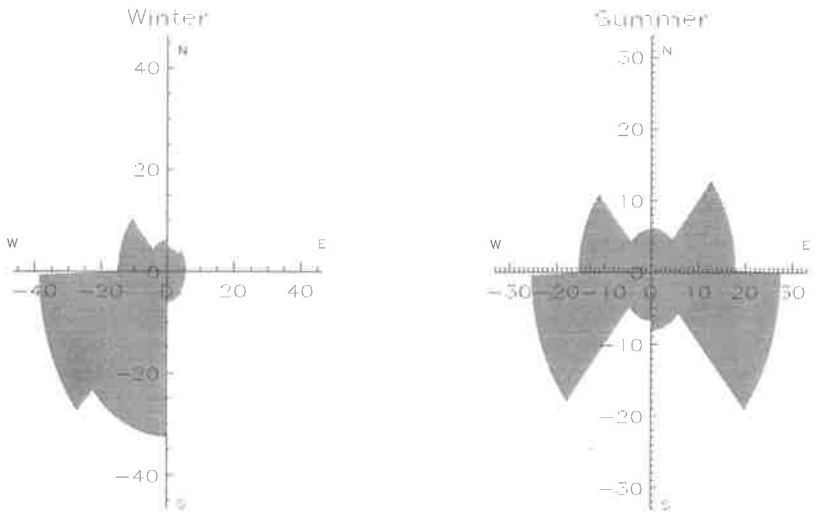

Figure 4.19: Average wave action flux as a function of intrinsic horizontal propagation direction for winter and summer. Units are Nm^{-1}.

to compensate for any radiation damping effects. We used a height resolution of 500 m and no interaction of the packets was allowed. As background atmosphere we used the COSPAR International Reference Atmosphere (CIRA) 1986 temperature and zonal winds of the respective month linearly interpolated to the required latitude of 55° S. A contour plot of the zonal wind profiles is given in Figure 4.21. The acceleration was calculated using Equation 4.8 with

$$\langle \rho u' w' \delta_{-} \rangle = \epsilon k A_f \tag{4.20}$$

computed for each wave packet.

Figure 4.22 shows a contour plot of the inferred zonal accelerations in the mesosphere. The accelerations are most significant at regions of high wind shear, at around 85 km during summer and between 60 and 80 km during winter. The magnitude of the wave drag in winter seems to be about two to three times higher than the average drag expected both from observations and theory [*Fritts & Vincent*, 1987; *Fritts & Yuan*, 1989; *Holton*, 1983]. The accelerations deduced from our model, however, are based on the data from a single station only and might deviate from a zonal average

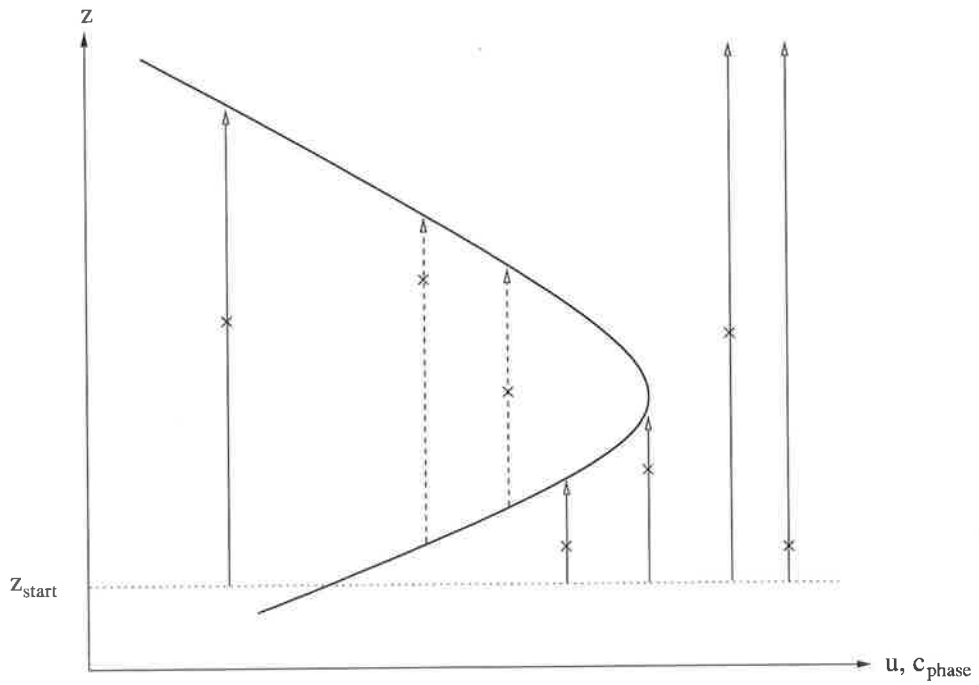

Figure 4.20: Illustration of the applied choice of starting levels. The thick line indicates the background velocity in wave propagation direction, u. The starting level for each wave packet was chosen as the lowest height above z_{start} from where a propagation of the wave packet to its level of detection (cross) was possible. Wave propagation from a uniform starting level z_{start} could not reproduce the effects of waves observed above a possible critical level.

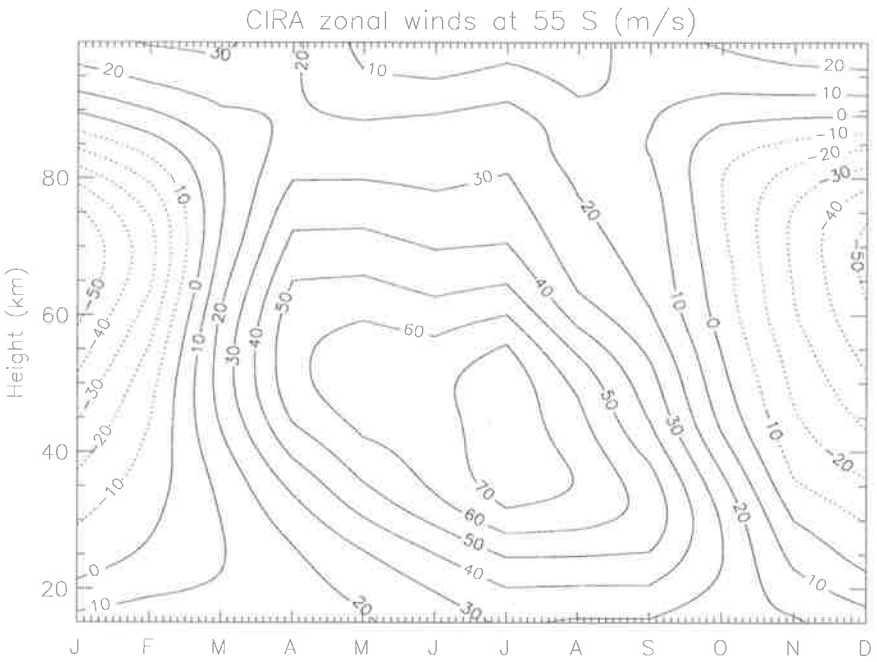

Figure 4.21: CIRA zonal winds linearly interpolated to 55° S.

over all longitudes.

In contrast to the deceleerative effect of the waves in the mesosphere, our model reveals an accelerative effect in the middle stratosphere (Figure 4.23). This is in agreement with calculations of *Alexander & Rosenlof* [1996] who used global measurements of temperature, wind, and chemical constituents to estimate the zonal mean forcing by unresolved waves in the stratosphere.

It is important to realize, that the analysis of the radiosonde data might be biased towards low intrinsic frequency waves, as these waves usually have larger amplitudes than their high frequency counterparts and are, thus, easier to detect. Waves of high intrinsic frequency, while smaller in amplitude, might still outweigh the effect of the observed low frequency waves. Nevertheless, our computations show, that waves with low intrinsic frequency in the stratosphere can have a profound impact on the circulation in the middle atmosphere, at least in our simple linear model.

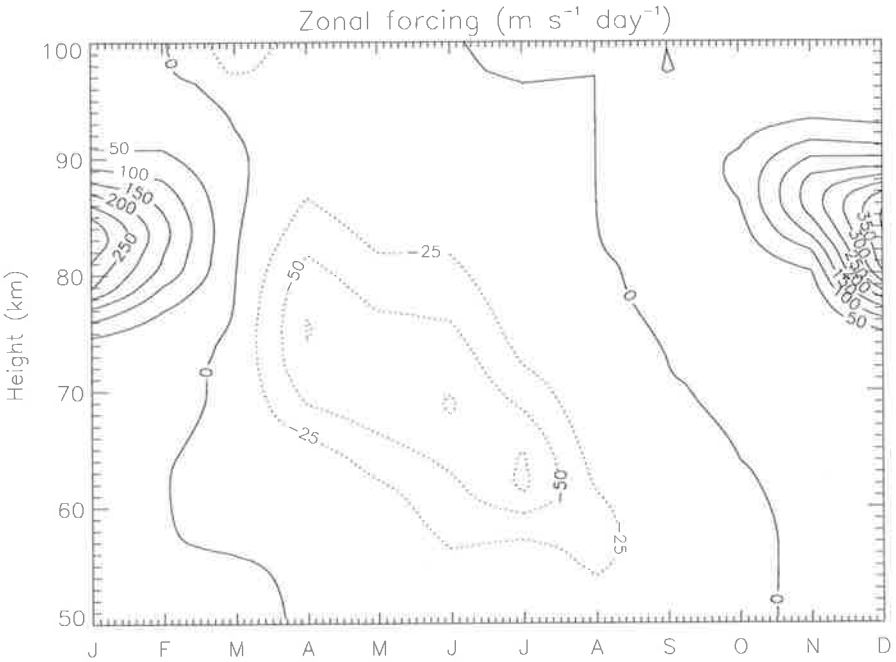

Figure 4.22: Inferred zonal accelerations in the mesosphere. Solid contour lines correspond to eastward acceleration.

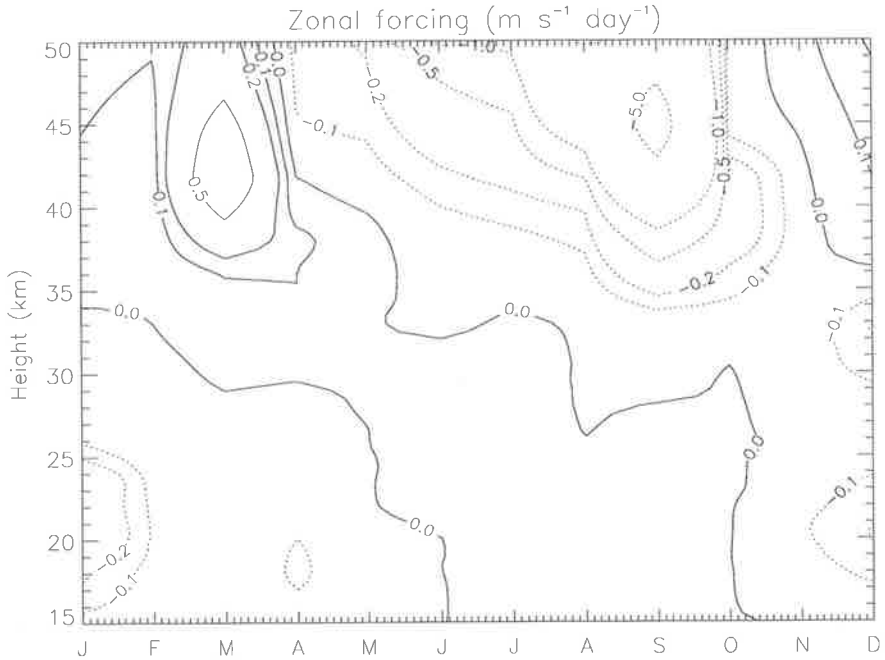

Figure 4.23: As Figure 4.22, but for the stratosphere.

4.5 Summary and conclusion

Application of the wavelet algorithm introduced in Chapter 3 to twice-daily radiosonde soundings of the lower stratosphere over Macquarie Island revealed a strong seasonal cycle in the total and downwards propagating gravity wave variance with a maximum in winter. This maximum in gravity wave variance coincides with a shift of the wave amplitude distribution to larger values. The variance-weighted intrinsic propagation direction during winter is predominantly south-southwest-wards, while it is nearly isotropic during summer. The observed wave field was found to be dominated by low frequency inertia gravity waves.

In the interpretation of these findings attention was paid to the limited vertical wavelength range observable with the radiosonde technique [*Alexander*, 1998]. Doppler-shifting of waves into and out of this wavelength band can lead to significant changes in the observed wave field and complicates the analysis. The usefulness of the presented observations is, therefore, mainly in conjunction with modeling studies. The wave characteristics were presented in terms of variables that are directly accessible by measurements, i.e. vertical wavelength and wind variance. A disadvantage of this approach is the fact that these variables undergo changes as the wave packet is Doppler-shifted by changes in the background wind with height, and, therefore, depend on the detection level of the wave packet.

We used the parameters of the detected wave packets to assess the influence of the observed gravity wave field on the mean-flow. While a direct computation of a vertical momentum flux profile corresponding to the wave packets observed at the respective heights is possible, the observational filter of the radiosonde technique, together with the Doppler-shifting of the wave packets due to a height variable background atmosphere, prohibit the determination of mean-flow accelerations from these profiles.

To overcome this problem, we input the detected waves in a linear ray tracing model from a common source level. The calculation of a momentum flux profile is then possible even at those heights, where the wave packets would be outside the

observationally accessible vertical wavenumber range. The definition of a wave source intermittency then allows the calculation of a temporally averaged momentum flux profile for each detected wave packet.

The inferred mean-flow decelerations in the mesosphere were shown to be up to a factor of 2 to 3 times higher than measurements and theory would predict. In the lower stratosphere, the waves lead to an acceleration of the mean-flow in accordance with theoretical predictions.

Chapter 5

Radar fundamentals

5.1 Introduction

While operational radiosonde data, as analyzed in the previous chapter, have good height resolution and almost global coverage, the individual soundings are usually spaced at least 6 or 12 hours apart and are restricted to altitudes below about 35 km. Atmospheric radars are an alternative way to probe the atmosphere. Radars are only available at a few locations worldwide, but they offer the advantage of time resolutions of a few minutes and, if powerful enough, can obtain measurements from altitudes up to some 100 km, albeit with a gap between 25 and 60 km. Furthermore, radars not only provide information about the 3-dimensional wind, but can also be used to directly measure turbulence parameters and momentum fluxes, variables strongly related to gravity wave activity. Radars, therefore, not only enable us to observe the gravity waves themselves, but also to directly observe some of the effects they have on the atmosphere.

In this chapter we give an overview of the atmospheric radar technique. Chapter 6 introduces some signal processing algorithms, and Chapter 7 deals with the possibility of turbulence measurements by radar. The introduced techniques are then applied to wind and turbulence measurements in Chapters 8 and 9, using the University of Adelaide's VHF radar at Buckland Park.

5.2 Beam forming and pulsed operation

Radar ("radio detection and ranging") systems work by transmitting a radio wave of certain frequency and listening to echoes from scatterers along the propagation path of the wave. To gather information about a certain volume of the atmosphere one has to use a well-defined sampling volume from which the radar echoes are obtained. To define the direction of transmission and reception, either antenna dishes or antenna arrays are used to form a radar beam. By defining the phase differences between the different antennas of an array, the transmitted radio waves are made to interfere constructively in the desired direction and destructively otherwise. The polar diagram for an array of N sources at positions $\mathbf{x}_i$ in direction of the wavenumber vector $\mathbf{k}$ is given as

$$P_{\text{array}}(\mathbf{k}) = |\sum_{i=1}^{N} A_i \exp(-j\mathbf{k}\mathbf{x}_i)|^2 \cdot P_{\text{antenna}}(\mathbf{k}), \tag{5.1}$$

where A_i is the complex amplitude of the electric field at antenna i and $P_{\text{antenna}}(\mathbf{k})$ is the polar diagram for a single antenna. Figure 5.1 shows the one-way polar diagram for the University of Adelaide's VHF radar at Buckland Park for a beam pointed at a zenith angle of 14.5° towards east.

A discrimination of the range is usually achieved using pulsed operation (Figure 5.2). Radar pulses of a certain duration Δt_{Tx} are transmitted at time intervals of the inter-pulse-period T_{IPP} (Pulse 1). An echo pulse received a time T_R after transmission (Pulse 2) has then traveled over a distance cT_R, where $c = 3 \cdot 10^8 \text{ms}^{-1}$ is the speed of light. For a mono-static radar, i.e. a radar with colocated transmitting and receiving antennas, this echo can then be attributed to a scatterer at range $R_o = cT_R/2$ from the radar in the beam direction. Due to the limited bandwidth of the receiving path, the voltage detected at the receiver at time T_R after transmission is effectively an average over a time interval Δt_{Rx}. For optimal operation, the receiver bandwidth is matched to the transmitted pulse so that $\Delta t_{Tx} = \Delta t_{Rx} = \Delta t$. The echo pulse then contains information about the range interval from $R_o - c\Delta t/2$ to $R_o + c\Delta t/2$. Usually, the range resolution is expressed as $\Delta R = c\Delta t/2$, which corresponds to the full-width

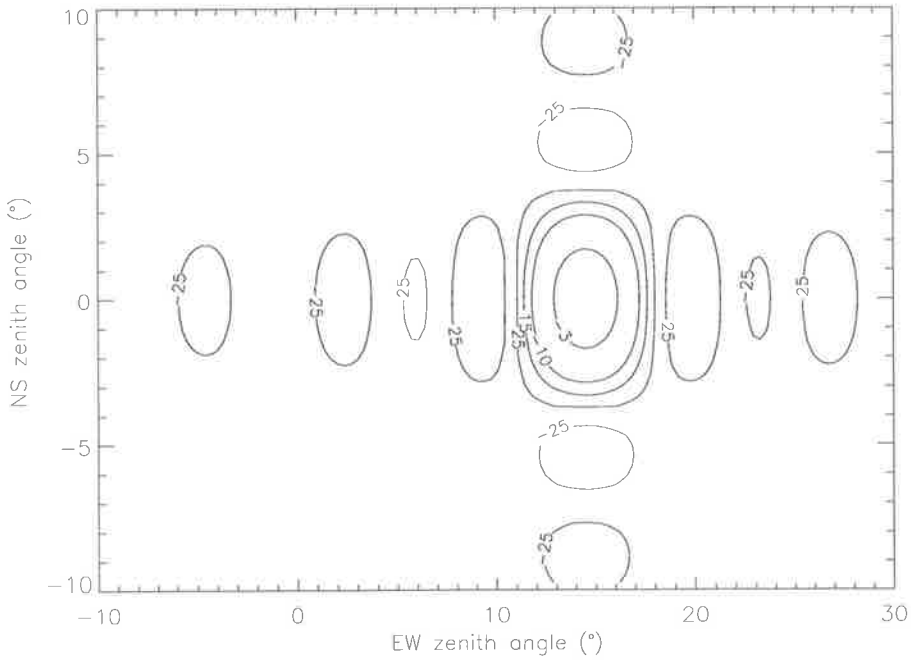

Figure 5.1: One-way polar diagram for the University of Adelaide's VHF radar at Buckland Park for a zenith angle of 14.5° east. The polar diagrams for the single dipoles of the array were assumed to be isotropic. The units of the contours are dB.

half-maximum of the weighting function. If the echoes from distant ranges are strong enough, range aliasing can occur (Pulse 3). Here the echo pulse is received after another pulse has been transmitted, and it is not clear to which of the transmitted pulses the echo belongs. However, as the power of volume-scattered radar echoes has an inverse square dependence on radar range, the range-aliased echoes are generally much weaker than the direct ones. A high maximum unaliased range and small height resolution are desirable for most applications, but, in practice, the choice is limited by radar parameters like transmitter power and receiving bandwidth. Increasing the inter-pulse-period T_{IPP} increases the maximum unaliased range

$$R_{max} = c\frac{T_{IPP} - \Delta t}{2}, \tag{5.2}$$

but it also decreases the average transmitted power

$$\overline{P_t} = \frac{\Delta t_{Tx}}{T_{IPP}} P_t, \tag{5.3}$$

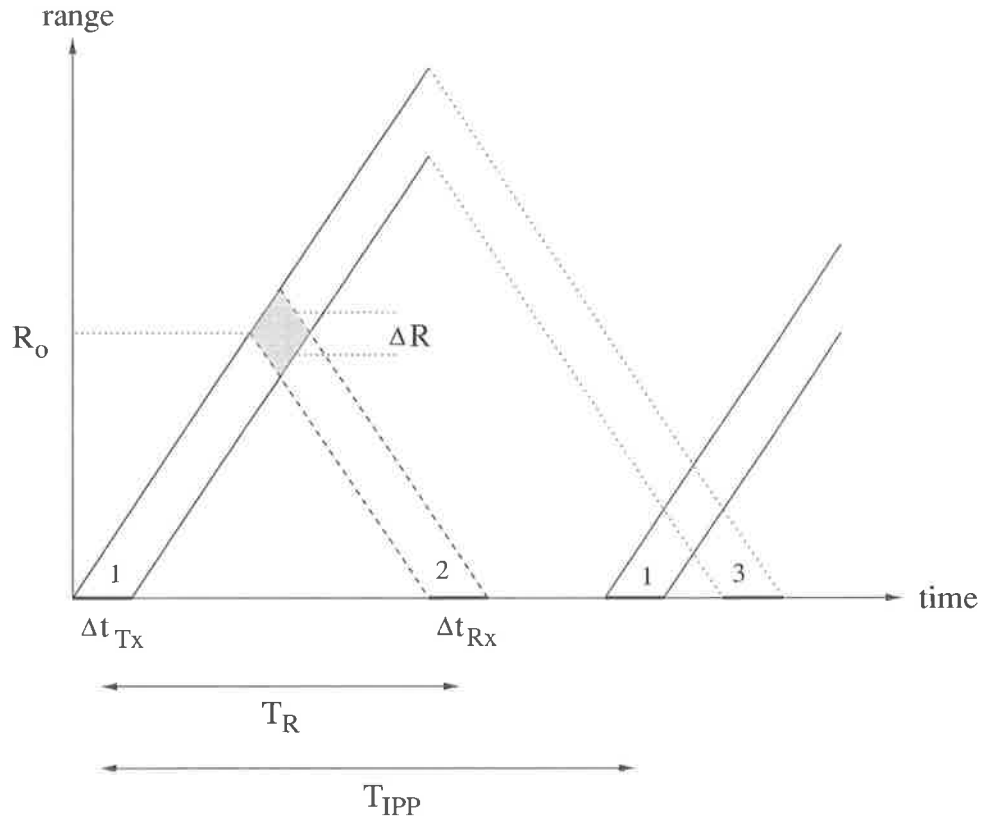

Figure 5.2: Range-time diagram of pulsed radar operation. See text for details.

where P_t is the (peak) transmitter power, and, hence, decreases the maximum range of usable radar echoes. The height resolution ΔR of a radar system is limited by the bandwidth of the (receiving) system and the requirement of sufficient average transmitted power $\overline{P_t}$.

5.3 Scattering and reflection mechanisms

Clear air radar echoes result from refractive index variations in the air with a scale of $\lambda/2$ along the beam, where λ is the radar wavelength. The waves backscattered from two scatterers a distance $\lambda/2$ apart will have a phase difference of 2π at the receiver and, thus, interfere constructively. These fluctuations in refractive index are generally associated with turbulence and small-scale waves or laminar structure.

The refractive index n of air at VHF (30-300 MHz) and UHF (300-3000 MHz)

frequencies is given by

$$n - 1 = 77.6 \cdot 10^{-6} \frac{p}{T} + 0.373 \frac{e}{T^2} - 40.3 \frac{N_e}{\nu}, \tag{5.4}$$

where e, p, and T are the partial pressure of water vapour (hPa), atmospheric pressure (hPa), and absolute temperature (K), respectively, N_e is the number density of free electrons (m^{-3}), and ν is the radar frequency (MHz) [*Gage & Balsley*, 1980]. The first two term express the contributions due to bound electrons through density fluctuations of dry air and water vapour, respectively, whereas the third term gives the contributions due to the presence of free electrons. Because of the high humidity, the second term is important mainly in the lower troposphere. The third term is only important from heights above 50 km, where solar radiation leads to a rapid increase of free electron density with height.

The scattering and reflection mechanisms important in the lower atmosphere can be characterized by the distances parallel and perpendicular to the radar beam over which the refractive index fluctuations are correlated within the radar volume.

In the case of *turbulent scatter*, the correlation lengths perpendicular to the radar beam are small enough that quadratic phase variations in the scattering integral, the so-called Fresnel term, can be neglected. For isotropic turbulence, where the correlation length of refractive index variations is independent of direction, the volume reflectivity is given by [*Tatarskii*, 1961]

$$\eta_{\text{turb}} = 0.38 C_n^2 \lambda^{-1/3}, \tag{5.5}$$

where the refractive index structure function constant for locally homogeneous and isotropic inertial range turbulence is given by

$$\overline{[n(\mathbf{r} + \mathbf{\Delta r}) - n(\mathbf{r})]^2} = C_n^2 |\mathbf{\Delta r}|^{2/3}. \tag{5.6}$$

For anisotropic turbulence the correlation lengths vary in three dimensions, which makes the volume reflectivity η_{turb} a function of direction. This leads to a dependency of returned power on the zenith (and azimuth) angle, an effect called aspect sensitivity.

If the correlation lengths perpendicular to the radar beam are comparable to the Fresnel zone radius $r_F = \sqrt{R\lambda/2}$, where R is the radar range, the quadratic phase variations in the scattering integral become important[1]. In the atmosphere, this usually means existence of horizontally coherent layers in the radar volume, which can occur in hydrostatically stable regions. *Fresnel scatter* arises if the refractive index discontinuities are randomly layered in the vertical. If the layers are ordered, or in the limiting case of a single layer, *Fresnel* or *partial reflection* occurs [*Gage & Balsley*, 1980]. Both of these mechanisms show strong aspect sensitivity.

The transition between these mechanisms is very gradual. The main difference between anisotropic turbulence and Fresnel scatter/reflection is the horizontal scale of the involved anisotropies: Anisotropic turbulent scatter is concerned with anisotropies on the scale of the radar wavelength, whereas Fresnel scatter/reflection deals with structures of the order of a few wavelengths. Larger coherence lengths lead to a more pronounced aspect sensitivity, and the determination of coherence lengths (using e.g. spaced antenna methods) or aspect sensitivity (using e.g. beam swinging experiments) can be used to differentiate between the above mechanisms to a certain degree [*Hocking et al.*, 1989; *Hocking et al.*, 1990].

5.4 The radar equation

The strength of the received echo as a function of radar parameters and scattering cross sections is given by the radar equation, which has been formulated for a variety of situations [*Tatarskii*, 1961; *Gage & Balsley*, 1980; *Doviak & Zirnic*, 1984]. Here we will only quote the equations for the two limiting cases in the forthcoming analysis.

For isotropic scattering, the received power for scattering of a radar pulse of length ΔR at range R is given by

$$P_r = \frac{\pi}{64} \frac{P_t A_e \alpha \Delta R}{R^2} \eta, \tag{5.7}$$

[1]For a more mathematical discussion of the importance of the Fresnel term see, for example, *Doviak & Zirnic* [1984], chapter 11

where P_t is the transmitted power, A_e is the effective antenna area, α is the total efficiency factor of the system, and η is the volume reflectivity. As the volume illuminated by the radar increases with the square of the range, the range dependence of volume scatter is an inverse square law, in contrast to the R^{-4} dependence of a point scatterer.

For reflection from a single, sharply bounded discontinuity, i.e. Fresnel reflection, the radar equation is given as

$$P_r = \frac{P_t A_e^2}{4\lambda^2 R^2} |\rho|^2, \tag{5.8}$$

with λ the radar wavelength and ρ the amplitude reflection coefficient.

With the appropriate expressions for the volume reflectivity η and the amplitude reflection coefficient ρ the power of the radar echoes can be readily computed.

5.5 Radar data acquisition and coherent integration

Figure 5.3 shows a schematic diagram of a radar to illustrate the signal flow (after *Tsuda* [1989]). A radio frequency carrier generated by a stable oscillator (OSC) is modulated by a pulse shape from the modulator (MOD). After amplification (Tx) the pulse passes through the transmit/receive switch (T/R) and is radiated from the antenna.

When the transmitted wave encounters refractive index variations of the scale of $\lambda/2$, a fraction of the pulse is back-scattered to the antenna. The task of the receiving system of a coherent radar is now to determine the amplitude and phase of the backscattered wave at the receiving antenna.

On reception, the radar echo received by the antenna passes through the T/R-switch and is preamplified by a radio frequency-amplifier. The T/R switch is needed to protect the receiving system from damage caused by the high power during the

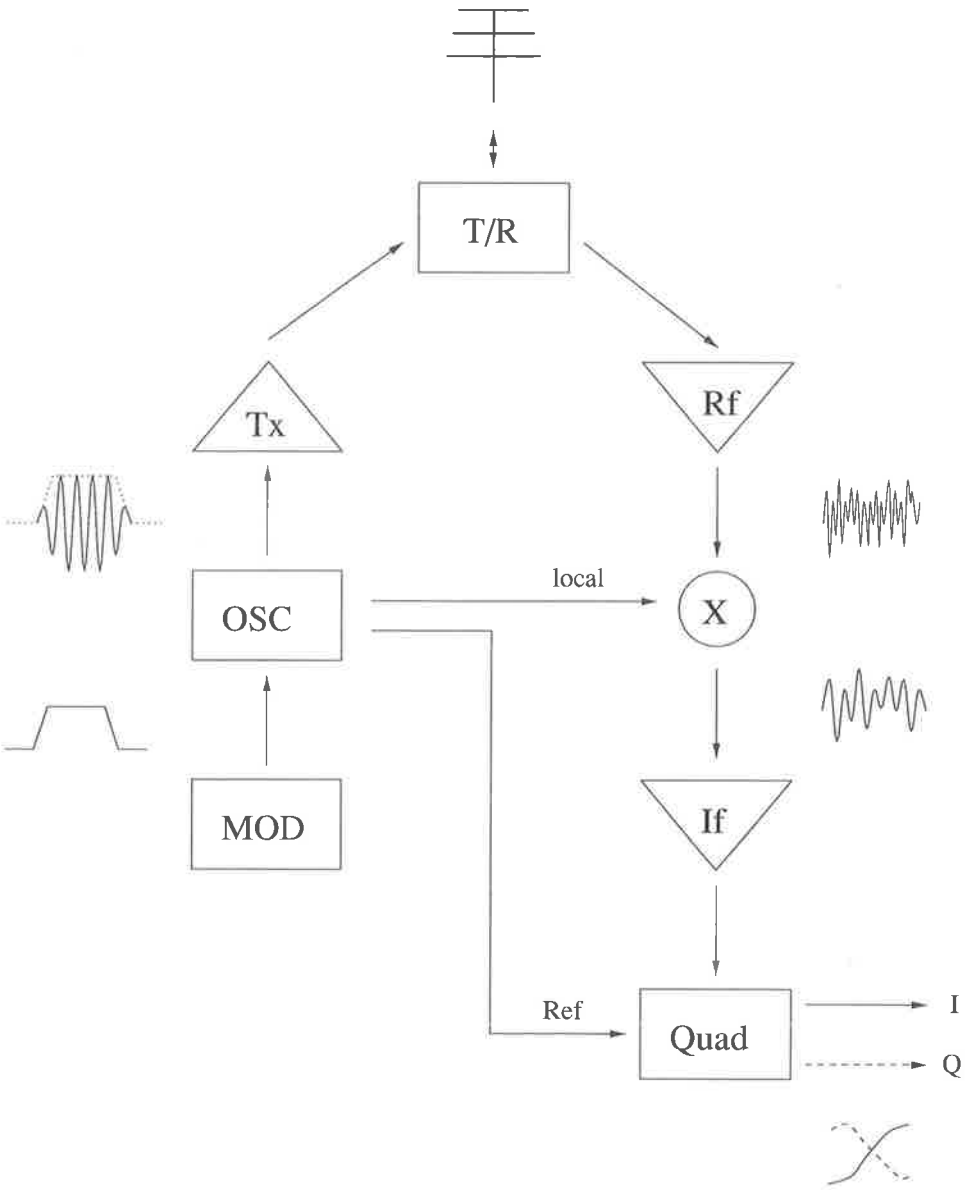

Figure 5.3: Radar schematic diagram, together with signal waveforms, to illustrate signal flow (after *Tsuda* [1989]).

transmission. The signal is then down-converted to an intermediate frequency by mixing with a coherent local signal (X). This frequency conversion alleviates the problem of possible feed back of the amplified signal into previous stages of the receiving system. The IF signal is further amplified and then demodulated in the quadrature detector by mixing with a coherent reference signal to yield the in-phase and quadrature component of the received signal. The demodulation of the received signal is thus achieved

in two steps. Instead of mixing the received signal directly with the carrier frequency, it is first mixed with a local frequency and subsequently with a reference frequency. Coherency of the involved signals is, therefore, of utmost importance. The in-phase and quadrature components are 90^o phase-shifted versions of each other and can be interpreted as a complex time series of the electro-magnetic field vector at the receiving antenna. They are usually converted into a digital signal by an analog-to-digital converter and further processed by a computer.

The phase of the electro-magnetic field vector at the receiving antenna depends (for a mono-static radar) on the distance r between antenna and scatterers as

$$\phi = 2kr + \text{const.}, \tag{5.9}$$

where $k = \frac{2\pi}{\lambda}$ is the radar wavenumber. Radial motion of the refractive index irregularities in the scattering volume corresponds to a rate of phase change

$$\frac{\mathrm{d}\phi}{\mathrm{d}t} = 2k\frac{\mathrm{d}r}{\mathrm{d}t} \tag{5.10}$$

in the time series of the in-phase and quadrature components detected by the receiver. In pulsed operation, the receiver output is sampled once per inter-pulse-period T_{IPP} for each range gate, i.e. the data points in the time series for each range gate are spaced by T_{IPP}. The radial velocities of the scatterers, however, are limited to values below about 30 ms^{-1} for commonly used beam-pointing angles. The phase of the electro-magnetic field vector, hence, changes very slowly compared to the sampling rate T_{IPP} and is almost constant between successive data points. To reduce the data flow rate one can, therefore, replace several successive data points in the time series of each range gate with their average, without unduly distorting the information contained in that time series. This technique is called coherent integration and is often performed by specially designed digital signal averagers.

To understand the effects of coherent integration, we consider it to be made up of two separate operations [*Farley*, 1983; *Rastogi*, 1983]:

1. Filter the (complex) receiver time series for range gate R, $v(R, t_j)$, $t_j = jT_{IPP}$,

with a running average of duration NT_{IPP}, i.e.

$$w(R, t_k) = \frac{1}{N} \sum_{j=k}^{k+N-1} v(R, t_j), \tag{5.11}$$

2. sample $w(R, t_k)$ at time intervals $T = NT_{IPP}$.

The effect of the running average in the frequency domain is to weight the time-averaged periodogram $P(f)$, i.e. the estimate of the power spectrum of $v(R, t_j)$, with a frequency window

$$\begin{aligned} G(f) &= \left\| \sum_{k=0}^{N-1} \frac{1}{N} \exp(i2\pi f k T_{IPP}) \right\|^2 \\ &= \frac{\sin^2(\pi f T_{IPP} N)}{N^2 \sin^2(\pi f T_{IPP})} \end{aligned} \tag{5.12}$$

This window is a comb filter with maxima at multiples of $1/T_{IPP}$. Between any two maxima there are $N-1$ minima with zero weight at multiples of $1/NT_{IPP}$. The effect of the sampling at time intervals $T = NT_{IPP}$ leads to a new Nyquist frequency of $1/2T$, i.e. the frequencies $-1/2T_{IPP} \leq f \leq 1/2T_{IPP}$ are aliased into the frequency window $-1/2T \leq f \leq 1/2T$. The comb filter is illustrated in Figure 5.4 for $N = 5$.

It is worth noting, that a flat spectrum is left flat by the combined effect of filtering and aliasing, i.e. white noise is transformed into white noise. The effect on signal power, however, depends on the Doppler-shift of the signal leading to a biased spectrum estimate. While this is generally of minor concern in the estimation of Doppler-shifts and broadening, it can bias measurements where echo strength is important, e.g. measurements of aspect sensitivity.

5.6 Data analysis techniques

The first step in data analysis is to extract atmospheric parameters from the (complex) time series at each range gate. This can be performed in either the time or the frequency domain [*Rastogi*, 1989; *Rastogi*, 1990].

Analysis in the frequency domain requires an estimate of the power spectrum of the atmospheric returns. Let $z(t_k)$, $t_k = kT$, $k = 0 \ldots M-1$, be the (complex)

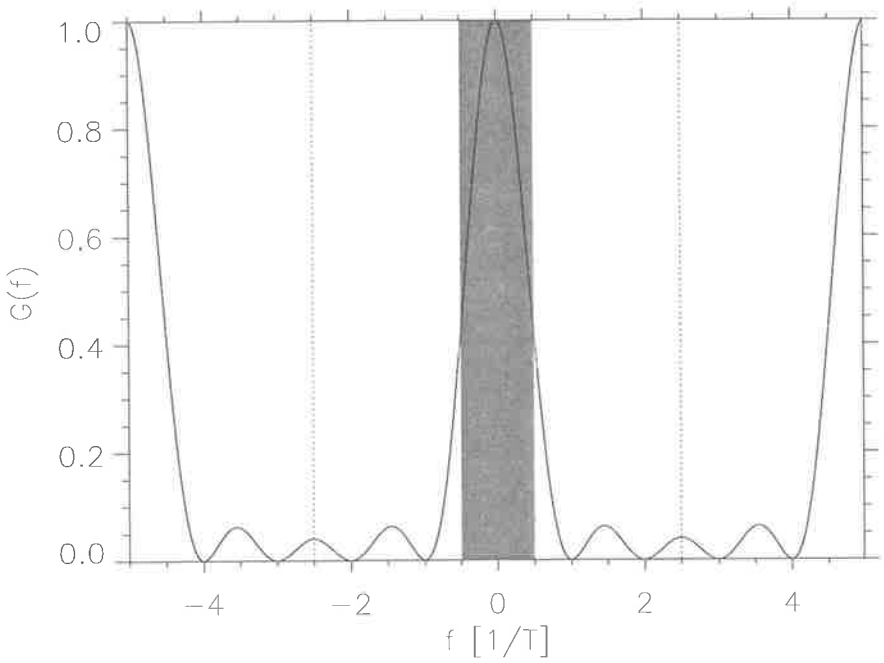

Figure 5.4: Comb filter (Equation 5.12) for $N = 5$ coherent integrations. The frequencies $-1/2T_{IPP} \leq f \leq 1/2T_{IPP}$ (dotted lines) are aliased into the frequency window $-1/2T \leq f \leq 1/2T$ (shaded).

voltage (after coherent integration) at sample intervals T for a certain range. After multiplication with a window function $w(t_k)$ to minimize spectral leakage, the time series can be Fourier transformed to obtain

$$Z(f_n) = \frac{1}{M} \sum_{k=0}^{M-1} z(t_k) w(t_k) \exp(-i \frac{2\pi n k}{M}). \tag{5.13}$$

The periodogram

$$P(f_n) = \frac{MTZ(f_n)Z^*(f_n)}{\sum_{k=0}^{M-1} w(t_k)^2} \tag{5.14}$$

is then an estimate of the power spectrum of the atmospheric returns at frequencies $-\frac{1}{2T} \leq f_n = \frac{n}{MT} < \frac{1}{2T}$.

An idealized periodogram is shown in Figure 5.5. The Doppler-shift f depends on the radial velocity $\frac{\mathrm{d}r}{\mathrm{d}t}$ of the scatterers in the radar sampling volume via

$$f = \frac{1}{2\pi} \frac{\mathrm{d}\phi}{\mathrm{d}t} = \frac{k}{\pi} \frac{\mathrm{d}r}{\mathrm{d}t} \tag{5.15}$$

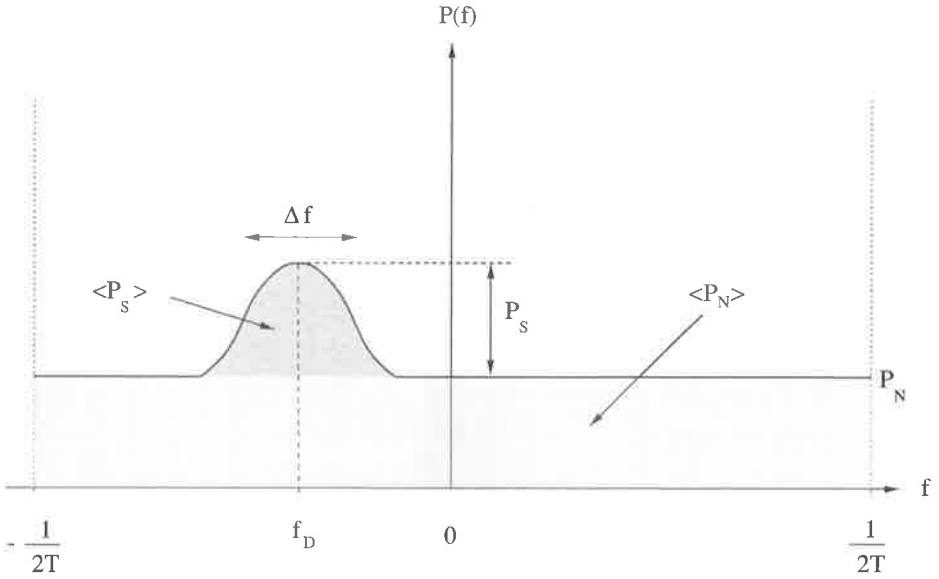

Figure 5.5: Idealized periodogram of atmospheric returns illustrating the basic parameters.

and its unaliased range is limited by the sampling period T to $-\frac{1}{2T} \leq f < \frac{1}{2T}$. The basic quantities that can be derived from the power spectrum are the integrated noise power $< P_N >$, the noise level P_N, the signal power given as the area under the signal peak, $< P_S >$, the height P_S of the signal peak above the noise level, and the Doppler-shift f_D and width Δf of the signal peak. In the case of turbulent scatter, the radar equation (Equation 5.7) can be used to relate the signal power $< P_S >$ to the volume reflectivity η and, hence, turbulence properties of the radar sample volume. From the Doppler-shift f_D and the frequency spread Δf one can extract the radial velocity distribution of the scatterers.

In the time domain, the parameters are extracted from the autocovariance (or autocorrelation) function given in its discrete form by

$$\begin{aligned} R(m) &= \frac{1}{M-m} \sum_{k=0}^{M-m-1} z^*(t_k) z(t_{k+m}) \\ &= \rho(\tau) \exp(-i\phi(\tau)), \end{aligned} \tag{5.16}$$

where $\tau = mT$ is the lag, and $\rho(\tau)$ and $\phi(\tau)$ are the amplitude and phase of the autocovariance function, respectively. Figure 5.6 presents amplitude and phase of an

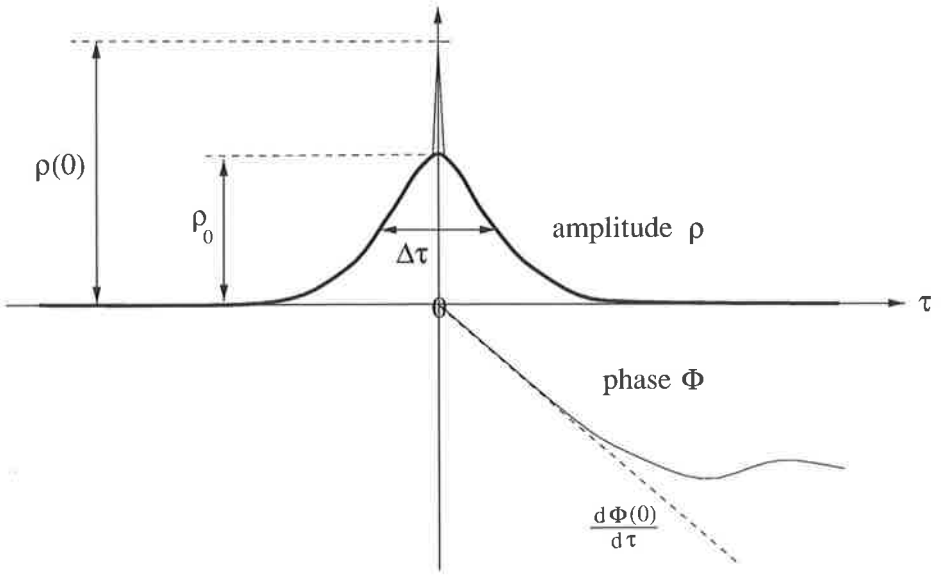

Figure 5.6: Amplitude and phase of an idealized autocovariance function. The thick line represents an interpolation of the amplitude over zero lag.

idealized autocovariance function. The sharp peak at zero lag is due to white noise in the corresponding time series. The peak occurs only at zero lag as the fluctuations due to white noise at different times are uncorrelated. Interpolating the amplitude of the autocovariance function over the zero lag, thus, removes the effects of white noise.

The Wiener-Khinchine theorem states, that for a stationary time series the autocovariance function and the periodogram comprise a Fourier transform pair. In that case, the n-th classical spectral moment M_n and the n-th derivative of the autocovariance function at zero lag are related through

$$M_n = \int_{-1/2T}^{1/2T} f^n P(f) \mathrm{d}f = \frac{1}{(i2\pi)^n} R^{[n]}(0). \tag{5.17}$$

Using the interpolated value ρ_0 of the autocovariance function at zero lag[2], noise power, signal power, Doppler-shift and frequency spread can then be obtained using

$$< P_N > \;=\; \rho(0) - \rho_0 \tag{5.18}$$

$$< P_S > \;=\; \rho_0 \tag{5.19}$$

[2]This corresponds to a computation of spectral moments using only the signal contributions $P(f) - P_N$

$$f_D \approx \frac{1}{2\pi}\frac{\phi(\tau)}{\tau} \tag{5.20}$$

$$(\Delta f)^2 \approx 2\frac{1-\rho(\tau)}{\rho_0 \tau^2}, \tag{5.21}$$

for τ sufficiently small.

5.7 Radar measurements of wind

As described above, clear air radar echoes are due to refractive index irregularities on the scale of $\lambda/2$. If one applies the Taylor-hypothesis, that these scatterers move with the mean wind $\mathbf{u} = (u, v, w)$, determination of the 3-dimensional wind vector is possible by measuring the motion of the scatterers.

5.7.1 Doppler techniques

In the Doppler technique a narrow beam is used to measure the radial velocity of the scatterers in the radar sampling volume. For a beam pointed to an azimuth angle φ and zenith angle χ the radial velocity is given by

$$v_r(\varphi, \chi) = u \sin\varphi \sin\chi + v \cos\varphi \sin\chi + w \cos\chi. \tag{5.22}$$

The use of three non-coplanar beam directions results in three equations for v_r which can be solved simultaneously to determine the three-dimensional wind vector $\mathbf{u}$. As different volumes are probed with the radar for different beam pointing angles, the additional assumption of a locally horizontally isotropic wind field is necessary. If the contribution of the vertical velocity w to v_r is negligible, two beams suffice to determine the horizontal wind speed.

The use of additional beams, however, increases the accuracy of the wind speed estimates. In the velocity azimuth display (VAD) technique, the radar beam scans the azimuth angle φ for a constant zenith angle χ. Fourier analysis of $v_r(\varphi)$ directly yields the horizontal wind vector, as well as the vertical velocity from the constant offset. In the velocity elevation display (VED) technique, on the other hand, the azimuth angle φ is held constant, while the zenith angle χ is varied.

A possible problem with the Doppler technique is the accurate determination of the effective beam pointing angle. Due to the aspect sensitivity of the scatterers the effective polar diagram is the product of the antenna beam pattern with the angular distribution of aspect sensitivity, which produces an effective beam pointing angle biased to the zenith [*Roettger*, 1980; *Thomas et al.*, 1997]. Measurements of aspect sensitivity [*Hocking et al.*, 1990] or interferometric radar techniques can be used to calculate the effective beam pointing angle. It is apparent that the bias decreases for narrower antenna beams.

Roettger [1984] and *Roettger & Larsen* [1990] summarize different arguments for the choice of zenith angle χ. Aspect sensitivity leads to increased returned power for small zenith angles at the cost of a stronger bias in the effective beam direction. Furthermore, the volumes probed for different azimuth angles are more closely spaced, and the range to a given geometric height is less than that for large zenith angles, resulting in stronger radar echoes. For large zenith angles, on the other hand, the uncertainty in the estimation of v_r decreases, as the signal peak is shifted to larger frequencies f_D without an increase in spectral width Δf.[3] Large zenith angles, however, require a rapid sampling rate to avoid aliasing and attenuation by the comb-filter of coherent integration. Zenith angles between 7 and 15 degrees are usually considered an effective compromise.

Extensive comparisons between winds as determined by radar Doppler techniques and radio sondes [*Fukao et al.*, 1982; *Weber & Wuertz*, 1990; *May*, 1993; *Thomas et al.*, 1997] and aircraft [*Angevine & MacPherson*, 1995] show good agreement within the joint error ranges of the techniques. Comparisons between the different Doppler techniques (VAD, VED, and fixed beam) were performed by *Koscielny et al.* [1984].

[3]This only holds for sufficiently short measurement intervals. Extending the measurement over too long a time interval, gravity waves will contribute to the width of the signal peak. Due to the stratification of the atmosphere the fluctuations in horizontal wind speed are much larger than the ones in vertical wind speed. An increase in zenith angle, therefore, would also increase the contribution of gravity waves to the spectral width.

5.7.2 Spaced Antenna techniques

In the spaced antenna method, the diffraction pattern produced by a vertically directed radar beam scattering off irregularities in the atmosphere is sampled at a number of spaced receiving antennas. Each of the antennas essentially samples a cross section of the diffraction pattern. In the presence of a horizontal wind, the fluctuations in echo strength at the spaced antennas show relative time displacements, from which the apparent velocity **v** of the diffraction pattern on the ground can be calculated. The history of the spaced antenna technique has been reviewed by *Briggs* [1993], and the theoretical details are presented in *Briggs* [1984]. Here we will only illustrate the principle of the technique:

Let $z(x, y, t)$ be the complex voltage measured at an antenna at position (x, y) at the ground at time t.[4] The correlation function between the voltages received at two antennas separated by (ξ, η) at time lag τ is then given by

$$\rho(\xi, \eta, \tau) = \frac{< z^*(x, y, t) z(x + \xi, y + \eta, t + \tau) >}{< |z(x, y, t)|^2 >}, \tag{5.23}$$

where $<>$ denotes average in time and/or space. The basic idea of the full correlation analysis is to parameterize the correlation function in (ξ, η, τ) space and to interpret these parameters in terms of atmospheric quantities. Estimation of the parameters is then performed from the actually measured correlation functions between the spaced antennas.

The simplest case is the case of a correlation function isotropic in space and independent of time, corresponding to scattering from isotropic irregularities without mean motion.[5] The value of the correlation function at a point (ξ, η, τ) then only depends on $\xi^2 + \eta^2$,

$$\rho(\xi, \eta, \tau) = \rho(\xi^2 + \eta^2), \tag{5.24}$$

and the contour lines of the correlation function are concentric circles around the origin (Figure 5.7 a). Note, that the full correlation analysis only makes assumptions about

[4] For simplicity we consider only one range gate.

[5] The shape of the diffraction pattern is determined by the correlation of the irregularities and the shape of the radar sampling volume.

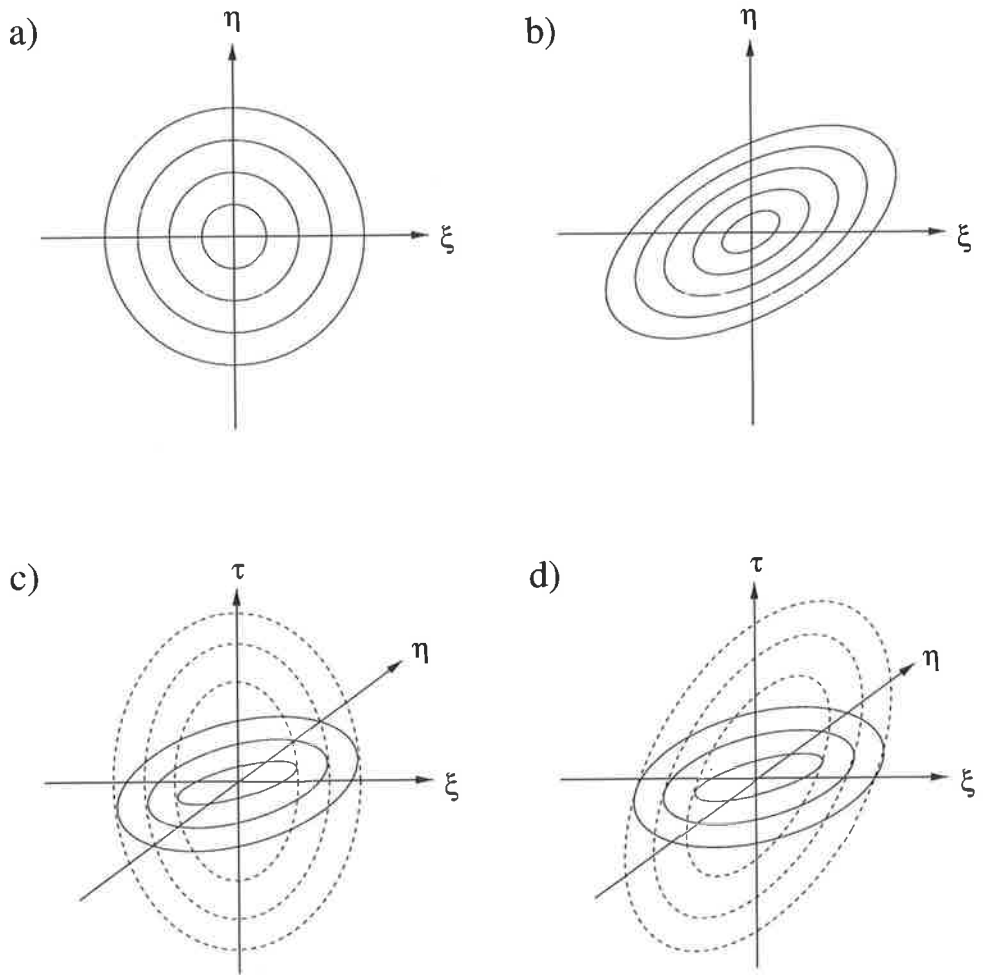

Figure 5.7: Contour plots of the correlation function $\rho(\xi, \eta, \tau)$ for different symmetries. See text for details.

the symmetry of the correlation function, but not about its functional form, i.e. it only specifies relations between the arguments ξ, η, and τ, but not whether ρ is Gaussian in shape or not.

Generalization to anisotropic correlations can be achieved by stretching the contours of ρ to form ellipses (Figure 5.7 b). Their symmetry can then be expressed as

$$\rho(\xi, \eta, \tau) = \rho(A\xi^2 + B\eta^2 + 2H\xi\eta). \tag{5.25}$$

Even if the irregularities have no mean motion do they evolve randomly in time, which, in turn, leads to a slow change in the diffraction pattern and, therefore, temporal decorrelation. The simplest way to take this decorrelation into account is to extend the elliptical contours in (ξ, η) space to ellipsoids in (ξ, η, τ) space with one axis in the τ direction (Figure 5.7 c). The axis has to be in τ direction, as any tilt of the ellipsoid would move the point of maximum correlation from the origin in the (ξ, η) plane and, thus, would be incompatible with the assumption of no mean motion. This yields

$$\rho(\xi, \eta, \tau) = \rho(A\xi^2 + B\eta^2 + K\tau^2 + 2H\xi\eta), \tag{5.26}$$

as any terms in $\xi\tau$ or $\eta\tau$ would result in a tilt of the ellipsoid. In using Equation 5.26, however, we inherently assume that the temporal autocorrelation function $\rho(0, 0, \tau) = \rho(K\tau^2)$ is of the same functional form as the spatial correlation function, e.g. that both are Gaussian shaped.

To finally include horizontal motion of the irregularities we transform Equation 5.26 from a coordinate system (ξ, η, τ) moving with the diffraction pattern to a stationary coordinate system (ξ', η', τ') using the transformation

$$\begin{aligned} \xi' &= \xi - V_x\tau \\ \eta' &= \eta - V_y\tau \\ \tau' &= \tau \end{aligned} \tag{5.27}$$

where (V_x, V_y) is the velocity of the observed diffraction pattern. This results in an

expression of the form

$$\rho(\xi', \eta', \tau') = \rho(A\xi'^2 + B\eta'^2 + C\tau'^2 + 2F\xi'\tau' + 2G\eta'\tau' + 2H\xi'\eta'), \tag{5.28}$$

where the corresponding tilt of the ellipsoids in Figure 5.7d is due to the horizontal motion of the randomly changing pattern.

Using three antennas at positions $(0,0)$, $(\xi_0,0)$, and $(0,\eta_0)$ one can obtain the parameters τ_ξ, τ_η, τ_x, τ_y, τ_{xy}, $\tau_{0.5}$ determined by

$$\begin{aligned}
\frac{\partial}{\partial\tau}\rho(\xi_0, 0, \tau_\xi) &= 0 \\
\frac{\partial}{\partial\tau}\rho(0, \eta_0, \tau_\eta) &= 0 \\
\rho(0,0,\tau_x) &= \rho(\xi_0, 0, 0) \qquad (5.29) \\
\rho(0,0,\tau_y) &= \rho(0, \eta_0, 0) \\
\rho(0,0,\tau_{xy}) &= \rho(\xi_0, \eta_0, 0) \\
\rho(0,0,\tau_{0.5}) &= 0.5. \qquad (5.30)
\end{aligned}$$

From this set of equations one can determine A, B, C, F, G, and H in Equation 5.28, and then calculate the values of the pattern velocity. Other atmospheric parameters that can be deduced are summarized by *Hocking et al.* [1989].

Precursors of the full correlation analysis did not take the random changes of the pattern into account. This can lead to overestimates in pattern velocity. Let's assume, for simplicity, that the pattern is isotropic without any random changes and that the antennas are positioned at $(0,0)$, $(\xi_0,0)$, and $(0,\eta_0)$. Horizontal movement of the diffraction pattern then corresponds to a shift of the contours in Figure 5.7a along the pattern trajectory. The maximum in the cross-correlation functions (solid line in the left-handside of Figure 5.8) will occur when the center of the diffraction pattern and the antenna are on a line perpendicular to the trajectory of the pattern. From the time lags of maximum cross-correlation the pattern velocity $\mathbf{v}$ can be constructed as shown in the right-handside of Figure 5.8. If random changes are included, the temporal decorrelation causes the magnitude of the cross-correlation functions to decrease in time (dashed line in the left-handside of Figure 5.8). The maxima in the

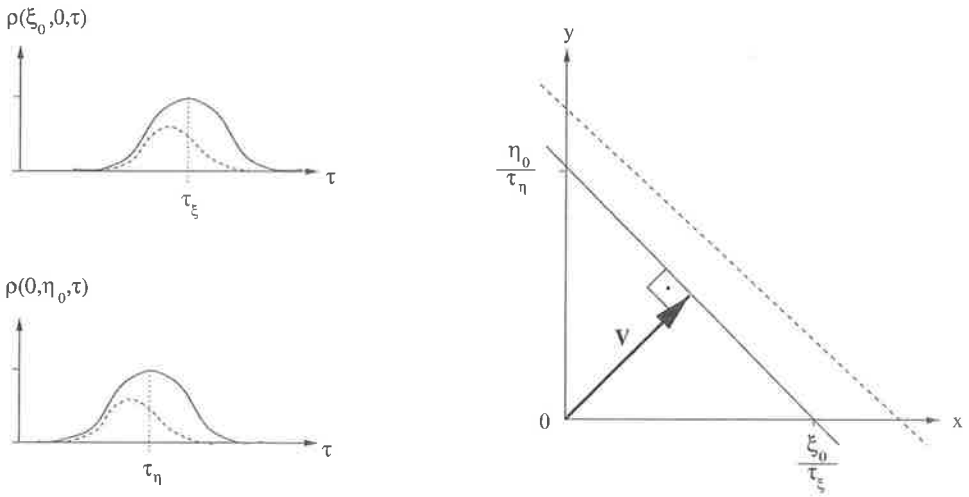

Figure 5.8: Cross-correlation functions (left) and construction of pattern velocity (right) for an isotropic correlation function. The solid lines correspond to a pattern without random changes, while random changes are included for the dashed lines. Neglect of the temporal decorrelation in the construction of the pattern velocity leads to an overestimate.

cross-correlation functions, therefore, occur at smaller time lags, which, if the same construction technique is applied, leads to an overestimate in pattern velocity(dashed line in the right-handside of Figure 5.8). This velocity is called apparent velocity in the full correlation analysis.

Briggs [1984] gives a number of rejection criteria to be employed in practical implementations of the full correlation analysis, and *May* [1988] discusses statistical errors in the wind estimates made with the spaced antenna technique. An advantage of this technique compared to Doppler methods is the fact that only a single sampling volume is used to measure the wind velocities. The use of a vertical beam also makes use of the aspect sensitivity of the scatterers. Furthermore, one can use a smaller antenna array, as the requirements for the beam diameter are far less stringent than for the Doppler technique. The spacing of the receiving antennas, however, is important, as this determines at what spatial lags ξ and η the correlation function can be sampled. Generally, the antenna spacing should be comparable to the size of the diffraction patterns. Variations of scatterer correlation scales in altitude and time can mean that

the (usually fixed) antenna spacing is less than optimal for certain time and height ranges. For VHF work in the troposphere and lower stratosphere, a pattern scale of about 50 m seems typical [*Vincent et al.*, 1987; *VanBaelen et al.*, 1990].

Spaced antenna winds compare well with other techniques like rocket [*Vincent et al.*, 1977], meteor drift [*Cervera & Reid*, 1995], radio sonde [*Vincent & Roettger*, 1980], and Doppler measurements [*Reid*, 1988]. Uncompensated receiver noise and inappropriate sampling rates, however, can lead to underestimates in the observed wind speeds [*Holdsworth & Reid*, 1995*a*; *Holdsworth & Reid*, 1995*b*].

Chapter 6

Signal processing algorithms

The radar experiments described in this thesis were performed with the University of Adelaide's VHF radar at Buckland Park (35°S, 138°E). The radar is located close to the flight paths of a busy airport (Parafield Airport) resulting in a high frequency of airplane echoes in the raw data series. To be able to analyze the contaminated time series for atmospheric signals, these clutter contaminations have to be removed. An algorithm to remove clutter identified by its intermittency in the radar time series is described in Section 6.1.

While analysis routines for the Full Correlation Analysis were implemented at the Buckland Park radar, the existing analysis routines for Doppler Beam Swinging experiments were not suitable for our purposes, as they did not yield satisfactory height coverage. Therefore, a new algorithm for Doppler experiments was developed during the course of this thesis, which is introduced in Section 6.2.

6.1 An algorithm for intermittent clutter removal

Radar signals are often contaminated by intermittent clutter, like airplane echoes (possibly from the antenna sidelobes) or interference.[1]

In this section, we describe the development of a method to remove intermittent

[1] At VHF the echoes from birds or insects are usually much weaker than atmospheric echoes, and hardly constitute a problem.

clutter from the radar time series to enable estimation of the frequently much weaker atmospheric signal. The method relies on the intermittency of the clutter signal, i.e. we assume that the atmospheric signal is present at all times, while the clutter appears only for a certain time fraction in the data record.

In the time domain, one method would be to bin the data record into several intervals of length ΔT and to compute the signal variance within each bin. The variance of the bins, which contain clutter, will exceed the variance of bins containing only the atmospheric signal. Using a threshold or some other criteria, those bins can be flagged as outliers and their data set to zero or replaced with random noise. Unfortunately, not only the clutter, but also the atmospheric signal in those bins will be lost. In the case of weak atmospheric returns, this reduction in signal strength can make detection of the signal impossible.

In the frequency domain, on the other hand, an algorithm might look for multiple peaks in the periodogram. Those peaks which are identified as clutter by certain criteria such as Doppler-shift, width, or power could then be flagged and the respective frequency ranges notched out. Often, however, such an identification is impossible, as airplanes moving through sidelobes of the antenna pattern might show power returns similar to atmospheric echoes (in the main lobe), and clutter signals are frequently attenuated and aliased by coherent integration. Even if identification as clutter can be achieved, contributions to the atmospheric signal in the flagged frequency range would be filtered out as well, leading to a loss in detected signal power as before.

It is also possible to combine the two methods by computing periodograms (instead of variances) for each bin of the time series [*Merritt*, 1995]. According to our assumption, peaks due to atmospheric returns appear in the periodograms of all bins, while the clutter signal, due to its intermittency, only appears in some. The frequency ranges occupied by clutter peaks are then only filtered in those bins, where clutter really appears. Consequently, contributions of the atmospheric returns in these frequency ranges are only filtered out in those bins which contain clutter, but are kept in all other bins. Renormalization of these frequency ranges leads to a fair estimate of

the atmospheric echoes.

It is not a priori clear, however, what bin width ΔT one should choose. If one computes periodograms of neighbouring bins for small bin widths ΔT, it becomes evident, that the amplitudes of peaks at high frequencies can change much quicker between adjacent bins than the amplitudes of low frequency peaks; Low frequency signals cannot be as well localized in time as high frequency signals. In other words, the amplitude $a(t)$ of a signal $a(t)\exp(i\omega t)$ has to change much slower than its phase for it to have a well defined frequency ω. When looking at low frequencies, it is, therefore, preferable to increase the bin width ΔT at the gain of a decreased frequency resolution $\Delta\omega$ of the periodograms. Instead of calculating periodograms for each bin for all the different bin widths, it is easier to apply an efficient implementation of a discrete transform using a so-called harmonic wavelet [*Newland*, 1993]. The harmonic wavelet transform of *Newland* [1993] bins the Nyquist range of a complex data series of length NT, $N = 2^k$, and spacing T into frequency bands $0 \ldots \pm \frac{1}{NT}$ and $\pm(\frac{2^{j-1}}{NT} \ldots \frac{2^j}{NT})$, $j = 1 \ldots k-1$. As the power within each frequency range can only change within a certain time scale, the complex amplitudes in the j-th frequency bin are calculated for bin widths $\Delta T_0 = NT$ and $\Delta T_j = \frac{N}{2^{j-1}}T$, resulting in a tiling of frequency-time-space as indicated in Figure 6.1. The N complex amplitude coefficients are independent of each other[2] and the transform can be inverted to reconstruct the data series without any loss of information.

The method is applied as follows. First, the complex time series $z(t)$ of the receiver voltage for a certain range gate is wavelet transformed using the implementation described by *Newland* [1993]. Then the modulus of the complex amplitude coefficients is calculated separately for each frequency range. Coefficients which are identified to be due to clutter (see below) are set to zero, and the remaining amplitudes are renormalized to correct for the incorrect removal of signal power within that frequency range; if, say, m of n complex amplitude coefficients in a certain frequency range have been set to zero, then the remaining amplitudes are multiplied by $\sqrt{\frac{n}{n-m}}$. Application of

[2]The wavelet transform is orthogonal.

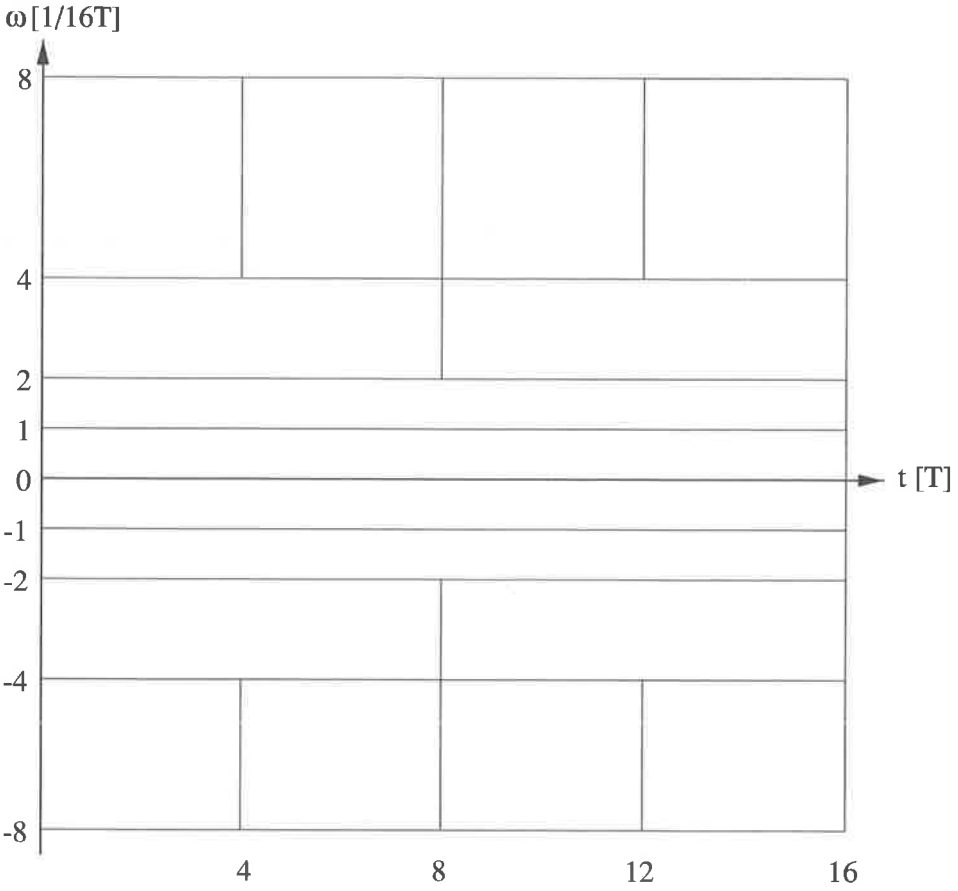

Figure 6.1: Tiling of the time-frequency space as resulting from the wavelet transform, here shown for a data series of length $16T$. Each tile corresponds to one complex amplitude coefficient. As the modulus of a quickly oscillating signal can change quicker than the modulus of a slowly oscillating signal, the (complex) amplitude of the high frequency components has to be calculated more often.

the inverse transform yields the cleaned complex time series.

We performed the identification and removal of amplitude coefficients influenced by clutter in an iterative way. Median and standard deviation of the modulus of all the amplitude coefficients within a frequency range are calculated. Those coefficients, whose modulus exceed the median by more than a given multiple of the standard deviation are set to zero. This process is repeated until no coefficient exceeds the threshold. Then the renormalization is applied to the remaining coefficients. Note that the calculation of the standard deviation is only meaningful for a sufficient number of coefficients. Therefore, this method works best for the higher frequency ranges where more amplitude coefficients are available. For less than four coefficients the method cannot be applied, rendering it ineffective for the removal of low frequency contaminations like ground clutter.

How well can we expect this wavelet algorithm to work and what are its advantages over removal of airplane clutter in the time- or frequency domain? If the atmospheric and the airplane echo occur in different frequency ranges (of the wavelet transform), the algorithm can readily identify and remove the intermittent airplane echo. In contrast to the time domain method, no part of the atmospheric signal will be lost. The advantage over the frequency domain method is the easy identification of the clutter signal through its intermittency. On the other hand, if the atmospheric and the airplane echo occur in the same frequency range, the algorithm is basically equivalent to the time domain method. For sufficiently different signal amplitudes, as usually is the case, the intermittent signal can be identified and the corresponding part of the time series discarded. That is, even if only one peak occurs in the periodogram, the effect of the intermittent signal can be removed and an estimate of the atmospheric echo can still be obtained. For signal amplitudes that are too similar, however, the intermittency of the clutter signal cannot be recognized in the wavelet domain. The periodogram, on the other hand, due to its better frequency resolution, might be able to resolve two separate peaks, and a distinction between signal and clutter peak might still be possible in the frequency domain.

To evaluate the effectiveness of the algorithm computer simulations were performed. Time series of atmospheric returns were generated following *Zrnic* [1975]. Zrnic's method assumes Rayleigh-distributed envelopes and uniformly distributed phases of both weather echo and noise. To generate a time series of length mT with spacing T, the desired signal spectrum $S(\omega_k)$, with $\omega_k = (k - \frac{m}{2})\frac{2\pi}{mT}$, $k = 0 \ldots m-1$, has to be defined. In our simulations, we used a Gaussian specified by its peak amplitude, width, and Doppler-shift. The noise level N was defined in terms of the signal-to-noise ratio

$$SNR = \frac{1}{mN} \sum_{k=0}^{m-1} S(\omega_k). \tag{6.1}$$

A realization of a periodogram is then given by

$$P(\omega_k) = -(S(\omega_k) + N) \ln X_k, \tag{6.2}$$

where X_k is a sequence of uniformly distributed random numbers in $[0, 1]$. The in-phase and quadrature components can be obtained by inverse Fourier transform of $\sqrt{P(\omega_k)} \exp(i\Theta_k)$, with Θ_k uniformly distributed in $[0, 2\pi]$.

As a clutter signal we use the echo of a hard target, e.g. an airplane, flying through the radar beam or an antenna sidelobe. The electro-magnetic field vector at the receiving antenna located at the origin is given by

$$\mathbf{E}(t) = A(\mathbf{r}(t)) \exp(i\frac{4\pi}{\lambda} r(t)), \tag{6.3}$$

where $\mathbf{r}(t)$ is the position of the hard target, λ the radar wavelength, and $A(\mathbf{r})$ the two-way polar diagram for a certain range gate. For each point in the radar data record the position of the airplane is updated and phase and amplitude of the receiver voltage are calculated.

Figure 6.2 shows time series and periodograms[3] for simulated atmospheric echoes (Gaussian with peak of 20 units at 30 rad s^{-1} with FWHM of 3 rad s^{-1} at a SNR of 0.5) with and without airplane clutter together with the cleaned data record. A threshold of three standard deviations was used in the wavelet algorithm. Although

[3]The periodograms were smoothed over 8 adjacent frequency bins to reduce the scatter.

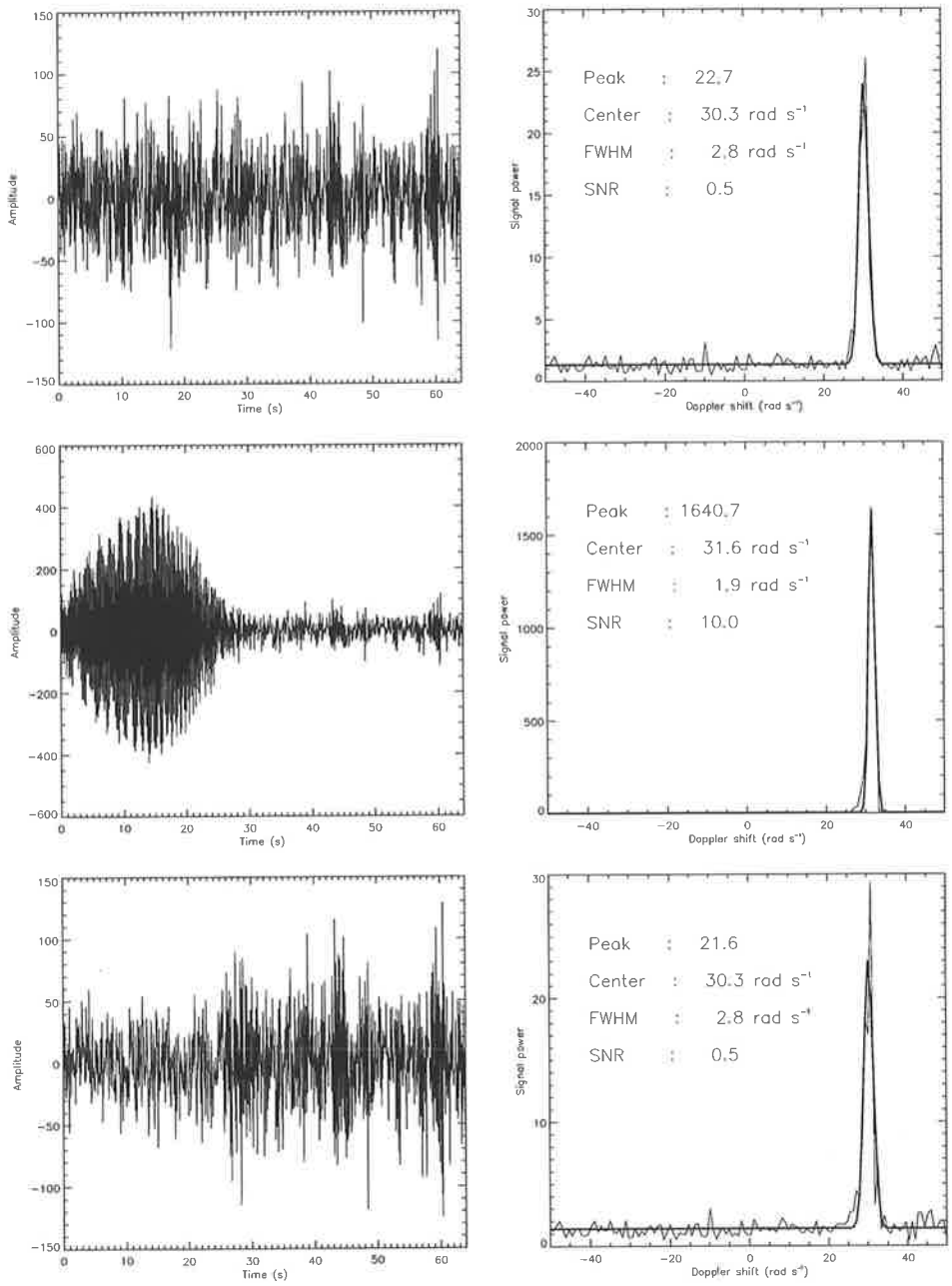

Figure 6.2: Computer simulation of the wavelet based clutter removal algorithm. The diagrams on the left show the real part of the simulated receiver voltage for the atmospheric echo (top), atmospheric echo and clutter (middle), and the cleaned time series (bottom). The diagrams on the right are the corresponding periodograms. The indicated parameters correspond to a Gaussian fit (thick line) to the periodogram. Note the different ordinates!

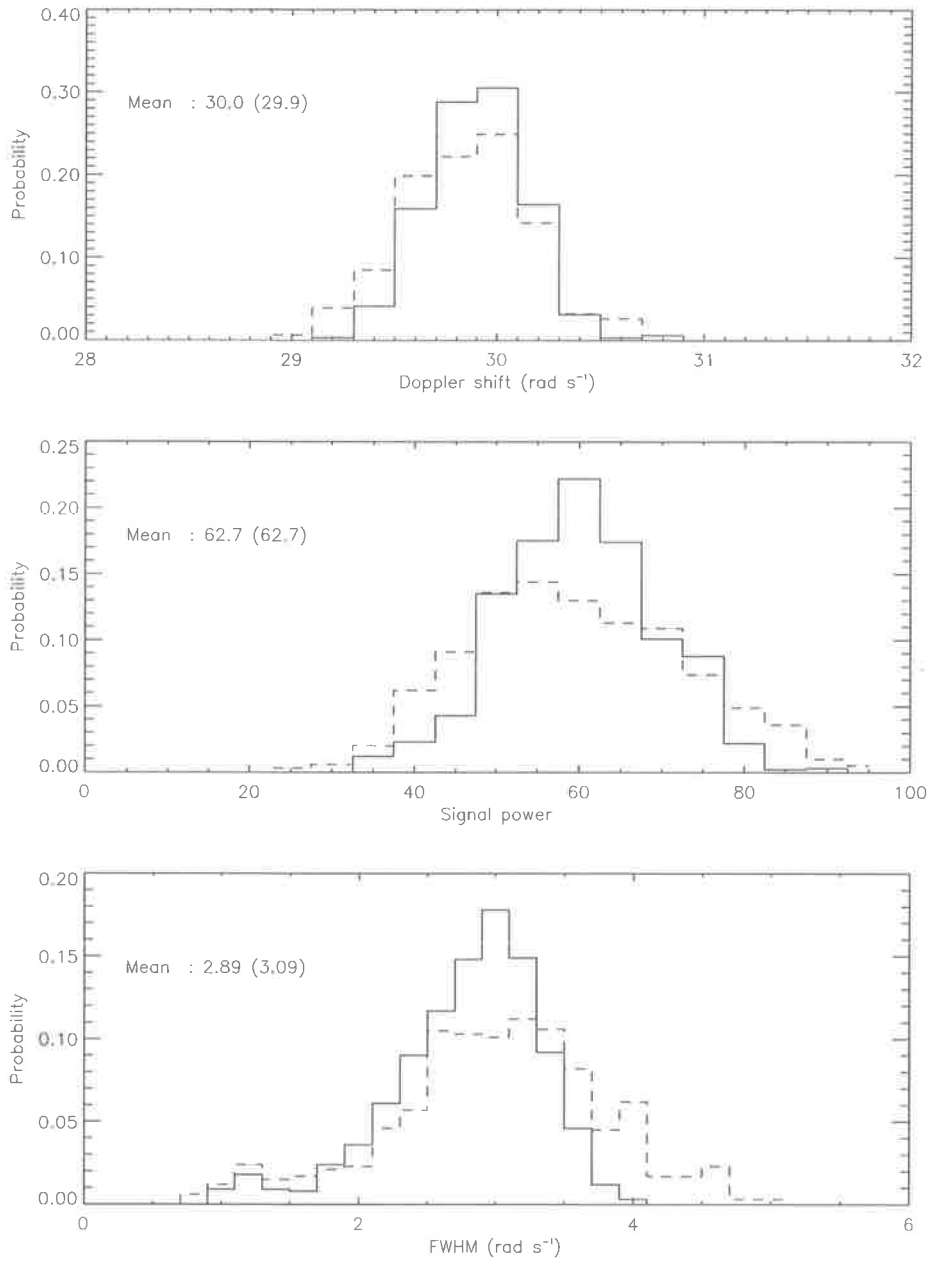

Figure 6.3: Histograms of estimated Doppler shift, integrated signal power, and spectral width for 1000 time series of atmospheric returns. The solid line corresponds to parameter estimates of the atmospheric echo alone. The dashed line represents the probability density functions of the parameter estimates after the same time series with the airplane clutter superimposed were cleaned using the wavelet algorithm. The means of the probability density functions for the atmospheric echo alone and after wavelet processing (in brackets) are indicated.

atmospheric and airplane echoes appear in the same frequency range, a good estimate of the atmospheric echo can be obtained from the contaminated time series after processing.

Figure 6.3 shows histograms of estimated Doppler shift, integrated signal power, and spectral width for 1000 time series of atmospheric returns using the same parameters as above, except for a SNR of 5. The solid lines indicate the probability density function of the parameters obtained via a Gaussian fit to the periodogram of the atmospheric echo alone. The dashed line represents the probability density functions after wavelet processing the same time series with the airplane echo superimposed. The uncertainty in the estimates for the atmospheric echo alone is due to the uncertainty inherent in the periodogram estimates. While the probability density functions of the parameters after wavelet processing are slightly broader than those of the original time series, the bias seems negligible. Note, however, that the estimates would be worse for clutter amplitudes more similar to the atmospheric echo amplitudes, when a distinction between clutter and atmospheric signal is not as easy.

Another, rather heuristic, approach to remove clutter from radar signals using the wavelet transform was applied by *Jordan et al.* [1997]. Their method basically works by simply clipping the wavelet coefficients in the first half of the wavelet transform (describing the low frequency part of the signal) to a certain threshold value which is determined by the magnitude of the largest coefficient in the second half of the wavelet transform (corresponding to the high frequency part of the signal). While the authors claim reasonable results even for the removal of ground clutter, our simulations applying their algorithm were not very satisfactory. We, therefore, believe that the detection of intermittency of the clutter signal is the essential part of our algorithm.

Very recently, a method was proposed by *Boisse et al.* [1999] that restricts the calculation of wavelet coefficients for computational reasons to two frequencies only. Airplane clutter is then identified by wavelet coefficents exceeding a certain threshold determined from preceeding radar time series. By replacing the contaminated parts of the time series detected airplane clutter can be removed. The threshold determination

of *Boisse et al.* [1999], however, is not frequency dependent. Intermittent air plane clutter with an amplitude comparable to the atmospheric echo cannot, therefore, be removed by their algorithm, in contrast to our algorithm introduced above. Concerning the computational efficiency, we believe that the use of an efficient algorithm for the wavelet transform can render the algorithm much faster and make the restriction to two frequencies unnecessary.

6.2 Development of a DBS algorithm

In Figure 5.5 we showed a highly idealized periodogram of atmospheric returns to introduce the basic parameters. In reality, however, one often deals with radar returns that contain clutter, due to objects in antenna sidelobes, for example, and interference. Furthermore, the noise in the periodogram usually shows a large variance σ_N^2 around its mean $\overline{P_N}$, which can make detection of the signal peak rather difficult. A more realistic spectrum is shown in Figure 6.4. Any present clutter and interference have to be removed before an estimation of atmospheric parameters is attempted. In this section we describe an algorithm to estimate atmospheric parameters from realistic time series in the frequency domain.

6.2.1 Signal-to-noise ratio vs. detectability, coherent and incoherent averages

An often used parameter to characterize the usability of periodograms is the (apparent) signal-to-noise ratio defined as the ratio of integrated signal to integrated noise power

$$SNR = \frac{< P_S >}{< P_N >}. \tag{6.4}$$

The signal-to-noise ratio by itself, however, does not say much about the confidence with which a signal can be detected in the periodogram. A better parameter is the ratio of the maximum height of the signal peak to the standard deviation of the noise,

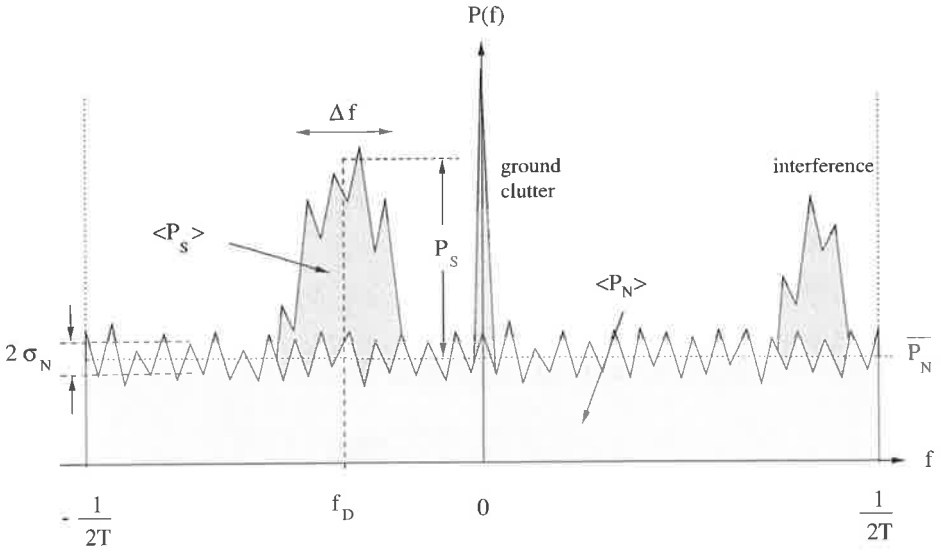

Figure 6.4: A more realistic periodogram containing contributions due to ground clutter and interference.

the so-called detectability [*Gage & Balsley*, 1978]

$$d = \frac{P_S}{\sigma_N}. \tag{6.5}$$

It indicates how deep the signal peak is buried in the *fluctuations* of the noise level.

Coherent integration decreases the integrated noise power $< P_N >$ by a reduction of the Nyquist range, but leaves the average noise power P_N constant and decreases the noise variance σ_N only insignificantly.[4] The SNR is, therefore, increased without any (significant) improvement in the detectability d. The main purpose of coherent integration is, therefore, the reduction of data flow rates.

The detectability d can be increased by averaging over adjacent frequency bins of the periodogram or by averaging successive periodograms. The latter process is called incoherent averaging. The improvement in d can be derived with some assumptions about the statistical properties of the noise.

Let X be a random variable with mean $\mu = 0$ and variance $\sigma^2 = 1$ and a Gaussian

[4]Due to the aliasing inherent in the coherent integration, the value of the periodogram at a certain frequency bin is an average over the corresponding aliased frequency bins weighted by the comb-filter. As the weight of the aliased frequency bins is very small, however, the variance of the periodogram estimate is only insignificantly decreased.

probability density function

$$pdf(X) = \frac{1}{\sqrt{2\pi}} \exp(-X^2/2). \tag{6.6}$$

If a new random variable Y is formed by summation of the square of M independent realizations of X, i.e.

$$Y = X_1^2 + X_2^2 + \ldots + X_M^2, \tag{6.7}$$

then Y has a χ^2-distribution with M degrees of freedom

$$pdf(Y) = \frac{(Y/2)^{M/2-1} \exp(-Y/2)}{2^{M/2}\Gamma(M/2)}, \tag{6.8}$$

with mean $\mu = M$ and variance $\sigma^2 = 2M$, where $\Gamma()$ is the gamma function.

Assuming that the in-phase and quadrature voltages corresponding to the noise are Gaussian distributed, then the periodogram estimates for a given frequency bin obey a χ^2-distribution with 2 degrees of freedom and $\sigma_N = \overline{P_N}$. Averaging over M periodograms or M adjacent frequency bins results in $2M$ degrees of freedom and a decreased $\sigma_N = \overline{P_N}/\sqrt{M}$ [*Welch*, 1967]. It is important to note, that the noise variance does not depend on the length of the time series used to form a single periodogram, but only on the number of averaged frequency bins. The use of longer time series only affects the frequency resolution of the periodogram. If one assumes a Gaussian signal peak the signal-to-noise ratio and the detectability are related through

$$SNR = d\frac{\sqrt{\pi}T\Delta f}{\sqrt{M}}, \tag{6.9}$$

where Δf is the width of the signal peak and T the sample spacing after coherent integration.

6.2.2 Objective determination of the noise level

The relation $\sigma_N = \overline{P_N}/\sqrt{M}$ between the standard deviation of the noise estimate and its mean value has been used by *Hildebrand & Sekhon* [1974] to develop an algorithm for the objective determination of noise levels in periodograms. The algorithm works by sorting the N frequency bins of a periodogram according to their magnitude. Starting

with $n = 1$ it then calculates the variance $\sigma(n)$ and mean $\mu(n)$ of the n frequency bins with the smallest power estimates. The value of n is successively increased, as long as $\sigma(n) < \mu(n)/\sqrt{M}$, where M is the number of incoherent averages applied for the computation of the periodogram. The power in the resulting n frequency bins is then assumed to be due to noise only, with a mean noise power $P_N = \mu(n)$ and a standard deviation $\sigma_N = \sigma(n)$. An example is given in Figure 6.5.

6.2.3 Statistical averaging method to remove intermittent clutter

Merritt [1995] applied the same principle to reject intermittent clutter contributions from periodograms before they are incoherently averaged. He divided the time series into M segments of equal length and calculated the periodogram for each segment. Assuming that the power estimates for atmospheric signals and noise for a given frequency bin (as a function of time) are χ^2-distributed with two degrees of freedom (one each for the in-phase and quadrature component), only the lowest $m \leq M$ estimates whose standard deviation $\sigma(m)$ is smaller than their mean $\mu(m)$ are considered to be due to atmospheric returns. The remaining $M - m$ are attributed to clutter or interference and set to zero. After the algorithm is applied to each frequency bin, the cleaned periodograms are averaged. The resulting average is then treated as an incoherent average over M periodograms. The statistical averaging method (SAM) is illustrated in Figure 6.6:

Figure 6.6a shows $M = 32$ periodograms with 64 frequency bins each. The atmospheric signal and two intermittent clutter peaks are clearly visible. The detection of intermittent clutter is presented in Figure 6.6b for the twelfth frequency bin: The power estimates as a function of time (top) are sorted according to their magnitude (middle) and the standard deviation $\sigma(m)$ (dashed line) and the mean $\mu(m)$ (solid line) of the m smallest power estimates is calculated (bottom). As the standard deviation exceeds the mean for $m > 28$, only the 28 smallest power estimates are accepted

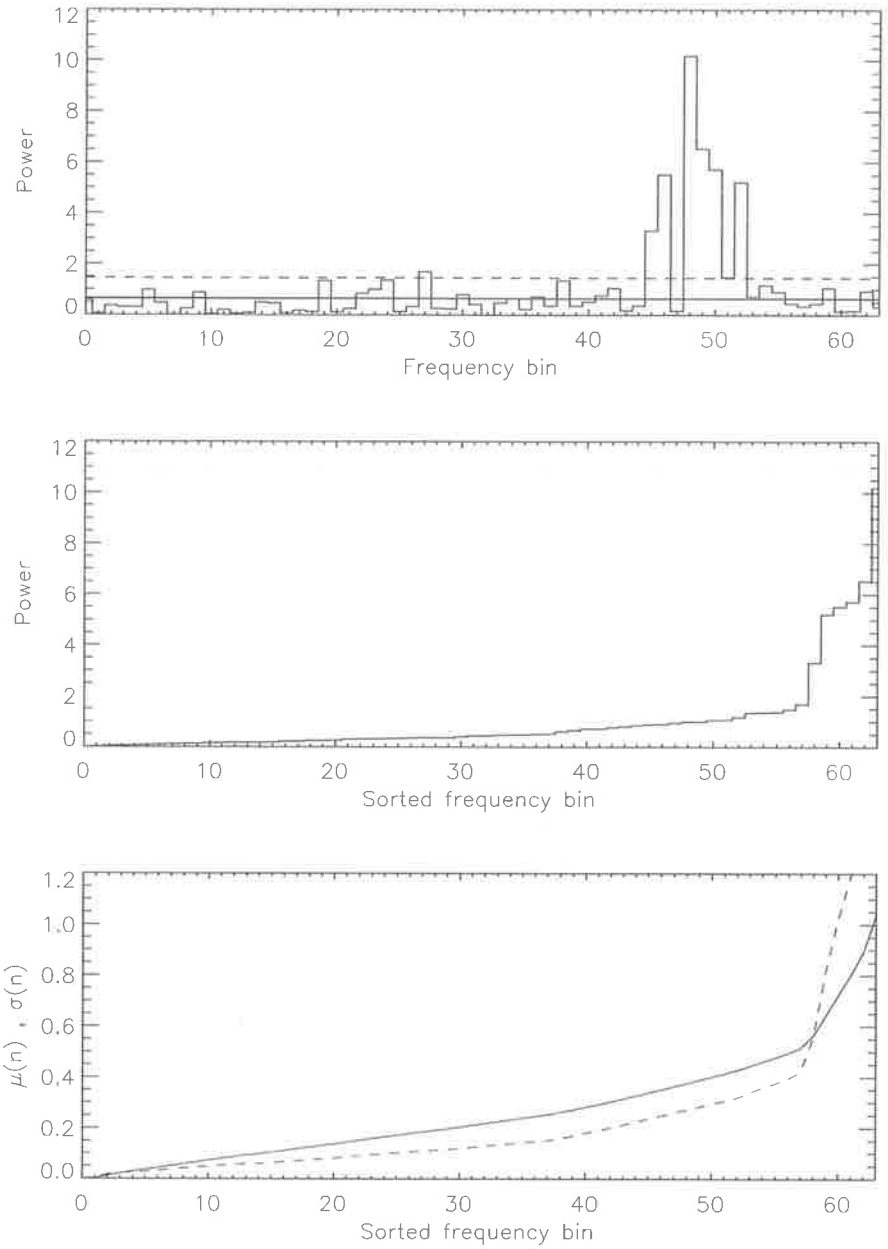

Figure 6.5: Illustration of the Hildebrandt-Sekhon algorithm to objectively determine the noise level for a periodogram with $N = 64$ frequency bins. The diagram shows the periodogram (top), the sorted frequency bins (middle), and the mean $\mu(n)$ (solid) and standard deviation $\sigma(n)$ (dashed) as a function of the number of included n frequency bins with the smallest power estimates (bottom). The standard deviation exceeds the mean for $n > 58$, resulting in an average noise level $\overline{P_N} = \mu(58)$ with a standard deviation $\sigma_N = \sigma(58)$ as indicated by the solid and dashed lines, respectively, in the top diagram.

as atmospheric returns (thick line in top diagram). Figure 6.6c shows the 32 periodograms after all 64 frequency bins have been cleaned. The average of the cleaned periodograms (dotted line) is finally presented in Figure 6.6d (thick line).

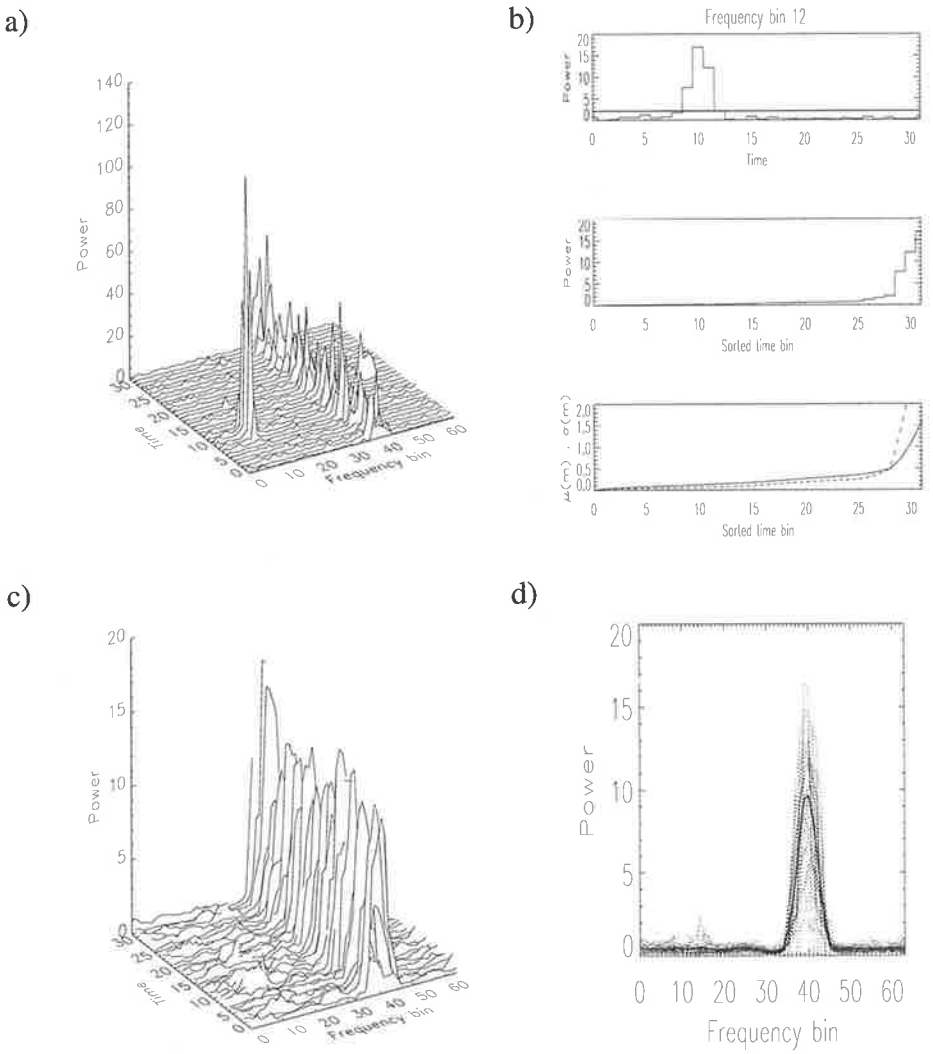

Figure 6.6: Illustration of the statistical averaging method (SAM) after *Merritt* [1995]. See text for details.

6.2.4 The DBS algorithm

In the DBS algorithm developed for the radar work in this thesis we take all L time series for a given beam pointing angle and range bin within a certain time window, usually one hour, and divide each of them into M segments of equal length. The number M of segments per time series is chosen according to the desired frequency resolution. Each of the $M \cdot L$ time series segments is detrended with a low-order polynomial to remove the effects of ground clutter [*May & Strauch*, 1998], then the periodograms are calculated and averaged using the statistical averaging method described above. At the cost of a coarser time resolution we, thus, obtain incoherently averaged periodograms which a much increased detectability compared to the periodograms of a single time series. This increased detectability adds several kilometers to the height range of usable radar echoes. While the noise in the radar time series is basically independent of the radar range R, the signal power for volume scatter decreases as R^{-2}, leading to a decrease in detectability with height. Furthermore, due to the statistical test performed on the power estimates within each frequency bin, any intermittent clutter will be removed. Depending on the beam pointing angle narrow regions of the averaged periodogram corresponding to (remaining) ground or sea clutter can then be notched out and interpolated over using a cubic spline. Finally, the mean noise level $\overline{P_N}$ and its standard deviation σ_N are determined using the *Hildebrand & Sekhon* [1974] algorithm, and a Gaussian is fitted to the averaged periodogram minus the mean noise level. As initial guesses for the signal power P_S and the Doppler shift f_D we use position and height of the maximum of the averaged periodogram, while the width Δf is guessed using a constant. The method is repeated for all available beam pointing angles and range gates and the time window shifted 30 minutes.

To ensure the quality of the fitted parameters only records with a detectability $d > 3$ are accepted. Furthermore, consistency checks of the parameters in height and time and, if available, with the opposite beam direction are performed. This was done manually for data sets presented in this thesis, but an automatisation of this procedure

using, for example, a fuzzy logic algorithm along the lines of *Cornman et al.* [1998] would be preferable for more extensive observation periods. If any corrections are applicable, the averaged periodograms are refitted using the corrected parameters as initial guesses. The quality controlled parameters are then a reliable estimate for the chosen averaging period of one hour.

Subsequently, the length of the time window can be decreased, if required even down to a single segment, and the quality controlled parameters used to form initial guesses for the Gaussian fits. The resulting fit is only accepted if the deviations from the initial guess are sufficiently small and the detectability d larger than a certain threshold d_c chosen according to the application.

This algorithm is much preferable to more commonly applied methods where the parameters are estimated from a single time series only and then consensus averaged over a longer period. It leads to a better height coverage, quasi-automatic removal of intermittent clutter, and more confidence in the obtained parameters.

We do not use the wavelet algorithm for intermittent clutter removal here, as the applied statistical averaging method by *Merritt* [1995] already performs this task. Within our chosen time interval of one hour, we get a sufficient number of periodograms with adequate frequency resolution for this method to work well. The gained increase in time resolution for larger frequencies when the wavelet algorithm was applied would, therefore, not justify the computational effort.

Chapter 7

Turbulence theory

7.1 Basic turbulence theory

In this section Kolmogorov theory of inertial range turbulence [*Tatarskii*, 1961; *Batchelor*, 1953] is briefly discussed, as necessary for the understanding of the turbulence work in this thesis.

It is useful to view turbulent motion as a collection of vortices or eddies that cascade energy from large scales to smaller and smaller scales until it is finally dissipated as heat by viscous forces. Kolmogorov's theory of inertial range turbulence is valid at those intermediate scales, where the effects of viscosity and buoyancy forces are negligible and where the energy is simply cascaded to smaller scales without being dissipated or created. The two limiting scales are the inner scale l_o and the buoyancy or outer scale L_B. The flow rate of kinetic energy is constant throughout the inertial range and equals the rate with which the energy is dissipated at the smallest scales. It is known as the (kinetic) energy dissipation rate ϵ. The Kolmogorov microscale η is the scale where the viscous dissipation rate equals the energy transfer rate ϵ and can be derived by dimensional analysis [*Tatarskii*, 1961]: If an eddy of scale l has a characteristic velocity v_l, then we can define a time scale for energy transfer associated with eddies of that scale as $\tau_l = l/v_l$. The energy transfer rate at that scale (and all other scales within the inertial range) is then given as $\epsilon = v_l^2/\tau_l = v_l^3/l$. The heat dissipation in

the viscous range is given by $\epsilon = \nu\nabla^2\mathbf{v} = \nu v_l/l^2$ for an eddy of scale l. Equating the two expressions for ϵ at a scale η yields

$$\eta = \left(\frac{\nu^3}{\epsilon}\right)^{\frac{1}{4}}. \tag{7.1}$$

The Kolmogorov microscale η is well within the viscous range as the effect of viscosity at this scale is substantial. For temperature fluctuations in air, for example, *Hill & Clifford* [1978] derived $l_o = 7.4\eta$. On the other end of the spectrum, the inertial range is limited to scales less than the buoyancy scale L_B by the emission of gravity waves generated by vertically fluctuating air parcels. For scales larger than L_B the resulting gravity waves are undamped and can extract a substantial part of the kinetic energy from the turbulent motion. An expression for the buoyancy scale was derived by *Weinstock* [1978] for stably stratified flows as

$$L_B \approx 10\epsilon^{1/2}N^{-3/2}, \tag{7.2}$$

where N is the buoyancy frequency.

7.1.1 Structure functions and spectrum of the turbulent velocity field

To describe the turbulent motion in a statistical manner, one usually decomposes atmospheric parameters into their slowly varying mean and fluctuations. The characteristics of these fluctuations, however, can depend considerably on what is considered as mean and what as perturbation. To avoid this difficulty, in turbulence theory one often uses structure functions instead of correlation functions. The structure tensor of a velocity field $\mathbf{v}(\mathbf{r})$ in 3-dimensional space is defined as

$$D_{ik}(\mathbf{r_1}, \mathbf{r_2}) = \overline{[v_i(\mathbf{r_1}) - v_i(\mathbf{r_2})][v_k(\mathbf{r_1}) - v_k(\mathbf{r_2})]}, \tag{7.3}$$

where the overbar denotes average. The velocity field is called locally homogeneous in a region G if its structure tensor only depends on $\mathbf{r_1} - \mathbf{r_2}$ for all $\mathbf{r_1}$, $\mathbf{r_2}$ in G, it is called locally isotropic in G, if its structure tensor depends on $\|\mathbf{r_1} - \mathbf{r_2}\|$ only, for all

$\mathbf{r_1}$, $\mathbf{r_2}$ in G. The structure tensor of a locally homogeneous velocity field can also be expressed in terms of the spectral tensor $\Phi_{ik}(\mathbf{k})$ as

$$D_{ik}(\mathbf{r}) = 2\int_{-\infty}^{+\infty}[1-\cos(\mathbf{kr})]\Phi_{ik}(\mathbf{k})\mathrm{d}^3\mathbf{k}. \tag{7.4}$$

The total velocity variance is then given by

$$\overline{v^2} = \int_{-\infty}^{+\infty}[\Phi_{11}(\mathbf{k})+\Phi_{22}(\mathbf{k})+\Phi_{33}(\mathbf{k})]\mathrm{d}^3\mathbf{k}. \tag{7.5}$$

In the case of a locally isotropic velocity field, the symmetry of an isotropic second-order tensor requires

$$D_{ik}(\mathbf{r}) = [D_{rr}(r)-D_{tt}(r)]n_i n_k + D_{tt}\delta_{ik}, \tag{7.6}$$

where D_{rr} and D_{tt} are the longitudinal and transversal structure functions, respectively, δ_{ik} is the Kronecker delta, and n_i is the component of the unit vector in direction of $\mathbf{r}$. For velocities v small compared to the velocity of sound, the fluid can be regarded as incompressible, i.e. $\nabla\mathbf{v} = 0$. The tensor D_{ik}, therefore, has to obey $\frac{\partial D_{ik}}{\partial x_i} = 0$, which yields

$$D_{tt}(r) = \frac{1}{2r}\frac{\mathrm{d}}{\mathrm{d}r}\left(r^2 D_{rr}(r)\right). \tag{7.7}$$

For the spectral velocity tensor the same conditions yield

$$\Phi_{ik}(\mathbf{k}) = \frac{E(k)}{4\pi k^2}(k^2\delta_{ij}-k_i k_j). \tag{7.8}$$

In his theory of inertial range turbulence, Kolmogorov assumed that eddies of a sufficiently small scale are no longer influenced by the spatial geometry of the fluid flow but can be considered as isotropic. For distances r large compared to the inner scale l_o and small compared to the outer scale L_B, the structure function $D_{rr}(r)$ is then only a function of r and ϵ. Dimensional arguments require

$$D_{rr}(r) = C(\epsilon r)^{2/3} \tag{7.9}$$

and, using Equation 7.7,

$$D_{tt}(r) = \frac{4}{3}C(\epsilon r)^{2/3}. \tag{7.10}$$

Using this and Equations 7.4, 7.6 and 7.8 we obtain

$$E(k) = 0.061\ C\epsilon^{2/3}k^{-11/3}. \tag{7.11}$$

From measurements in the atmosphere it is known that $C = 2.0$ [*Kaimal et al.*, 1972].

7.1.2 Structure function of a passive tracer in a turbulent flow

Often one is not interested in the turbulent velocity field itself, but in the effects the turbulent motion has on passive tracers within the medium.[1] In the case of radar studies, for example, the backscattered power depends on the refractive index fluctuations within the radar sampling volume. Relations between the refractive index irregularities and turbulence parameters can, therefore, be used to infer turbulence characteristics from the backscattered power.

Let $\xi(\mathbf{r})$ be the concentration of such a passive tracer. The evolution of the field $\xi(\mathbf{r})$ is determined by the effects of turbulent mixing on the one hand and molecular diffusion on the other hand. Picture $\xi = \overline{\xi} + \xi'$ as having a gradient in z-direction. Turbulent mixing leads to an exchange of air parcels from different heights and, therefore, produces fluctuations $\overline{\xi'^2}$. In analogy to molecular diffusion, the rate of production of these inhomogeneities is often written as $K_\xi \left(\frac{\mathrm{d}\overline{\xi}}{\mathrm{d}z}\right)^2$, where K_ξ is the so-called eddy diffusion coefficient for ξ. Placing a parcel from one height to another height leads to very large local gradients in ξ' at the parcel boundaries. Molecular diffusion then acts to smooth out these local gradients. The rate at which the fluctuations are smoothed out is given by $D\overline{\left(\frac{\mathrm{d}\xi'}{\mathrm{d}z}\right)^2}$ with D the molecular diffusion coefficient. The production and leveling out of the fluctuations in ξ, therefore, happen on very different scales. In the stationary case, both processes balance each other and the rate with which inhomogeneities are produced or leveled out is

$$\epsilon_\xi = D\overline{\left(\frac{\mathrm{d}\xi'}{\mathrm{d}z}\right)^2} = K_\xi \left(\frac{\mathrm{d}\overline{\xi}}{\mathrm{d}z}\right)^2. \tag{7.12}$$

[1] A passive tracer is a conservative additive that does not affect the dynamical regime of turbulence.

The structure function for ξ is given by

$$D_\xi(\mathbf{r_1}, \mathbf{r_2}) = \overline{[\xi(\mathbf{r_1}) - \xi(\mathbf{r_2})]^2}. \tag{7.13}$$

For sufficiently small eddies in the inertial range, we can assume that $\xi(\mathbf{r})$ is locally isotropic and that the structure function depends only on $r = \|\mathbf{r_1} - \mathbf{r_2}\|$, ϵ and ϵ_ξ. Dimensional arguments then require

$$D_\xi(r) = C_\xi^2 r^{2/3} = \frac{a^2 \epsilon_\xi}{\epsilon^{1/3}} r^{2/3} \tag{7.14}$$

with a a dimensionless constant constant, usually taken as $a^2 = 2.8$ [*VanZandt et al.*, 1978]. For an horizontally homogeneous shear flow in a stably stratified atmosphere, the ratio between the production of mean square fluctuations in ξ and the production of turbulent kinetic energy can be written as [*Ottersten*, 1969]

$$\frac{\epsilon_\xi}{\epsilon} = \frac{\overline{\xi' w'} \frac{\mathrm{d}\overline{\xi}}{\mathrm{d}z}}{\overline{u' w'} \frac{\mathrm{d}\overline{u}}{\mathrm{d}z}(1 - R_f)} = \frac{K_\xi \left(\frac{\mathrm{d}\overline{\xi}}{\mathrm{d}z}\right)^2}{K_m \left(\frac{\mathrm{d}\overline{u}}{\mathrm{d}z}\right)^2 (1 - R_f)}, \tag{7.15}$$

where $\overline{u}$ is the mean background wind, K_ξ and K_m are the eddy diffusion coefficients for ξ and momentum, respectively, and

$$R_f = \frac{K_h}{K_m} Ri = \frac{K_h}{K_m} \frac{N^2}{\left(\frac{\mathrm{d}\overline{u}}{\mathrm{d}z}\right)^2} \tag{7.16}$$

is the flux Richardson number with K_h the eddy diffusion coefficient for heat. The factor $(1 - R_f)$ in the denominator of Equation 7.15 is due to the fact that not all of the energy extracted from the shear flow is converted to turbulent kinetic energy, but part of it is converted into potential energy due to the stratification of the atmosphere. Using Equations 7.14,7.15 and 7.16 the structure function constant C_ξ^2 can be expressed as

$$C_\xi^2 = a^2 \epsilon^{2/3} \frac{R_f}{1 - R_f} \frac{K_\xi}{K_h} \frac{\left(\frac{\mathrm{d}\overline{\xi}}{\mathrm{d}z}\right)^2}{N^2}. \tag{7.17}$$

7.2 Turbulence measurements by radar

Different techniques have been used in the past to measure atmospheric turbulence parameters in-situ. Two large projects, TOPCAT [*Reiter & Burns*, 1966] and HICAT

[*Lilly et al.*, 1974], were designed in the 1960s to study clear-air turbulence with aircraft in the tropo- and stratosphere, respectively. By recording velocity fluctuations along the flight path of an instrumented aircraft the dissipation rate can be inferred from properties of the velocity spectrum or fluctuations in the vertical velocity field [*Chen*, 1974]. The evolution of smoke puffs [*Kellogg*, 1956] and vapour trails released from rockets [*Roper*, 1996] has also been studied using high resolution photographs. The growth or diffusion rate of the trail provides information about the strength of local eddies. Another possibility are high-resolution balloon measurements of velocity and temperature [*Barat*, 1982; *Barat & Bertin*, 1984*a*; *Luce et al.*, 1997] which allow calculation of spectra or direct measurement of the structure function constant.

Radars offer an alternative means to monitor turbulence in the atmosphere, with a greatly improved time resolution compared to in-situ methods. Radars are susceptible to refractive index irregularities on the scale of half the radar wavelength. Therefore, radar echoes contain information about the density (returned power) and velocity distribution (spectral width) of refractive index irregularities of that scale within the radar sampling volume. In the following sections we will describe two methods to deduce turbulence parameters from these two quantities.

7.2.1 Power method

In the power method the power returned by the scatterers in the radar sampling volume is related to the average energy dissipation rate within that volume. Using the backscattering cross section for isotropic turbulence [*Tatarskii*, 1961]

$$\sigma^{\text{scat}} = 0.00655\pi^{4/3}C_n^2\lambda^{-1/3} \tag{7.18}$$

the average refractive index structure function $\overline{C_n^2}$ can be expressed as a function of the power P_r received by the radar and the radar parameters as [*Hocking*, 1985; *Hocking & Mu*, 1997]

$$\overline{C_n^2} = 66.4\frac{P_r r^2 \lambda^{1/3}}{P_t A_{eff} e_R e_T 2\Delta r}, \tag{7.19}$$

where P_t is the transmitted (peak) power, A_{eff} the effective antenna area, e_R and e_T the receiver and transmitter efficiencies, λ the radar wavelength, r the radar range, and Δr the range resolution (HWHM). To ensure that the received power is due to isotropic turbulence and not contaminated by Fresnel scatter or reflection, a zenith angle of more than about 10° has to be used for the radar beam [*Hobbs*, 1998]. The required knowledge of P_r in absolute units makes a calibration of the radar system necessary. Assuming that a fraction F of the radar sampling volume is filled with turbulent layers of (equal) energy dissipation rate ϵ, the measured average refractive index structure function $\overline{C_n^2}$ and the average energy dissipation rate within the radar sampling volume, $\bar{\epsilon}$, can be expressed as

$$\begin{aligned} \overline{C_n^2} &= F C_n^2 \\ \bar{\epsilon} &= F\epsilon, \end{aligned} \tag{7.20}$$

where C_n^2 and ϵ are the local refractive index structure constant and energy dissipation rate, respectively, for the turbulent layers that are present. Substituting Equations 7.20 into Equation 7.17 yields

$$\bar{\epsilon} = \left(\frac{1}{a^2} \frac{1 - R_f}{R_f} \frac{K_h}{K_n} \frac{\overline{C_n^2} N^2}{F^{1/3} M^2} \right)^{3/2}, \tag{7.21}$$

where

$$\begin{aligned} M &= \frac{\partial n}{\partial \Theta} \frac{\partial \Theta}{\partial z} + \frac{\partial n}{\partial q} \frac{\partial q}{\partial z} \\ &= -77.6 \cdot 10^{-6} \frac{p}{T} \frac{\partial \ln \Theta}{\partial z} \underbrace{\left[1 + \frac{15500 q}{T} \left(1 - \frac{1}{2} \frac{\frac{\partial \ln q}{\partial z}}{\frac{\partial \ln \Theta}{\partial z}} \right) \right]}_{\chi} \end{aligned} \tag{7.22}$$

is the potential refractive index gradient[2] with potential temperature Θ and specific humidity q. The term in brackets, χ, accounts for contributions due to humidity

[2]Equation 7.17 relates the energy dissipation rate to the structure function constant of a passive, conservative scalar. The refractive index $n(p, q, \Theta)$, however, is not conserved when a parcel is moved adiabatically, as the parcel assumes the pressure of its environment. Equation 7.17 can still be applied, if one takes into account that the displacement of a parcel over a vertical distance Δz leads to a change in refractive index of $\Delta n = M \Delta z$ instead of $\Delta n = \frac{\mathrm{d}n}{\mathrm{d}z} \Delta z$.

gradients. Equation 7.21 is only applicable for $M \neq 0$, i.e. if the potential temperature Θ or the specific humidity q vary with altitude in the height range considered. If potential temperature and specific humidity are constant with height, turbulent mixing does not lead to refractive index variations and cannot, therefore, be detected with the radar.

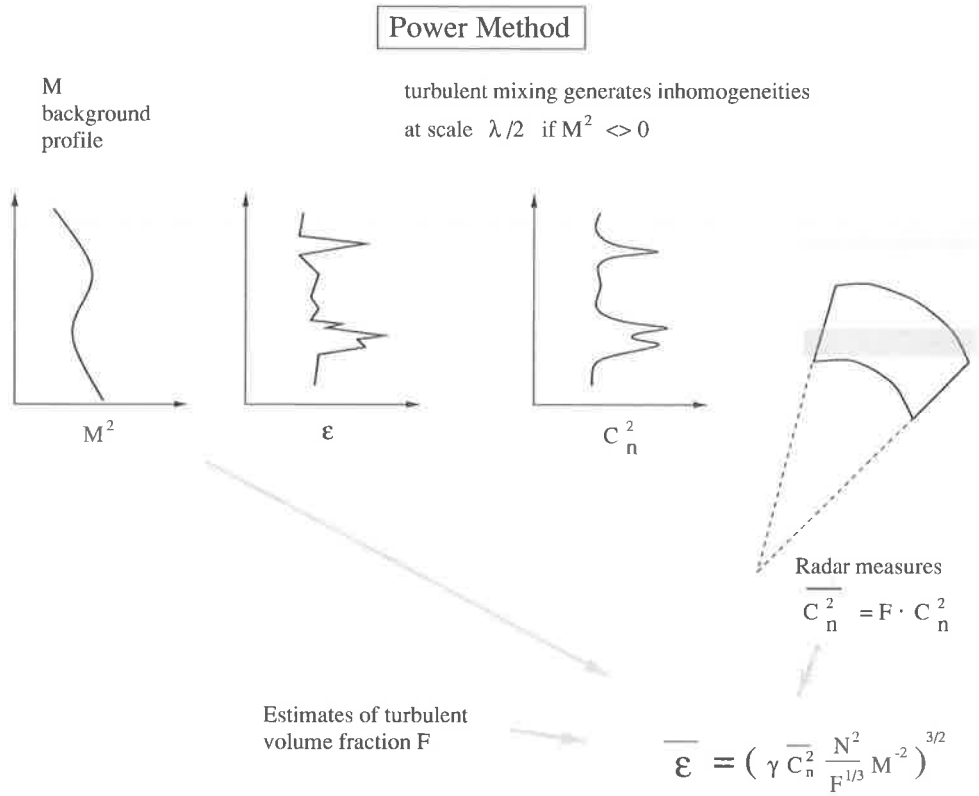

Figure 7.1: Illustration of the power method: Turbulence, characterized by ϵ, acts on the background potential refractive index gradient resulting in refractive index irregularities (C_n^2) which can be detected by the radar. The power returned from turbulent layers in the radar sampling volume can be converted into $\overline{C_n^2}$. Estimates of the turbulent volume fraction F then allow the computation of an average energy dissipation rate.

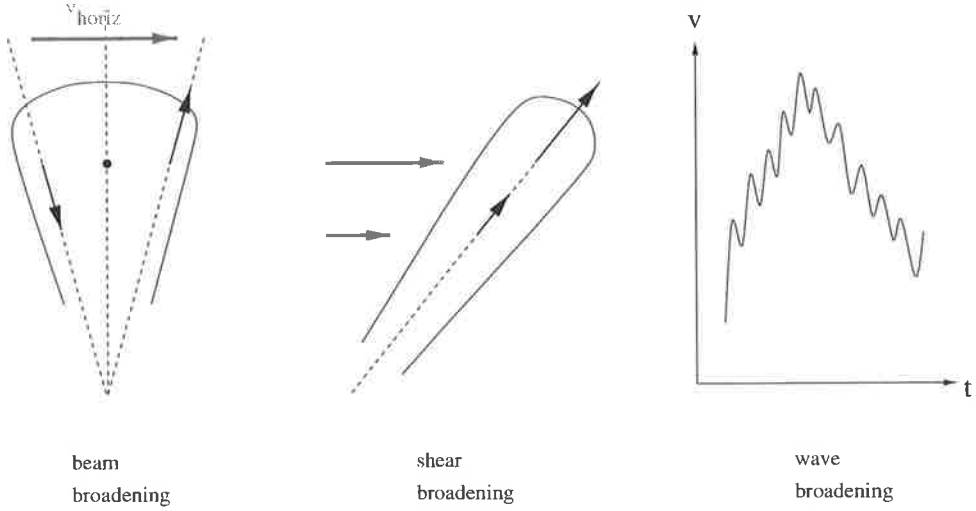

Figure 7.2: Illustration of non-turbulent contributions to the spectral width in radar Doppler spectra.

7.2.2 Spectral width method

The spectral width of radar returns contains information about the root mean square velocity of scatterers in the radar sampling volume and can be used to deduce turbulence parameters [*Srivastava & Atlas*, 1974; *Frisch & Clifford*, 1974; *Frisch & Strauch*, 1976; *Sato & Woodman*, 1982*a*; *Hocking*, 1985; *Doviak & Zirnic*, 1984]. Broadening due to non-turbulent processes, however, has to be taken into account before any conclusions about the strength of the turbulence can be drawn. As turbulent and non-turbulent processes are assumed to be independent Gaussian processes, the total velocity variance is given by the sum of the turbulent and non-turbulent variances:

$$\sigma^2_{\text{total}} = \sigma^2_{\text{turb}} + \sigma^2_{\text{nonturb}}. \tag{7.23}$$

The relevant non-turbulent processes have been discussed by *Sloss & Atlas* [1968], *Atlas et al.* [1969], *Hocking* [1983], and *Murphy et al.* [1994], for example, and are illustrated in Figure 7.2:

Beam broadening is an effect caused by the finite width of the radar beam. Due to the finite range of zenith angles between scatterers in the radar volume and the receiving antenna the radial velocity of the scatterers will vary even if the horizontal

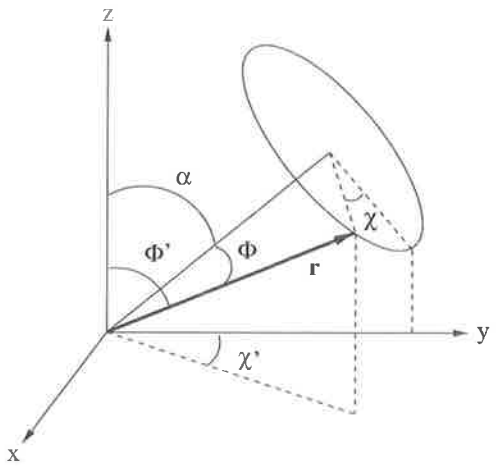

Figure 7.3: Geometry of the radar beam for the computation of non-turbulent contributions to spectral broadening.

wind speed is uniform. Shear broadening, on the other hand, is due to the finite range window over which radar returns are obtained. Variations of the wind speed with height can lead to variations of radial velocity within a range gate. If the wind field and the geometry of the radar sampling volume are known, however, one can correct for these effects as shown below. A third effect is due to temporal variations of the wind field as caused by gravity waves, for example. *Hocking* [1988]and *Nastrom & Eaton* [1997] derived formulas to correct for this wave broadening if the parameters of the gravity wave are known. In practice, however, the best strategy is to keep the time series short to minimize temporal fluctuations of the background wind velocity.

7.2.2.1 Estimation of non-turbulent contributions to the spectral width due to the radar beam geometry

The non-turbulent contributions due to the radar beam geometry can be calculated by integrating over the non-turbulent motion of the scatterers in the radar sampling volume. Since the density distribution of the scatterers is not known one has to make some assumption. Here we apply the commonly used assumption of uniform distribution of the scatterers throughout the sampling volume.

In a first step we compute the spectral broadening due to the mean background

velocity as measured by the radar. Following *Nastrom* [1997] we use a radar beam tilted a zenith angle α in y-direction. The other angles are as designated as in Figure 7.3. The angles are related via

$$\phi' = \cos^{-1}(\cos\phi\cos\alpha - \sin\phi\cos\chi\sin\alpha) \tag{7.24}$$

$$\chi' = \tan^{-1}\left(\frac{\sin\phi\sin\chi}{\sin\phi\cos\chi\cos\alpha + \cos\phi\sin\alpha}\right), \tag{7.25}$$

and the radial velocity is given by

$$v_{\mathrm{rad}}(r,\phi',\chi') = u(r\cos\phi')\cos\chi'\sin\phi' + v(r\cos\phi')\sin\chi'\sin\phi'. \tag{7.26}$$

The mean radial velocity for the range gate centered at R_0 can then be computed as

$$\overline{v}_{\mathrm{rad}}(R_0) = \frac{\int\int\int W(r,\phi)v_{\mathrm{rad}}(r,\phi,\chi)r^2\sin\phi\mathrm{d}r\mathrm{d}\phi\mathrm{d}\chi}{\int\int\int W(r,\phi)r^2\sin\phi\mathrm{d}r\mathrm{d}\phi\mathrm{d}\chi}, \tag{7.27}$$

where

$$W(r,\phi) = \frac{1}{r^4}\exp\left(-\ln 2\frac{\phi^2}{\Delta\phi^2} - \ln 2\frac{(r-R_0)^2}{\Delta r^2}\right) \tag{7.28}$$

is the two-way polar diagram for the range gate at R_0 with beam width $\Delta\phi$ and range window Δr (HWHM). The mean square radial velocity $\overline{v^2}_{\mathrm{rad}}(R_0)$ can be obtained by replacing v_{rad} in the integral by v^2_{rad}, allowing the calculation of the velocity variance sought

$$\sigma^2_{\mathrm{beam}}(R_0) = \overline{v^2}_{\mathrm{rad}}(R_0) - \overline{v}^2_{\mathrm{rad}}(R_0). \tag{7.29}$$

This velocity variance is the non-turbulent contribution to the spectral width of the radar echo due to the background wind field at scales larger than the radar resolution.

7.2.2.2 Estimation of the turbulent contribution to the spectral width

The turbulent contribution to the spectral width is obtained by integrating over the turbulent motion of radar scatterers in the radar sampling volume. As the radar is only susceptible to refractive index irregularities of the scale $\lambda/2$, only motions on a scale equal or greater to this have to be integrated. This assumes that eddies of a scale smaller than $\lambda/2$ do not influence the motion of eddies of a larger scale. The integration

has to be performed up to the largest scales of the inertial spectrum within the radar sampling volume. If a sufficiently narrow beam along the (arbitrarily directed) z-axis is assumed[3], the variance due to turbulent motions can be expressed as [*Srivastava & Atlas*, 1974; *Frisch & Clifford*, 1974]

$$\sigma^2_{\text{turb}} = \int_{||k||=2\pi/L_B}^{4\pi/\lambda} \Phi_{zz}(\mathbf{k}) \left(1 - \|F(\mathbf{k})\|^2\right) \mathrm{d}^3k, \tag{7.30}$$

where $F(\mathbf{k})$ is the Fourier transform of the two-way beam illumination function at the considered range gate. For an isotropic Kolmogorov spectrum

$$\Phi_{zz}(\mathbf{k}) = \left(1 - \frac{k_z^2}{k^2}\right) \frac{E(k)}{4\pi k^2} \tag{7.31}$$

with

$$E(k) = 0.7655 C \epsilon^{2/3} k^{-5/3} \tag{7.32}$$

and $C = 2.0$ (cf. Equations 7.8 and 7.11).

For narrow beamwidth radars with good height resolution the integration in Equation 7.30 is limited by the beam dimensions and approximately independent of L_B. The energy dissipation rate ϵ can then be computed directly from the turbulent variance σ^2_{turb} and the dimensions of the radar sampling volume, without any further knowledge about other atmospheric quantities [*Frisch & Clifford*, 1974].

For radars with coarse height resolution, on the other hand, the integration is limited by the buoyancy length L_B rather than the beam dimensions. Using an expression for L_B as derived by *Weinstock* [1978] for stably stratified flows (Equation 7.2) and replacing the upper integration boundary in Equation 7.30 by infinity we obtain [*Hocking*, 1986]

$$\epsilon = 0.49 \sigma^2_{\text{turb}} N. \tag{7.33}$$

The method, therefore, requires additional knowledge about the buoyancy frequency N at the time of measurement and is only valid for stably stratified regions of the

[3] If the beam is sufficiently narrow the radial velocity of all scatterers within the sampling volume is approximately parallel to the beam pointing direction, i.e. Φ_{zz} can be used to calculate the radial velocity variance.

atmosphere. A graphical illustration of the spectral width method is given in Figure 7.4.

From the treatment above it becomes clear, that the spectral width method inherently assumes a uniform distribution of scatterers throughout the radar sampling volume. While this assumption might be approximately valid for high resolution radars, it is probably violated for radars with a coarse height resolution of 1 km or more. If a dominant layer exists in the sampling volume, then the shear broadening effect will be overestimated and the turbulent velocity variance underestimated. Furthermore, the turbulent velocity variance will correspond to the dominating layer only.

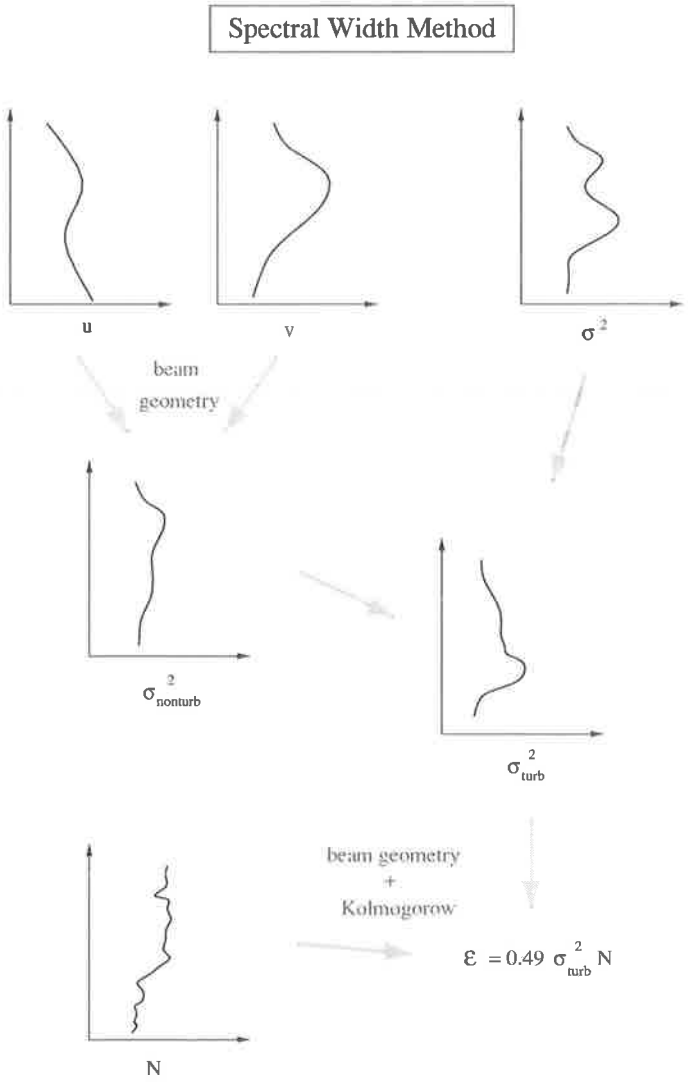

Figure 7.4: Graphical illustration of the spectral width method (for a radar with coarse height resolution): The radar measures zonal (u) and meridional (v) wind speeds and velocity variance (σ^2) as a function of height. The non-turbulent contributions to the velocity variance are due to beam and shear broadening effects and can be estimated if the beam geometry is known. The remaining variance is attributed to inertial range turbulence in the radar sampling volume. Using estimates for the outer scale L_B from simultaneous measurements of the buoyancy frequency N the corresponding energy dissipation rate can be computed.

7.2.3 In-situ observations of turbulence and consequences for radar measurements

Both the power and the spectral width method require sufficient refractive index irregularities in a turbulent layer to be able to detect it. These irregularities are generated by mixing of air parcels from different height levels. If the potential refractive index of the air is constant over a certain height range, the turbulent mixing will not yield any irregularities in refractive index and the height range is invisible to the radar. This situation can occur just below the tropopause, where the potential refractive index gradient often vanishes. Turbulent mixing itself, on the other hand, tends to even out any differences in potential refractive index within the turbulent layer. The radar can, therefore, often only detect the boundaries of a well-developed turbulence layer. This is evident from modeling studies [*Sykes & Lewellen*, 1982] and radar [*Browning & Watkins*, 1970] and in-situ observations [*Barat & Bertin*, 1984*b*; *Bertin et al.*, 1997]. *Bertin et al.* [1997] performed high-resolution balloon soundings of the stratosphere and directly measured turbulent velocity and temperature fluctuations within 7 turbulent layers. Their observations show that the potential temperature gradient is strongly eroded by turbulent mixing within fully developed turbulent layers. This results in a refractive index structure constant C_n^2 that is strongly reduced within the layer and exhibits maxima on its boundaries, while the turbulent velocity structure constant, $C_V^2 = C\epsilon^{2/3}$ in our terminology, is approximately constant throughout the layer and decreases at its boundaries. The erosion of the potential temperature gradient, furthermore, leads to significant variations of the gradient Richardson number Ri within the turbulent layer. *Bertin et al.* [1997] , therefore, suggest that the flux Richardson number R_f, which stayed within the range of about $0.15 \ldots .3$ throughout the observed turbulent layers, should be used instead of the gradient Richardson number Ri to monitor turbulence activity within turbulent layers. They conclude that application of Equation 7.17 with $R_f = 0.25$ leads to a good agreement between the

kinetic energy dissipation rates ϵ deduced from measurements of C_V^2 and C_n^2, respectively, when the turbulent layer is resolved with sufficient height resolution. In spite of the erosion of the potential temperature gradient by turbulence, the extraction of the energy dissipation rate ϵ from measurements of C_n^2 is, therefore, still feasible at heights where the turbulent activity is observable by radars, i.e. at the layer boundaries. In the case of the spectral width method, the erosion of the temperature gradient leads to a non-uniform distribution of scatterers in the turbulent layer, and the inferred energy dissipation rate is again not an average over the layer but corresponds to the boundaries only.

Chapter 8

Measurements of wind and turbulence

Having introduced the necessary background theory in Chapters 5 to 7, we now can apply the radar technique to measurements of wind and turbulence during a campaign in August 1998. The campaign was initiated to study refractive index turbulence in a jet stream region and was performed in collaboration with the US Air Force, Airborne Research Australia [1], and the Atmospheric Physics group at the University of Adelaide. During the campaign simultaneous measurements of turbulence parameters were undertaken using an high-altitude aircraft, thermosondes, and the University of Adelaide's VHF radar at Buckland Park. In this chapter we compare the wind and turbulence measurements as obtained by the radar and the thermosondes and apply gravity wave theory to explore the relationship between the observed turbulence layers and the observed gravity wave field.

[1] affiliated with Flinders University, Adelaide.

8.1 Instrumentation and data processing

8.1.1 The Buckland Park VHF radar

The Buckland Park VHF radar operates at a frequency of 54.1 MHz with 32 kW peak power. The antenna system consists of two orthogonal coaxial-collinear (CoCo) antenna arrays [*Balsley & Ecklund*, 1972; *Judasz et al.*, 1987], as shown in Figure 8.1. The original East-West array features 32 CoCo rows of 48 half-wave dipoles aligned in north-south direction. The array is split into two groups of 16 rows to accommodate the transmitter caravan between them. The later installed North-South array has 32 CoCo rows of 22 half-wave dipoles each on either side of the caravan. The rows, which are separated by $\lambda/2$ and raised $\lambda/4$ above ground, are center fed from the transmitter caravan. A ground plane consisting of individual copper wires spaced $\lambda/12$ apart in both directions improves the efficiency of the array. The beam steering capability of the system is achieved by inserting phase delay cables between the transmitter and the antenna rows. The CoCo arrays are used for both transmission and reception in Doppler mode. In spaced antenna mode, it is also possible to receive on three sets of 16 Yagi antennas each situated to the west of the CoCo arrays.

During the campaign the radar was used in a five beam Doppler beam steering configuration with parameters as given in Table 8.1. The raw data was analyzed using the DBS algorithm described in Chapter 6, where each single time series was divided into 3 segments and hourly averages were calculated for each full and half hour of the day. For transmission on the vertical beam, the radar echoes received with the three Yagi groups were also analyzed using the Full Correlation Analysis.

8.1.1.1 Radar calibration

In order to relate the returned power P_r to the average refractive index structure function $\overline{C_{n,\mathrm{radar}}^2}$ in the radar sampling volume, the radar system has to be calibrated. This can be achieved by injecting a signal of known power into the receiving path or by comparison with other instruments.

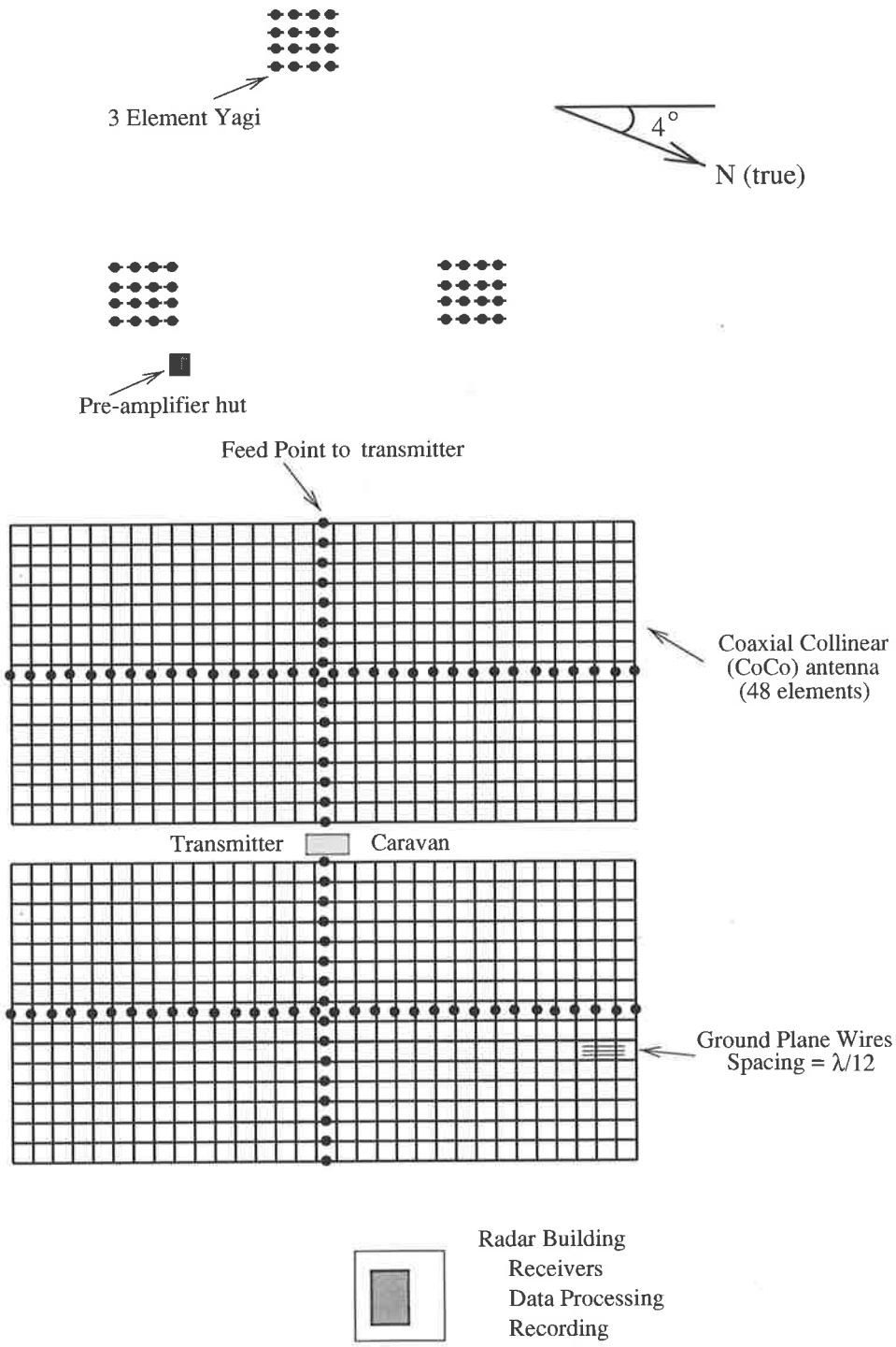

Figure 8.1: The Buckland Park VHF radar site (after *Hobbs* [1998]).

beam	14.5° N,S,E,W	vertical
PRF	4096 s^{-1}	4096 s^{-1}
coh. integrations	256	512
dwell time	56.25 s	50 s
sampling ranges	1200-19200 m	1200-19200 m
range resolution	1000 m	1000 m
	(500 m oversampled)	(500 m oversampled)

Table 8.1: Radar configuration during the turbulence campaign.

To calibrate the digitized output at the receivers to absolute power levels at the antenna output a noise signal of known temperature T_{noise} was fed into the antenna preamplifier and the signal units at the receiver output were recorded after coherent integration. Due to the finite bandwidth Δf of the receiving path only the noise power within that bandwidth,

$$P_{\text{noise,in}} = k_B T_{\text{noise}} \Delta f, \tag{8.1}$$

with k_B the Boltzmann constant, affects the signal level at the receiver output. This is given by

$$\overline{S^2}_{\text{noise,out}} = N g^2 P_{\text{noise,in}}, \tag{8.2}$$

where N is the number of coherent integrations and g the voltage amplification factor of the receiving path. From a linear fit of the signal level at the receiver output as a function of noise temperature the voltage amplification factor g can be readily obtained. The power of a (coherent) signal present at the preamplifier input can then be deduced from the signal level at the receiver output as

$$P_{\text{signal,in}} = \frac{\overline{S^2}_{\text{signal,out}}}{N^2 g^2}, \tag{8.3}$$

where the number of coherent integrations N appears squared due to the coherency of the signal. Figure 8.2 shows the obtained calibration curve for the receiver. The receiver characteristics are well approximated by a linear fit over the range of available noise temperatures up to 12000 K.

A full calibration of the radar also requires knowledge about the antenna efficiency

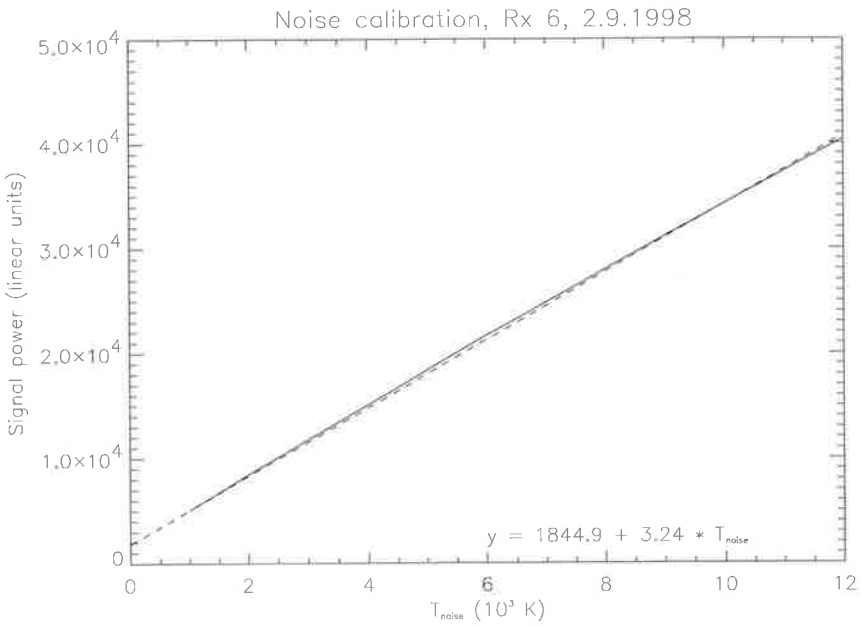

Figure 8.2: Calibration curve (solid) and linear fit (dashed) for the receiver used in the turbulence measurements. The receiver characteristics are approximately linear over the whole accessible noise temperature range.

e. For a nominal transmitter power of P_T, only a fraction eP_T will actually be radiated into the atmosphere. Similarly, only a fraction eP_R will be received at the antenna output, for an incident power of P_R. The efficiency of the Buckland Park East-West array was deduced by D. Neudegg in 1987 by comparison with a reference Yagi antenna. Assuming an efficiency of 100% for the Yagi antenna, he obtained an efficiency of 37% for the East-West array. Comparison of signal levels for atmospheric measurements between the East-West and North-South arrays during our campaign would then indicate an efficiency of 52% for the North-South array. These values seem rather large compared to other CoCo array efficiencies reported in the literature [*Judasz et al.*, 1987], and are probably due to an efficiency of less than 100% for the used Yagi reference antenna.

An alternative method is to calibrate the radar system by comparison of the $\overline{C_{n,\mathrm{radar}}^2}$ obtained from the hourly averaged power spectra using Equation 7.19 with the $\overline{C_{n,\mathrm{sonde}}^2}$

values. We restricted ourselves to measurements above a height of 7.5 km where humidity is negligible to avoid differences between radar and thermosonde measurements due to differences in humidity at the radar and sonde locations. The calibration revealed that the use of antenna efficiencies of 37% and 52% for the East-West and North-South array, respectively, leads to overestimates of $\overline{C_{n,\mathrm{radar}}^2}$ of 55%. We, therefore, adjusted the antenna efficiencies to 24% and 34% for the East-West and North-South array, respectively. This adjustment also takes other system losses and uncertainties in the actual transmitter power into account.

8.1.2 Thermosondes

The thermosonde is attached to a standard radiosonde package and measures fine scale temperature differences across a fixed horizontal distance of 1m. This signal is then filtered and averaged to compute a running temperature structure function, where a time constant of 3.75 seconds is used. The structure function is sampled every 1.2 seconds by a spare channel of the radiosonde and relayed to the ground station together with the temperature, pressure, humidity and wind data from the standard radiosonde. To avoid perturbations of the measurements by the wake of the balloon the instrumentation gondola is attached to the balloon using a line of 100 m length [*Jumper et al.*, 1999].

The running average of the differential temperature measurements ΔT at a distance of 1 m directly yields the potential temperature structure function constant $C_\Theta^2 = \langle \Delta T^2 \rangle$. This can be converted to C_n^2 by

$$C_n^2 = \left(77.6 \cdot 10^{-6} \frac{p}{T^2} \chi\right)^2 C_\Theta^2, \tag{8.4}$$

with the humidity correction χ as defined in Equation 7.22.

The radar and thermosonde data are obtained with different altitude resolutions of some 20 m and 1 km, respectively.[2] To allow a comparison and combination of

[2]The thermosonde time constant of 3.75 s together with an assumed balloon ascent rate of 5 m/s results in an average height resolution of about 20m.

the two data sets the thermosonde data was convolved with the radar resolution. We used a triangular window of the same width as the radar pulse as convolution kernel and rejected 5% of the lowest and highest values within the kernel range to allow for outliers. The convolution was performed on profiles of u, v, ϵ, C_n^2, M^2, and N^2, i.e. the profiles were computed using high resolution data and then smoothed to obtain profiles of $\overline{u}$, $\overline{v}$, $\overline{\epsilon}_{,\mathrm{sonde}}$, $\overline{C_{n,\mathrm{sonde}}^2}$, $\overline{M^2}$, and $\overline{N^2}$, respectively.

Three thermosondes were launched daily after sunset for six consecutive days at Gawler (34° 37' S, 138° 44' E). Figure 8.3 shows a map of the region around the radar site together with the thermosonde trajectories for the six campaign days. Crosses along the trajectories mark 5 km height intervals up to 20 km.

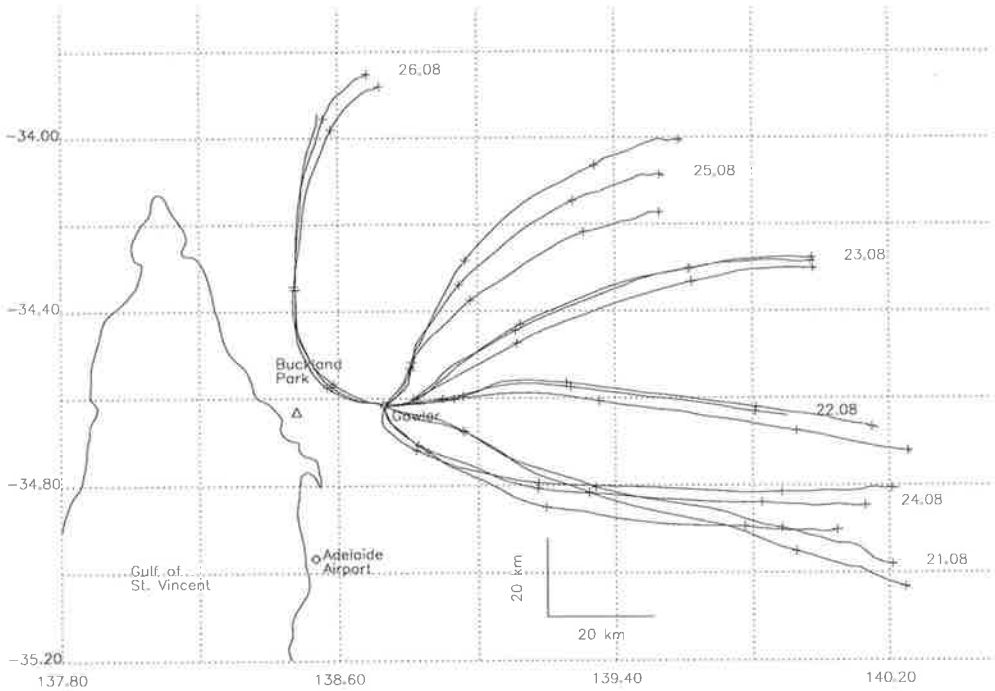

Figure 8.3: Map of the region around the radar site together with the thermosonde trajectories. Crosses along the trajectories mark 5 km height intervals.

8.2 Wind measurements

To evaluate the performance of the DBS algorithm introduced in Section 6.2, the radar winds obtained with this algorithm were compared with the wind measurements by the thermosondes, convolved with the radar resolution as described above. A sliding height window was used in the data comparison. The radar winds correspond to an hourly average around the time, when the respective sonde passed through the corresponding radar range gate. Figure 8.4 shows a scatter plot of wind measurements obtained by thermosonde and Doppler radar for the 17 sondes launched at Gawler between 21.8.98 and 26.8.98. The radar height coverage was up to 18 km. Taking the horizontal distance between radar and thermosonde of sometimes more than 100 km into account, the two techniques are found to agree very well.

For completeness, we also present a comparison between the thermosonde winds and winds obtained by the Full Correlation Analysis of radar echoes received on the three Yagi groups. Here, single time series were analyzed and the obtained wind values were averaged over one hour. The corresponding scatter plots are given in Figure 8.5. The number of data points is strongly reduced, as the radar returns covered heights less than 10 km only.

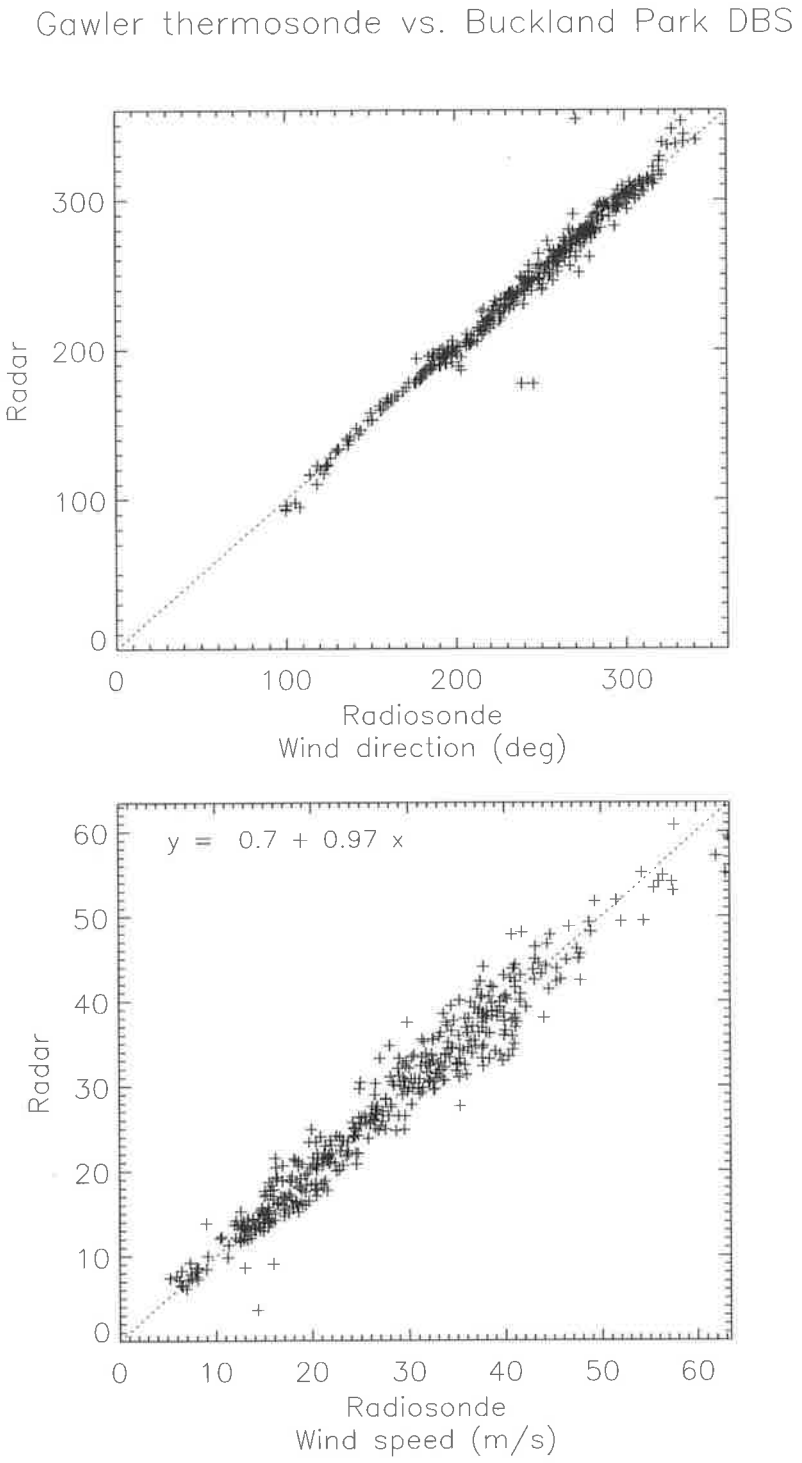

Figure 8.4: Comparison of wind measurements obtained by radiosondes launched at Gawler with hourly averaged Doppler radar measurements performed at Buckland Park, 30 km west of Gawler. The dotted lines correspond to $y = x$. A total of 17 sonde flights were analyzed.

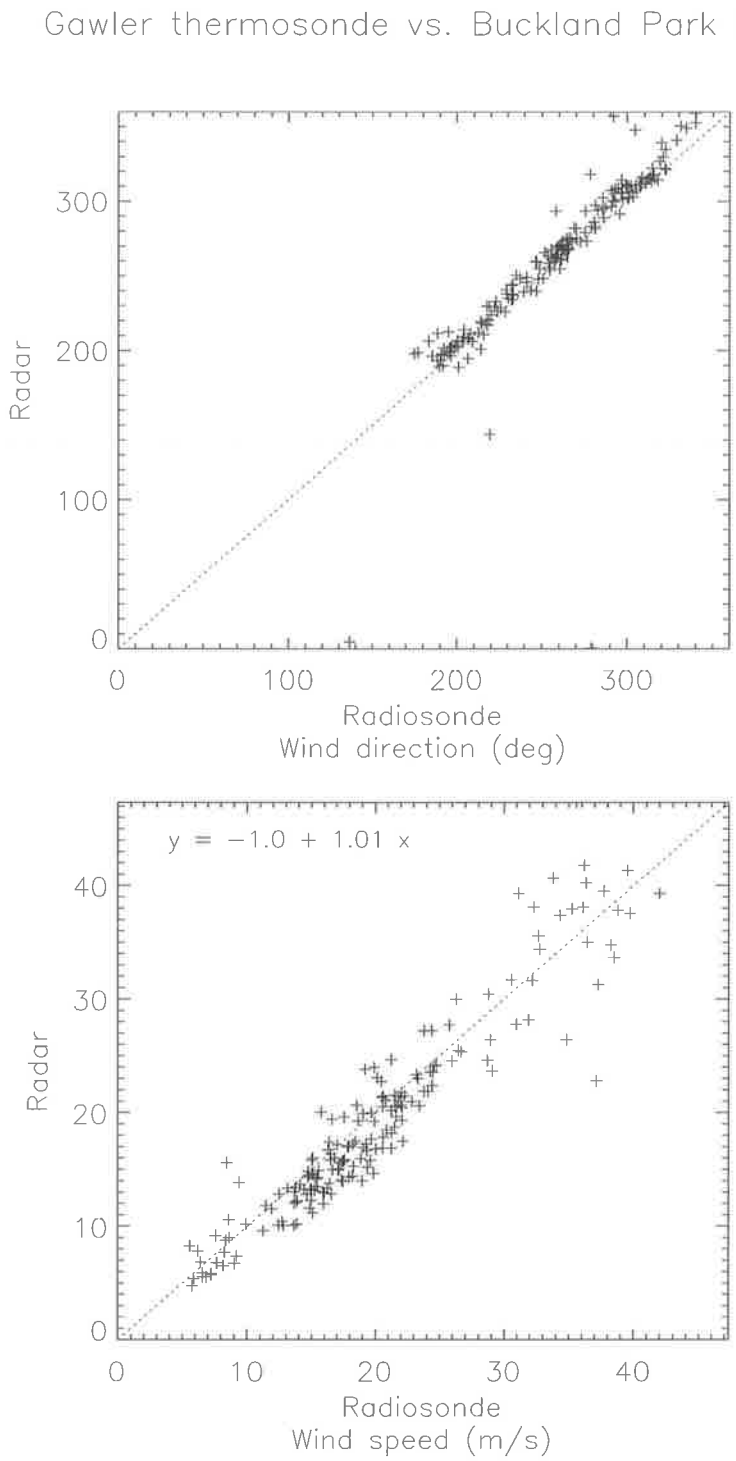

Figure 8.5: Same as Figure 8.4, but for FCA radar measurements.

8.3 Turbulence measurements

The power and spectral width methods have been used in many radar studies to infer turbulence parameters in the lower and middle atmosphere [*Frisch & Strauch*, 1976; *Crane*, 1980; *Weinstock*, 1981; *Hocking*, 1988; *Fukao et al.*, 1994; *Cohn*, 1995; *Hocking & Mu*, 1997; *Nastrom & Eaton*, 1997; *Gossard*, 1998; *Hooper & Thomas*, 1998; *Pepler et al.*, 1998; *Hermawan & Tsuda*, 1999]. Due to the lack of colocated in-situ observations, however, the validity of the radar measurements can often only be justified by the right order of magnitude of the derived turbulence parameters or by agreement with similar observations. While a few direct comparisons of VHF radar echoes with direct balloon estimates exist [*Eaton et al.*, 1988; *Luce et al.*, 1996; *Luce et al.*, 1997], further case studies are needed.

8.3.1 Comparison of the average refractive index structure function constant $\overline{C_n^2}$

We applied Equation 7.19 to convert P_r, the power back-scattered from the radar sampling volume, to the average refractive index structure function constant $\overline{C_{n,\mathrm{radar}}^2}$ within that volume. Table 8.2 lists the relevant radar parameters for the Buckland Park radar used in Equation 7.19. $\overline{C_{n,\mathrm{radar}}^2}$ was calculated for each of the four oblique beams from the hourly averaged DBS data set closest to the sounding time, and then averaged over the four beam directions. In the comparison between thermosonde and radar measurements we had to restrict ourselves to measurements above a height of 7.5 km where humidity is negligible to avoid differences between radar and thermosonde measurements due to differences in humidity at the radar and sonde locations. The left diagram in Figure 8.6 shows a histogram of $\log \frac{\overline{C_{n,\mathrm{radar}}^2}}{\overline{C_{n,\mathrm{sonde}}^2}}$ for measurements above 7.5 km. Data from all six campaign days were used. A Gaussian fit to the data (dashed line) shows that this ratio is approximately log-normal distributed with a standard deviation $\sigma = 0.27$, i.e. 95 % of $\overline{C_{n,\mathrm{radar}}^2}$ are within a factor of 3.3 $\overline{C_{n,\mathrm{sonde}}^2}$. A scatter plot of $\overline{C_{n,\mathrm{radar}}^2}$ versa $\overline{C_{n,\mathrm{sonde}}^2}$ for the same data is presented in the bottom diagram.

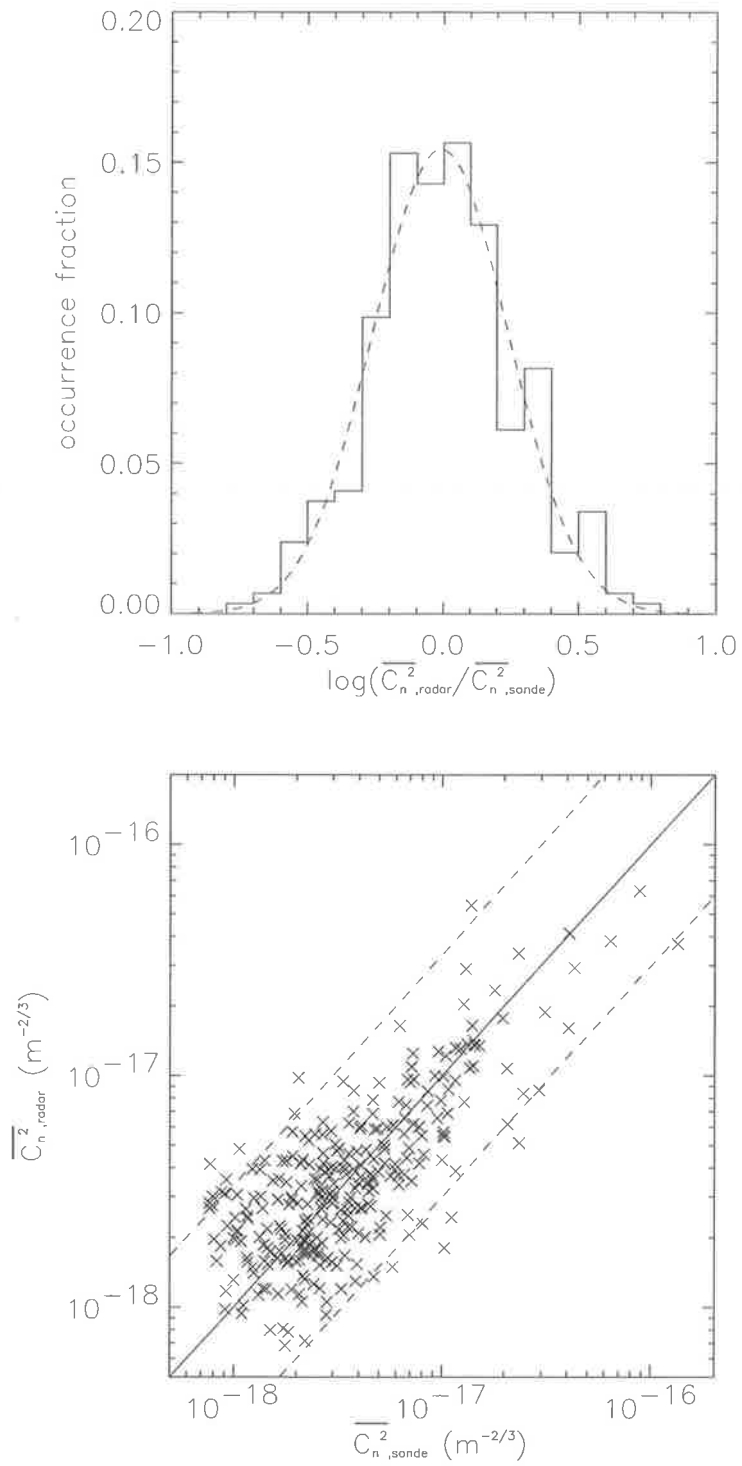

Figure 8.6: Comparison of $\overline{C_n^2}$ measurements obtained by radar and thermosonde above 7.5 km during the six days of the campaign. The ratio of $\overline{C_{n,\mathrm{radar}}^2}$ to $\overline{C_{n,\mathrm{sonde}}^2}$ is approximately log-normal distributed with a standard deviation of $\sigma = 0.27$ (top). A scatter plot shows good agreement between the two methods (bottom). The dashed lines correspond to the 95% confidence interval.

λ	5.545 m
P_t	32 kW
A_{eff}	8700 m^2
e_T, e_R (east-west)	.24
e_T, e_R (north-south)	.34
Δr	500 m

Table 8.2: Radar parameters of the Buckland Park radar for use in Equation 7.19.

Figure 8.7 illustrates the importance of incoherent averaging especially for larger radar ranges. The thin and thick lines correspond to $\overline{C_{n,\text{sonde}}^2}$ and $\overline{C_{n,\text{radar}}^2}$, obtained from hourly averaged periodograms, respectively. The squares indicate $\overline{C_{n,\text{radar}}^2}$ values as determined from single periodograms of all one minute radar time series within one hour around the sonde launch. When no incoherent averaging was performed, only signals with relatively high power were accepted in the analysis, leading to a bias toward large $\overline{C_{n,\text{radar}}^2}$ values. This is evident at heights above around 10 km. By incoherently averaging over all available power spectra within one hour, on the other hand, the detectability of signals is strongly increased. In our case, $\overline{C_{n,\text{radar}}^2}$ values up to an order of magnitude less than without incoherent averaging can be detected with confidence. The height range of usable radar returns can, therefore, be increased by around 8 km. This increase in height range is gained at the cost of a reduced time resolution. Due to the large distances between the radar and sondes, and the scatter of the $\overline{C_{n,\text{radar}}^2}$ values from periodograms of one-minute time series, however, we believe that a better time resolution would lead to a deterioration in the comparison between the techniques.

Considering the, at times, rather large separation between sondes and radar and the variability of $\overline{C_{n,\text{radar}}^2}$ in time, as evident from Figure 8.7, the two methods are found to agree well. Note, that while we calibrated the radar using the thermosonde data, this calibration only leads to a shift of the distribution in the left diagram of Figure 8.6 of 0.2 units, but does not change its width. It is the width, however, that reveals the good correlation between the two methods.

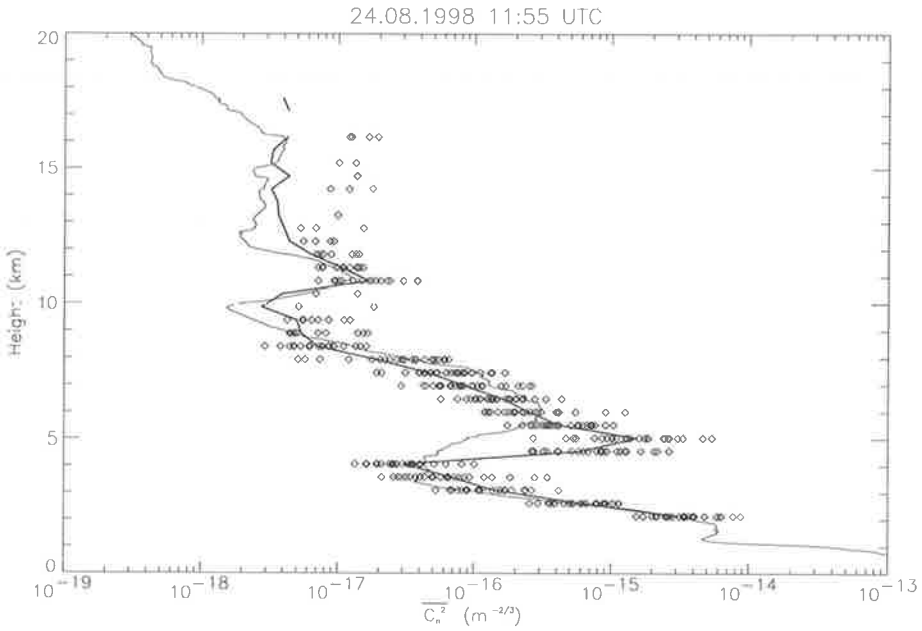

Figure 8.7: Comparison of $\overline{C_n^2}$ obtained from thermosonde and radar measurements for the launch on 24.8.98, 11:55 UTC. Shown are $\overline{C_{n,\text{sonde}}^2}$ (thin line), $\overline{C_{n,\text{radar}}^2}$ from hourly averaged power spectra (thick line), and $\overline{C_{n,\text{radar}}^2}$ for power spectra of one-minute radar time series within one hour around the sonde launch (squares).

8.3.2 Comparison of the average energy dissipation rate $\bar{\epsilon}$ using the power method

Once the average refractive index structure function constant $\overline{C_n^2}$ is known, one can try to deduce the average energy dissipation rate $\bar{\epsilon}$ if information about the background atmosphere is available. Due to the nonlinear relationship between ϵ and C_n^2, however, the volume fraction F of turbulent layers in the radar sampling volume appears in Equation 7.21. We will use F as a fitting parameter to achieve agreement between $\bar{\epsilon}_{\text{radar}}$ and $\bar{\epsilon}_{\text{sonde}}$ and, subsequently, compare the obtained value with estimates of the turbulent volume fraction from the high resolution thermosonde data.

The energy dissipation rate for the thermosonde is calculated from high resolution values of N^2, M^2 and $C_{n,\text{sonde}}^2$ as (Equation 7.21 with $F = 1$)

$$\epsilon_{\text{sonde}} = \left(\frac{3}{2.8} \frac{C_{n,\text{sonde}}^2 N^2}{M^2} \right)^{3/2} \tag{8.5}$$

and, subsequently, convolved with the radar resolution to yield $\bar{\epsilon}_{\text{sonde}}$. For the radar, M^2 and N^2 are first convolved with the radar resolution, and the resulting profiles of $\overline{M^2}$ and $\overline{N^2}$ are then used to calculate

$$\bar{\epsilon}_{\text{radar}} = \left(\frac{3}{2.8} \frac{\overline{C_{n,\text{radar}}^2}\,\overline{N^2}}{F^{1/3}\overline{M^2}} \right)^{3/2} . \tag{8.6}$$

Note, that the use of $\frac{\overline{N^2}}{\overline{M^2}}$ is much less sensitive to layers with $M^2 \approx 0$ than $\overline{\left(\frac{N^2}{M^2}\right)}$.

In addition to the humidity effects mentioned above, we have to restrict ourselves to measurements above 7.5 km as our choice of $R_f = 0.25$ in Equation 7.21 assumes a stably stratified background atmosphere. Application of this formula to statically unstable regions of the atmosphere might lead to erroneous results. Figure 8.8 shows a histogram of $\log \frac{\bar{\epsilon}_{\text{radar}}}{\bar{\epsilon}_{\text{sonde}}}$ and a scatter plot of the corresponding data. The ratio of $\bar{\epsilon}_{\text{radar}}$ to $\bar{\epsilon}_{\text{sonde}}$ has a standard deviation $\sigma_\epsilon = 0.42$, i.e. 95 % of $\bar{\epsilon}_{\text{radar}}$ are within a factor 6.5 of $\bar{\epsilon}_{\text{sonde}}$, and is approximately log-normal distributed. A factor $F = 0.21$ had to be chosen in order to center the distribution at zero.

It is interesting to note that the choice of a *constant* F leads to a standard deviation $\sigma_\epsilon = 0.42$ that is only marginally larger than $\frac{3}{2}\sigma_{C_n^2} = 0.40$, a minimum value to

be expected from the $(C_n^2)^{3/2}$ dependence of ϵ. The physical meaning of the parameter F is the volume fraction of turbulent layers in the radar sampling volume, where all turbulent layers are assumed to have the same energy dissipation rate ϵ. The availability of high resolution thermosonde data enables us to estimate this volume fraction directly from in-situ observations. Due to spurious fluctuations of small wavelength in the wind data from the thermosondes, however, a direct calculation of the Richardson number Ri is not feasible at a height resolution of 20 m. But the criterion $Ri \leq 0.25$ for turbulent layers is not always fulfilled in observations anyway [*Bertin et al.*, 1997], and a more reliable criterion is the energy dissipation rate ϵ itself. We calculated profiles of ϵ_{sonde} and $\overline{\epsilon}_{\text{sonde}}$ according to Equation 8.5 and identified layers for which $\epsilon_{\text{sonde}} > \overline{\epsilon}_{\text{sonde}}$ as turbulent layers. The resulting average profile (solid line) with standard deviation (dashed lines) is given in Figure 8.9. The choice of $F = 0.21$ (dotted line) underestimates the obtained average turbulent volume fraction slightly, especially for larger heights. Note, however, that the assumption of equal energy dissipation rate for all layers within the radar sampling volume, which led to Equation 7.21, might not be fulfilled due to the existence of dominant layers. This would lead to an effective F to be used in Equation 7.21 that is smaller than the average turbulent volume fraction as determined by the above criterion. As $\overline{\epsilon}_{\text{radar}}$ is only weakly dependent on F as $\overline{\epsilon}_{\text{radar}} \propto F^{-1/2}$, however, (small) errors in the estimation of F will not affect the $\overline{\epsilon}_{\text{radar}}$ estimates drastically.

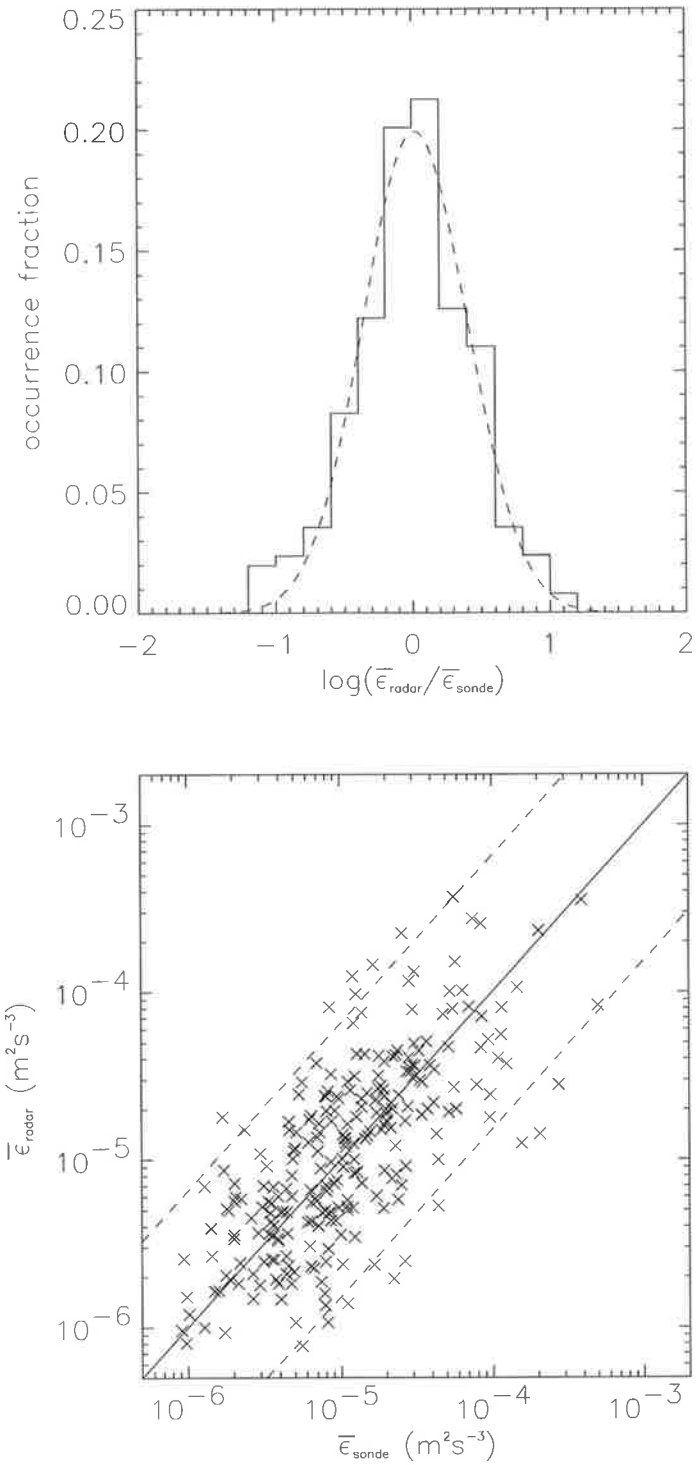

Figure 8.8: Comparison of $\overline{\epsilon}$ measurements obtained by radar and thermosonde above 7.5 km during the six days of the campaign. The ratio of $\overline{\epsilon}_{\text{radar}}$ to $\overline{\epsilon}_{\text{sonde}}$ is approximately log-normal distributed with a standard deviation of $\sigma = 0.42$ (top). A scatter plot shows good agreement between the two methods (bottom). The dashed lines correspond to the 95% confidence interval.

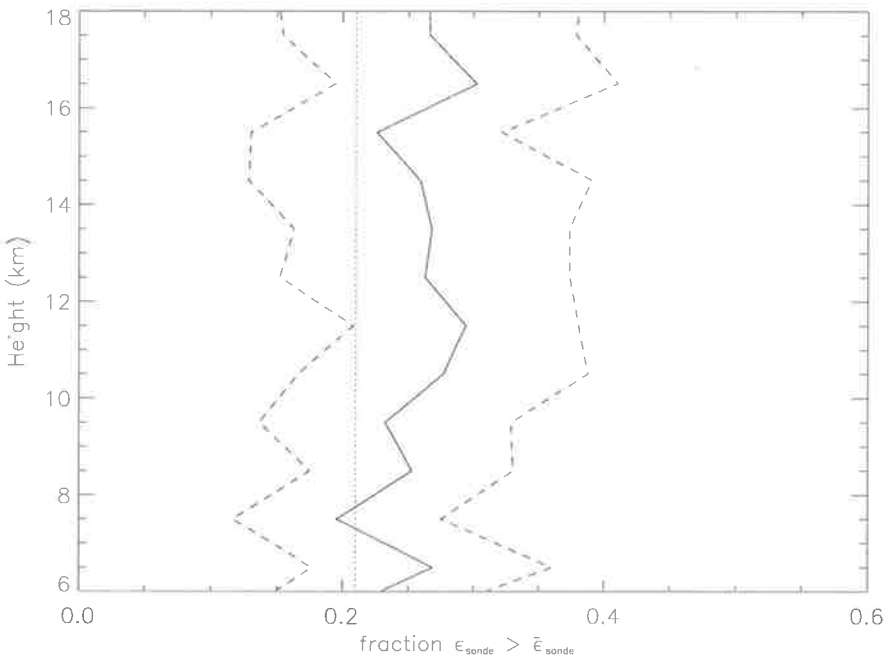

Figure 8.9: Estimation of the turbulent volume fraction from high resolution thermosonde data. Layers with $\epsilon_{\text{sonde}} > \bar{\epsilon}_{\text{sonde}}$ are assumed to be turbulent. The diagrams show the average turbulent volume fraction over all thermosonde launches within the six days (solid line) together with its standard deviation (dashed lines). The dotted line indicates $F = 0.21$.

8.3.3 Estimation of the energy dissipation rate ϵ using the spectral width method

The comparison of the energy dissipation rate ϵ as obtained by the thermosonde and the spectral width method is complicated by the coarse height resolution of the Buckland Park radar. As the inertial range of turbulence is restricted to scales less than the radar sampling volume, the integral for the turbulent contribution to the spectral variance, Equation 7.30, depends on the buoyancy scale L_B. Equation 7.2 provides an estimate for L_B from accessible atmospheric parameters, but it is only valid for stably stratified flows. Application of the spectral width method to the lower troposphere, where statically unstable layers with $N^2 < 0$ dominate, can, therefore, lead to erroneous estimates of ϵ. We encountered a similar restriction for the power method, where our choice of $R_f = 0.25$ assumed a statically stable atmosphere. In the latter case, however, we were able to use power estimates from spectra which were incoherently averaged over an hour and could, therefore, achieve a height coverage of usable radar returns of up to 18 km. In the spectral width method, we have to keep the measurement interval as short as possible (around 1 min), as the change in background wind speed over a longer time interval would lead to a significant broadening of the spectral width (gravity wave broadening) and an overestimation of ϵ. Hence, we only achieve a height coverage of around 10 km. The coarse height resolution, furthermore, yields a large possible contribution from gravity waves on scales less than the radar resolution, so that only layers of intense turbulence can be identified by this method.

Due to the difficulties mentioned above, we only give results for a single day of the campaign, the 25.8.1998. Figure 8.10 shows contour plots of the zonal and meridional wind velocity as functions of time and height. The wind field was calculated using the DBS algorithm introduced above. Some missing data points above 15 km were linearly interpolated over using surrounding data points in time and height. The jet stream at a height of around 8 km is clearly visible, with the wind direction changing from eastwards to northwards at around 0800 UTC. The resulting vertical shear at the radar

resolution is shown in the top contour plot of Figure 8.11. Shear values of more than 18 ms^{-1} km^{-1} were reached just below the tropospheric jet. The bottom diagram shows the turbulent velocity variance corrected for shear and beam broadening. Single time series of about one minute duration have been used to estimate the spectral width to avoid gravity wave broadening. Only signals with a detectability $d > 5$ were accepted to ensure meaningful spectral width estimates. Comparison of the diagrams reveals a clear correlation between regions of high wind shear and high velocity variance. While we went through great effort to correct for effects of finite beam geometry by numerical integration of the wind field over the radar sampling volume, deviations from our assumption of uniform scatterer distribution within the sampling volume could lead to errors in the variance estimates, especially in regions of large shear. Figure 8.12, finally, gives a comparison of the energy dissipation rates as obtained with the different techniques for the launches at 0830 UTC and 1143 UTC. The energy dissipation rate from the spectral width method (dashed line) was obtained by averaging the results of Equation 7.33 over one hour centered around the launch time. The values for the other methods were obtained as described before. The energy dissipation rate determined from the spectral width method shows distinctive peaks at around 6 to 7 km and, for the later launch, at around 10 km, coinciding with heights of increased turbulence as observed with the other two methods. The spectral width method is expected to yield the energy dissipation rate of the layers with the largest C_n^2 in the radar sampling volume, which corresponds to the most turbulent layers if N^2 and M^2 are assumed constant over one radar range gate. Quantitatively, the spectral width peaks agree approximately with the largest peaks of the high resolution thermosonde profile at these radar range gates. The background value of the spectral width profile, on the other hand, might not be due to turbulent motion but could be dominated by spatial gravity wave fluctuations with vertical scales smaller than the radar height resolution.

The existence of simultaneous radio sonde measurements with a vertical resolution of some 20 meters allows us to test this hypothesis. The gravity wave contributions to

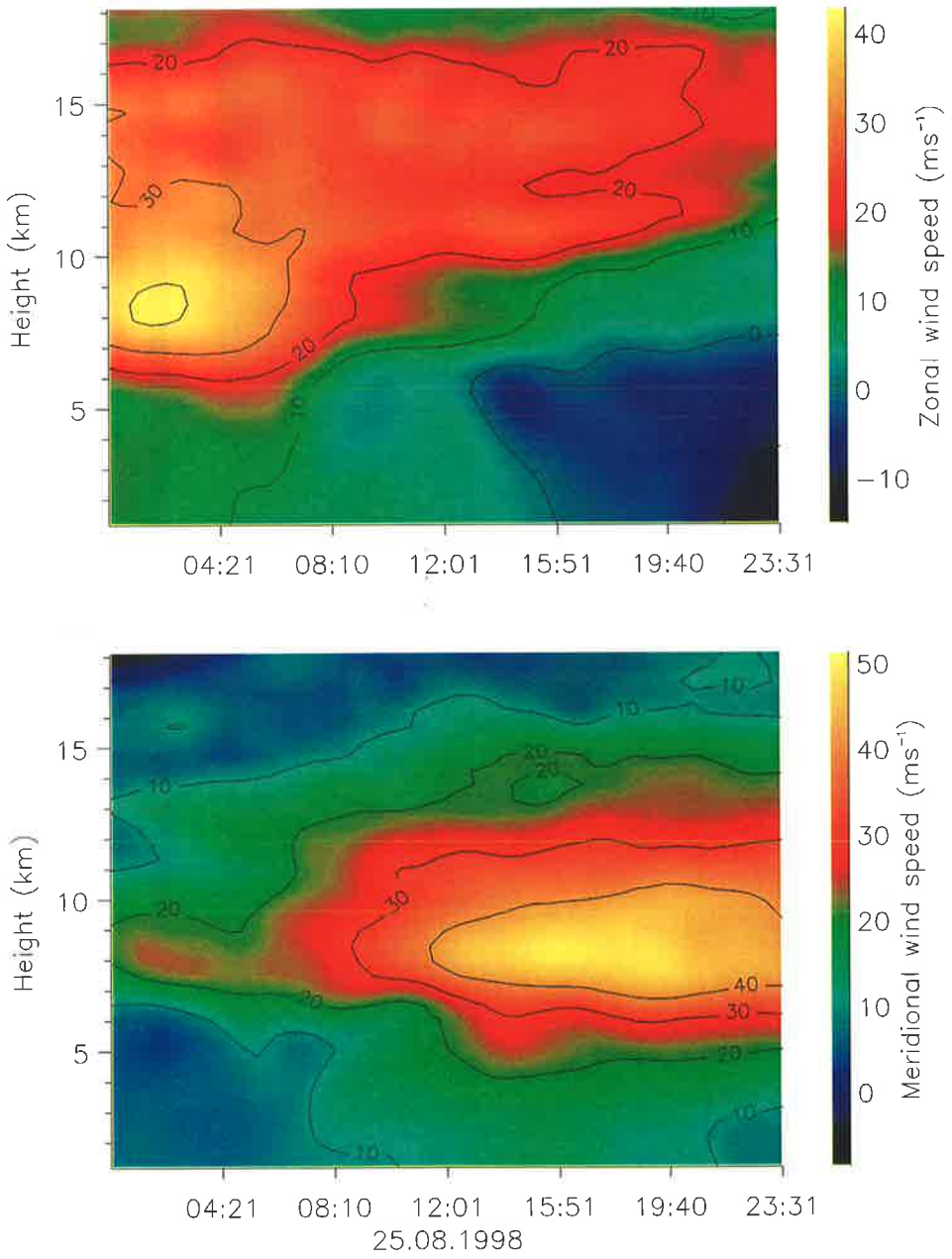

Figure 8.10: Contour plots of zonal and meridional wind speeds as measured with the Buckland Park radar on 25.08.1998. Some missing data points above 15 km have been interpolated over.

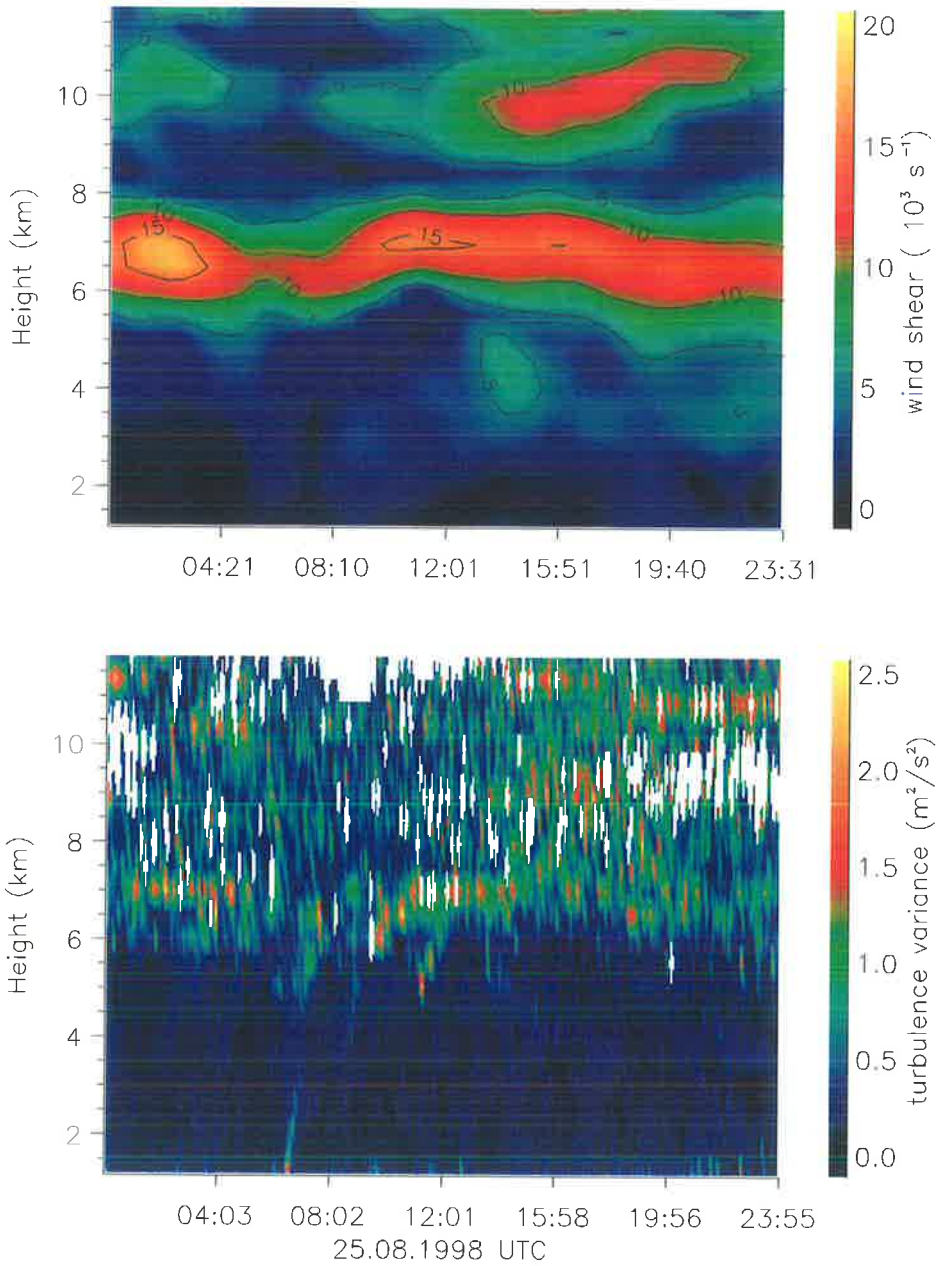

Figure 8.11: Contour plots of vertical shear and turbulent velocity variance. The velocity variance has been corrected for beam and shear broadening by integrating the windfield of Figure 8.10 over the radar sampling volume.

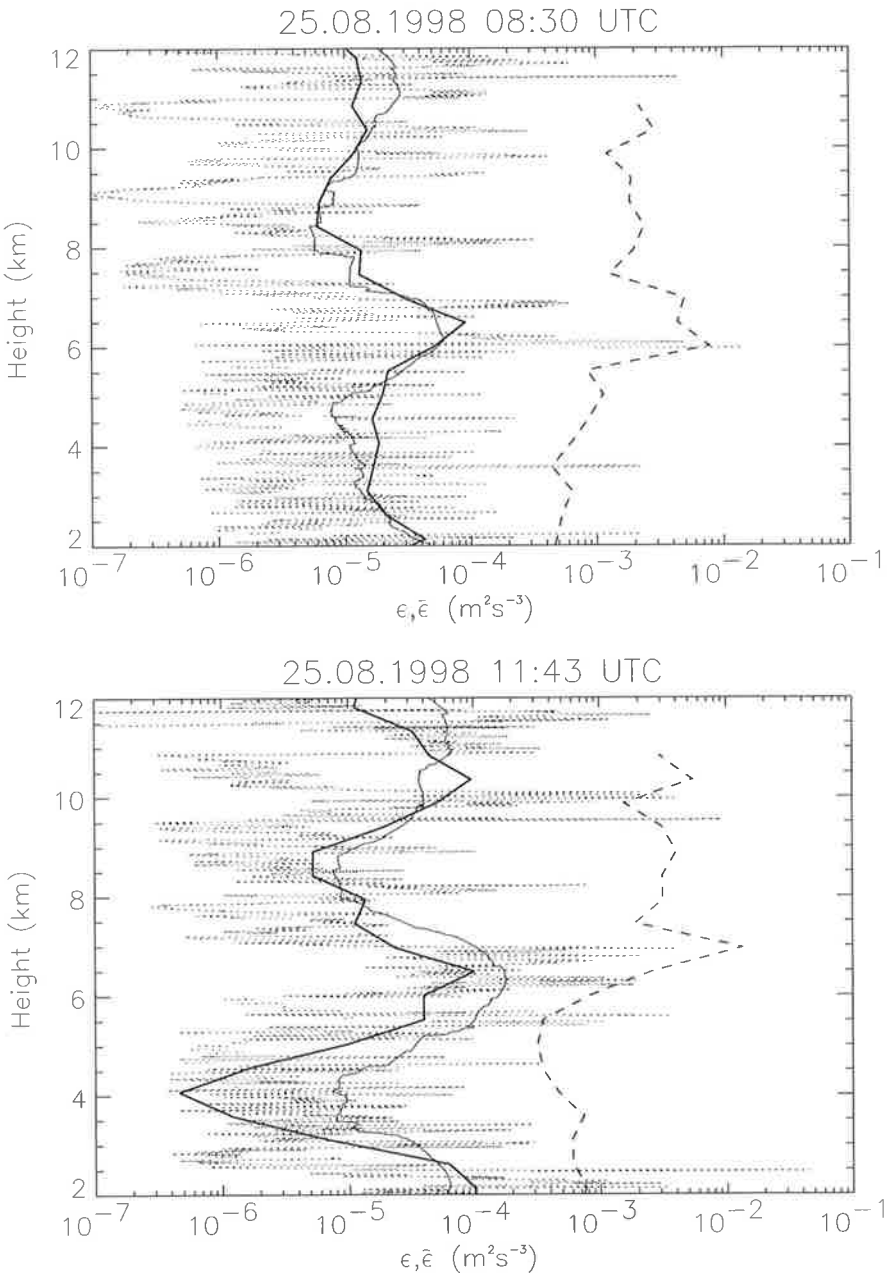

Figure 8.12: Comparison of the energy dissipation rate as obtained by the different techniques for two thermosonde launches on 25.08.1998. The solid lines show the energy dissipation rate $\bar{\epsilon}$ averaged over the radar height resolution from thermosonde (thin line) and radar (thick line) data using the power method. The dotted and dashed lines correspond to the energy dissipation rate ϵ as measured by the thermosonde and the spectral width method, respectively.

measurements of spectral width can be approximated as (cf. Equation 7.30)

$$\sigma_{gw}^2 = \int_0^{2\pi/L_B} \left(1 - \|F(m)\|^2\right) \left(\Sigma_h(m) \sin^2 \alpha + \Sigma_w(m) \cos^2 \alpha\right) \mathrm{d}m, \tag{8.7}$$

where $\Sigma_h(m)$ and $\Sigma_w(m)$ are, respectively, the variance spectra of horizontal and vertical wind fluctuations, α is the zenith angle of the beam,

$$F(m) = \exp\left(-\frac{m^2 \Delta r^2}{4 \ln 2}\right) \tag{8.8}$$

is the Fourier transform of the two-way beam illumination function for the vertical direction, and L_B the buoyancy length or outer scale, i.e. the vertical scale where the variance of the wind fluctuations is mainly due to buoyancy waves.

As only the horizontal wind fluctuations can be reliably obtained from radio sonde soundings, values for the vertical wind variance have to be estimated using gravity wave theory. *Fritts & VanZandt* [1993] provide a parameterization of gravity wave variance spectra separable in intrinsic frequency $\hat{\omega}$ and vertical wavenumber m. The ratio of horizontal to vertical variance at arbitrary wavenumber m can, thus, be obtained by integration of the two variance spectra over the allowed intrinsic frequency range as

$$\frac{\Sigma_h(m)}{\Sigma_w(m)} = \frac{\int_f^N \hat{\omega}^{-5/3} \left[1 + \left(\frac{f}{\hat{\omega}}\right)^2\right] \left[1 - \left(\frac{\hat{\omega}}{N}\right)^2\right] \mathrm{d}\hat{\omega}}{\int_f^N \hat{\omega}^{-5/3} \left(\frac{\hat{\omega}}{N}\right)^2 \left[1 - \left(\frac{f}{\hat{\omega}}\right)^2\right] \mathrm{d}\hat{\omega}}, \tag{8.9}$$

where f is the inertial frequency and N the buoyancy frequency. Figure 8.13 shows a contour plot of this ratio as a function of buoyancy frequency and latitude. Typical values for the buoyancy frequency are 0.01 rad s^{-1} in the troposphere and 0.02 rad s^{-1} in the stratosphere.

The variance spectrum $\Sigma_h(m)$ for horizontal wind fluctuations was obtained by Fourier transforming the horizontal wind from a radio sonde launch using a Hamming window over the height range from 1 to 9 km. Using a ratio of horizontal to vertical wind variance of 60, corresponding to the troposphere at the latitude of Adelaide, a height resolution Δr of 500 m (HWHM), and a zenith angle $\alpha = 14.5°$, the contribution of gravity waves to the spectral width was calculated as a function of the buoyancy

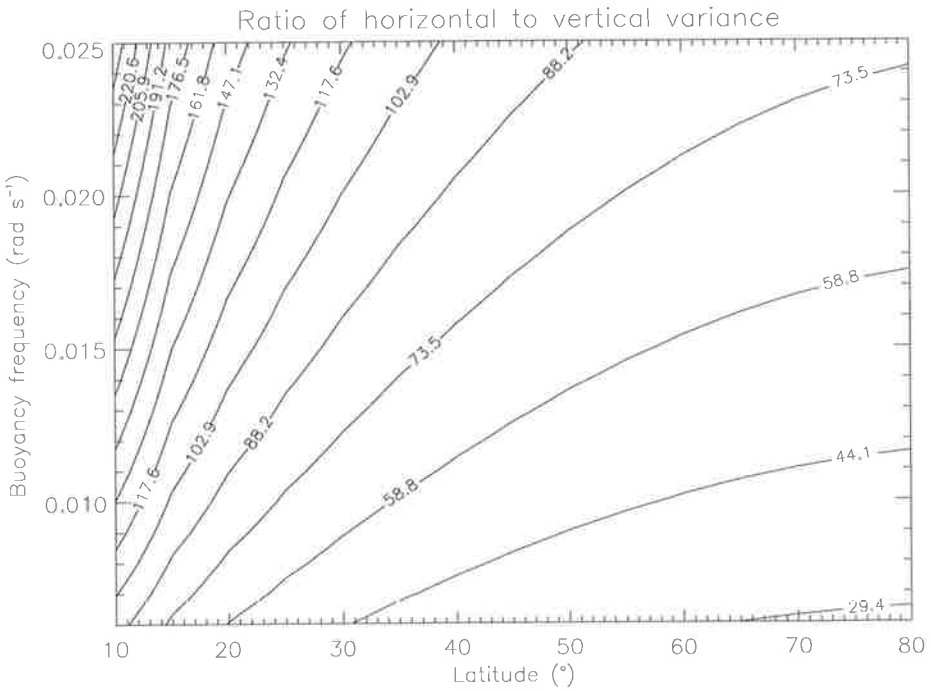

Figure 8.13: Contour plot of the ratio of horizontal to vertical wind variance as given by Equation 8.9

length L_B using Equation 8.7 (Figure 8.14). For a typical buoyancy length of 200 m [*Weinstock*, 1978] the variance due to gravity waves in the radar sampling volume is around 0.27 m^2s^{-2}, equivalent to an energy dissipation rate of around 10^{-3} m^2s^{-3} when Equation 7.33 is applied with $N = 0.01$ rad s^{-1}. This agrees approximately with the background value for $\bar{\epsilon}$ as obtained from the spectral width method (Figure 8.12).

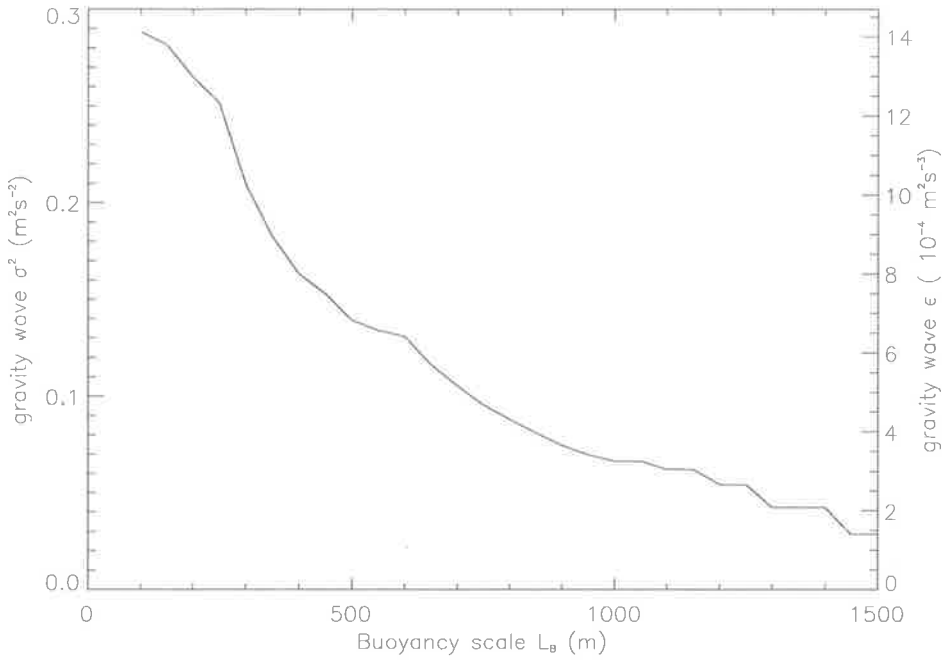

Figure 8.14: Spectral width due to gravity waves in the radar sampling volume computed using Equation 8.7. A ratio of horizontal to vertical wind variance of 60, a range resolution of 500 m (HWHM), and a zenith angle $\alpha = 14.5°$ were assumed. For the corresponding energy dissipation rate a buoyancy frequency of $N = 0.01$ rad s^{-1} was used.

8.3.4 Relation between turbulence layers and gravity wave field

8.3.4.1 Turbulent volume fraction

Usually no direct information about the turbulent volume fraction is available and it has to be estimated from accessible atmospheric parameters. A frequently applied model to estimate the volume fraction F from low-resolution vertical profiles of wind shear and buoyancy frequency was developed by *VanZandt et al.* [1978]. The authors superimposed small-scale fluctuations of a certain variance on the measured wind shear, and considered layers where the resulting Richardson number was less than 0.25 as turbulent. Their model, however, neglects small-scale fluctuations in buoyancy frequency and is not concerned with the physical origin of the small-scale fluctuations.

Physically somewhat more insightful models were proposed by *Bretherton* [1969*b*] and *Hines* [1991*a*], which relate the small-scale fluctuations to gravity wave activity. After an explanation of the basic principle behind these models, we will extend them to more realistic situations and compare them with our data.

The basic hypothesis of the models is that the observed fluctuations result from a spectrum of freely propagating, non-interacting gravity waves, superimposed on a background atmosphere slowly varying with height [*Hines*, 1991*a*]. The buoyancy frequency can then be expressed as

$$\begin{aligned} N^2 &= g\frac{\overline{\Theta}_z + \Theta'_z}{\overline{\Theta} + \Theta'} \approx g\frac{\overline{\Theta}_z + \Theta'_z}{\overline{\Theta}} \\ &= N_0^2\left(1 + \frac{\Theta'_z}{\overline{\Theta}_z}\right) = N_0^2(1+Z), \end{aligned} \tag{8.10}$$

where overline and prime indicate background and perturbation values, respectively, a subscribed z denotes vertical derivative, and N_0 is the background buoyancy frequency. The vertical wind shears, nondimensionalized via division by N_0, are

$$X = \frac{u_z}{N_0} \tag{8.11}$$

$$Y = \frac{v_z}{N_0} \tag{8.12}$$

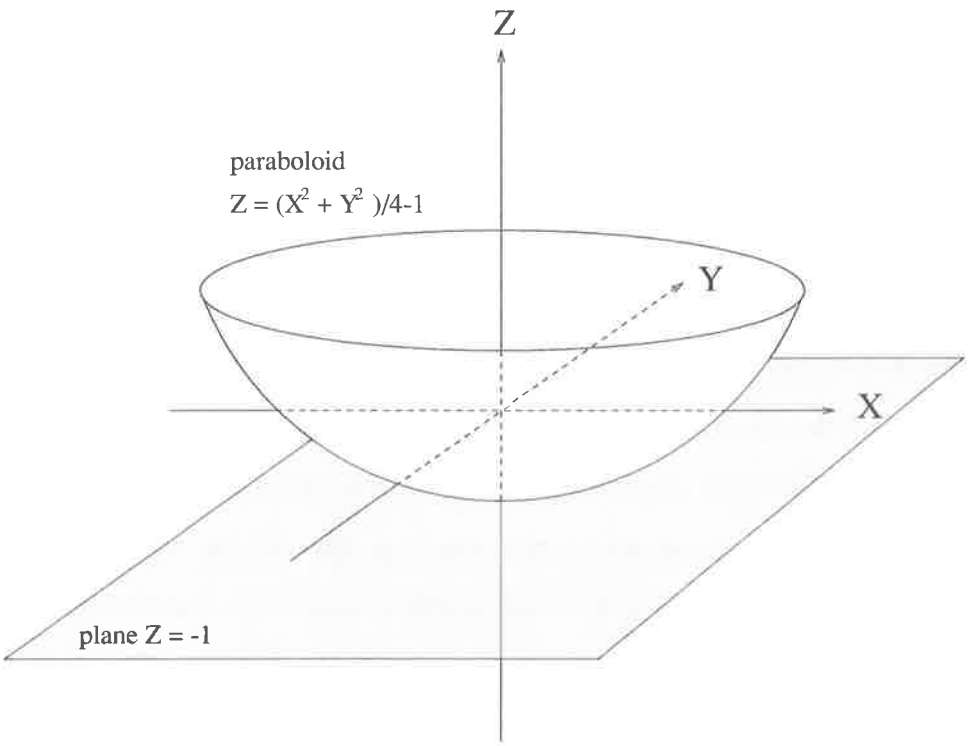

Figure 8.15: Illustration of statically and dynamically unstable regions in (X, Y, Z) space (after *Hines* [1991*a*]). Points within the paraboloid are stable, points between the paraboloid and the plane $Z = -1$ are dynamically unstable, and points below the plane $Z = -1$ are statically unstable.

and the gradient Richardson number is given by

$$Ri = \frac{N^2}{u_z^2 + v_z^2} = \frac{1 + Z}{X^2 + Y^2}. \tag{8.13}$$

For $Z < -1$, $Ri < 0$ and static instability occurs. For $-1 < Z < \frac{X^2+Y^2}{4} - 1$, on the other hand, $0 < Ri < 1/4$, and the atmosphere is dynamically unstable. The regions of static and dynamic instability in (X, Y, Z) space are illustrated in Figure 8.15.

If the fluctuations in wind shear and buoyancy frequency are due to gravity waves, then X, Y, and Z are related via the gravity wave polarization equations. In the case of a single monochromatic wave one obtains the instability criteria as described in *Hodges Jr.* [1967] and *Fritts & Rastogi* [1985]. *Bretherton* [1969*b*] and *Hines* [1991*a*], on the other hand, assumed a superposition of many independent waves. It is, then, possible to invoke the central limit theorem and treat X, Y, and Z as random variables

with a Gaussian probability distribution, i.e.

$$P_X(X)\mathrm{d}X = \frac{1}{\sqrt{2\pi}\sigma_X}\exp(-\frac{(X-X_0)^2}{2\sigma_X^2})\mathrm{d}X, \tag{8.14}$$

and equivalent for Y and Z. X_0 and Y_0 are the nondimensionalized vertical shears in background wind and $Z_0 = 0$. The vector (X, Y, Z) for the case of a single monochromatic gravity wave is then replaced by a probability density function $P(X,Y,Z) = P_X(X)P_Y(Y)P_Z(Z)$, corresponding to a probability cloud in Figure 8.15, and the probabilities for static and dynamic instabilities are given by

$$\begin{aligned} P_{\mathrm{st}} &= \int_{-\infty}^{-1} P_Z(Z)\mathrm{d}Z \\ &= 0.5[1-\mathrm{erf}(\frac{1}{\sqrt{2}\sigma_Z})], \end{aligned} \tag{8.15}$$

and

$$P_{\mathrm{dyn}} = \int_{-\infty}^{\infty}\mathrm{d}X\int_{-\infty}^{\infty}\mathrm{d}Y\int_{-1}^{S^2/4-1}\mathrm{d}Z P_X(X)P_Y(Y)P_Z(Z), \tag{8.16}$$

where $S^2 = X^2 + Y^2$ is the total nondimensionalized vertical wind shear.

The variances in X, Y, and Z are related through the gravity wave polarization relations and assumptions about dominant propagation directions. Applying $\sigma_S^2 = \sigma_X^2 + \sigma_Y^2 = \sigma_Z^2$, corresponding to waves with $f \ll \hat{\omega} \ll N_0$, and neglecting background wind shear, *Hines* [1991*a*] could also derive an analytic expression for P_{dyn} for an isotropic wave field. Because of the frequently observed preponderance of low-frequency waves [*Vincent*, 1984; *Sato*, 1994; *Nastrom et al.*, 1997], however, we believe that the assumption of such a hydrostatic wave regime is not adequate for our purpose. We, therefore, extended the model formulation of *Hines* [1991*a*] to accommodate the whole range of possible frequencies $f < \hat{\omega} < N$. Using the spectral parameterization of *Fritts & VanZandt* [1993] as described in Section 2.9.2, we can express the wind shear variance spectra of a gravity wave field as

$$s_S^2(m,\hat{\omega},\phi) = s_X^2(m,\hat{\omega},\phi) + s_Y^2(m,\hat{\omega},\phi) = \frac{m^2}{N_0^2}E(m,\hat{\omega},\phi)\delta_+\gamma. \tag{8.17}$$

Linearizing the adiabatic gas equation (Equation 2.5) yields

$$\Theta_t' = w'\overline{\Theta}_z \tag{8.18}$$

and, therefore,

$$Z = \frac{\Theta'_z}{\overline{\Theta}_z} = \frac{m}{\hat{\omega}} w'. \tag{8.19}$$

The variance spectrum of Z can, thus, be expressed in terms of the spectral variance of vertical perturbation velocity,

$$s_Z^2(m, \hat{\omega}, \phi) = \frac{m^2}{\hat{\omega}^2} E_w(m, \hat{\omega}, \phi) = \frac{m^2}{N_0^2} E(m, \hat{\omega}, \phi) \delta_-. \tag{8.20}$$

The relationship between the variance spectra of nondimensionalized vertical wind shear and Z is, thus,

$$s_Z^2(m, \hat{\omega}, \phi) = \frac{\delta_-}{\delta_+ \gamma} s_S^2(m, \hat{\omega}, \phi). \tag{8.21}$$

It is noteworthy that the ratio of s_Z^2 to s_S^2 in this model is independent of the vertical wavenumber m or any anisotropy of the spectrum. Only the dependency on intrinsic frequency $\hat{\omega}$ is important. This is due to the separability of the assumed spectrum in m, $\hat{\omega}$ and ϕ. For waves with $f \ll \hat{\omega} \ll N_0$ we obtain $s_Z^2(m, \hat{\omega}, \phi) \approx s_S^2(m, \hat{\omega}, \phi)$ in agreement with the assumptions of *Bretherton* [1969*b*] and *Hines* [1991*a*]. Note, however, that the probability of instability does depend on the anisotropy of the spectrum via the integration in Equation 8.16.

The ratio of σ_Z^2 to σ_S^2 can be computed by integrating Equation 8.21 over the energy spectrum, or, alternatively, by specification of a dominant intrinsic frequency in Equation 8.21. The dominant intrinsic frequency is the intrinsic frequency of a single, monochromatic wave with the specified ratio of σ_Z to σ_S. Figure 8.16 presents the ratio of σ_Z to σ_S for a spectrum of the form $\hat{\omega}^{-p}$, $\hat{\omega} = f \ldots 240\ f$, as a function of p together with the corresponding dominant frequency. For an exponent $p = -5/3$, as assumed in the parameterization of *Fritts & VanZandt* [1993], we obtain $\sigma_Z/\sigma_S = 0.77$, corresponding to a dominant intrinsic frequency of 2 f. The mean energy-weighted frequency for $p = -5/3$, on the other hand, is 10.7 f. Possible anisotropy of the wave spectrum can be incorporated in the model by different values for σ_X and σ_Y and rotation of the coordinate system, if necessary. Numerical integration of Equation 8.16 together with Equation 8.15 then yields the probability of instability for a given background atmosphere.

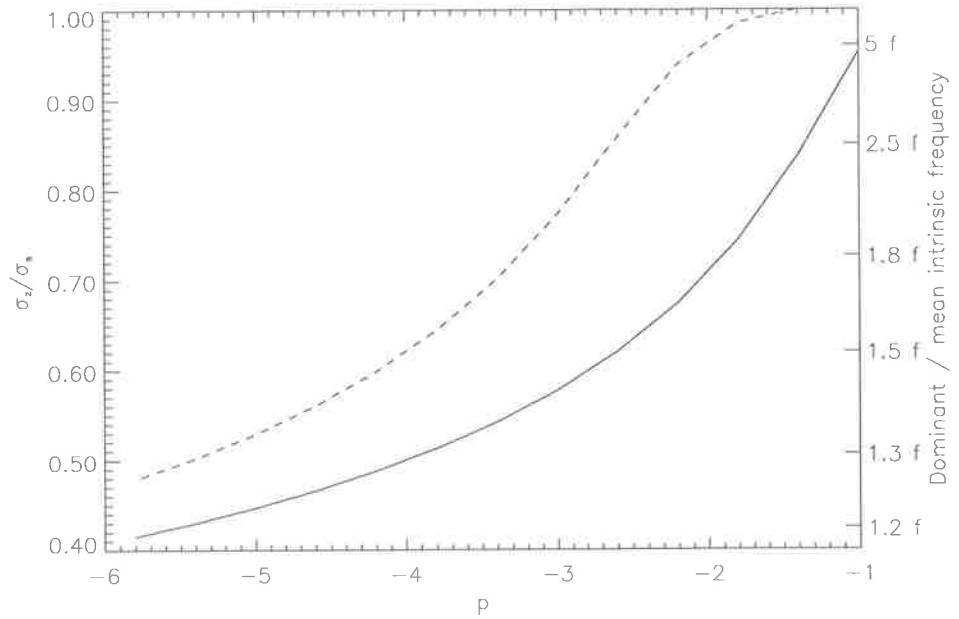

Figure 8.16: Ratio of σ_Z to σ_S as computed by integration of Equation 8.21 over a spectrum of the form $\hat{\omega}^{-p}$, $\hat{\omega} = f \ldots 240\ f$, as a function of p (solid line). The axis on the right handside presents the corresponding dominant intrinsic frequency for use in Equation 8.21. The dashed line indicates the mean energy-weighted intrinsic frequency.

To illustrate the effect of the dominant intrinsic frequency of the gravity wave field, probabilities for static and dynamic instability are presented in Figure 8.17 as a function of nondimensionalized vertical wind shear σ_S. Three isotropic wave fields with intrinsic frequencies of 1.2 f (solid line), 20 f (dotted line), and 220 f (dashed line), respectively, were assumed. With a buoyancy frequency $N_0 = 0.02$ rad s^{-1} $= 240f$, a value typical for the lower stratosphere over Adelaide, these correspond to ratios of σ_Z to σ_S of 0.4, 1.0, and 2.5, respectively. Vertical wind shears in the background atmosphere were taken to be zero in these calculations. The probability of static instability, $P_{\rm st}$, is dependent on σ_Z only (Equation 8.15). As the intrinsic frequency $\hat{\omega}$ of the wave field determines the ratio of σ_Z to σ_S (Equation 8.21), however, the graph for $P_{\rm st}$ as a function of σ_S is stretched or shrunk along the x-axis, depending on the choice of $\hat{\omega}$ (top diagram). The dependence of the probability for dynamic instability, $P_{\rm dyn}$, is somewhat more complicated (middle diagram), but can be understood using the picture of the probability cloud in Figure 8.15. For small $\hat{\omega}$ and, therefore, small σ_Z, the probability cloud is confined to close proximity of the $Z = 0$ plane and is, thus, rather dense. σ_X and σ_Y have to reach a certain value for a considerable part of the cloud to stretch into the volume between the paraboloid and the $Z = -1$ plane, i.e. the region corresponding to dynamic instability. The high density of the cloud leads to a strong increase of $P_{\rm dyn}$ once this threshold is reached. For large values of σ_Z, on the other hand, corresponding to large $\hat{\omega}$, the probability cloud stretches far to positive and negative Z values. Even for small σ_X and σ_Y values, parts of the cloud stretch into the region of dynamic instability, close to the $Z = -1$ plane. Due to its greater volume, however, the density of the cloud is strongly reduced. Increasing σ_X and σ_Y values, therefore, lead to only small increases in $P_{\rm dyn}$. Finally, the total probability of instability is presented in the bottom diagram. The existence of a background wind shear would shift the probability cloud along the $Z = 0$ plane. While this would influence the probability of dynamic instability, the probability of static instability would be unaffected.

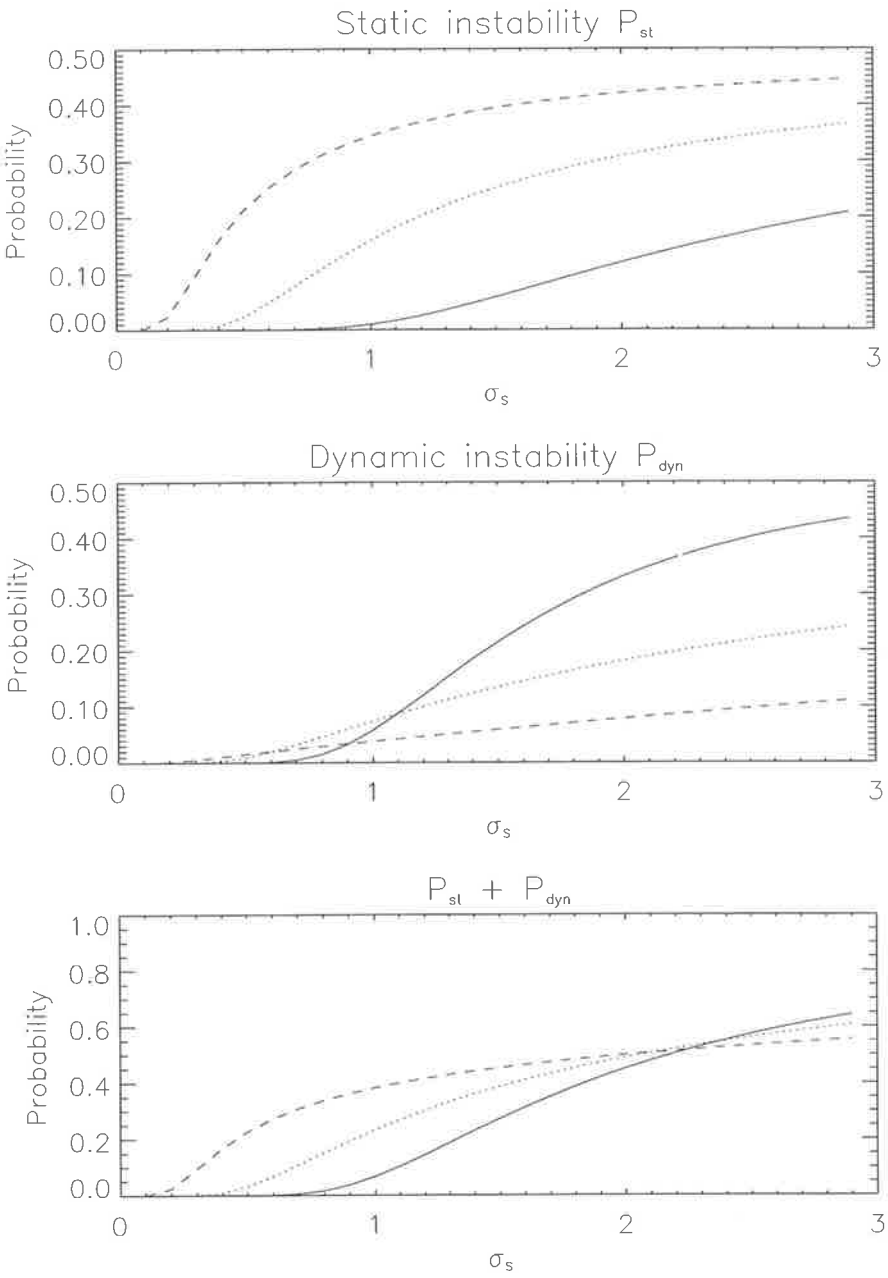

Figure 8.17: Probabilities of instability as a function of nondimensionalized vertical wind shear σ_S for an atmosphere without background wind shear. Three isotropic wave fields with intrinsic frequencies of 1.2 f (solid line), 20 f (dotted line), and 220 f (dashed line), respectively, were assumed. The buoyancy frequency was chosen as $N = 240f$, a value typical for the lower stratosphere over Adelaide.

Numerical models and experimental observations of turbulence often show an increase in the number of layers with low Richardson number Ri when the height resolution is increased [*Gage & VanZandt*, 1983; *Ericksen*, 1982]. This is not due to the increased height resolution per se, but due to the increased shear variance when fluctuations of smaller scale are taken into account. The extent to which σ_S is affected by the height resolution can be calculated from Equation 8.17. As $E(m, \hat{\omega}) \propto m^{-3}$ for m sufficiently large, and $s_S \propto m^2 E(m, \hat{\omega})$, we obtain $\sigma_S^2 \propto m^{-1}$. If experimental measurements of $\sigma^2_{S,\mathrm{meas}}$ account for vertical wave numbers in the range $m_l \ldots m_h$, then these measurements can be extrapolated to the range $m_L \ldots m_H$ by

$$\sigma_S^2 = \frac{\ln m_H - \ln m_L}{\ln m_h - \ln m_l} \sigma^2_{S,\mathrm{meas}}. \tag{8.22}$$

Figure 8.18 shows spectra of potential temperature and horizontal wind speed for the launch on 22.8.1998 at 10:15 UTC for heights between 7.5 and 18 km. The data were gridded to 20 m height resolution using cubic splines and Fourier transformed after multiplication with a Hamming window. While the slope for the potential temperature spectrum is fairly constant for wavelengths down to the minimum resolvable wavelength of 40 m (bottom diagram), the slope for the horizontal wind spectrum flattens for wavelengths less than about 150 m (top diagram). Fluctuations in horizontal wind speed on scales less than 150 m are, therefore, unlikely due to gravity waves and could lead to overestimates of σ_S if not treated properly.

To compare the sonde data with the model the vertical profiles of zonal and meridional winds and potential temperature were gridded to 20 m height resolution and filtered with a low pass filter with 150 m cutoff to include fluctuations due to gravity waves only. The filtered height profiles were then binned into 1 km height intervals. The observed probabilities of static and dynamic instability were computed as the fraction of height levels in the respective height bin with $Ri < 0$ and $0 < Ri < 1/4$, respectively, where the gradient Richardson number Ri was computed from the filtered profiles. The means of X and Y and the variances of X, Y, and Z were used to calculate the theoretical probabilities of instability for each height bin according to Equations

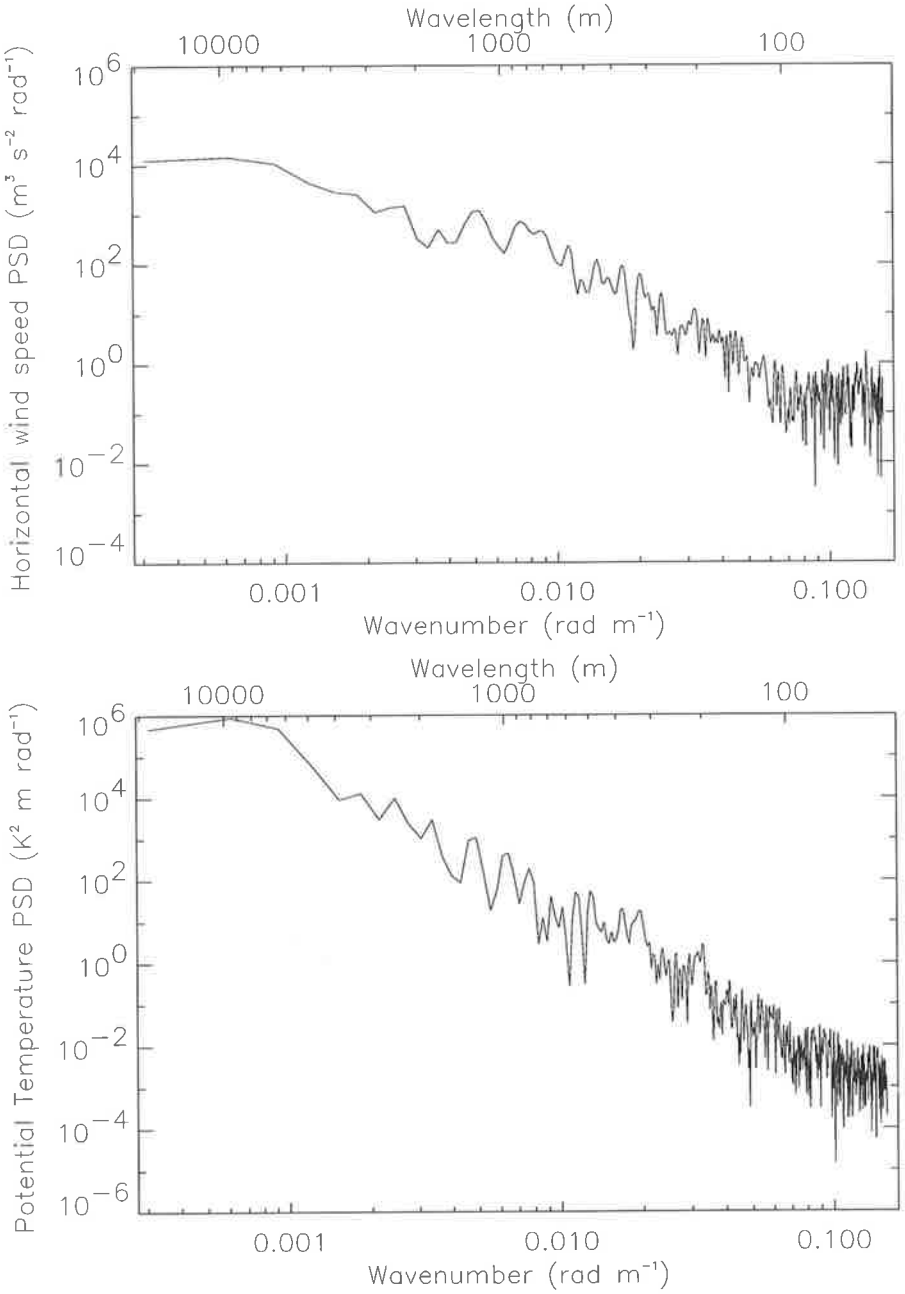

Figure 8.18: Power spectra for horizontal wind speed and potential temperature for the launch on 22.8.1998 at 10:15 UTC for heights between 7.5 and 18 km.

8.15 and 8.16, where we assumed an isotropic wave field with $\sigma_S^2 = \sigma_X^2 + \sigma_Y^2$. Comparisons between the sonde data and the model calculations are presented in Figure 8.19. The diagrams on the left handside show scatter plots of observed and theoretical probabilities of instability with a linear fit to the data indicated by the solid line. On the right handside of Figure 8.19 we present vertical profiles of the average observed and modeled probabilities of instability and of the average ratio of σ_Z to σ_S. The horizontal bars indicate the standard deviations of the respective variables. The plots reveal a good agreement between the observed and modeled instability probabilities. The ratio of σ_Z to σ_S is close to 0.4 throughout the lower atmosphere, corresponding to a dominant intrinsic frequency of around 1.2 f. The obtained values are significantly lower than the values expected for a frequency spectrum proportional to $\hat{\omega}^{-5/3}$ (cf. Figure 8.16).

Possible error sources which could lead to an underestimation of the inferred dominant frequency are systematic errors in the measurements of σ_S and σ_Z, due to different signal processing routines for wind and temperature measurements, for example, or deviations from our assumption of separability of the wave spectrum in $\hat{\omega}$ and m. On the other hand, it is also possible that the inferred ratio of σ_Z to σ_S does correspond to the physical wave field, and that the assumed spectral form proportional to $\hat{\omega}^{-5/3}$ underestimates the contribution of low-frequency waves. A corresponding preponderance of gravity waves with intrinsic frequencies close to the inertial frequency f was also found in other studies [*Vincent*, 1984; *Sato*, 1994; *Nastrom et al.*, 1997].

For such a low dominant frequency as deduced here, the velocity perturbations parallel and perpendicular to the horizontal wave propagation direction are almost equal in variance and a possible anisotropy in gravity wave propagation directions does not have to be examined any further. Application of the model with σ_Z set equal to the observed σ_S, corresponding to the assumption $f \ll \hat{\omega} \ll N_0$ made in *Bretherton* [1969*b*] and *Hines* [1991*a*], leads to significant deviations from the observed instability probabilities (Figure 8.20).

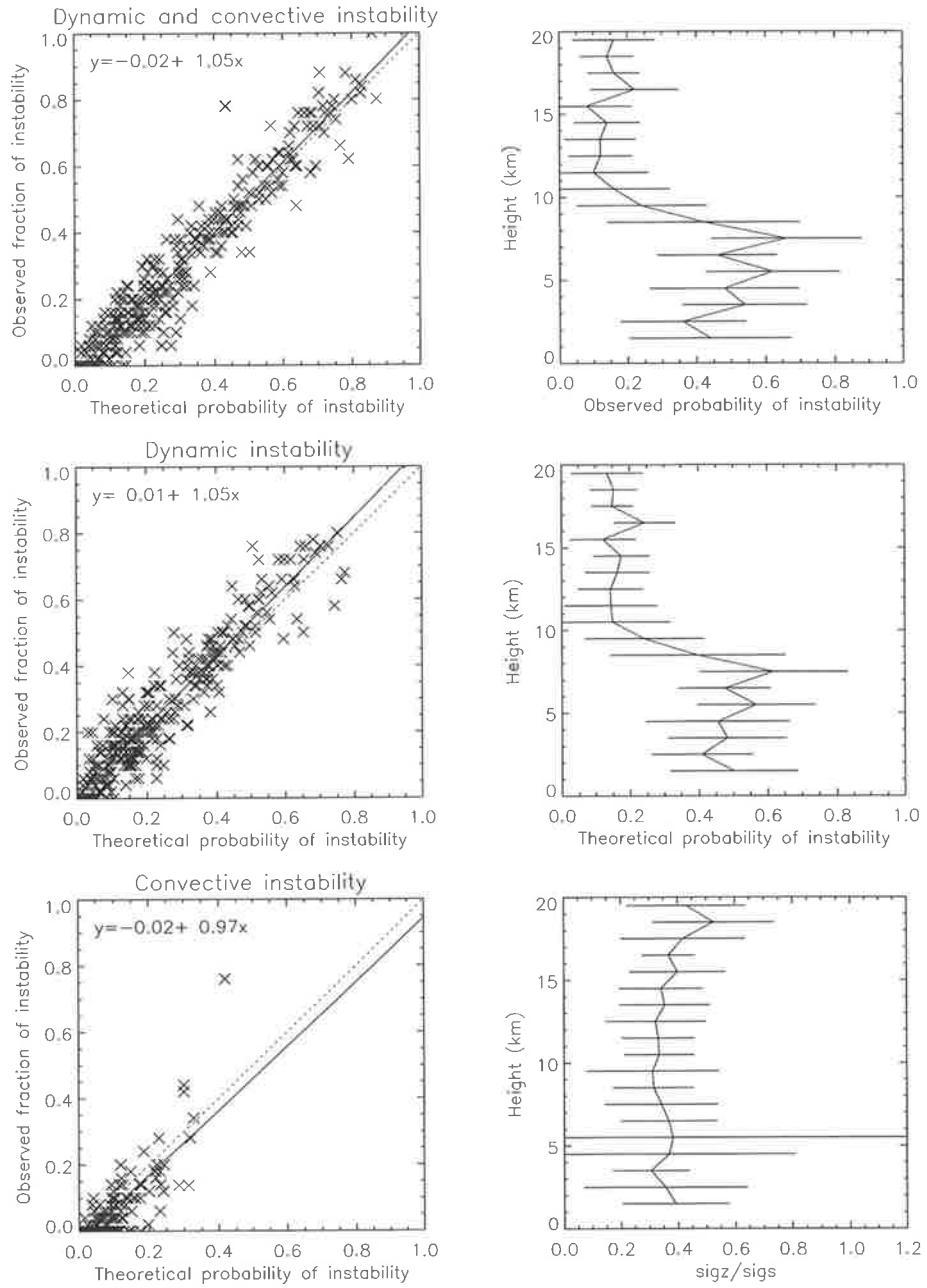

Figure 8.19: Left: Scatter plots of observed and theoretical probabilities of instability. The solid line indicates a linear fit to our data. Right: Vertical profiles of the average observed and modeled probabilities of instability and of the average ratio of σ_Z to σ_S. Horizontal bars indicate standard deviations.

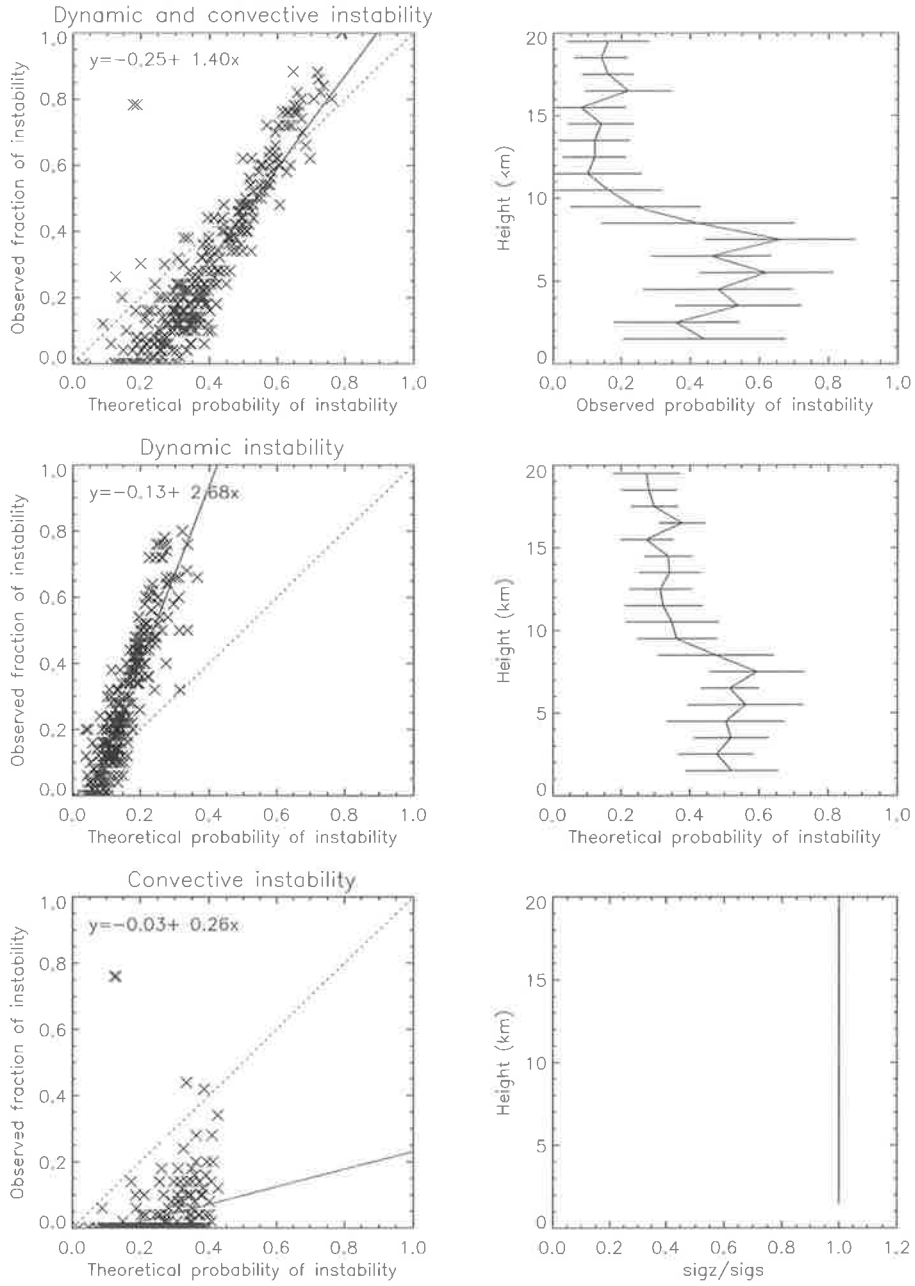

Figure 8.20: Same as Figure 8.19, but with σ_Z set equal to the observed σ_S.

8.3.4.2 Thickness and spacing of turbulent layers

The shape of the gravity wave spectrum as a function of vertical wavenumber m has no effect on the instability probabilities in our model. The width of the vertical wavenumber spectrum, however, determines over what length scales the wind and potential temperature fluctuations are correlated, respectively. The shape of the gravity wave spectrum as a function of vertical wavenumber m, therefore, affects the distributions of thickness and spacing of the turbulent layers. To test the hypothesis of turbulence generation due to gravity waves further, it is instructive to compare the observed thickness and spacing distributions with those generated by a model spectrum in a simulation.

For each of the thermosonde soundings ϵ_{sonde} and $\bar{\epsilon}_{\text{sonde}}$ were calculated according to Equation 8.5 with a height resolution of 20 m for the heights between 10 and 20 km. Layers with $\epsilon_{\text{sonde}} > \bar{\epsilon}_{\text{sonde}}$ were considered as turbulent and the distributions for layer thickness and spacing were computed. The parameters for the background atmosphere were obtained by lowpass filtering the vertical profiles of horizontal winds and potential temperature with a cutoff wavelength of 2000 m. Averages of σ_S and σ_Z were calculated from fluctuations with vertical scales between 2000 and 150 m and extrapolated to an effective height resolution of 20 m using Equation 8.22. In a Monte Carlo simulation we then generated vertical profiles of horizontal wind and temperature fluctuations of a gravity wave field with the given σ_S and σ_Z and a resolution of 20 m. The complex amplitude spectrum for gravity wave perturbations in zonal direction was constructed in Fourier (vertical wave number) space. We used the variance spectrum as derived by *Fritts & VanZandt* [1993],

$$E_u(m,\hat{\omega},\phi) = E(m,\hat{\omega},\phi)\left[\cos^2\phi + \left(\frac{f}{\hat{\omega}}\right)^2 \sin^2\phi\right]\gamma, \tag{8.23}$$

with variables defined as in Section 2.9.2 and $m^* = 2\pi/2000\text{m}$. The intrinsic frequency $\hat{\omega}$ was determined from Equation 8.21 (assuming $\hat{\omega} \ll N$) as

$$\hat{\omega} = \sqrt{\frac{1+(\sigma_Z/\sigma_S)^2}{1-(\sigma_Z/\sigma_S)^2}}f, \tag{8.24}$$

and phases and propagation directions were chosen randomly from a uniform distribution in $[0, 2\pi[$. The complex amplitude spectra for meridional wind and temperature perturbations were computed from the polarization relations 2.20. After Fourier transformation the obtained height profiles of horizontal wind and temperature perturbations were superimposed on the background atmosphere and the distributions of turbulent layer thickness and spacing were computed. We restricted ourselves to the height range from 10 to 20 km, as the values for the background buoyancy frequency N_0 and σ_S are fairly constant at these altitudes.

Figure 8.21 shows the distributions of turbulent layer thickness and spacing for all available soundings between 10 and 20 km altitude in histogram form (thin line), together with scaled distributions from the Monte Carlo simulation (thick lines). The solid, dotted, and dashed thick line correspond to vertical wavenumber spectra with slopes of -3, -3.5, and -2.5, respectively. One hundred realizations of the gravity wave spectrum were used for each sounding and spectral shape. For a slope of -3, simulation and observation agree rather well, especially for the thickness distribution. A fit to the horizontal wind speed spectra for wavelengths in the range between 150 and 2000 m revealed a slope of -3.0 ± 0.2 averaged over the 17 available soundings.

The shape of the gravity wave spectrum as a function of vertical wave number determines the distribution of thickness and spacing of the turbulent layers in height. Similarly, the time fractions during which turbulence is present or absent at a certain point in space are determined by the shape of the gravity wave spectrum as a function of frequency. Measurements with a high-resolution radar could provide information about the characteristics of this turbulence intermittency and allow a comparison of the observed temporal turbulence structure with observations. The present height resolution of the Buckland Park radar, however, is much too coarse to resolve single turbulence layers and, therefore, such a comparison is not feasible with the available radar data.

Nevertheless, we can show at least qualitative agreement of high-resolution radar observations of turbulence layers with a Monte Carlo simulation of a gravity wave field

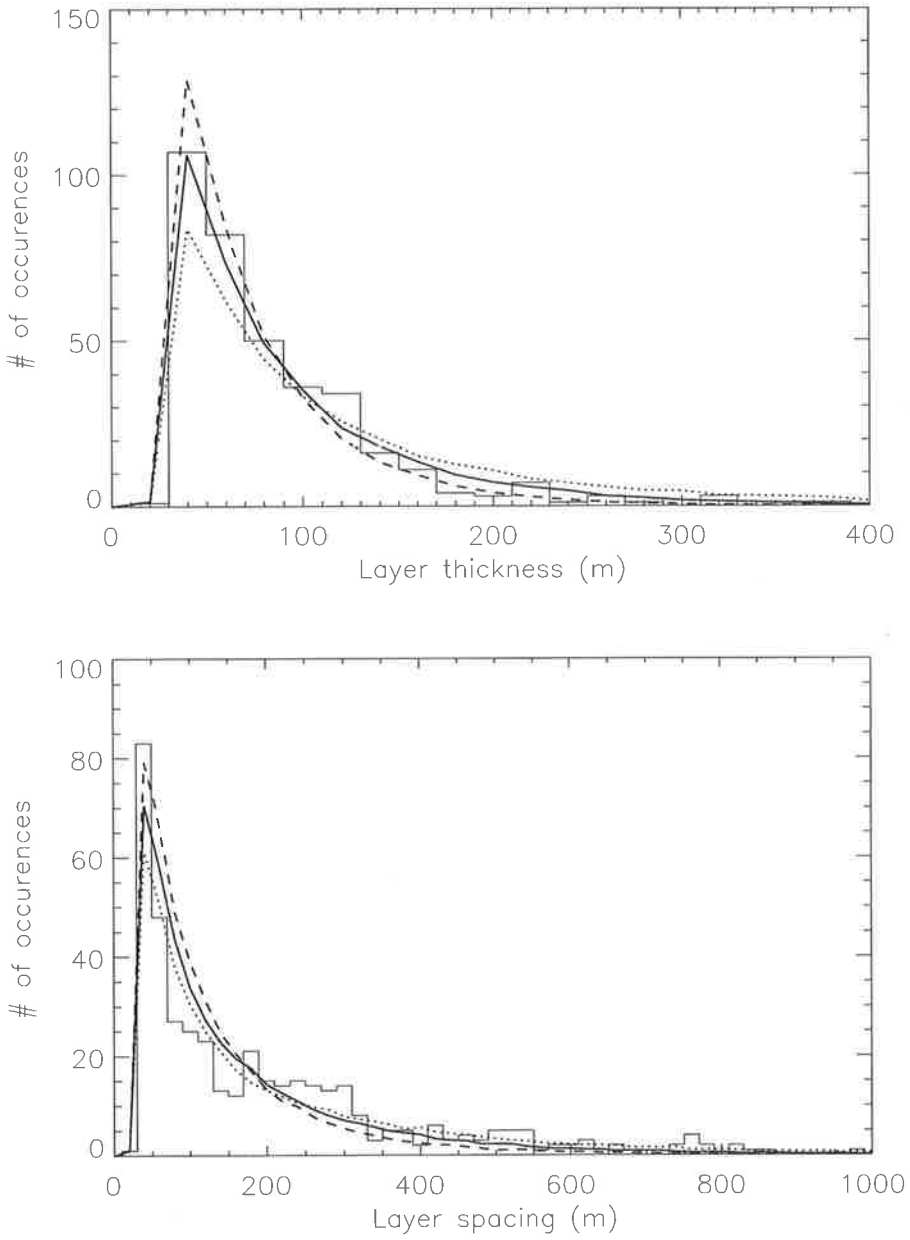

Figure 8.21: Distributions of turbulent layer thickness and spacing for the available soundings in histogram form (thin line), together with scaled distributions from the Monte Carlo simulations (thick lines). The solid, dotted, and dashed thick line correspond to vertical wavenumber spectra with slopes of -3, -3.5, and -2.5, respectively.

evolving in time. The complex amplitude spectrum for gravity wave perturbations in zonal direction was constructed in 2-dimensional Fourier space using the parameterization of *Fritts & VanZandt* [1993] (Equation 8.23). A height resolution of 20 m and a time resolution of 2 min was used, and phases and propagation directions were chosen randomly from a uniform distribution in $[0, 2\pi[$. After computation of the amplitude spectra for meridional wind and temperature perturbations using the polarization equations 2.20 and application of the inverse Fourier transform the obtained height profiles (as a function of time) were superimposed on the background atmosphere. We used a constant temperature gradient of -1Kkm^{-1} between 10 and 20 km corresponding to a mean buoyancy frequency of 0.019 rad s^{-1}. The meridional background velocity was set to zero and for the zonal component we chose a profile as depicted on the left-handside of Figure 8.22. The corresponding distribution of turbulence layers is shown in the diagram on the right-handside of Figure 8.22, where the black and grey regions correspond to locations of static and dynamic instability, respectively. Because of the upward energy propagation of the specified waves the turbulent layers are descending with time. The probability of instability is strongly enhanced at lower heights due to the increase in dynamic instability caused by the strong background shear. The modeled turbulence layers are qualitatively in good agreement with the high-resolution radar observations of stratospheric turbulence layers over Arecibo, Puerto Rico, by *Sato & Woodman* [1982*a*] (Figure 8.23). If the statistical distribution of the duration and temporal spacing of the turbulence layers at a constant height range was known, the slope p of the gravity wave frequency spectrum (Equation 2.49) in the model could be adjusted to test for quantitative agreement between model and observation.

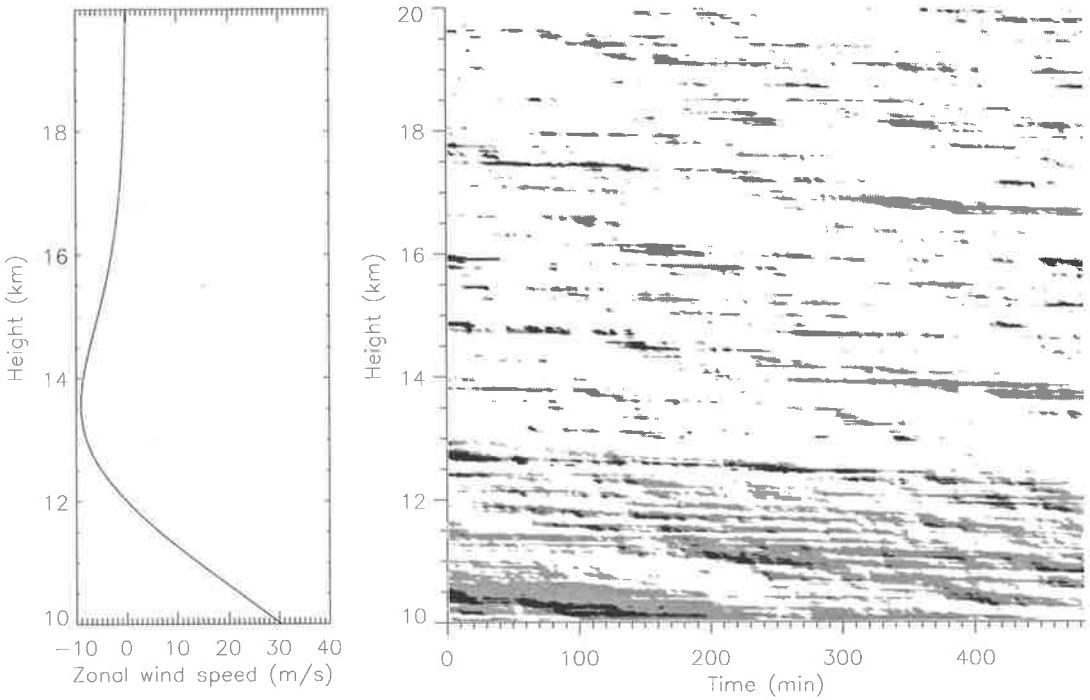

Figure 8.22: Profile of zonal background wind speed (left) and corresponding distribution of turbulence layers (right) as obtained from a Monte Carlo simulation. The black and grey shaded regions correspond to locations of static and dynamic instability, respectively.

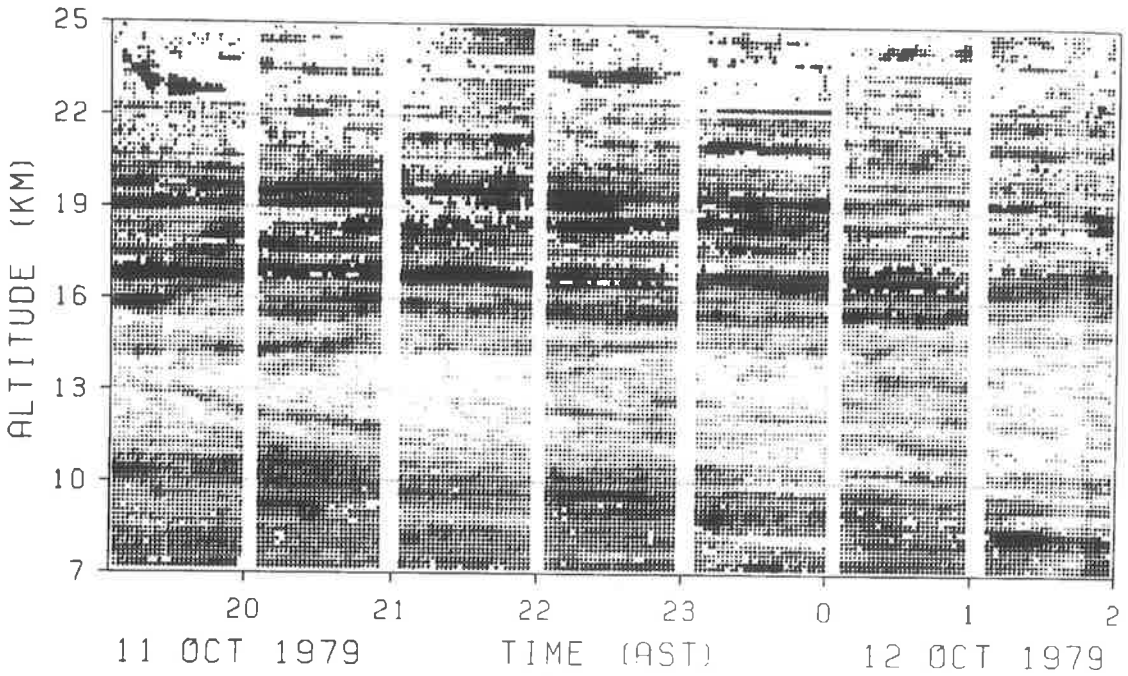

Figure 8.23: Time-height cross section of turbulence intensity in the lower stratosphere over Arecibo, Puerto Rico (from *Sato & Woodman* [1982*a*]).

8.4 Summary

We compared measurements of wind and turbulence by radar and thermosonde during a six day campaign in August 1998. Radar measurements of horizontal wind speed and direction yield good agreement with results obtained by the thermosondes, both for Doppler and Spaced Antenna modes.

After calibration of the radar system values for backscattered power could be converted to averages of the refractive index structure function constant $\overline{C_n^2}$ in the radar sampling volume. Comparison with in-situ measurements of C_n^2 by the thermosondes revealed reasonable agreement between the two methods.

Knowledge of the background buoyancy frequency N and the potential refractive index gradient M also allowed the computation of the energy dissipation rate $\bar{\epsilon}$ for both thermosonde and radar measurements. Using the turbulent volume fraction in the radar sampling volume, F, as a fitting parameter, reasonable agreement between the sonde and radar measurements could be achieved. Likely reasons for the slight deviations between the value of F obtained from the fit and the observed turbulent volume fraction were given.

To explore the relationship between the observed turbulence layers and the present gravity wave field theoretical instability probabilities were computed from observed gravity wave parameters and compared with the observed turbulent volume fraction. Furthermore, a Monte Carlo simulation was applied to model the distributions of turbulent layer thickness and spacing for the observed background atmosphere. The observations could be well reproduced by the models showing that the observed structure of turbulent layers in height is consistent with the generation of turbulence by a gravity wave field superimposed on the background atmosphere.

Chapter 9

Stratospheric inertio gravity waves: A case study

9.1 Introduction

In this case study we use the radar data obtained with the Buckland Park VHF radar during the refractive index turbulence campaign in August 1998 to infer the parameters of an inertio gravity wave detected in the lower stratosphere. The availability of numerical model data from the LAPS model of the Australian Bureau of Meteorology [*Puri et al.*, 1998] allows a qualitative comparison of the proposed generation mechanism with the model of *O'Sullivan & Dunkerton* [1995].

Inertio gravity waves are commonly observed in the upper troposphere and lower stratosphere using balloons [*Thompson*, 1978; *Cadet & Teitelbaum*, 1979] and radars [*Sato & Woodman*, 1982*b*; *Barat*, 1983; *Hirota & Niki*, 1986; *Cornish & Larsen*, 1989; *Yamanaka et al.*, 1989; *Thomas et al.*, 1992; *Maekawa et al.*, 1984; *Sato*, 1994; *Cho*, 1995; *Thomas et al.*, 1999]. The observed waves show typical vertical wavelengths of around 1 to 5 km and periods of several hours. Hodograph analysis typically reveals upwards energy propagation in the lower stratosphere, a much reduced downwards energy propagation below the tropopause, and a preference for meridional propagation, suggestive of a zonally aligned source at around tropopause level [*Hirota & Niki*,

1986; *Yamanaka et al.*, 1989; *Sato*, 1994; *Thomas et al.*, 1992].

Increased gravity wave activity has often been connected with nearby synoptic weather systems [*Sato*, 1989; *Sato*, 1993; *Chan et al.*, 1991; *Thomas et al.*, 1992; *Eckermann & Vincent*, 1993]. While a large part of this wave activity is attributed to high-frequency gravity waves generated by moist convection and shear instabilities within frontal zones, geostrophic adjustment of the flow as it relaxes to a balanced state is expected to launch low-frequency inertio gravity waves [*O'Sullivan & Dunkerton*, 1995; *Fritts & Luo*, 1992; *Luo & Fritts*, 1993].

9.2 Radar data

The radar data used in this chapter is identical with the data used in Chapter 8, and the reader is referred to Section 8.1.1 for more details. Figure 9.1 shows the hourly averaged zonal and meridional radar winds during the campaign in August 1998. The winds were calculated from the radial velocities of the East and North beam of the Buckland Park VHF radar at a zenith angle of 14.5°. The vertical velocities were small enough to be neglected in the calculations. The dashed line illustrates the height of the tropopause as obtained from operational radiosonde soundings at Adelaide airport, 40 km south of Buckland Park. The diagrams illustrate a strong eastward jet with wind speeds reaching up to 60 ms^{-1} at a height of 12 km during the night between August, 23rd and 24th. During the 24th and 25th of August, the winds in that height region turn counterclockwise until the jet is aligned in north-south direction at the 26th of August. The rapid adjustment of the jet leads to unbalanced winds, and the consequent geostrophic adjustment of the winds can act as a generation mechanism for inertio-gravity waves.

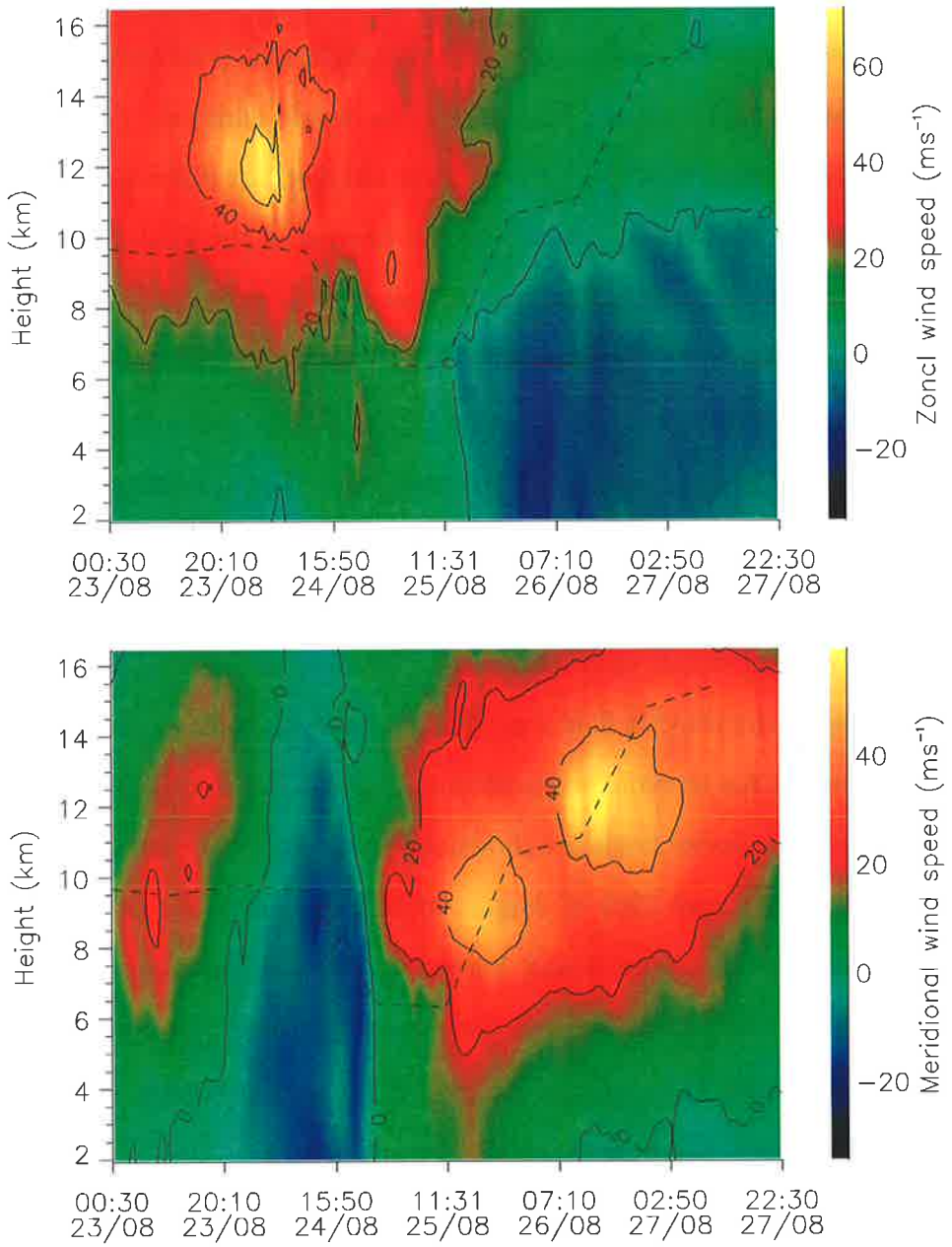

Figure 9.1: Hourly averaged zonal and meridional wind fields. Missing data points have been linearly interpolated over. The dashed line indicates the tropopause height.

9.3 Wind perturbations

The reasonable resolution of the radar data in time and height allows for filtering in frequency and vertical wavelength to reveal the possible existence of gravity waves in the observed wind field. In analogy to Chapter 3, two-dimensional wavelet analysis could be used to separate wave packets not only in height and (vertical) wave number, but also in time and (ground-based) frequency. This would eliminate the possibilty of multiple wave packets with identical vertical wave number but different ground-based frequencies in a single hodograph, which was still present in the analysis technique in Chapter 3. For simplicity, however, we here choose a two-dimensional bandpass filter in height and time with center wave numbers and frequencies determined heuristically to result in an easily detectable wave packet. Figure 9.2a presents schematically the bandpass filter applied to the hourly averaged wind field. The shaded areas in the four quadrants present the vertical and temporal scales that are passed by the filter. The filter was constructed from Butterworth filters with -3 dB cutoff frequencies of $2\pi/12$h and $2\pi/24h$ and vertical cutoff wave numbers of $2\pi/5$km and $2\pi/1$km. Outliers and missing data points in the velocity field were linearly interpolated over and the data was padded in height and time to avoid wrap-around effects in the Fourier transform. The resulting perturbation velocity fields are shown in Figure 9.3. Wave activity can clearly be identified on the 24th and 25th of August at heights above the tropopause. The pattern of amplitude troughs and peaks, however, indicates the presence of multiple waves in that region, with upwards and downwards directed (ground-based) phase velocities. The wave trains that are present have to be separated before an analysis of the wave parameters from the hodograph can be attempted.

While rotary spectra allow a decomposition of the wave field into clockwise and counterclockwise rotating, circular polarized wave components, an identification of these components as different physical waves is usually not possible, as every elliptical polarized wave can be decomposed into clockwise and counterclockwise rotating circular polarized components. A decomposition of the wave field into two components with

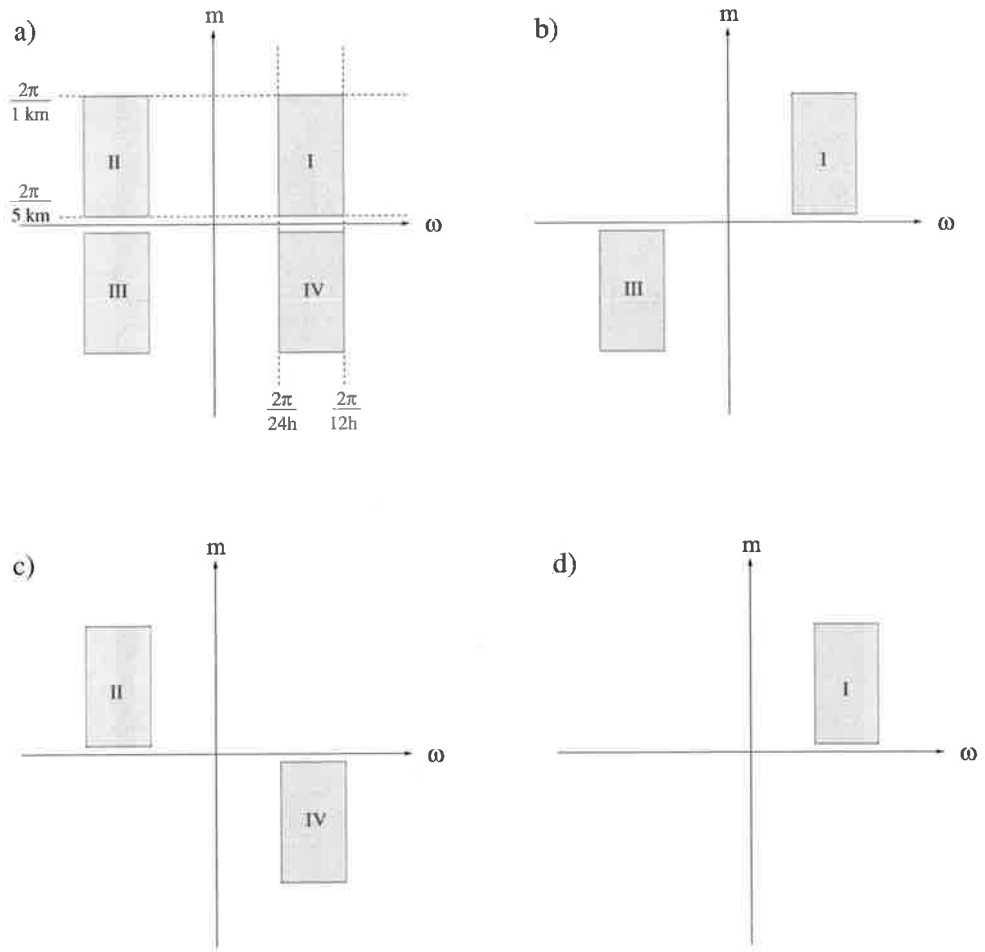

Figure 9.2: Schematic illustration of several bandpass filters in the frequency-wave number domain. Shaded areas describe the vertical and temporal scales that are passed by each filter.

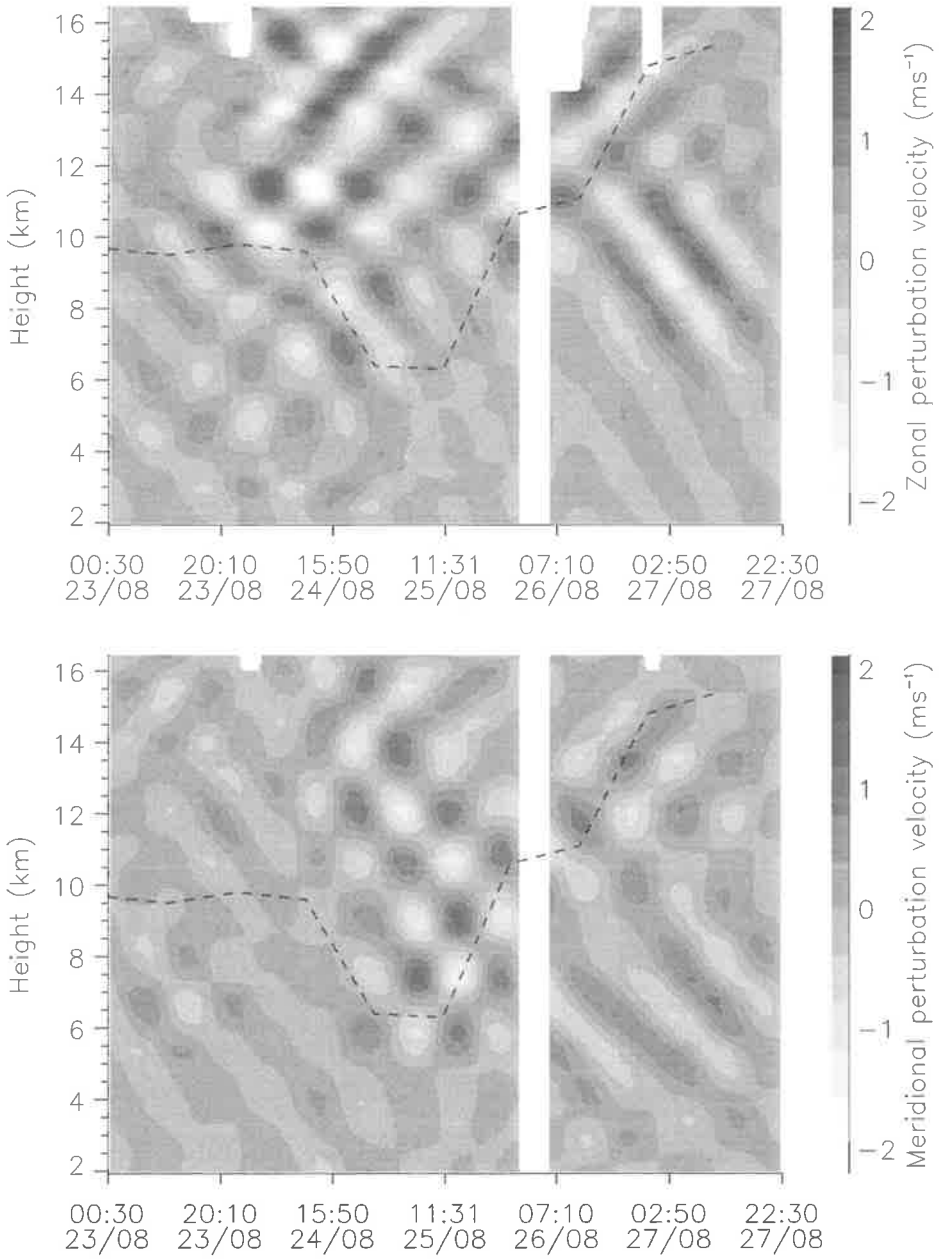

Figure 9.3: Zonal and meridional perturbation velocity fields for the wind fields in Figure 9.1. White areas correspond to gaps in the radar data. Only perturbations with vertical scales between 1 and 5 km and temporal scales between 12 and 24 hours were considered (filter a in Figure 9.2). The dashed line indicates the tropopause height.

upward and downward propagating phases, on the other hand, very likely corresponds to different physical waves and seems more appropriate. We adopt the convention of a positive intrinsic frequency $\hat{\omega}$, and define a negative vertical wavenumber m for waves propagating energy upwards. While the intrinsic vertical phase speed, $\hat{c}_z = \hat{\omega}/m$, is always directed opposite to the intrinsic vertical group velocity, $\hat{c}_{g,z}$, this is not always true for the ground-based vertical phase velocity $c_z = \omega/m$. The Doppler-shift between ω and $\hat{\omega}$ (Equation 4.3) leads to a sign of the ground-based frequency ω as illustrated in Figure 9.4. For $\omega < 0$ the ground-based vertical phase propagation is in the same direction as the (intrinsic) energy propagation of the wave packet.

A separation into waves with upward and downward ground-based phase propagation is achieved by using the filters illustrated in Figure 9.2b and c, respectively. Figure 9.5 shows the zonal and meridional perturbation velocity fields for upwards directed ground-based phase propagation, where now only a single wave packet is evident in the region of interest.

To calculate the vertical wavenumber m and ground-based frequency ω of the wave packet we computed the so-called instantaneous wavenumber and frequency [*Cohen*, 1995]. The instantaneous wavenumber m and frequency ω of a signal are defined as the derivative of the phase $\phi(z,t)$ of the signal by height, $m(z,t) = \partial\phi(z,t)/\partial z$, and time, $\omega(z,t) = \partial\phi(z,t)/\partial t$, respectively. The phase of a real signal can be obtained by adding an imaginary function to the signal that is 90° phase-shifted with respect to the original signal, i.e. its Hilbert transform, and defining the argument of the resulting complex function as the phase. The definition of the instantaneous frequency and wavenumber is only meaningful for signals whose magnitude is varying much slower than its phase [*Cohen*, 1995]. In our case this is ensured by the choice of the filter parameters. The filtering and extension of the signal to a complex function can be achieved simultaneously by the use of a filter function with a pass band restricted to positive wave numbers, for example (filter d in Figure 9.2). Application of such a filter to a real function yields a complex result, with the real part the filtered signal and the

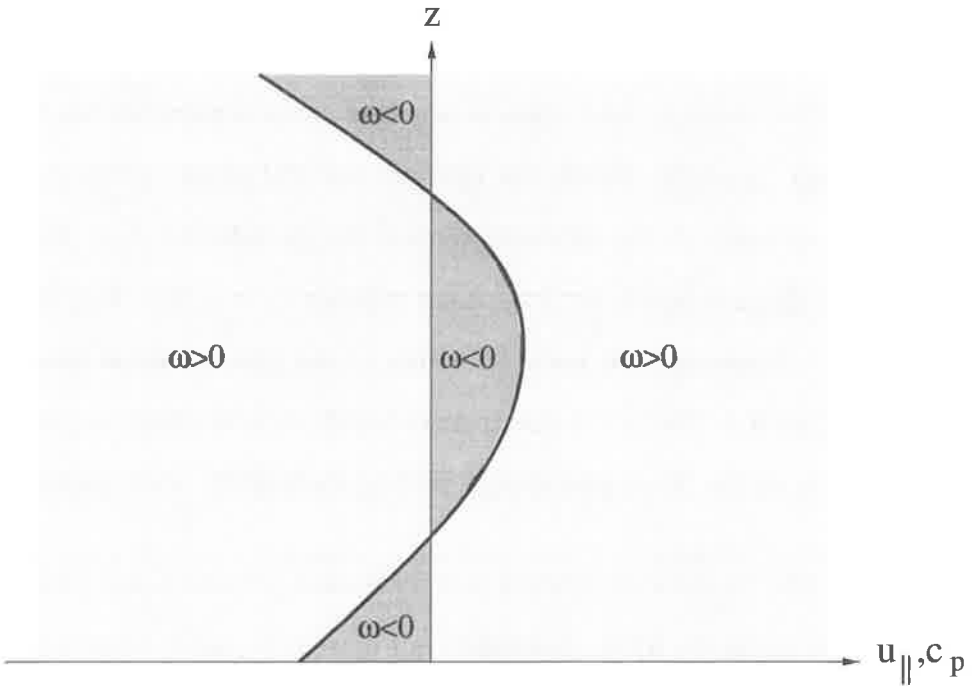

Figure 9.4: Sign of the ground-based frequency ω. The thick line indicates the background wind speed parallel to the intrinsic wave propagation direction, i.e. parallel to $\mathbf{k_h}$. Waves with ground-based horizontal phase speeds c_p as indicated by the lightly shaded areas have $\omega > 0$, while waves with phase speeds as indicated by the darkly shaded regions have $\omega < 0$.

imaginary part its 90° phase-shifted version.[1]

[1] As only half of the Fourier components are used in the transformation, the result has to be multiplied by a factor of 2 to yield the correct amplitudes.

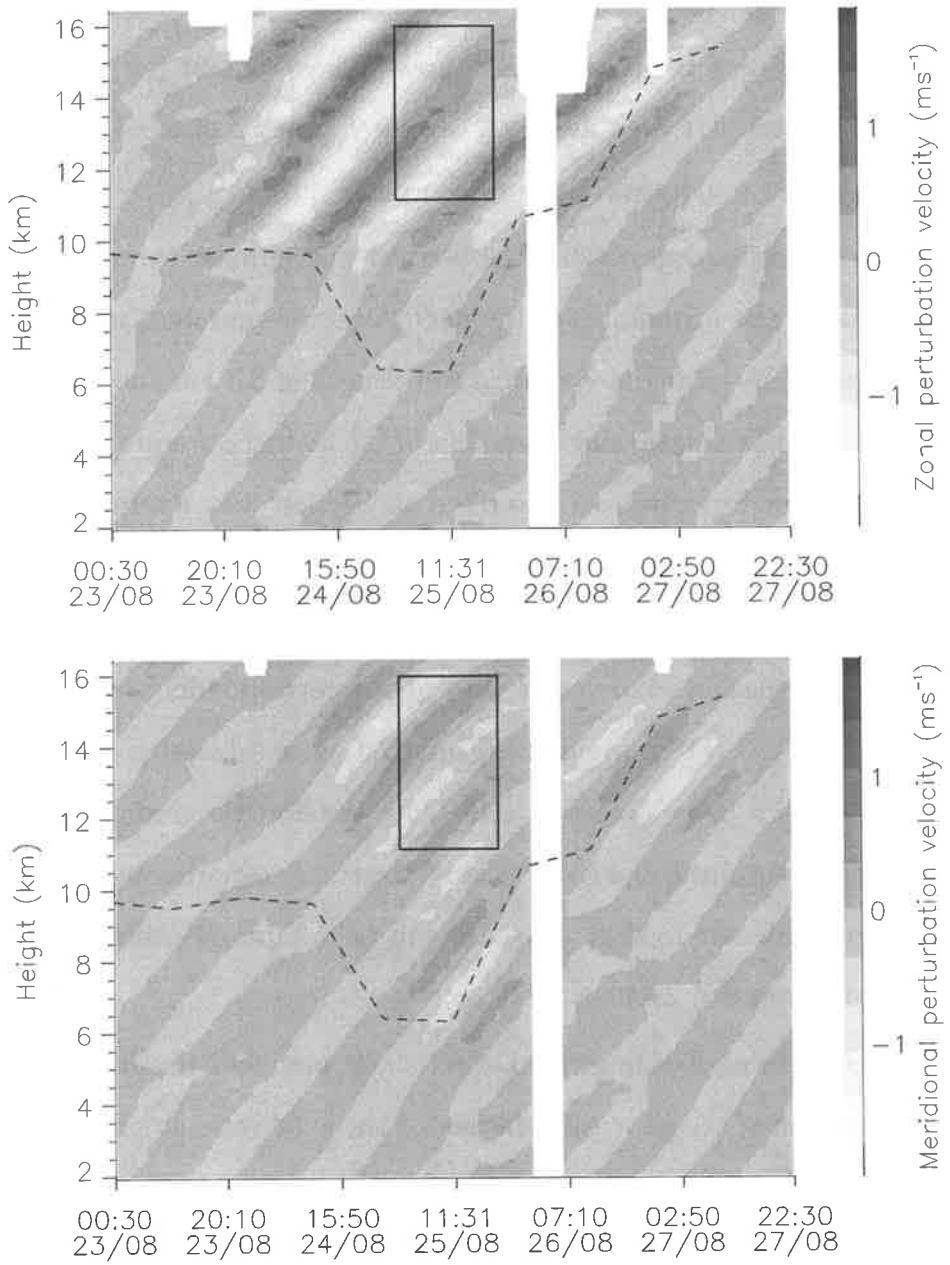

Figure 9.5: Zonal and meridional perturbation velocity fields for the wind fields in Figure 9.1. White areas correspond to gaps in the radar data. Only upwards phase propagating perturbations with vertical scales between 1 and 5 km and temporal scales between 12 and 24 hours were considered (cf. filter b and d in Figure 9.2). The dashed line indicates the tropopause height. The wave packet of interest is bordered.

9.4 Gravity wave parameters

We restrict ourselves to the analysis of the gravity wave packet in the height range from 11 to 16 km between 2:00 and 18:00 UTC on August, 25th, 1998. This region was chosen as it clearly shows the presence of a gravity wave packet (cf. Figure 9.5) and the background atmosphere does not show strong variations of wind speed in height or time so that simple gravity wave theory can be applied.

The ground-based frequency ω and the vertical wavenumber m were computed as the average value of the instantaneous frequency and wavenumber, respectively, over the region of interest, resulting in a vertical wavelength of 3.4 km and a ground-based period of 19.7 h. The axial ratio and alignment of the hodograph were calculated using the Stokes parameter formalism as described in Section 3.5, where the hodograph was constructed from all data points of meridional and zonal wind velocity in the analyzed region (Figure 9.6). The hodograph shows a counterclockwise rotation of the horizontal perturbation wind vector with height corresponding to upward energy propagation, i.e. $m < 0$. From the upward directed ground-based phase speed of the wave packet, $c_z = \frac{\omega}{m} > 0$, we obtain $\omega < 0$. Once the horizontal alignment direction of the hodograph is obtained, the horizontal background velocities and vertical shears parallel and perpendicular to that direction can be computed using the coordinate transformation in Equation 3.15.

In the case of non-negligible vertical wind shear perpendicular to the horizontal propagation direction of the wave the relation for the axial ratio axr of the hodograph ellipse is modified to [*Kunze*, 1985; *Sato*, 1994]

$$\frac{1}{axr} = \| \frac{f}{\hat{\omega}} - \frac{k_h}{m\hat{\omega}} \frac{\mathrm{d}v_\perp}{\mathrm{d}z} \|, \tag{9.1}$$

where $\frac{\mathrm{d}v_\perp}{\mathrm{d}z}$ is the vertical wind shear perpendicular to the wave propagation direction. The second term on the right hand side of Equation 9.1 is due to the vertical motion induced by the gravity wave, which raises and lowers the atmosphere together with its background wind field and associated shears [*Hines*, 1988*c*]. Equation 9.1 can be

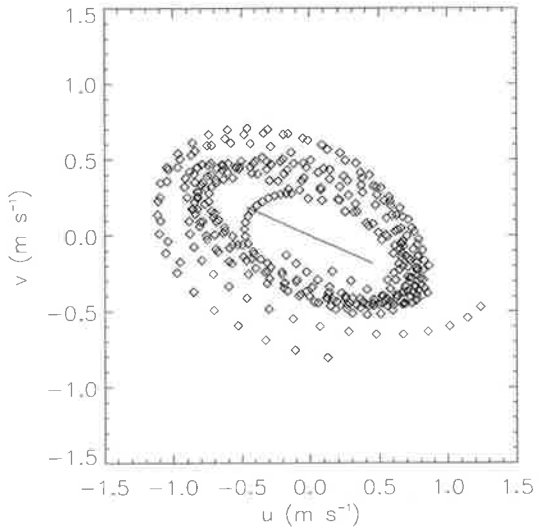

Vertical wavelength : 3.42 km
Ground-based period : −19.7 h
Direction : 112
Axial ratio : 2.39
Intrinsic frequency (f) : 1.71
Ground-based frequency (f) : −1.07
Horizontal wavelength (km): −437.60
Inferred N (rad/s) : 0.017
$U_{parallel}$ (m/s) : 16.2
$V_{perpendicular}$ (m/s) : 27.3
$dU_{parallel}/dz$ (1/s) : 0.0012
$dV_{perpendicular}/dz$ (1/s) : −0.0031

Figure 9.6: Hodograph of the gravity wave packet indicated in Figure 9.5 and inferred background and wave parameters.

solved simultaneously with the equation for the Doppler-shift,

$$\hat{\omega} = \omega - k_h u_{\parallel}, \tag{9.2}$$

to yield $\hat{\omega}$ and k_h. If we assume that the transverse background shear is not large enough to alter the sense of rotation of the hodograph, then the second term on the right hand side of Equation 9.1 does not change the sign of the expression within the modulus sign. Taking into account that $f < 0$ in the southern hemisphere the expression within the modulus sign is assumed to be negative and we obtain

$$\hat{\omega} = \frac{f - \frac{\omega}{u_{\parallel} m} \frac{\mathrm{d}v_{\perp}}{\mathrm{d}z}}{-\frac{1}{axr} - \frac{1}{u_{\parallel} m} \frac{\mathrm{d}v_{\perp}}{\mathrm{d}z}} \tag{9.3}$$

and

$$k_h = \frac{\omega - \hat{\omega}}{u_{\parallel}}. \tag{9.4}$$

Note that the knowledge of the ground-based frequency allows us to deduce all wave parameters directly from the radar wind measurements without the need for an estimate of the background buoyancy frequency N. The dispersion relation in the Boussinesq

approximation for a wave with transverse vertical wind shear [*Sato*, 1994; *Thomas et al.*, 1999],

$$\hat{\omega} = f^2 + \frac{N^2 k_h^2}{m^2} - 2f\frac{k_h}{m}\frac{\mathrm{d}v_\perp}{\mathrm{d}z}, \tag{9.5}$$

can then be used to verify the calculations by comparing the inferred buoyancy frequency with the observed value. In the case of the observed gravity wave packet, the buoyancy frequency inferred from the dispersion relation Equation 9.5 (cf. Figure 9.6) agrees well with the average buoyancy frequency of 0.018 rad s^{-1} observed in the analyzed height range for the radiosonde launch at 11:09 UTC at Adelaide airport.

The radar height resolution or 1 km (FWHM) is of the same order of magnitude as the observed vertical wavelength and results in an attenuation of the measured perturbation velocities. If we assume a Gaussian radar pulse with half width half maximum Δr, then a perturbation with vertical wavenumber m will be attenuated by a factor $\exp(-\frac{m^2\Delta r^2}{4\ln 2})$ in amplitude. In our case of a vertical wavelength of 3.4 km this corresponds to an amplitude attenuation factor of 0.73, resulting in a peak horizontal perturbation amplitude parallel to the intrinsic wave propagation direction of 1.7 ms^{-1}.

Knowledge of the wave amplitude together with the intrinsic frequency and the background buoyancy frequency can be applied to infer the momentum flux carried by the wave packet. Using the polarization relations 2.20 the momentum flux in wave propagation direction can be expressed as

$$\overline{u'_\parallel w'} = \frac{\hat{\omega}}{N}\sqrt{\frac{1 - f^2/\hat{\omega}^2}{1 - \hat{\omega}^2/N^2}}\overline{u'^2_\parallel}, \tag{9.6}$$

resulting in a momentum flux $\overline{u'_\parallel w'} = 0.01$ $m^2 s^{-2}$.

The wave packet propagates energy with an intrinsic horizontal group velocity of 7.8 ms^{-1} toward 292° and a vertical group velocity of 0.06 ms^{-1}. Using the background parameters as indicated in Figure 9.6 we can determine the ground-based horizontal group velocity as 28.6 ms^{-1} toward 39° and the ground-based zonal phase velocity as 6.3 ms^{-1} toward 112°. The inferred wave parameters are summarized in Table 9.1.

Vertical wavelength	3.4 km
Ground-based period	-19.7 h
Ground-based frequency	-1.06 f
Intrinsic propagation direction	292°
Intrinsic frequency	1.71 f
Horizontal wavelength	437.6 km
Intrinsic horizontal group velocity, $\hat{\mathbf{c}}_{\mathbf{gh}}$	7.8 ms^{-1}/292°
Ground-based horizontal group velocity, $\mathbf{c}_{\mathbf{gh}}$	28.6 ms^{-1}/39°
Vertical group velocity, c_{gz}	0.06 ms^{-1}
Ground-based horizontal phase velocity, $\mathbf{c}_{\mathbf{ph}}$	6.3 ms^{-1}/112°
Wave amplitude, $u'_{\parallel}$	1.7 ms^{-1}
Momentum flux, $\overline{u'_{\parallel} w'}$	0.01 $\mathrm{m}^2\mathrm{s}^{-2}$

Table 9.1: Wave parameters of the observed stratospheric gravity wave packet.

The intrinsic horizontal propagation direction was inferred above from the alignment of the major axis of the hodograph. As the vertical wind shear transverse to the propagation direction can affect the axial ratio of the hodograph ellipse, it is possible that the actual horizontal propagation direction was parallel to the minor hodograph axis and the axial ratio (Equation 9.1) was dominated by the vertical wind shear perpendicular to that direction, $\frac{\mathrm{d}u_{\parallel}}{\mathrm{d}z}$. To test this hypothesis, let us assume that the intrinsic propagation direction is parallel to the minor axis of the hodograph in Figure 9.6. The fact that $\omega < 0$ then implies intrinsic propagation against the background wind, i.e. southward. For that direction, however, $\frac{\mathrm{d}v_{\perp}}{\mathrm{d}z} > 0$ and the transverse perturbation velocity would be decreased instead of increased as assumed above. The hypothesis of an intrinsic propagation parallel to the minor axis of the hodograph is, therefore, to be rejected.

9.5 Discussion

Geostrophic adjustment as a generation mechanism of inertia gravity waves for similar observations was proposed by different authors [*Yamanaka et al.*, 1989; *Thomas et al.*, 1992] and its importance was corroborated by theoretical studies [*Fritts & Luo*, 1992; *Luo & Fritts*, 1993; *O'Sullivan & Dunkerton*, 1995]. Our observations are in good agreement with the modeling study of *O'Sullivan & Dunkerton* [1995], who simulated the distortion of the tropospheric jet stream by baroclinic instability and the subsequent generation of inertio gravity waves by geostrophic adjustment. In their model inertio gravity waves arose primarily in the jet stream exit region[2] at heights above the tropopause (Figure 9.7). The waves were confined to the vicinity of the jet stream and their propagation direction was parallel to the jet axis at mid stream but at an angle to the jet along its flanks. As the waves were approximately stationary relative to the jet stream pattern, their intrinsic phase and group velocities were directed upstream. This does not, however, indicate energy propagation towards the jet maximum, as the jet pattern is not simply advected by the wind but reveals an intrinsic downstream propagation itself.

Figures 9.8 and 9.9 show contours of geopotential height and horizontal wind speed at the 300 hPa level over Australia for different times during the observation period. The data was obtained from the numerical LAPS forecast of the Bureau of Meteorology [*Puri et al.*, 1998][3]. The position of the Buckland Park VHF radar is indicated by a black dot. As can be seen from Figures 9.1 and 9.8, the jet was aligned approximately zonally on August 23rd, and was distorted towards meridional alignment over the Buckland Park radar towards August 26th. The situation is basically the mirror image of the northern hemisphere case from *O'Sullivan & Dunkerton* [1995] shown in Figure 9.7a. The distortion of the jet stream leads to a deflection of the flow in the jet stream exit region and, in analogy to the flow over an obstacle, to the

[2] *O'Sullivan & Dunkerton* [1995] use the term exit region to describe the relatively weak, tightly curved flow downstream of the jet maximum

[3] We thank Dr. Chris Lucas for the use of his chart plotting program.

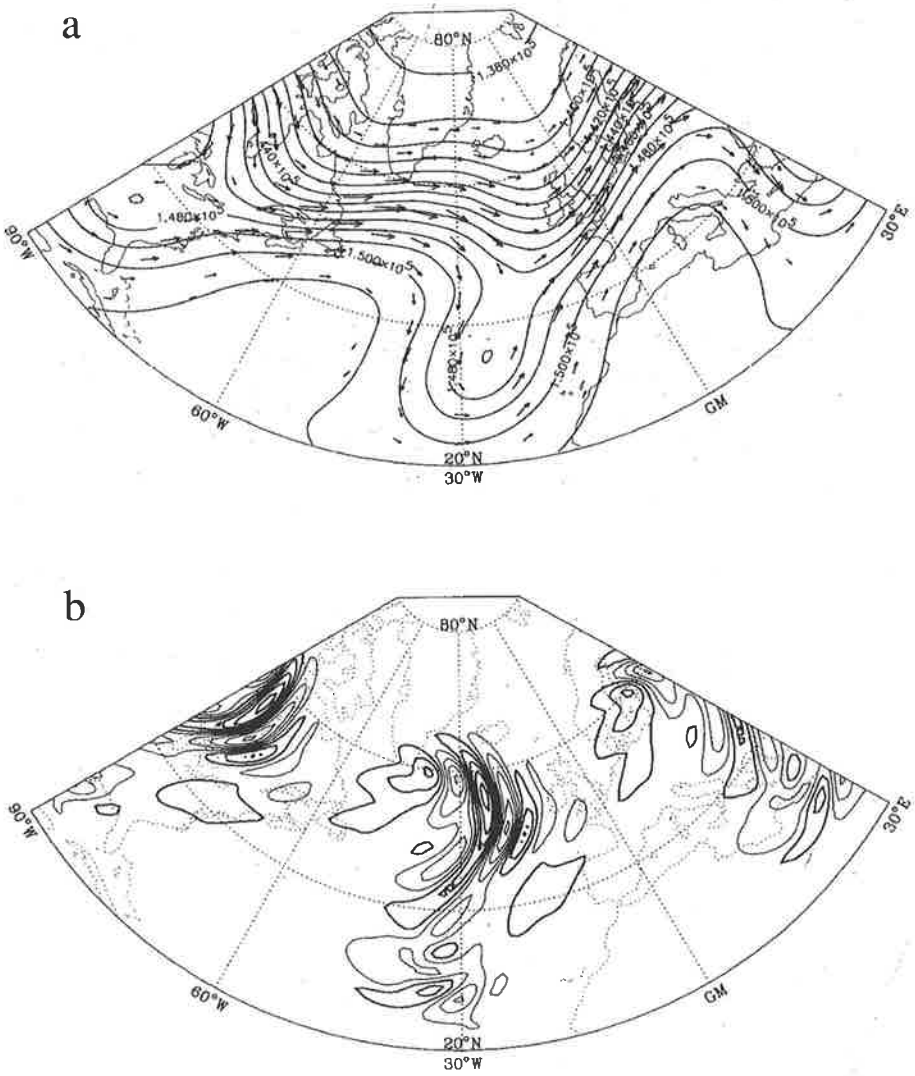

Figure 9.7: a) Geopotential height with horizontal wind vectors and b) horizontal velocity divergence at the 130 hPa level for the model run of *O'Sullivan & Dunkerton* [1995].

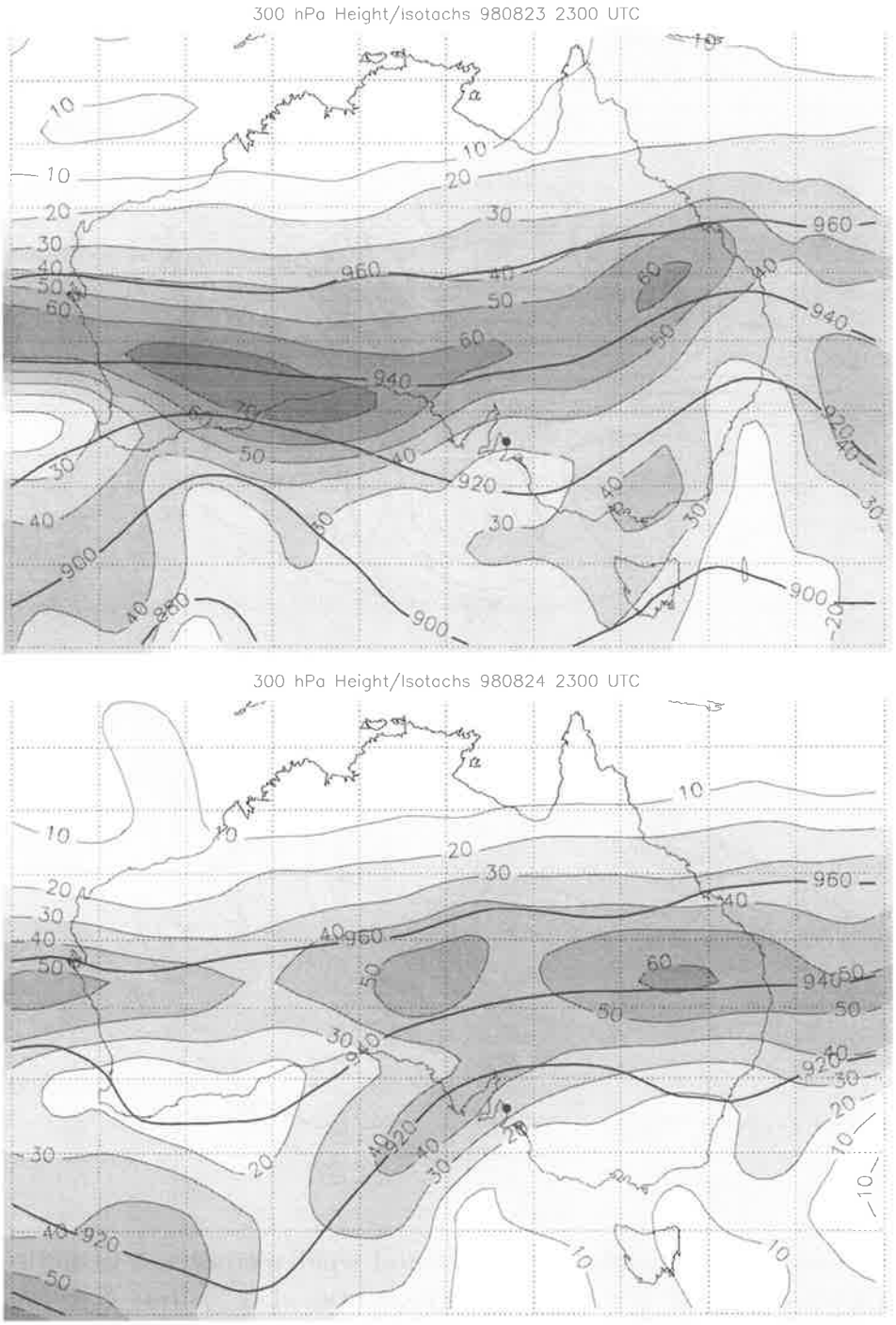

Figure 9.8: Geopotential height (thick lines) and horizontal wind speed (shaded areas and thin lines) at the 300 hPa level for 23.8.1998 23:00 UTC and 24.8.1998 23:00 UTC. The units for the geopotential height are 10 m, the horizontal wind speed is given in ms^{-1}. The position of the Buckland Park VHF radar is indicated by a black dot.

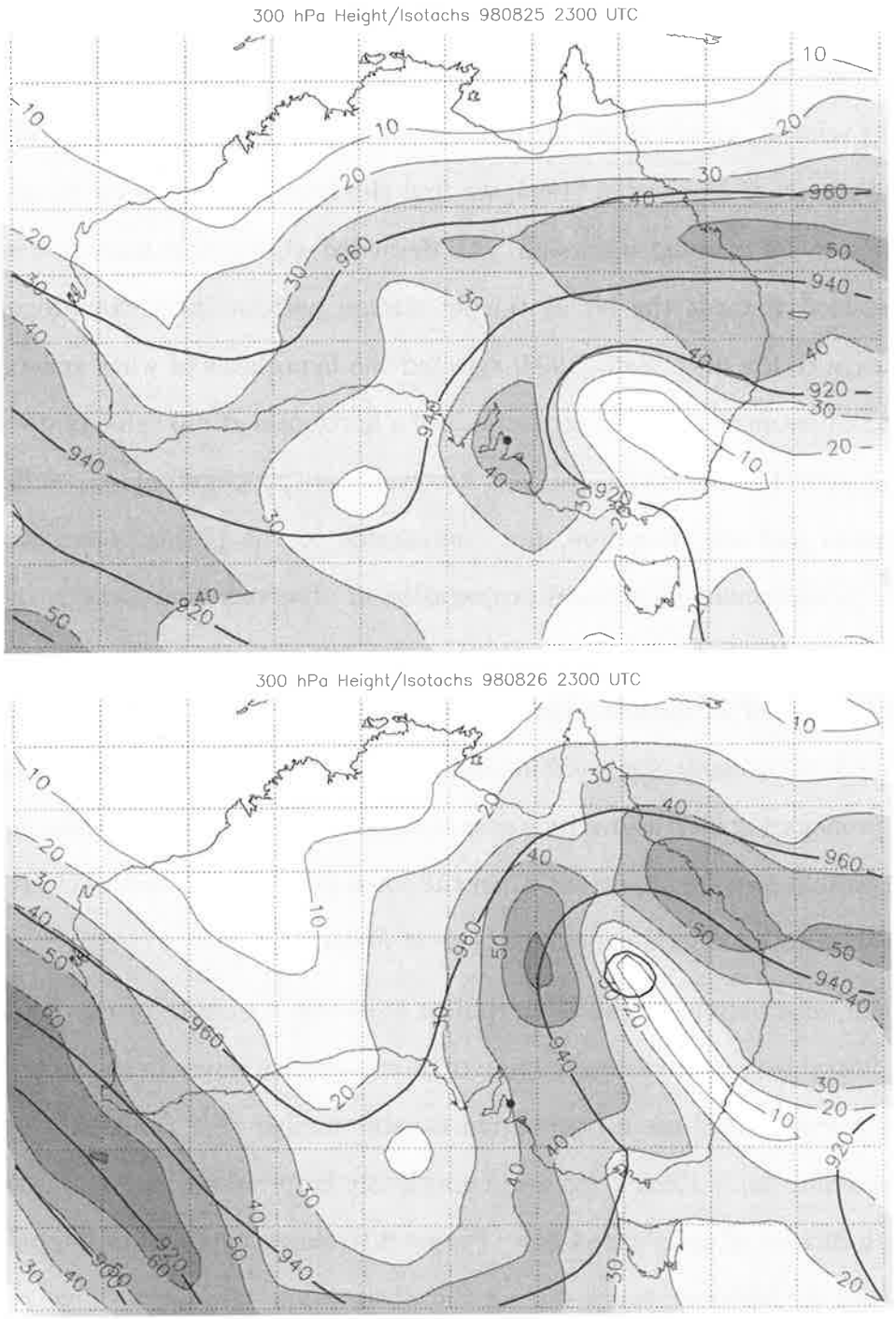

Figure 9.9: Same as Figure 9.8, but for 25.8.1998 23:00 UTC and 26.8.1998 23:00 UTC.

generation of gravity waves with a propagation direction approximately parallel to the (original) jet axis [*O'Sullivan & Dunkerton*, 1995], in good agreement with our observations. The continuous generation of inertio gravity waves leads to a constant height of the lower wave packet boundary (cf. Figure 9.5), in spite of the upwards directed group velocity, which would remove the wave packet from its source region. Similar to *O'Sullivan & Dunkerton* [1995] we find the intrinsic horizontal phase and group velocities to be directed upstream. As discussed above, this does not imply energy propagation towards the jet as the jet stream pattern itself can propagate upstream relative to the flow. *Sato* [1994] rejected the hypothesis of wave generation by geostrophic adjustment of the jet on grounds of a horizontal group velocity directed towards the jet axis. The waves she observed, however, were propagating perpendicular to the jet stream and are, therefore, not comparable to the present observations. In light of the predominant meridional propagation of observed stratospheric inertio gravity waves, *O'Sullivan & Dunkerton* [1995] point out that there are likely to be several different types of jet stream development that can result in inertio gravity wave generation. While for zonally elongated imbalances of the jet stream the generation of meridionally propagating inertio gravity waves is expected, zonally propagating inertio gravity waves should become important when the zonal extent of the imbalance region is reduced relative to its meridional extent [*Luo & Fritts*, 1993].

To get some information on the geographical fine-scale structure of gravity wave activity, it is desirable to relate the excitation of inertio gravity waves to the large-scale flow. *Koch & Dorian* [1988] use a Lagrangian Rossby number $R_o^{(L)} = |\mathrm{d}\mathbf{u}/\mathrm{d}t|/f|\mathbf{u}| \geq 0.5$ in a region where $|\mathbf{u}| > 10\mathrm{ms}^{-1}$ (to avoid spuriously large values for small denominators) as an indicator of unbalanced flow. Figure 9.10 shows contours of Lagrangian Rossby numbers for different times during the observation campaign. Due to the crude time resolution of the available LAPS data, the local derivative $\partial\mathbf{u}/\partial t$ had to be neglected relative to the advective derivative $\mathbf{u} \cdot \nabla\mathbf{u}$.[4] Nevertheless, inspection of

[4] In the simulations of *O'Sullivan & Dunkerton* [1995], the local derivative amounted to up to 30% of the advective derivative.

Figures 9.5 and 9.10 indicates good correlation between the Lagrangian Rossby number $R_o^{(L)}$ over the radar site and the production (or existence) of the observed wave packet at the assumed source level of around 9 to 10 km. Wave activity at that height level coincides with a Lagrangian Rossby number greater than 0.5. Large Lagrangian Rossby numbers also provided a useful diagnostic of inertio gravity wave generation in the model of *O'Sullivan & Dunkerton* [1995], but further case studies are needed to establish the general usefulness of this criterion.

An alternative to geostrophic adjustment as the generation mechanism of the observed wave packet is excitation by shear instability. The thermosonde measurements in Chapter 8 indicate the existence of unstable layers throughout the observed atmosphere and, especially, at the lower and upper jet flanks. Different mechanisms for inertio gravity wave excitation in stratified parallel flows have been proposed. In the linear models, the presence of a rigid lower boundary leads to the existence of an additional mode in the Kelvin-Helmholtz instability, that can couple directly with a propagating wave field in the upper levels of the model [*Lindzen*, 1974; *Davis & Peltier*, 1976; *Lalas & Einaudi*, 1976; *Mastrantonio et al.*, 1976]. *Sutherland & Peltier* [1994] showed that this direct coupling could be very effective even without the presence of a lower boundary, when the region of small background buoyancy frequency extended to the region of maximum shear (at the upper jet flank) and the atmosphere would become more stable at larger heights. This circumstance might be realized through ageostrophic effects connected with a baroclinic wave [*Sutherland & Peltier*, 1995]. For a direct coupling of the wave field to the Kelvin-Helmholtz instability, a critical level for the generated inertio gravity wave should exist within the unstable layer as a consequence of the semicircle theorem of *Howard* [1961], which requires such a critical level for the unstable Kelvin-Helmholtz wave. Inspection of Figure 9.1, however, indicates the lack of such a critical level as the zonal wind speed in the height region of interest is much larger than the ground-based phase speed of the detected wave packet. While there is still the possibility that the observed wave packet was generated by nonlinear wave-wave interactions of two Kelvin-Helmholtz modes, a mechanism often referred

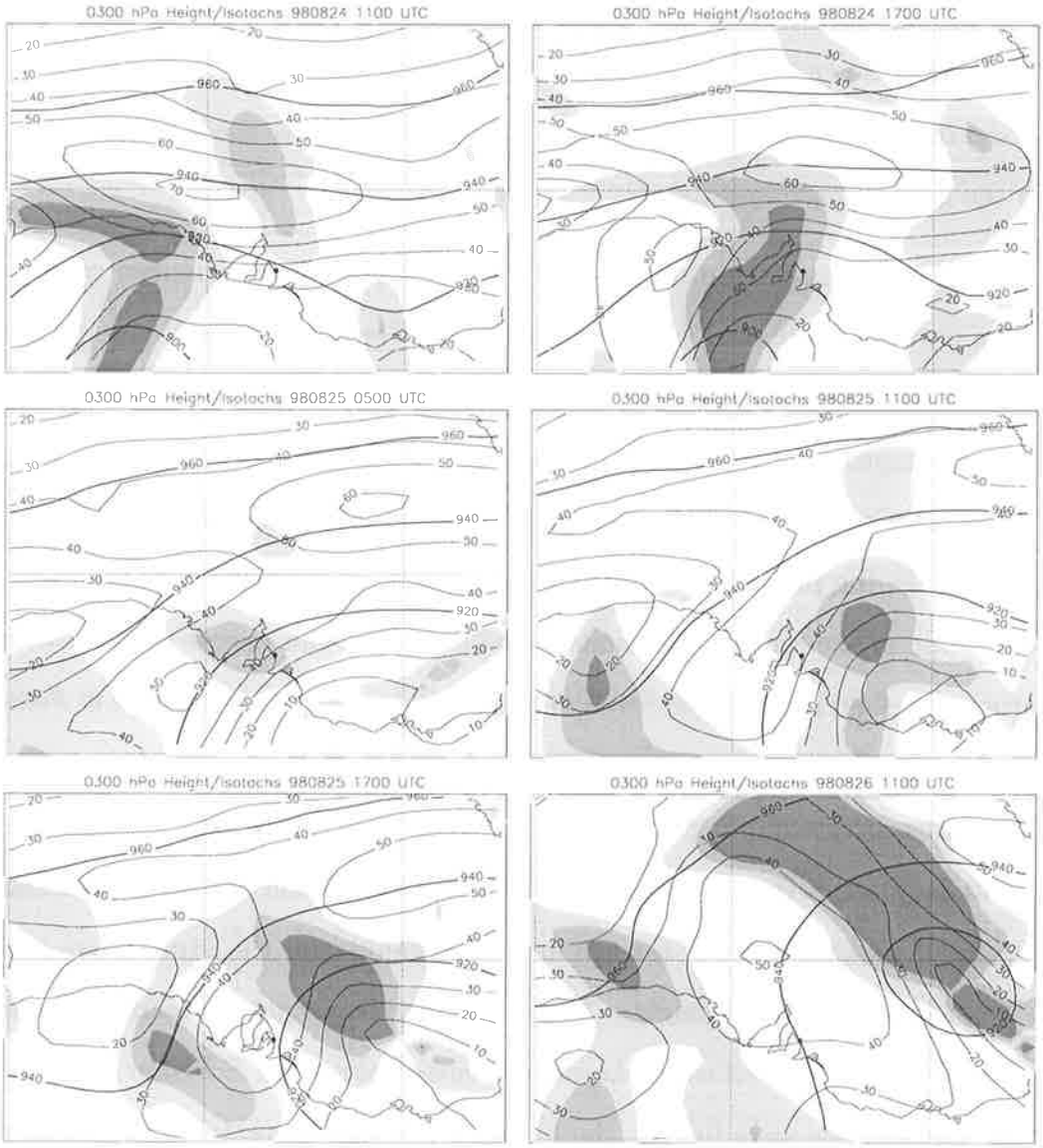

Figure 9.10: Geopotential height (in 10 m, thick lines), horizontal wind speed (in ms^{-1}, thin lines) and Lagrangian Rossby number at the 300 hPa level for different times during the observation period. The three shades of grey correspond to Lagrangian Rossby numbers $R_o^{(L)}$ of 0.5, 0.7 and 0.9, respectively. The position of the Buckland Park VHF radar is indicated by a black dot.

to as envelope radiation [*Fritts*, 1982; *Fritts*, 1984*b*; *Chimonas & Grant*, 1984], the lack of more detailed observational data does not allow further examination of this possibility.

9.6 Summary

Radar measurements during a 5 day campaign in August 1998 at Buckland Park revealed the existence of an inertio gravity wave in the lower stratosphere associated with a jet stream exit region. Two dimensional filtering of the radar data in time and height allowed the isolation and consequent hodograph analysis of the wave packet. Unambiguous wave parameters could be extracted from the radar data taking the transverse background shear into account. Using data from the numerical LAPS model of the Australian Bureau of Meteorology the observed gravity wave event could be compared to the numerical simulation of *O'Sullivan & Dunkerton* [1995] and was found to be consistent with wave generation by geostrophic adjustment of the jet stream. The possibility of an alternative wave generation mechanism, excitation by shear instability, could not be excluded, however.

Chapter 10

Thesis summary

In this thesis, several aspects of gravity waves and their effects on, and interactions with the atmosphere are examined. Subjects include wave generation mechanisms, source spectra, intermittency, and effects such as generation of turbulence and acceleration of the background flow. Measurements by radiosonde, radar, and thermosonde were analyzed, with each method giving insight into different aspects of the observed wave field.

The application of wavelet analysis to operational radiosonde soundings over Macquarie Island allowed the detection of gravity wave packets in the wind field. In contrast to more traditional Fourier methods, wavelet analysis provides information about the height extent and, thus, the intermittency of the wave packets. While the observation of packet-like wave structures in vertical wind profiles is not new, our study is the first to interpret the observed intermittency in a quantitative way.

Knowledge of wave intermittency allowed us to compute temporal averages of momentum flux and, therefore, mean-flow accelerations in a linear ray-tracing model. Even though the radiosonde observations were limited to waves with low intrinsic frequencies, the deduced mean-flow accelerations in the mesosphere were a factor of 2 to 3 larger than what is expected from observations and theory. This overestimation might be due to the omission of wave superposition effects in our linear model. Wave

superposition turned out to be very important in reproducing the observed characteristics of turbulence layers from parameters of the observed wave field in Chapter 8. Nevertheless, the model shows that waves with frequencies close to the inertial frequency in the stratosphere might have important effects in the mesosphere, which are larger than commonly assumed. Further studies should address the effects of wave superposition and try to obtain information about the intermittency of high-frequency waves, which are neglected here.

In the interpretation of the radiosonde data, great attention was paid to the bias in the observations due to the observational filter inherent in the radiosonde method. As each technique can only observe a certain part of the gravity wave spectrum, different techniques should be used together to obtain a more complete picture of the wave spectrum. In this thesis, atmospheric radar was used as an alternative observation technique. In addition to making high-time resolution observations of the wind field, radars can also provide information about turbulence parameters. Different signal processing algorithms were adapted into the radar software to increase the usable height range of radar returns by several kilometers and to achieve better sensitivity for turbulence measurements. The increased height range enabled us to compare radar and in-situ measurements of turbulence by thermosondes in the upper troposphere and lower stratosphere up to heights near 18 km. Radar measurements agreed well with in-situ observations when the power of the radar echoes was used to infer turbulence intensity. Due to the coarse radar height resolution during our study, however, the spectral width of the radar return was shown to be significantly affected by spatial gravity wave fluctuations, making the deduction of turbulence strength from spectral width measurements rather insensitive and impractical. An upgrade of the Buckland Park VHF radar in April 2000 will enable measurements with increased height resolution and allow studies of turbulence structures with much greater detail using both the power and spectral width method.

Using the high-resolution thermosonde data, a strong correlation between the structure of the observed turbulence layers and the observed gravity wave field was revealed

in a modeling study. A superposition of gravity waves with a vertical wave number spectrum corresponding to the observed wind fluctuations could reproduce the observed distributions of turbulent layer thickness and spacing in height. As the turbulence layers correspond to wave breaking levels, and therefore interactions of the wave field with the background atmosphere, our study indicates that wave superposition effects are important for the realistic determination of wave breaking levels and wave mean-flow interactions. It seems, therefore, important to include wave superposition in future modeling and ray-tracing studies.

If gravity wave effects are to be successfully included in general circulation models, more information is required about the relative importance of different source mechanisms. The combined radar/thermosonde observations gave the opportunity to explore the wave field during a period when the jet stream was intense. By filtering the radar wind field in height and time, we could detect an inertio gravity wave packet in the lower stratosphere and deduce its wave parameters. Comparison with a numerical model allowed us to tentatively identify its generation mechanism as geostrophic adjustment of the jet stream. The increased transmitter power of the Buckland Park radar after the upgrade in April 2000 will provide the possibility to monitor the lower stratosphere with increased height and time resolution, and the future analysis of more extended data sets could contribute significantly to our understanding of wave generation mechanisms and their variability at locations where wave generation by topography is of minor importance. Two-dimensional wavelet analysis could be applied to the radar data to identify wave packets, and the time interval during which a wave packet is observed at a certain height level could be used to estimate its intermittency (in time). Furthermore, if the criterion for the Lagrangian Rossby number $R_o^{(L)}$ can be proven to be a reliable indicator of inertio gravity wave excitation, then numerical forecasting models could be used to gain some insight into the importance of geostrophic adjustment as a wave generation machanism and the spatial intermittency of these waves.

Appendix A

A VHF boundary layer radar: First results

This is a reprint of a paper published in *Radio Science* **33**, 845-860 (1998).

Radio Science, Volume 33, Number 4, Pages 845–860, July–August 1998

A VHF boundary layer radar: First results

R. A. Vincent, S. Dullaway, A. MacKinnon, I. M. Reid, and F. Zink
Department of Physics, University of Adelaide, Adelaide, South Australia, Australia

P. T. May
Bureau of Meteorology Research Centre, Melbourne, Victoria, Australia

B. H. Johnson
Atmospheric Radar Systems, Adelaide, South Australia, Australia

Abstract. The development of a novel VHF radar designed to measure winds and temperatures in the planetary boundary layer is described. The radar operates at 54.1 MHz and is compact and easily transportable. The antenna system consists of 12 Yagis grouped into three subarrays arranged in the form of an equilateral triangle. Transmission takes place on the whole array, and reception takes place on the three subarrays, with winds measured by the spaced antenna technique over a height range between 300 and 3000 m. Results from field trials conducted in southern Australia in a variety of meteorological conditions are presented. Comparisons with high-resolution radiosondes launched from the radar site show excellent agreement, with rms differences between radiosonde and radar wind components being about 1.5 m s^{-1}. Observations carried out in rain show that echoes from precipitation are clearly distinguishable from clear-air echoes. Unlike UHF radars, this means that vertical air velocities can be measured during precipitation, and the evolution of drop-size distributions can be studied down to low altitudes. It is shown that temperatures derived from a radio acoustic sounding system are measured up to heights near 2 km, depending on background wind conditions.

1. Introduction

Stratosphere-troposphere (ST) radars or wind profilers are powerful tools for atmospheric research and operational meteorology [e.g., *Gage*, 1990]. While the ST radar field is relatively mature, development has proceeded in step with advances in technology. In the last few years, the advent of cheap, powerful computers, together with inexpensive computer memory for storing raw data and reliable solid-state transmitters, have opened up new possibilities for ground-based radar studies of the atmosphere. Developments in conceptual techniques include the use of interferometry to improve estimates of pointing directions and correct such important parameters as vertical air velocity. The ultimate aim is to derive as many atmospheric parameters as possible in real time to aid research and forecasting.

The last decade has seen the development and large-scale deployment of boundary layer (BL) profilers. These low-power systems have been designed for the express purpose of observing many of the important meteorological phenomena that occur in the lowest part of the troposphere. Typically, frequencies near 1 GHz are used for UHF boundary layer radars. Examples are the widely used radar system developed at NOAA's Aeronomy Laboratory which uses a frequency of 915 MHz [e.g., *Ecklund et al.*, 1988, 1990; *Carter et al.*, 1995] and the L-band (1.357 GHz) system developed by the Kyoto University group [e.g., *Hashiguchi et al.*, 1995]. Systems such as these are being used to investigate boundary layer wind and temperature fields and, since they are sensitive to hydrometeors, the precipitation field.

Paper number 98RS00828.
0048-6604/98/98RS-00828$11.00

Radars operating in the lower VHF band (~50 MHz) have primarily been used to measure winds to as high an altitude as possible, which requires the use of physically large antennas and high transmitter powers. However, effects such as long recovery times in transmit-receive systems and reflections or ringing in antennas and transmission cables mean that these larger systems generally cannot make measurements in the lowest 1–2 km of the atmosphere. However, pioneering work by the French group in Toulon show that it is possible to use small antennas and make useful BL measurements at VHF [e.g., *Crochet et al.*, 1994; *Fillot et al.*, 1997].

Operating at UHF offers many advantages. These include (1) the use of antennas that are physically small but relatively large compared with the radar wavelength, so that narrow beams can be generated; (2) low external noise; and (3) the availability of wide bandwidths, which means good height resolution. On the other hand, when precipitation or heavy cloud is present, echoes from hydrometeors dominate echoes from the clear air, which makes measurements of vertical velocity difficult. This is a particular limitation when radio acoustic sounding systems (RASS) are used to measure atmospheric temperatures at UHF with vertical pointing beams, since the sound velocity should be corrected for the vertical wind [e.g., *Angevine et al.*, 1994a]. Another limitation with RASS at UHF is that the acoustic frequencies (~0.8–1.6 KHz) suffer rapid attenuation, which limits the upper height to which temperatures can be obtained [*May et al.*, 1988].

The advantages in operating at VHF include the following:

1. Precipitation echoes are comparable in strength to, or weaker than, the clear-air echoes, and the precipitation and clear-air echoes are usually well separated in the Doppler spectrum. Hence a single VHF radar can simultaneously study the dynamics and cloud microphysics of precipitating clouds [e.g., *Rajopadhyaya et al.*, 1993].

2. Measurement of the vertical gradient of the vertical velocity gives the divergence of the wind field, especially in storm conditions when the vertical motions and gradients are large.

3. VHF BL radars are unlikely to suffer the problems with contamination by bird and bat echoes that UHF BL radars often encounter [*Wilczak et al.*, 1995; *May*, 1995].

4. A VHF/RASS boundary layer system should also have a better height coverage than a similar UHF system because the lower-frequency sound waves used suffer much less attenuation.

Thus a 50-MHz BL system has many advantages for the study of shallow weather systems, such as summertime cold fronts across southern Australia [*Wilson and Stern*, 1985]. Other applications include sea-breeze fronts which trigger convection. Finally, there is much that we do not understand about scattering processes from the atmosphere. Measurements should be made at a range of frequencies in the VHF and UHF bands to investigate these processes as well as exploit the research and operational potential of all systems.

The Atmospheric Physics group at the University of Adelaide has been developing radars at MF/HF and VHF for studies of both the upper and lower atmospheres. A major design goal has been to develop systems that have as many features in common as possible. Here we describe a VHF (54.1 MHz) radar that has been developed since 1994 for boundary layer studies. The aim is to study winds and temperatures in the lowest 2–3 km of the atmosphere with good height and time resolution and to extend the scope of boundary layer studies to include precipitation and vertical air motions in the presence of precipitation. The overall system design is briefly described in section 2, and some of the first wind and RASS measurements are presented and discussed in section 3.

2. System Design

A number of factors were taken into account in the development of the Adelaide VHF boundary layer (BL) radar. The prime requirements were that the system should be flexible in operation, relatively easy to transport, and power efficient so that it could be used at remote sites. A lower height limit of about 300 m was specified, and it was required to measure winds regularly to heights of 2–3 km in order to overlap with observations made with a ST VHF radar located at the Buckland Park field site [*Vincent et al.*, 1987].

To achieve these aims, the system shares a number of features common to other radar systems recently developed by our group in Adelaide. In order to obtain high mean power it was decided to use a compact, modular, solid-state transmitter that is capable of a high duty cycle (10%). The modular nature of the transmitter means that transmit-receive antennas can be configured in different ways to allow differ-

ent wind measuring techniques (e.g., Doppler, spaced antenna, and interferometric) to be investigated and used as appropriate. A receiver and data acquisition system (RDAS) was developed with wide dynamic range and sufficient amounts of memory (RAM) for the temporary storage of raw data. The data are then downloaded to the host computer for on-line analysis/permanent storage while the next sequence of data is being acquired. For operational flexibility, as many operating parameters (e.g., receiver gain, height range, height increment, etc.) as possible are placed under computer control. This enables a wide range of experiments to be configured in software and operated sequentially. System control and data analyses are undertaken with a PC computer that is easily networked. It is therefore both simple and inexpensive to add more computing power as required. Data are analyzed with a proprietary data analysis and display package and stored on disk for further off-line processing. Raw data can also be stored for later analysis in other ways.

2.1. Antenna Configuration

The low-height performance of 50-MHz ST systems is limited by the use of large antenna arrays and problems associated with ringing after the transmitter pulse, which hampers receiver recovery. Thus a VHF BL radar requires small antennas, which implies wide beam widths, so that ground clutter and interference to and from other operators may be a problem. Fast transmit-receive switches must be used and antenna ringing minimized to ensure reception at low heights. It was decided to utilize a spaced antenna (SA) configuration so that only vertically pointing beams are used. This arrangement is more compact than Doppler systems, and it eliminates the height-smearing problem that occurs when obliquely pointing wide beams are used for Doppler sounding [*Fillot et al.*, 1997] as well as potential problems associated with anisotropic backscatter which complicate wide-beam Doppler measurements [*Röttger*, 1984]. Another potential advantage of the SA configuration is that the data can be used for interferometric studies as well as conventional spaced antenna wind measurements. Interferometric techniques can then be used to study the scattering irregularities and have the potential to correct for possible contamination of the vertical velocity measurements caused by tilted layers [*Vincent and Röttger*, 1980].

Figure 1 shows the antenna configuration adopted for initial measurements with the VHF BL system. The arrangement is a compromise between making the subarrays as small as possible to minimize ringing and large enough to ensure an adequate power-aperture product. Three subarrays, each consisting of groups of four three-element Yagis, are arranged in an equilateral triangle. The whole array is used for transmission and each group is used for reception. An equilateral triangle arrangement reduces the chances of systematic biases in SA wind measurements, as can occur if other configurations, such as a right-angle triangle, are used. The optimum spacing of antennas in SA mode is when the mean cross correlation at zero lag is about 0.5 [*Briggs*, 1984]. Preliminary trials showed that the basic spacing should be at least 1.5λ (8.32 m), and this was chosen as the initial spacing. A reevaluation of the spacing took place after the radar had operated in a variety of meteorological conditions, as discussed in section 3.1.

The configuration adopted ensures that grating lobes on transmission are not significant. Figure 2 shows plots of the one-way polar diagrams for the receiving and transmitting arrays. The transmitting array has a half-power half width of 10°, corresponding to an effective area of about 250 m^2, while the respective values for the receiving antennas are 18° and about 80 m^2. However, as *May* [1990] has shown, the overall effective area of the system depends on the scattering mechanism. For the situation of isotropic volume-scatter the effective area is given by

$$A_{\text{eff}} = \frac{2A_T A_R}{(A_T + A_R)} \tag{1}$$

where A_T and A_R are the respective areas for the transmitting and receiving antennas. In this case, $A_{\text{eff}} \approx 120$ m^2. One problem with such relatively wide beams is the possible effects of ground clutter, but by suitably spacing and orientating the Yagi antennas it is possible to partly null out clutter and interference that arrive at low elevations.

2.2. Operating Parameters

Table 1 summarizes the range of possible operating parameters. In the evaluation of the system a 1-μs pulse length was used to achieve the desired 150-m range resolution, and a 2-MHz receiver bandwidth was selected to ensure that fast receiver recovery occurs and the desired lower height limit of about 300 m is attained. A particular feature of the system is the high degree of computer control of the system configuration, such as height coverage, range resolution, and so on. If necessary, a number of different ex-

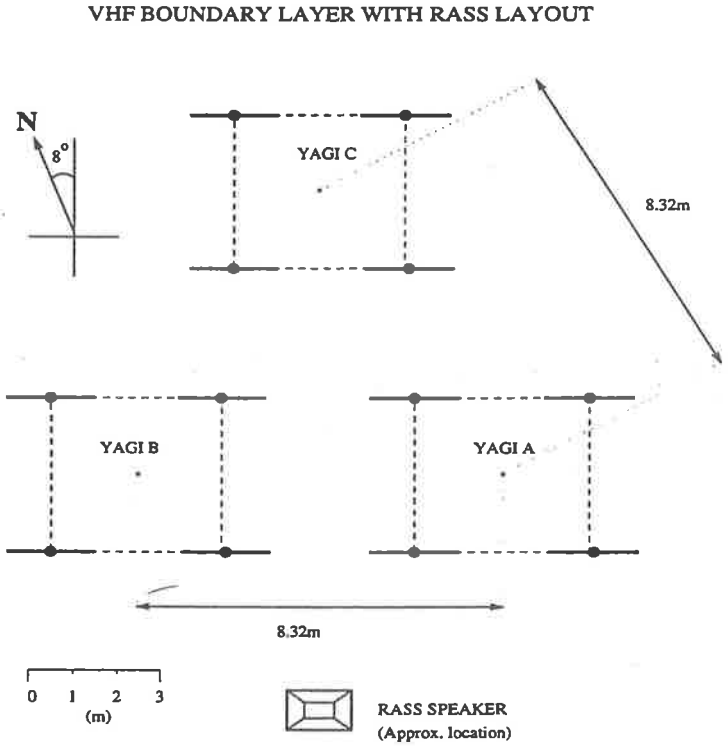

Figure 1. Plan view of VHF boundary layer radar antennas.

periments can be programmed to take place in any desired sequence. This is particularly useful while, as at present, the optimum operating parameters for SA wind and RASS measurements were being determined.

Initial tests suggest that in the spaced antenna mode the operating parameters shown in Table 2 give satisfactory performance. These values give a lower detectable wind speed of $\sim$1 m s^{-1} and an upper limit of about 80 m s^{-1}. With these settings the mean power is about 20 W, giving a power-aperture product of at least 2500 W m^2. The complex amplitudes received at the three antennas are analyzed in the standard method using the full correlation analysis (FCA) discussed by *Briggs* [1984]. The quality of the data was assessed using the standard criteria described by *Briggs* [1984], although only data with signal-to-noise ratios (SNR) greater than 0 dB (after coherent integration) were accepted, as modeling studies show that the accuracy of SA wind determinations decreases rapidly for smaller signal-to-noise ratios [*Holdsworth*, 1995].

3. Initial Results

Initial tests of the BL system were carried out at the University of Adelaide's Buckland Park field station (35°S, 138°E), where it is located immediately adjacent to a VHF ST profiler [*Vincent et al.*, 1987]. The site is very flat and upwind of any significant topography. However, the site is rather crowded with buildings, antenna masts, etc., and there is the potential for significant ground clutter, which can make the detection of the clear-air echoes difficult. Fortunately, clutter has not proved to be a major problem, except at the lowest range gates of 300–450 m, and is easily distinguished from atmospheric echoes by its characteristic slow fading. A number of algorithms are being tested to reduce the effects of ground clutter and intermittent clutter due to aircraft, including the use of wavelet transforms [*Jordan et al.*, 1997].

In order to assess the performance of the radar, a series of intercomparisons were made during the period July 31 to September 26, 1997, with simultaneous measurements made with high-resolution ra-

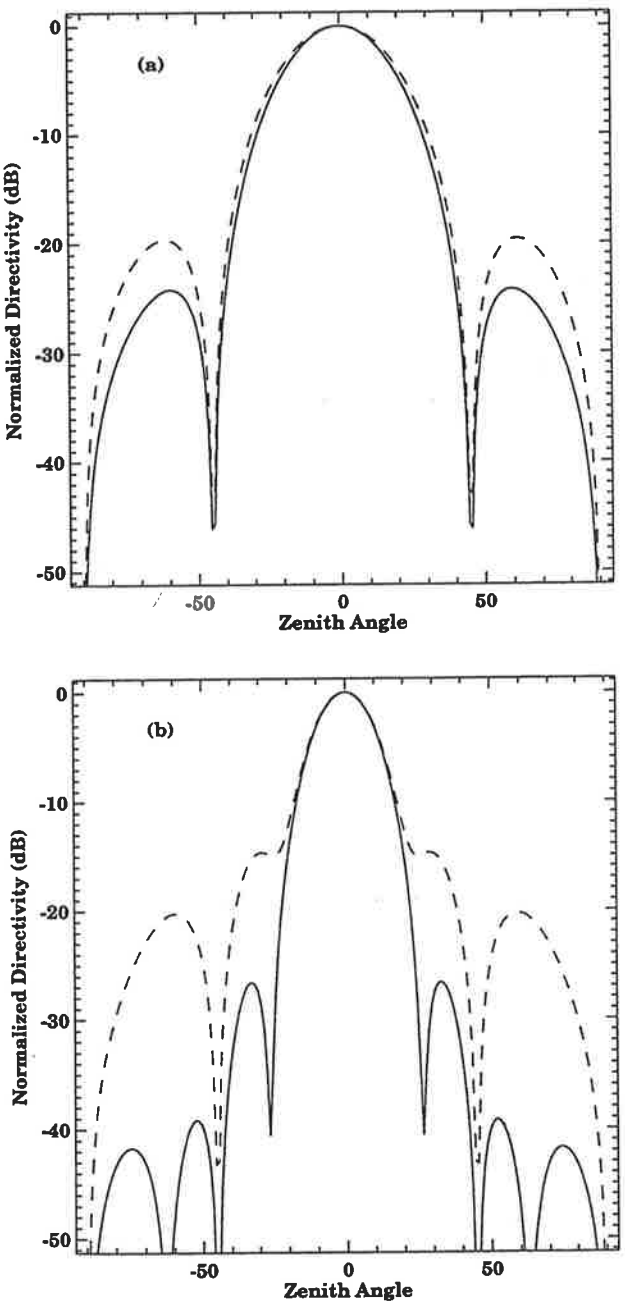

Figure 2. Antenna polar diagrams. The solid lines indicate the E plane, and the dashed lines indicate the H plane. (a) Receiving antenna. (b) Transmitting antenna.

diosondes (Vaisala RS80-15) launched from Buckland Park. Three campaigns were carried out in a variety of meteorological conditions, including significant precipitation. Campaign I occurred between July 31 and August 1, campaign II took place between September 12 and 15, and the final campaign occurred on September 26, 1997. Results from all three campaigns were used to evaluate the performance of the radar, such as accuracy of wind measurements. To illustrate the capabilities of the system, we focus on some of the results from the first two campaigns, which were conducted under very different weather conditions.

Table 1. Operating Parameters of the VHF Boundary Layer Radar

Parameter	Value
Transmitter power	3×350 W peak envelope power
Transmit/receive switch	passive, ~1-μs recovery time
Antenna bandwidth	~4 MHz
Receiver bandwidth*	2 MHz to 250 kHz
Pulse length*	0.7–10 μs
Maximum duty cycle	10%
Sample height*	100-m minimum, 25-m increments
Pulse repetition frequency*	up to 50 kHz
Coherent integration*	up to 4096 points
Digitizers	12-bit
Signal averagers	24-bit
Memory	1 Mbyte per receiver

*Software selectable.

Table 2. Typical Spaced Antenna Parameters Used in Campaigns

Parameter	Value
Parameter	Value
Pulse repetition frequency*	20,480 Hz
Number of coherent integrations*	1,024
Number of data points per sample*	1,024
Height coverage*	300–3200 m
Record length*	52.4 s
Range resolution*	150 m
Maximum lag*	4 s
Sample rate	0.05 s

*Software selectable.

3.1. Radar and Radiosonde Wind Comparisons

A primary goal of the campaigns was to assess the accuracy of the radar wind measurements by comparing them with radiosondes equipped with medium- to high-resolution wind-finding systems. For campaign I a Global Positioning System (GPS) tracking system was used, while for the campaigns starting on September 12 and 26, the balloons were tracked using VLF Omega navigation signals. For each flight the radar winds at each 150-m range gate were averaged over a period of 20 min, centered on the time at which the balloon had reached an altitude of 1 km. At least three radar observations were required at a given level to produce a mean value. No consensus averaging [*Strauch et al.*, 1984] was used in producing the mean wind velocities. In all, there were 29 flights and 144 samples.

Figure 3 shows scatterplots of the zonal (u) and meridional wind (v) components. It is apparent that the observations are highly correlated ($r = 0.95$), with the points distributed reasonably evenly around the line of unit slope. Only in the case of the v component are there any significant outliers, with six points lying about 5 m s^{-1} away from the line. These points came from two consecutive soundings in which there appeared to be significant curvature in the wind field. Table 3 summarizes the results of the comparisons. There are two lines for each wind component, with the second line corresponding to the case where the two soundings mentioned previously were discounted. Whether these soundings are included or not, the comparisons are very good, with rms differences between the radar and radiosonde winds being about 1.5 m s^{-1}.

These results compare very favorably with the results from similar studies. Many earlier comparisons were between profiler and radiosonde release sites separated by many tens of kilometers, and so some of the differences could be ascribed to spatial variability. For example, *Vincent et al.* [1987] compared 50-MHz ST profiler winds measured at Buckland Park with radiosondes released from Adelaide Airport, situated some 36 km to the south. They found rms speed differences in the 2–6 km height range of 3–4 m s^{-1}. The most extensive intercomparison using collocated soundings is that of *Weber and Wuertz* [1990], who compared 915-MHz profiler and radiosonde observations conducted at Stapleton Airport in Denver, Colorado, over a 2-year period. After editing their data to remove outliers, they found rms component differences of about 2.5 m s^{-1}.

There are fewer comparisons of boundary layer measurements. *Hashiguhi et al.* [1995] report rms

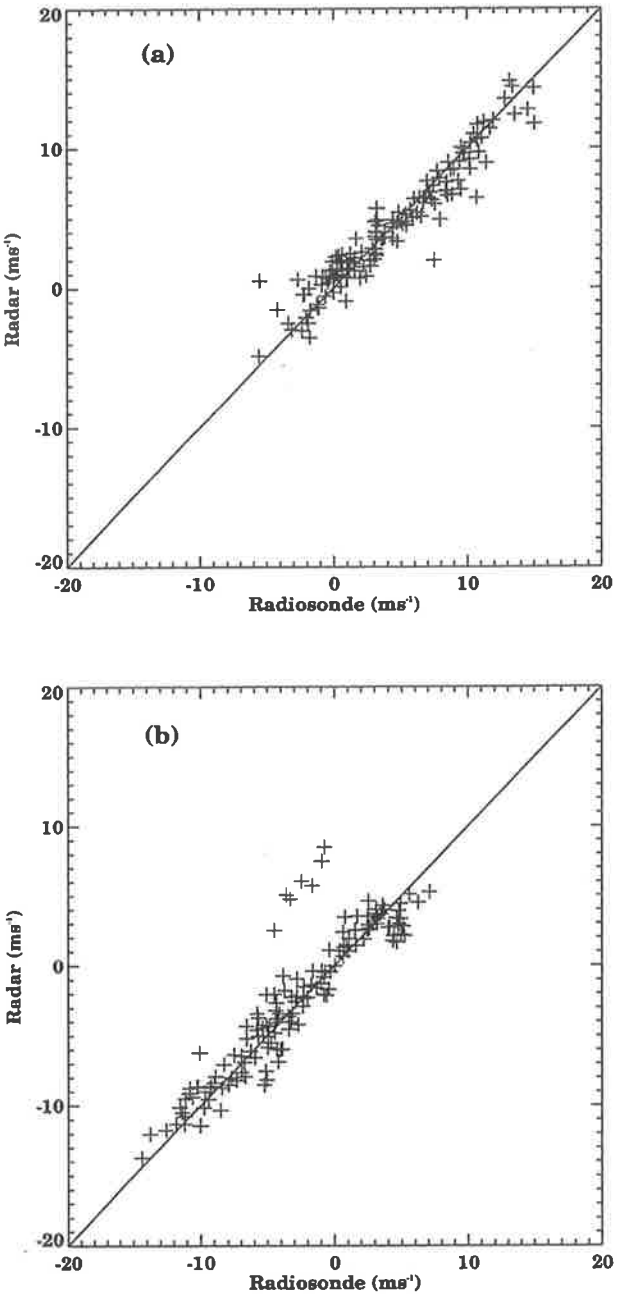

Figure 3. Scatterplot of wind velocities measured by radar and radiosondes. (a) zonal component and (b) meridional component. Lines of unit slope are shown.

Table 3. Statistics of Radiosonde/Profiler Comparisons for Zonal (u) and Meridional (v) Wind Components

	Correlation	Mean Difference, ms^{-1}	Intercept, ms^{-1}	Slope	RMS, ms^{-1}
u	0.96	-0.05	0.72	0.86	1.4
	(0.96)	(-0.10)	(0.74)	(0.83)	(1.4)
v	0.94	-0.47	0.12	0.93	2.2
	(0.98)	(-0.13)	(0.26)	(0.94)	(1.3)

Profiler observations are averaged over 20 min from the time of launch of the radiosondes, and comparisons were made at each radar range bin whenever there were three or more radar observations in that bin. There were a total of 29 profiles for each instrument. The intercept and slope refer to the weighted least squares fit straight line to the scatterplots shown in Figure 3, while the rms values indicate root-mean-square difference between radiosonde and radar data. The values in parentheses refer to comparisons with two flights removed (see text).

component differences of better than 3 m s^{-1} when they compared L-band boundary layer profiler winds with winds derived from radiosondes released from the radar site. An extensive comparison using Tropical Ocean-Global Atmosphere/Coupled Ocean-Atmosphere Response Experiment (TOGA-COARE) data taken with 915-MHz profilers and radiosondes reveals rms differences of less than 1 m s^{-1} [*Riddle et al.*, 1996]. *Angevine and MacPherson* [1995] compared 915-MHz profiler wind measurements with simultaneous aircraft observations and found rms differences of less than 1 m s^{-1}. The differences are site dependent. For example, *May* [1995] found differences of ~2–3 m s^{-1} in a highly convective boundary layer during the day in central Australia. Comparisons were even worse at night because of scattering from bats.

The excellent agreement between the wind velocities measured here by the two techniques probably reflects the low spatial variability inherent in this comparison. As noted, Buckland Park is situated on the flat Adelaide Plains upwind of any significant topography, so spatial variability was minimized as the balloons drifted away from the site. It should be noted, however, that this comparison ignores the errors inherent in the radiosonde soundings. One factor that is often ignored in these comparisons is the smoothing required to reduce the effects of the pendulum motion of the sonde package. This smoothing acts as a low-pass filter that reduces the amplitude of short-vertical-wavelength wind variations. The length of the filter in the GPS-sonde measurements was 60 s and was 240 s in the Omega-sonde wind determinations. Given the ~4 m s^{-1} ascent rate of the balloons, the effective height resolution of the radiosondes is several hundred meters. This reduces the small-scale wind variations relative to those observed by the radar. Some of the Omega-sonde data were reprocessed with a shorter filter length of 150 s to see how significant this effect was. The rms deviation from the wind speeds processed with the normal 240-s filter was about 0.7–1 m s^{-1}. As expected, the deviations were largest where the wind curvature was greatest.

There are a number of factors that influence the accuracy of radar wind measurements using the spaced antenna technique. As noted above, the optimum antenna spacing is where the spatial correlation is about 0.5. Ground-pattern statistics obtained from the full correlation analysis (FCA) were used to test how well this was satisfied with the present arrangement, as well as to provide other useful information on the scattering irregularities. In the FCA, the ground diffraction pattern is modeled as a series of concentric ellipses of constant correlation, ρ. The size and orientation of the characteristic ellipse for which $\rho = 0.5$ are convenient measures of the average pattern scale and orientation. Pattern-scale statistics obtained from spaced antenna measurements in the three campaigns are summarized in Table 4. The most probable value of 8.5 m is identical to the antenna spacing of 8.3 m (1.5λ), which shows that the spacing was close to optimal. Table 4 also shows another useful pattern parameter, the axial ratio, which

Table 4. Characteristics of Ground Diffraction Pattern

	Most Probable	Mean
Pattern scale, m	8.5	11.2
Axial ratio	1.125	1.48

is a measure of the elongation of the characteristic ellipse. The most probable and mean values are both less than 1.5, which in practice means that the average pattern is not significantly different from circular [*Wright and Pitteway*, 1978].

Profiles of the pattern scale with height, such as those given in Figure 4 for the first two campaigns, suggest that there is a small increase in pattern scale with increasing height. As the pattern scale and the angular spectrum or width of the backscattered radiation are a Fourier transform pair [e.g., *Briggs*, 1992], this indicates that there is a narrowing of the angular spectrum with height and hence a change in the aspect sensitivity of the scattering irregularities. In order to make a quantitative estimate of the width of the angular spectrum it is necessary to make some assumptions about the angular dependence of the antenna polar diagrams and of the angular spectra. The almost circular nature of the correlation functions suggests that energy is backscattered almost uniformly from around the zenith and is just a function of the zenith angle φ. Assuming that the antenna polar diagrams and angular spectrum have a Gaussian dependence and that the irregularities are confined to narrow layers, then the relationship between the spatial correlation function and angular spectrum has the simple form given by

$$\rho(r) = \exp(-\pi s_o^2 r^2), \tag{2}$$

where $s_o = \sin\varphi_o$ and r is the antenna separation in radar wavelengths [*Briggs*, 1992]. If

$$\sigma(s) \propto \exp(-s^2/s_I^2), \tag{3}$$

$$G_T(s) \propto \exp(-s^2/s_T^2), \tag{4}$$

$$G_R(s) \propto \exp(-s^2/s_R^2), \tag{5}$$

describe the angular spectrum s_I of the irregularities and G_T and G_R are the transmitter and receiver polar diagrams as a function of $s = \sin\varphi$, respectively, then

$$\frac{1}{s_o^2} = \frac{1}{s_I^2} + \frac{1}{s_T^2} + \frac{1}{s_R^2}. \tag{6}$$

In the present case, $\varphi_T = 12°$ and $\varphi_R = 21.8°$, so, from the measured values of pattern scale, $\rho_{0.5}$, it is straightforward to estimate φ_I, the angular width of the atmospheric echoes.

The scale at the top of Figure 4 gives the conversion of the pattern scale to angular width. An infinite value corresponds to isotropic scatter. The rather narrow angular widths observed in the lowest range gates are probably caused by incomplete removal of slow fading clutter. However, the decrease in φ_I with height is most likely real. There are at least two reasons for the effect. First, the backscattering irregularities may be more aspect sensitive in the more stable free atmosphere above the well-mixed boundary layer. Second, it is possibly a selection effect, as irregularities which scatter energy preferentially from overhead are more likely to be observed by the vertically pointing radar at longer ranges, where the SNR are smallest.

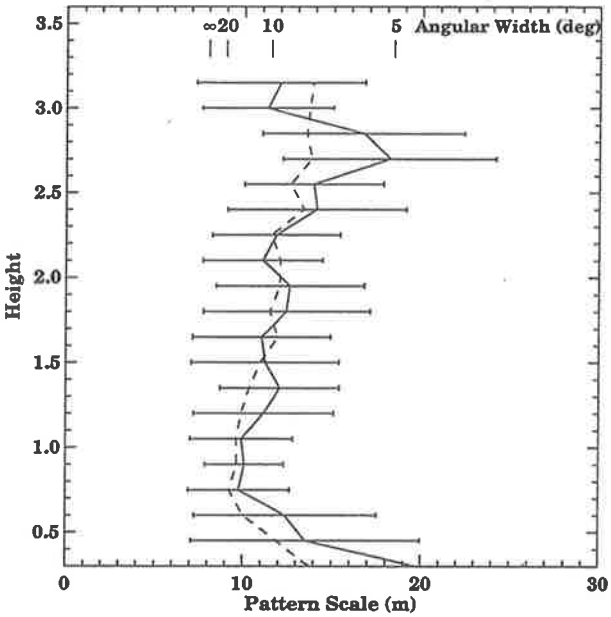

Figure 4. Vertical profiles of mean pattern scale for campaign I (solid line) and campaign II (dashed line). The scale at the top gives the angular width of the backscattered echoes.

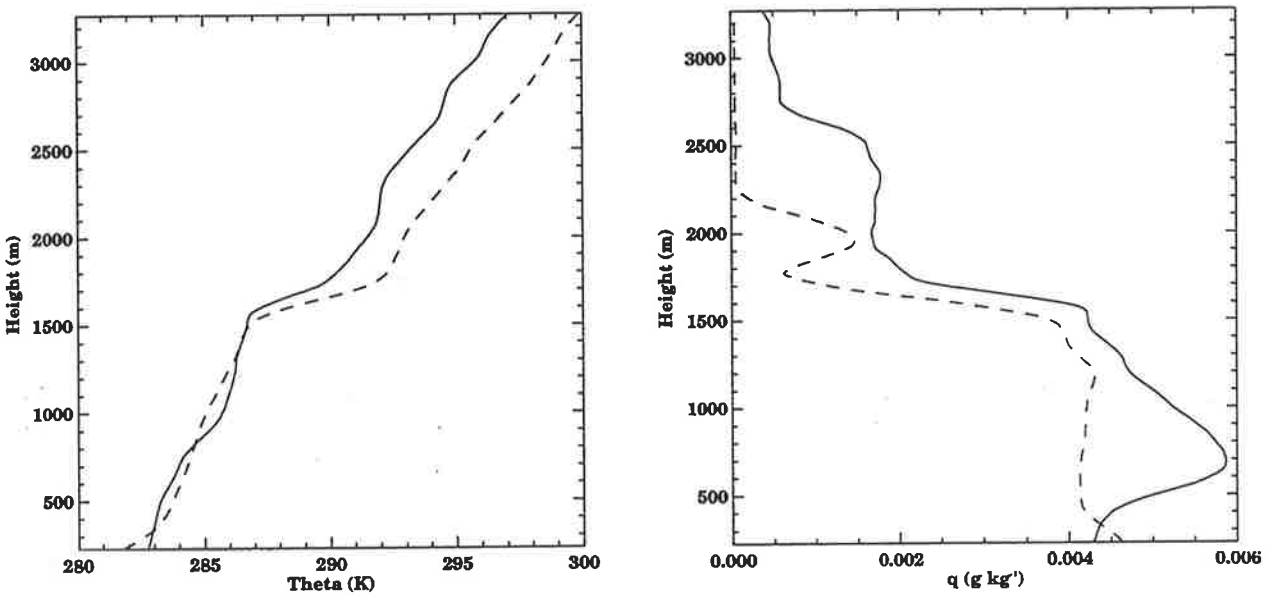

Figure 5. Vertical profiles of (left) potential temperature and (right) specific humidity derived from radiosonde soundings at 1206 LT (solid line) and 0206 LT (dashed line).

3.2. Campaign I

During this period a strong high-pressure region (~1035 hPa) was centered over the site. The BL observations were interleaved with observations with another radar also undergoing tests at Buckland Park, so the effective sample period was 2 min. Eleven radiosondes were launched at intervals of approximately 3 hours.

Day and night profiles of potential temperature and specific humidity q are shown in Figure 5. There is a marked subsidence inversion clearly evident in all profiles. The daytime boundary layer is reasonably well mixed but contains a localized stable layer at a height of about 800 m and a corresponding maximum in specific humidity. The nighttime profile shows a residual mixed layer overlying a typical ground-based radiation inversion. Figure 6 shows the time-height cross section of the signal-to-noise ratios (SNR). Values were smoothed over 30 min to reduce some of the short-term variability. There is a clear relationship between the strong subsidence inversion and the layer of enhanced reflectivity, analogous to the results of *Angevine et al.* [1994b] with a 915-MHz profiler. This example is particularly clear compared with typical 915-MHz estimates of boundary layer depth, but it is not evident if it is the result of the difference in radar frequency or of the intense subsidence inversion. The nighttime profiles show the growth of a nocturnal inversion at altitudes below 400 m and a fossil mixed layer (residual layer) that is very evident in q at heights below 1200 m. During the night, there is no heating from below to produce turbulent fluctuations of temperature and moisture (and hence scattering irregularities) in the fossil mixed layer, a condition exacerbated by the light winds.

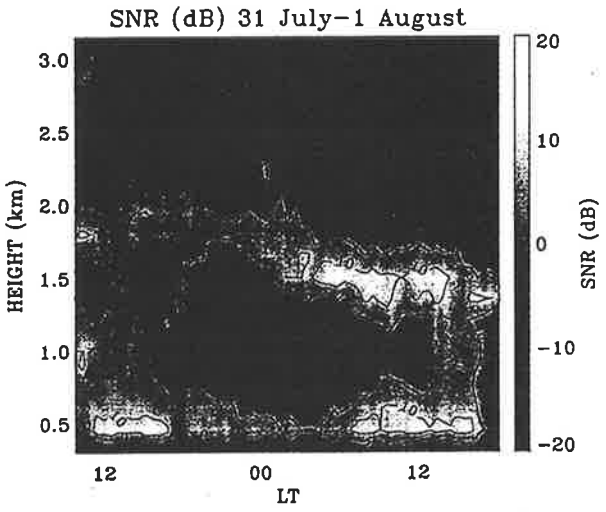

Figure 6. Time-height cross section of 30-min average signal-to-noise ratios observed in campaign I.

Meteorological parameters recorded during the radiosonde ascents can be used to gain some insight into radar performance. The received power P_R is related to the range R and radar reflectivity η by

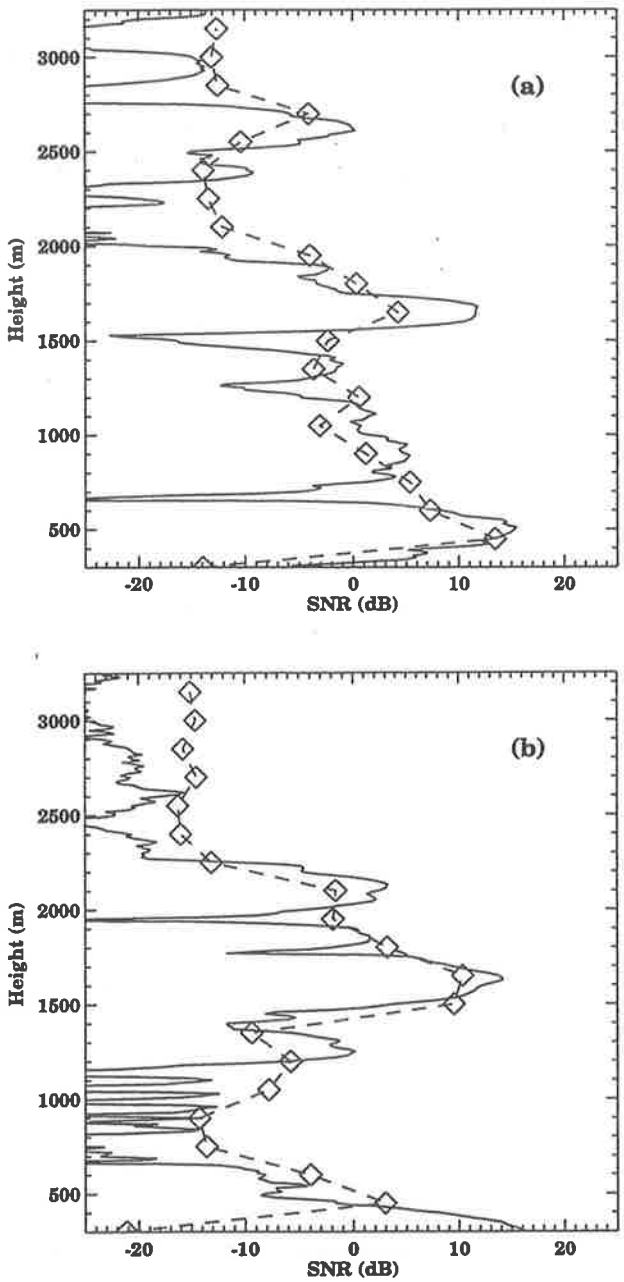

Figure 7. Vertical profiles of refractivity from radiosondes (solid line) and radar (dashed line) measurements for (a) 1200 LT July 31, 1997, and (b) 0206 LT August 1, 1997.

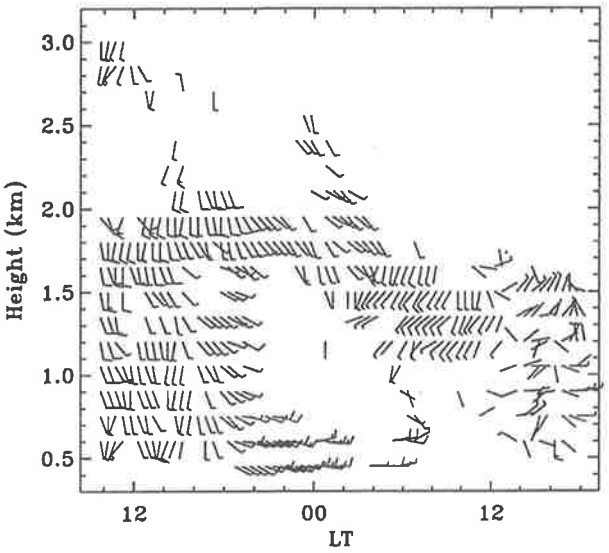

Figure 8. Half-hour average horizontal winds measured between July 31 and August 1, 1997. A half barb represents 2.5 m s^{-1}, and a full barb represents 5 m s^{-1}.

$$P_R \propto \frac{\eta}{R^2} \tag{7}$$

The reflectivity is related to the turbulent refractive index C_n^2, which, in turn, can be expressed in terms of the outer scale of turbulence and the gradient of radio refractive index, M, where

$$M = -77.610^{-6}\frac{p}{T}\left(\frac{\partial ln\theta}{\partial z}\right)\left[1+\frac{15500q}{T}\left(1-\frac{1}{2}\frac{\partial lnq/(\partial z)}{\partial ln\theta/(\partial z)}\right)\right] \tag{8}$$

and z is height [*VanZandt et al.*, 1978]. Vertical profiles of M^2 were constructed from profiles of temperature T, pressure p (measured in hectopascals), potential temperature q, and specific humidity. The observations were made with 2-s time resolution, equivalent to approximately 8–10 m height resolution.

Figure 7 compares SNR values in decibels observed by the radar and estimated from the radiosonde soundings during both day and night conditions. The range-corrected reflectivity profiles constructed from the sonde values have been smoothed to give a height resolution comparable to the radar and have been increased by an arbitrary factor of 175 dB to bring them into approximate coincidence with the radar

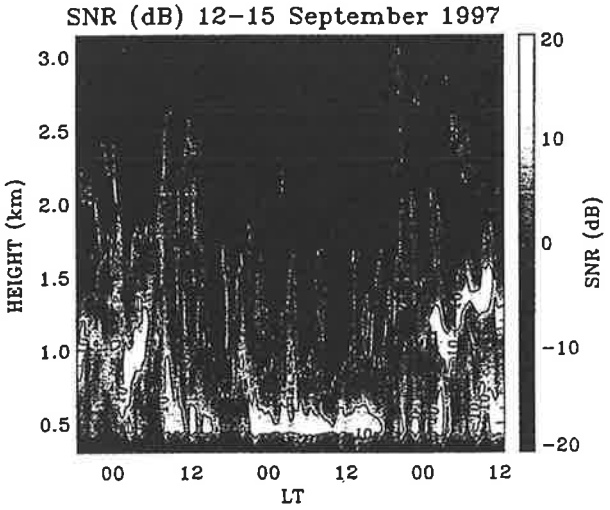

Figure 9. Same as for Figure 6, but for campaign II.

values. It is evident that the profiles agree rather well in shape and indicate that the time delays in the radar system were calibrated reasonably correctly. Both the sonde and radar profiles are characterized by strong peaks at heights near 1500 m and very weak reflectivities at night at heights between 500 and 1200 m.

The corresponding horizontal wind field is shown in Figure 8. The winds were very light, rarely exceeding 5 m s^{-1}. No winds were recorded in the lowest range gate at 300 m due to slower recovery in one of the receivers. However, winds were frequently measured at the second lowest range gate at 450 m, and observations extended to heights near or above 2 km. Noticeable gaps in the wind measurements occurred during periods centered on 0000 and 1000–1200 LT on August 1. In the latter interval, no winds were measured at heights near 0.5 km, despite the fact that the SNR was near 10 dB. The cause was the presence of stronger than average slow fading ground clutter superimposed on the atmospheric echoes. This emphasizes the need for improved clutter suppression. The gap centered on midnight was caused by SNR values that fell as low as -20 dB in the height range between 600 and 1500 m.

3.3. Campaign II

The second case study centered on the passage of a cutoff low across the radar site. A time-height cross section of SNR is shown in Figure 9, and Figure 10 shows the wind field, where its vortex nature is clearly evident. The SNR plot shows little evidence of the layering so evident in Figure 6, and this is also evident in profiles of potential temperature and humidity (Figure 11), which show a much smoother variation with height than is evident in the profiles in Figure 5. The high SNR means that there were often sufficient useful echoes to produce winds at most times at heights between 450 m and 3000 m.

During this campaign, quite heavy rain fell on occasion. The rain gave the opportunity to test the capability of the profiler to distinguish rain echoes from the signals scattered from the clear air despite the expected large amount of spectral broadening due to the wide beam width. That rain echoes can be detected is illustrated in Figure 12, which shows stacked plots of Doppler spectra normalized to the strongest signal in each spectrum. The spectra, which were constructed by averaging nine spectra obtained in a 16-min interval, show strong precipitation echoes with downward velocities in the range 5–10 m s^{-1} in the height range between 500 and 2000 m. At this time the precipitation system was quite shallow. Satellite measurements of cloud top temperatures over Adelaide at this time were only about -10°C, with deeper cloud about 300 km to the east.

The important point is that the clear-air echo can be used to measure the vertical air velocity as a function of height. The ability to distinguish the clear-air and precipitation echoes is also an impor-

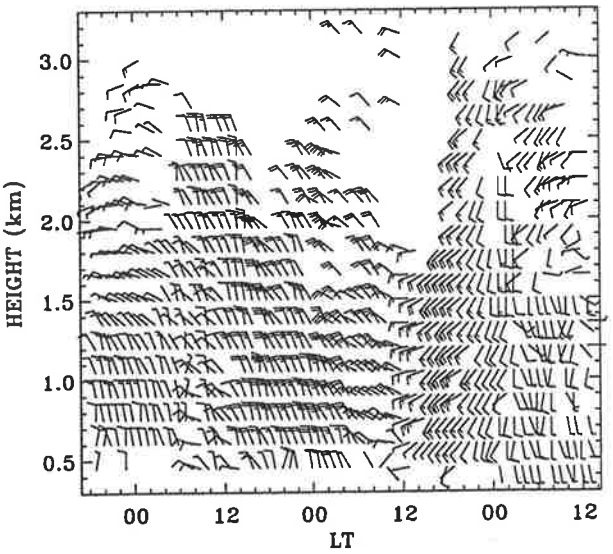

Figure 10. Same as for Figure 8, but for campaign II.

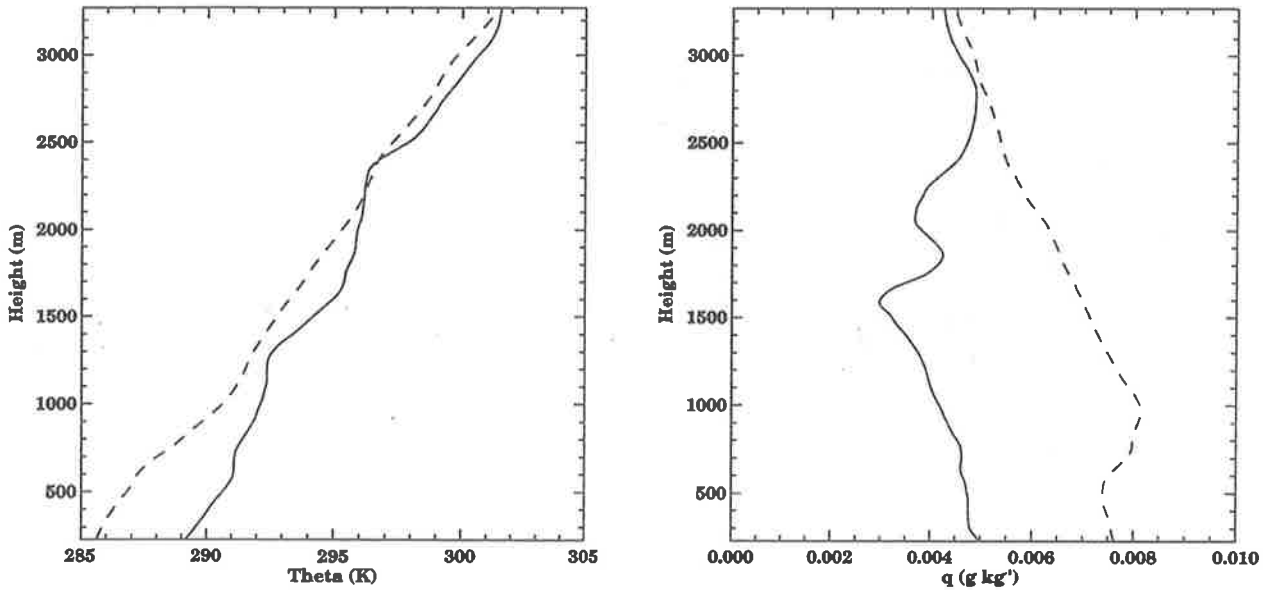

Figure 11. Velocity profiles of (left) potential temperature and (right) specific humidity derived from soundings on September 13 at 1057 LT (solid line) and 2348 LT (dashed line).

tant factor in the deconvolution procedures required to deduce drop-size distributions [*Rajopadhyaya et al.*, 1993]. All these factors illustrate the capability of the VHF profiler for observing mesoscale detail within weather systems, including vertical wind measurements in rain.

3.4. RASS Measurements

In common with other profiler-based RASS systems, the Adelaide BL RASS uses a FM CW acoustic excitation to ensure that a range of temperatures can be measured [*May et al.*, 1990]. Pseudorandom, sawtooth, and triangular sweep types are software selectable, together with appropriate bandwidths and dwell times to ensure a good match at the Bragg frequency [*May et al.*, 1990; *Angevine et al.*, 1994a]. The use of fast digitizers, and limited amounts of coherent integration give an effective sample rate of 320 Hz and ensure a Nyquist frequency significantly higher than the acoustic echo. The power spectra computed from the 1024 point samples at each height encompass both the acoustic-echo peak near 120 Hz and the clear-air echo near 0 Hz.

A number of different modes of operation of the RASS have been evaluated. The acoustic source, which is free running to ensure a flat spectrum over the range of operation [*Angevine et al.*, 1994a], is fed to a 1-kW audio amplifier which drives a vertically pointing stadium horn. Table 5 summarizes the mode of operation currently in use. Data are recorded for 6.4 s and then transferred to the computer; allowing for data transfer and power spectral analysis, the effective sample time is about 10 s. Usually, about 20–30 spectra are incoherently summed to improve the signal-to-noise ratios, which means that the time resolution of the temperature retrievals is 4–5 min. The spectral parameters for the acoustic echo are computed by the moment method, and the vertical velocity derived from the clear-air echo is used to correct the sound speed before it is converted to virtual temperature [e.g., *Angevine et al.*, 1994a].

Comparisons with RASS measurements and virtual temperatures computed from the temperature and humidity profiles derived from collocated radiosonde soundings are shown in Figure 13. RASS measurements were made over a period of 15–20 min near the time of the release of the sondes, and the values shown are the result of averaging four to five data sets so that the bars give an idea of the degree of variability in the retrieved temperatures. It is apparent that the agreement is excellent. The plots also illustrate that temperatures can be measured from heights as low as 500 m to as high as at least 2500 m. However, they also illustrate some of the difficulties that can be encountered with the present experimental setup. *Bauer and Peters* [1993] and *May*

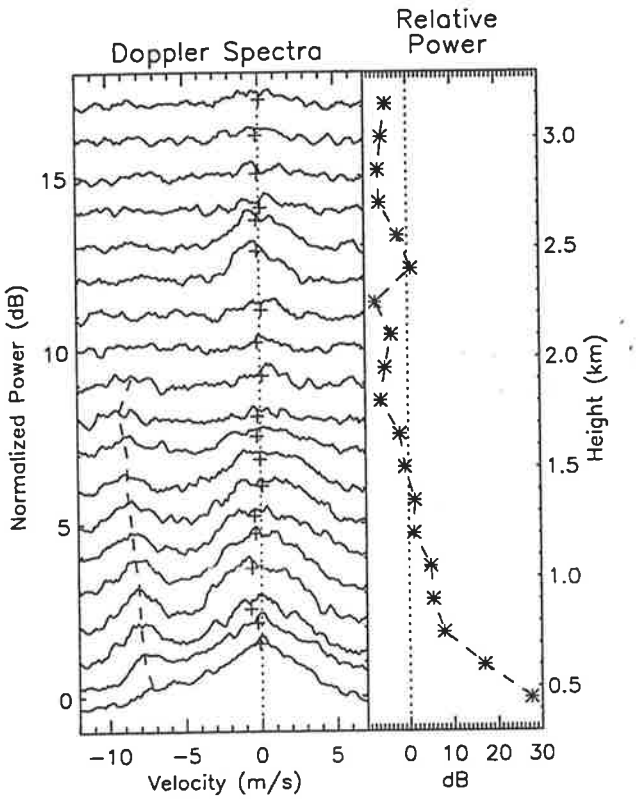

Figure 12. Stacked Doppler spectra obtained between 0400 and 0416 LT on September 14, 1997. At each height the first moment of the clear-air spectral peak, indicated by a plus sign, gives the vertical velocity. The dashed line shows the position of the peak of the precipitation echo. The vertical profile of relative echo power of the clear air peak is shown in the right panel.

et al. [1996] have shown that the RASS signal is focused onto a diffraction-limited spot approximately the size of the transmitting antenna. The small antennas used here mean that the acoustic spot is also small and is easily advected out of the radar beam by the background horizontal winds. It was necessary to carefully place the speaker upwind of the transmitting array to ensure the good height coverage evident in Figure 13a. Future developments include multiple acoustic sources.

4. Conclusions

Here we have discussed the development of a VHF (50 MHz) boundary layer radar and illustrated its capabilities with some of the first results obtained with the system. The system is compact and modular in nature so that it can be operated to use a range of wind-measuring techniques. A notable feature is that very useful wind and temperature measurements were obtained with quite small antennas for transmission and reception. The antennas are a compromise between wanting to make them as small as possible to minimize ringing and thus achieve the desired lower height limit and making them large enough to obtain sufficient gain to attain the desired upper height limit and to reduce clutter and interference.

Initial measurements made with the new boundary layer VHF radar show that its performance meets the design specifications, with wind and temperature measurements being made with good accuracy on a regular basis to over 2 km in altitude. The ability to distinguish rain echoes from the clear-air echo has also been demonstrated. This is an important attribute, which will allow the study of precipitation drop-size distributions to be extended downward into the boundary layer. Overall, the performance compares well with UHF profilers operating near 1 GHz at a similar stage of their development [*Ecklund et al.*, 1990; *Hashiguchi et al.*, 1995].

The next stage is to improve the height coverage. Wind and temperature measurements are made reg-

Table 5. Typical Radio Acoustic Sounding System Operating Parameters

Parameter	Value
Pulse repetition frequency*	20,480 Hz
Number of coherent integrations*	64
Number of data points per sample*	2,048
Height coverage*	100–3100 m
Record length	6.4 s
Range resolution*	150 m
Nyquist frequency	160 Hz
Acoustic frequency range*	118–126 Hz
Acoustic power	~150 W
Acoustic excitation*	FM CW sawtooth sweep
Acoustic steps*	200
Frequency step*	0.04 Hz
Dwell time (per frequency step)*	100 ms

*Software selectable.

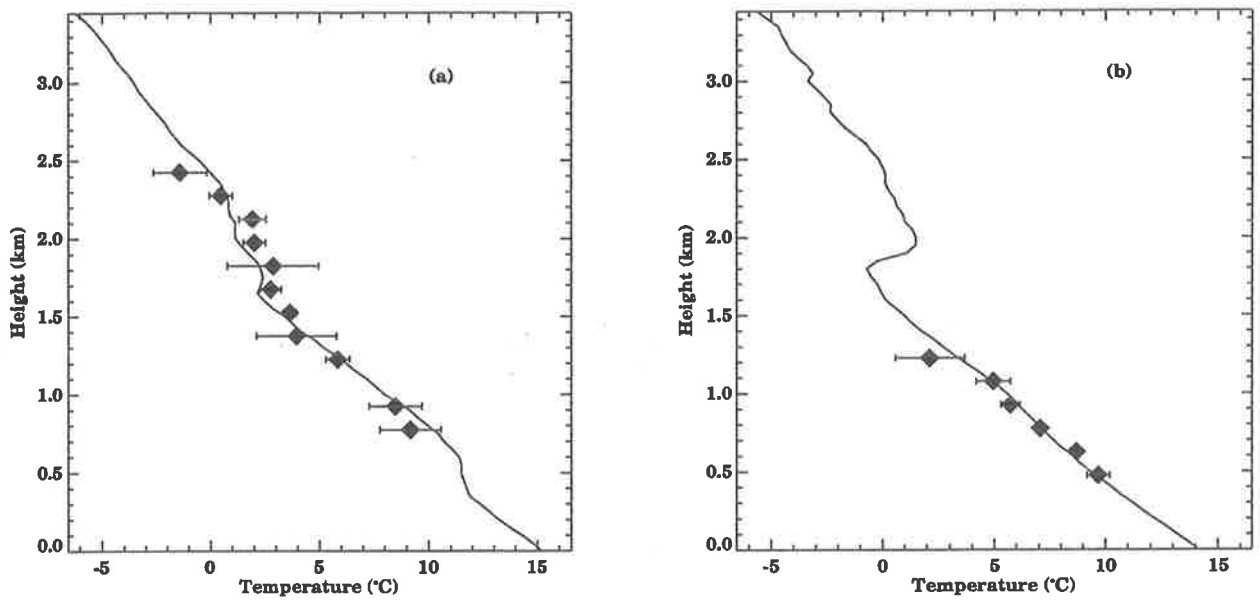

Figure 13. (a) Profile of virtual temperature derived from a radiosonde sounding at 1530 LT on October 18, 1997. Radio acoustic sounding system measurements made from 1500 to 1515 LT are indicated by diamonds. (b) Same as for (a), but for 1750 LT on October 19, 1997 with RASS measurements made from 1732 to 1805 LT.

ularly to heights as low as 450 m and sometimes as low as 300 m. Recent testing shows that it is possible to get to lower heights by using pulse lengths of 0.75 μs and exploiting the capacity of the system to make observations with a 100-m range resolution. Similarly, the upper height limit is improved by increasing the mean power, either by using pulse coding or using longer pulses to give a 300-m resolution. Using 300-m pulses, it has been possible to achieve observations as high as 5000 m. It should also be possible to use somewhat larger antennas for both transmission and reception, which will improve the power-aperture product and hence over-all system sensitivity. Tests of the system with these improvements are now in progress, as are tests using interferometric techniques to better define the dominant directions of scatter and correct the vertical velocities.

Acknowledgments. The development of the radar was made possible by the support of grant A69331543 from the Australian Research Council. The help and provision of radiosonde equipment by J. Stickland, Australian Bureau of Meteorology, and M. J. Reeder, Monash University, are gratefully acknowledged.

References

Angevine, W. M., and J. I. MacPherson, Comparison of wind profiler and aircraft wind measurements at Chebogue Point, Nova Scotia, *J. Atmos. Oceanic Technol., 12*, 421-426, 1995.

Angevine, W. M., W. L. Ecklund, D. A. Carter, K. S. Gage, and K. P. Moran, Improved radio acoustic sounding techniques, *J. Atmos. Oceanic Technol., 11*, 42-49, 1994a.

Angevine, W. M., A. B. White, and S. K. Avery, Boundary layer depth and entrainment zone characterization with a boundary layer profiler, *Boundary Layer Meteorol., 68*, 375-385, 1994b.

Bauer, M., and G. Peters, On the altitude coverage of temperature profiling by RASS, in *26th International Conference on Radar Meteorology*, pp. 487-489, Am. Meteorol. Soc., Boston, Mass., 1993.

Briggs, B. H., The analysis of spaced sensor records by correlation techniques, in *Handbook for MAP*, vol. 13, edited by R. A. Vincent, pp. 166-186, SCOSTEP, Secr. Univ. of Ill., Urbana, 1984.

Briggs, B. H., Radar measurements of aspect sensitivity of atmospheric scatterers using spaced-antenna correlation techniques, *J. Atmos. Sol. Terr. Phys., 54*, 153-165, 1992.

Carter, D. A., K. S. Gage, W. L. Ecklund, W. M. Angevine, P. E. Johnston, A. C. Riddle, J. Wilson, and C. R. Williams, Developments in UHF lower tropospheric wind profiling at NOAA's Aeronomy Laboratory, *Radio Sci., 30*, 977-1001, 1995.

Crochet, M., C. Bourdier, and E. Spano, VHF ST radar for low altitude investigations, in *Proceedings of the 6th Workshop on Technical and Scientific Aspects of MST Radar*, edited by B. Edwards, pp. 128-131, SCOSTEP, Secr. Univ. of Ill., Urbana, 1994.

Ecklund, W. L., D. A. Carter, and B. B. Balsley, A UHF wind profiler for the boundary layer: Brief description and initial results, *J. Atmos. Oceanic Technol., 5*, 432-441, 1988.

Ecklund, W. L., D. A. Carter, B. B. Balsley, P. E. Currier, J. L. Green, B. L. Weber, and K. S. Gage, Field tests of a lower tropospheric wind profiler, *Radio Sci., 25*, 899-906, 1990.

Fillol, J.-M., P. Broche, and M. Crochet, Retrieval of stratified atmospheric reflectivity and wind velocity using inverse methods: Application to a VHF ST mini-radar, *J. Atmos. Sol. Terr. Phys., 59*, 1159-1177, 1997.

Gage, K. S., Radar observations of the free atmosphere: Structure and dynamics, *Radar in Meteorology*, edited by D. Atlas, pp. 534-565, Am. Meteorol. Soc., Boston, Mass., 1990.

Hashiguchi, H., S. Fukao, T. Tsuda, M. D. Yamanaka, D. L. Tobing, T. Sribimati, S. W. Harijono, and H. Wiryosumarto, Observations of the planetary boundary layer over equatorial Indonesia with an L-band clear-air Doppler radar: Initial results, *Radio Sci., 30*, 1043-1054, 1995.

Holdsworth, D. A., Signal analysis with applications to atmospheric radars, Ph.D. thesis, 371 pp., Univ. of Adelaide, Adelaide, South Aust., Australia, 1995.

Jordan, J. R., R. J. Lataitis, and D. A. Carter, Removing ground and intermittent clutter contamination from wind profiler signals using wavelet transforms, *J. Atmos. Oceanic Technol., 14*, 1280-1297, 1997.

May, P. T., Spaced antenna versus Doppler radars: A comparison of techniques revisited, *Radio Sci., 25*, 1111-1119, 1990.

May, P. T., The Australian nocturnal jet and diurnal variations of boundary-layer winds over Mt. Isa in north-eastern Australia, *Q. J. R. Meteorol. Soc., 121*, 987-1003, 1995.

May, P. T., R. G. Strauch, and K. P. Moran, The altitude coverage of temperature measurements using RASS with wind profiler radars, *Geophys. Res. Lett., 15*, 1381-1384, 1988.

May, P. T., R. G. Strauch, K. P. Moran, and W. L. Ecklund, Temperature sounding by RASS with wind profiler radars: A preliminary study, *IEEE Trans. Geosci. Remote Sens., 28*, 19-28, 1990.

May, P. T., T. Adachi, T. Tsuda, and R. J. Lataitis, The spatial structure of RASS echoes, *J. Atmos. Oceanic Technol., 13*, 1275-1284, 1996.

Rajopadhyaya, D., P. T. May, and R. A. Vincent, A general approach to the retrieval of rain drop-size distributions from VHF wind profiler Doppler spectra: Modelling results, *J. Atmos. Oceanic Technol., 10*, 710-717, 1993.

Riddle, A. C., W. M. Angevine, W. L. Ecklund, E. R. Miller, D. B. Parsons, D. A. Carter, and K. S. Gage, In situ and remotely sensed horizontal winds and temperature intercomparisons obtained using integrated sounding systems during TOGA COARE, *Beitr. Phys. Atmos., 69*, 49-61, 1996.

Röttger, J., The MST radar technique, in *Handbook for MAP*, vol. 13, edited by R. A. Vincent, pp. 187-232, SCOSTEP, Secr., Univ. of Ill., Urbana, 1984.

Strauch, R. G., D. A. Merritt, K. P. Moran, K. B. Earnshaw, and D. Van de Kamp, The Colorado wind profiling network, *J. Atmos. Oceanic Technol., 1*, 37-49, 1984.

VanZandt, T. E., J. L. Green, K. S. Gage, and W. L. Clark, Vertical profiles of refractivity turbulence structure constant: Comparison of observations by the Sunset radar with a new theoretical model, *Radio Sci., 13*, 819-829, 1978.

Vincent, R. A., and J. Röttger, Spaced antenna VHF radar observations of tropospheric velocities and irregularities, *Radio Sci., 15*, 319-335, 1980.

Vincent, R. A., P. T. May, W. K. Hocking, W. G. Elford, B. H. Candy, and B. H. Briggs, First results with the Adelaide VHF radar: Spaced antenna studies of tropospheric winds, *J. Atmos. Sol. Terr. Phys., 49*, 353-366, 1987.

Weber, B. L., and D. A. Wuertz, Comparison of rawinsonde and wind profiler radar measurements, *J. Atmos. Oceanic Technol., 7*, 157-174, 1990.

Wilczak, J. M., et al., Contamination of wind profiler data by migrating birds: Characteristics of corrupted data and potential solutions, *J. Atmos. Oceanic Technol., 12*, 449-467, 1995.

Wilson, K. J., and H. Stern, The Australian summertime cool change, 1, Synoptic and sub-synoptic aspects, *Mon. Weather Rev., 113*, 177-201, 1985.

Wright, J. W., and M. L. V. Pitteway, Computer simulations of ionospheric radar drift measurements and their analysis by correlation methods, *Radio Sci., 13*, 189-210, 1978.

S. Dullaway, A. MacKinnon, I. M. Reid, R. A. Vincent, and F. Zink, Department of Physics, University of Adelaide, Adelaide, SA 5005, Australia. (e-mail: rvincent@physics.adelaide.edu.au)

B. H. Johnson, Atmospheric Radar Systems, 1/12 Sterling St., Thebarton, SA 5031, Australia. (e-mail: bjohnson@atrad.com.au)

P. T. May, Bureau of Meteorology Research Centre, PO Box 1289K, Melbourne, VIC 3001, Australia. (e-mail: p.may@bom.gov.au)

(Received December 17, 1997; revised March 5, 1998; accepted March 10, 1998.)

Appendix B

Wavelet analysis of stratospheric gravity wave packets over Macquarie Island, I: Wave parameters

This is a preprint of a paper submitted to the *Journal of Geophysical Research.*

Submitted to *J. Geophys. Res.*,

Wavelet analysis of stratospheric gravity wave packets over Macquarie Island, I: Wave parameters

Florian Zink and Robert A. Vincent

Department of Physics and Mathematical Physics, University of Adelaide, Adelaide, South Australia

Abstract. We describe a technique to detect gravity wave packets in high-resolution radiosonde soundings of horizontal wind and temperature. The vertical profiles of meridional and zonal wind speeds are transformed using the Morlet wavelet and regions of high wind variance in height-wavenumber space are identified as gravity wave packets. Application of the Stokes parameter analysis to horizontal wind and temperature profiles of the reconstructed wave packets yields the wave parameters. The technique was applied to twice-daily radiosonde launches at Macquarie Island (55°S, 159°E) between 1993 and 1995.

1. Introduction

Gravity waves play an important role in driving the circulation of the atmosphere as demonstrated in numerical modeling studies [*Lindzen*, 1981; *Holton*, 1982; *Dunkerton*, 1982; *Garcia and Solomon*, 1985]. Since the resolution of general circulation models is usually too coarse to adequately resolve gravity waves, several gravity wave parameterization schemes have been developed to take these unresolved wave effects into account [*Lindzen*, 1981; *Fritts and VanZandt*, 1993; *Hines*, 1997; *Warner and McIntyre*, 1999]. These models generally require information about the gravity wave spectrum at a certain source level which is then propagated through the atmosphere. In a physically realistic model the choice of this source spectrum is influenced by experimental observations of the gravity wave field at the source height and by the agreement of the parameterized effects with measurements throughout the atmosphere.

Many experimental campaigns have been conducted to study characteristics and effects of gravity waves in the lower, middle, and upper atmosphere over the last decades. While some methods aim to directly measure the momentum fluxes associated with the gravity wave field [*Vincent and Reid*, 1983; *Fritts et al.*, 1990; *Sato*, 1994; *Alexander and Pfister*, 1995], others try to obtain information about the gravity wave activity from gravity wave induced perturbations of the wind and temperature fields. Radar winds have been analyzed in the lower and middle atmosphere at several locations, but the geographical coverage of these campaigns is rather sparse. The increasing use of high resolution radiosondes for operational soundings of the lower atmosphere, on the other hand, has the potential to compile a global climatology of gravity wave activity around the world [*Hamilton and Vincent*, 1995]. As each method can only observe a part of the gravity wave spectrum, however, different methods have to be used together to enable a better understanding of the processes involved [*Alexander*, 1998].

Methods to extract gravity wave parameters from vertical profiles of wind (and temperature) usually rely on the polarization relations for a single monochromatic gravity wave. The existence of multiple waves in the analyzed profiles might lead to erroneous results as demonstrated, for example, by *Eckermann and Hocking* [1989]. It is, therefore, important to ensure that only a single wave is present in the analyzed height profile. One possible step towards this goal is the decomposition of the vertical profile into different height [*Sato*, 1994] or wavelength bands [*Gonella*, 1972; *Eckermann and Vincent*, 1989; *Cho*, 1995]. The choice of a uniform width of the height or wavelength bands, however, will favour the detection of waves of a certain scale. Narrow height bands, for example, favour the detection of waves with small vertical wavelengths, as a wave with large vertical wavelength would appear as a trend in the background wind [*Vincent et al.*, 1997]. Narrow wavelength bands, on the other hand, imply large height intervals which opens the possibility of the coexistence of different wave packets at different heights in the vertical profile. The application of wavelet analysis can solve this dilemma to a certain extent, as it automatically adapts the window height according to the wavelength under consideration, keeping a constant ratio of wavelength to window height. The detection of wave packets by wavelet analysis is, therefore, a more objective means for the detection of wave packets than the decomposition of the vertical profile into uniform height or wavelength bands. Furthermore,

it also yields information about the height extent of the gravity wave packets. This information will be used in a companion paper [*Zink and Vincent*, this issue], to gain some insight into source intermittency, i.e. the fraction of time the gravity wave source emits waves of a certain frequency and wavelength.

In this paper, we develop a wavelet-based method to decompose vertical profiles of horizontal wind into gravity wave packets. While wavelet analysis has been applied to wind and temperature fluctuations in the atmosphere previously [*Sato and Yamada*, 1994; *Chen et al.*, 1995; *Shimomai et al.*, 1996], these studies mainly concentrated on the changes of the wavelet spectrum with time or height, and less on the packet structure of the gravity wave field. Section 2 gives a short definition of the wavelet transform and describes its application to the extraction of wave packets and their characteristics from radiosonde data. In Section 3 we apply the algorithm to two years of radiosonde data from Macquarie Island and discuss the deduced gravity wave parameters. We end the paper with a short summary and conclusion in Section 4. The relevant gravity wave dispersion and polarization relations are derived in the Appendix.

2. The wavelet transform

2.1. Basic formalism

In this section we give the definitions necessary to implement the wavelet analysis described in this paper. For a more detailed description and a review of wavelet applications in geophysics see *Kumar and Foufoula-Georgiou* [1997] and references therein.

The term wavelets refers to a family of small waves generated from a single function $g(z)$, the so-called mother wavelet, by a series of dilations and translations. A sufficient condition for a function $g(z)$, real or complex, to qualify as a mother wavelet is admissibility,

$$c_g = \int_{-\infty}^{+\infty} \frac{|G(m)|^2}{|m|} \mathrm{d}m < \infty, \tag{1}$$

where $G(m)$ is the Fourier transform of $g(z)$. If $g(z)$ is an integrable function, it only has to be oscillatory, of finite energy and with an average value of zero to fulfill this criterion.

The continuous wavelet transform of a real function $f(z)$ with respect to a given admissible mother wavelet $g(z)$ at scale a and dilation b is then defined as

$$W_f(a,b) = \frac{1}{a} \int_{-\infty}^{+\infty} f(z) g^*(\frac{z-b}{a}) \mathrm{d}z, \tag{2}$$

where $a > 0$, $b \in \mathbf{R}$, and * denotes the complex conjugate. The wavelet transform gives the correlation between the original function $f(z)$ and the scaled and translated version of the mother wavelet, $g(\frac{z-b}{a})$, i.e. it measures how well the two signals match. The transform can also be expressed in Fourier space as

$$W_f(a,b) = \frac{1}{2\pi} \int_{-\infty}^{+\infty} G^*(am) F(m) \exp^{imb} \mathrm{d}m, \tag{3}$$

Admissibility is required to make sure that the original function $f(z)$ can be reconstructed from its wavelet transform without any loss of information. This reconstruction can be accomplished by summing scaled and translated versions of the mother wavelet appropriately weighted with the wavelet coefficients $W_f(a,b)$:

$$f(z) = \frac{1}{c_g} \int_0^{+\infty} \int_{-\infty}^{+\infty} W_f(a,b) g(\frac{z-b}{a}) \frac{\mathrm{d}b\mathrm{d}a}{a^2}. \tag{4}$$

The continuous wavelet transform (2) is calculated for all points of the $a > 0 - b \in \mathbf{R}$-plane and shows a high degree of redundancy. Due to this redundancy it is possible to reconstruct the original function using a completely different mother wavelet, e.g. the delta function [*Farge*, 1992]:

$$f(z) = \frac{1}{c_\delta} \int_0^{+\infty} W_f(a,z) \frac{\mathrm{d}a}{a}, \tag{5}$$

where

$$c_\delta = \int_0^{+\infty} W_\delta(a,0) \frac{\mathrm{d}a}{a}. \tag{6}$$

With the normalization chosen above, the modulus square of the wavelet coefficients, $E(a,b) = |W_f(a,b)|^2$, can be interpreted as an energy density, at least for bandfilter-like mother wavelets. The total energy of the signal is given by

$$E_{tot} = \frac{1}{c_g} \int_0^{+\infty} \int_{-\infty}^{+\infty} E(a,b) \mathrm{d}b \frac{\mathrm{d}a}{a}. \tag{7}$$

An important point in the application of the wavelet transform to real world data is the choice of a suitable mother wavelet. As the horizontal wind perturbations u' and v' of a gravity wave packet are essentially amplitude modulated sine waves, the Morlet wavelet seems to be an obvious choice. It has the representations

$$g(z) = e^{i \cdot 5.4 \cdot z} e^{-\frac{z^2}{2}} \tag{8}$$

$$G(m) = \sqrt{2\pi} e^{-\frac{(m-5.4)^2}{2}} \tag{9}$$

in real and Fourier space, respectively. As a progressive wavelet, the Morlet wavelet has non-zero contributions only for $m > 0$, i.e. its real and imaginary parts are 90° out of phase. The relation between wavelet scale a and equivalent Fourier wavelength λ of a certain mother wavelet can be derived by wavelet transforming a sine wave of given wavelength λ [*Meyers et al.*, 1993]. In the case of the Morlet wavelet (8) it is given by $\lambda = 1.14a$.

The Morlet wavelet is not orthogonal and the wavelet coefficients are not independent. This means that the total energy of a superposition of different wavelets is not necessarily equal to the sum of the energies of each of the wavelets. The choice of an orthogonal wavelet would resolve this problem, but one has to keep in mind that the propagation of gravity waves through the atmosphere includes nonlinear saturation effects. The proper treatment of these nonlinear effects requires knowledge about the peak amplitudes of the gravity wave packets as physical entities. While the wavelet coefficients of an orthogonal wavelet transform are independent in the mathematical sense, several of these coefficients have to be used together to represent an actual physical wave packet and to reconstruct its peak amplitude. We, therefore, find it more convenient to decompose the wind field using basis functions with a strong resemblance to the physical gravity wave packets. The assumed similarity of the physical wave packets with the Morlet wavelet also facilitates the extraction of wave parameters.

2.2. Practical implementation

The calculation of the wavelet transform was performed in Fourier space using (3) and implemented as follows:

First, the real data series $f(z)$ is padded on both sides to avoid wrap-around effects. The number of points to be added depends on the largest wavelength to be considered. Equation 2 states, that the wavelet transform for a scale a at position b is given by integrating over the product of the data series $f(z)$ and the wavelet of scale a with its center at b. As the Fourier transform assumes periodicity of the transformed data series, any overhang of the wavelet at the end of the data series is wrapped around to the start of the data series, leading to undesirable contributions to the integral. If we assume the largest scale wavelet to extend over a length of approximately $L/2$ on each side of its center, the data series has to be padded with this length to avoid any wrap-around effects. This padded data series is then Fourier transformed and, for each scale a of interest, multiplied by the Fourier transform $G(am)$ of the scaled mother wavelet. Inverse Fourier transforming and unpadding then yields the complex wavelet transform $W_f(a,b)$. Its real part contains the data series $f(z)$ bandpass filtered according to scale a, and its imaginary part a 90° phase-shifted version thereof. Its modulus corresponds to the envelope of the bandpass-filtered signal. Figure 1 gives an example of the wavelet transform of a hypothetical wind profile using the Morlet wavelet.

2.3. Application to radiosonde data

In order to detect wave packets in the horizontal wind data, we first calculate the wavelet coefficients $W_u(a,z)$ and $W_v(a,z)$ of the vertical profiles of zonal and meridional wind components, $u(z)$ and $v(z)$, respectively. Then we scan the surface $S(a,z) = |W_u(a,z)|^2 + |W_v(a,z)|^2$ for local maxima (cf. Figure 1c). Only maxima exceeding a certain threshold S_{thresh} are retained in the further analysis. For each of these maxima the extension of the corresponding wave packet is recorded. The boundaries (z_1, z_2 and a_1, a_2 for height and scale, respectively) are determined by scanning the surface $S(a,z)$ descending from the maximum at $(a_{\max}, z_{\max})$ until it drops to a value $\frac{1}{4}S(a_{\max}, z_{\max})$ or starts rising again.

The wave packets can now be reconstructed by adding up the complex wavelet coefficients of all contributing scales $a_1 \ldots a_2$ at each height $z_1 \ldots z_2$ for u, v, and T (Equation 5). The resulting profiles now contain the isolated wave packet as their real part, and its 90° phase-shifted (i.e. Hilbert transformed) version as their imaginary part. We use the full width half maximum

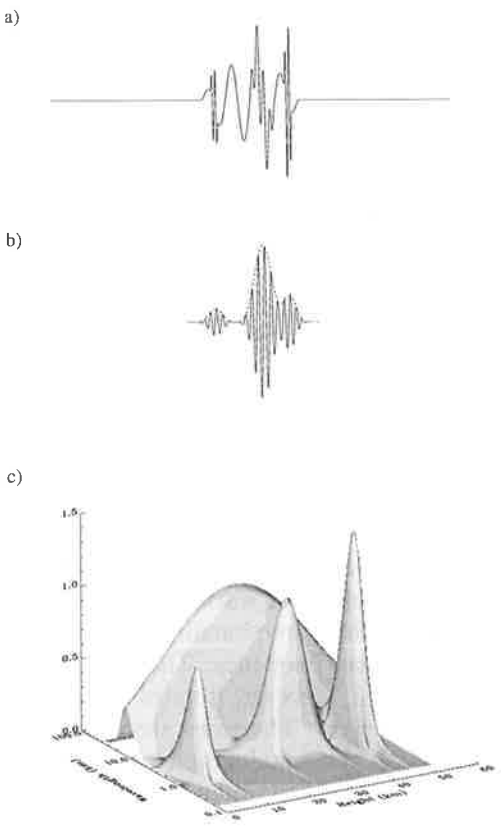

Figure 1. Example of the wavelet transform of a hypothetical wind profile using the Morlet wavelet. a) The hypothetical wind profile, padded to avoid wrap-around effects. b) Wavelet transform of the profile in a) for a certain scale a. The solid line represents the real part, the dashed line the modulus of the transform. c) Surface plot of the modulus of the wavelet transform as a function of wavelength and height. The four wave packets are clearly resolved.

of the horizontal wind variance of the reconstructed wave packet as its vertical extension. The horizontal and vertical propagation directions of the wave packet are extracted by Stokes parameter analysis [*Vincent and Fritts*, 1987; *Eckermann and Vincent*, 1989; *Eckermann*, 1996]. The ambiguity in the horizontal propagation direction is resolved using the phase differences between temperature and horizontal perturbation velocities (A12). The intrinsic frequency $\hat{\omega}$ is obtained from the ratio of the average horizontal perturbation velocities parallel and perpendicular to the wave propagation direction (A10), and the horizontal wavenumber is given by the dispersion relation (see Appendix). Hodograph analysis uses polarization relations for a single monochromatic gravity wave to infer the intrinsic frequency and orientation of the analyzed wave packet. *Eckermann and Hocking* [1989] demonstrated that in the case of multiple wave packets the inferred intrinsic frequency can be an effect of wave superposition and might indicate azimuthal directionality in wave propagation rather than mean frequency. The wavelet based method described here, however, isolates wave packets in wavenumber and height. Therefore, the possibility of multiple wave packets in the hodograph analysis is much reduced compared to more traditional Fourier methods, where the whole height range is analyzed as a single wave. The analysis of a single radiosonde sounding, however, does not allow filtering of the observed oscillations in frequency. It is, therefore, important to keep in mind, that it is not possible to distinguish different wave packets in a hodograph if they agree in vertical wavenumber.

If two wave packets are close in height-scale space, the boundaries used to reconstruct the wave packets might overlap, i.e. certain wavelet coefficients might be used for the reconstruction of more than one wave packet. In these cases, the horizontal wind variance corresponding to these wavelet coefficients is divided between the reconstructed wave packets in equal parts in order to conserve the total wind variance.

3. Observation of stratospheric gravity waves over Macquarie Island

3.1. Radiosonde Data and Background Atmosphere

Macquarie Island (55°S, 159°E) is situated approximately 1500 km south of Tasmania in the sub-antarctic storm track. It is aligned north-south with a length of 34 km and a maximum width of 5.5 km. Its maximum height is 433 m above sea level [*Crohn*, 1986]. The winds at Macquarie Island are predominantly eastward with a high frequency of gales. A front or depression center passes the island every 5 or 6 days [*Streten*, 1988].

The Australian Bureau of Meteorology has a weather station on the north part of the island. Operational

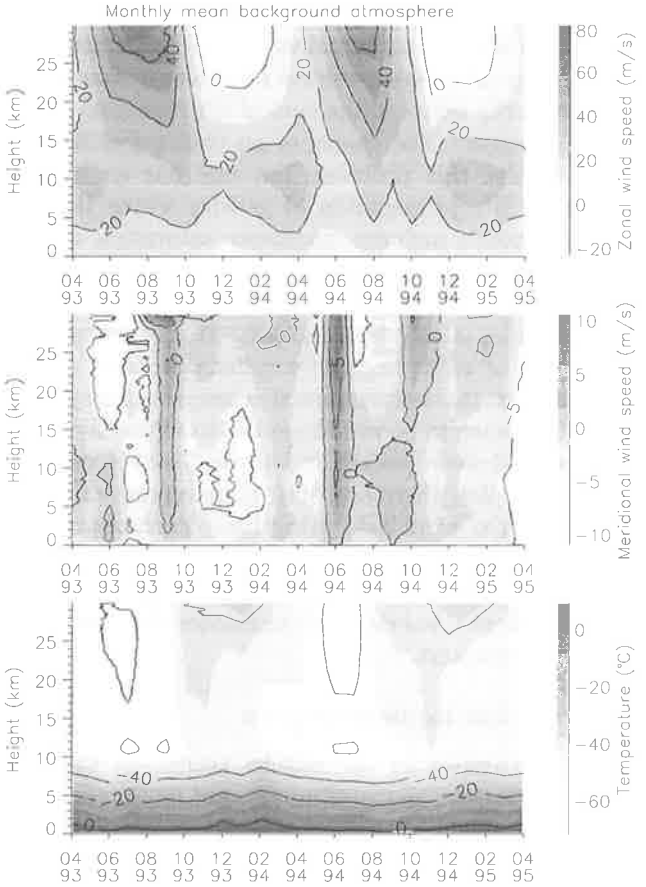

Figure 2. Monthly mean profiles of horizontal winds and temperature over Macquarie Island.

radiosonde soundings are usually performed twice daily, and the sondes reach typical heights of about 25 to 30 km. Every two seconds the radiosondes (Vaisala RS 80-15) measure the current values of pressure, temperature and humidity. After filtering and smoothing they are recorded at 10 s intervals at the ground station. With an average balloon ascent rate of 5 ms^{-1} this results in a height resolution for the temperature profile of about 50 m. The finite response time of the temperature sensor attenuates high wavenumber fluctuations to a certain extent. Although it is possible to compensate for this effect [*Allen and Vincent*, 1995], no attempts were made in the present study. The accuracy of the temperature measurements is specified as ±0.1° C rms. The zonal and meridional wind components, calculated from the radiosonde position over time, are reported every 10 s. After outlier removal a cubic spline is fitted over a running window of 130 s, corresponding to an actual height resolution of about 650 m. Wind fluctuations at scales smaller than this will therefore be attenuated in some way. Note, that this fitting interval was changed to 250 s (1250 m) at the end of January 1994. The rms random errors in each wind component are believed to be about 0.5 ms^{-1}. It is important to keep in mind

that the different treatment of temperature and wind data can distort amplitude and phase relations between these data sets.

Due to the finite ascent rate of the balloon, the gravity wave field undergoes changes while the profiles of wind and temperature are gathered (with an ascent rate of 5 ms^{-1} a launch to a final height of 30 km takes about 100 min), and the sonde itself experiences a horizontal drift. As we are not interested in the phase relation between packets in different height regions, we do not require different packets to be sampled simultaneously. We only require that the time taken to sample a certain coherent wave packet is small compared to its period. Deviations from an instantaneous, vertical profile are generally assumed to be insignificant if the mean winds are less than about 50 ms^{-1} [*Gardner and Gardner*, 1993].

Figure 2 presents the monthly mean horizontal winds and temperature over the analyzed time period. The monthly mean profiles were calculated as the average over all radiosonde launches within that particular month. The zonal winds are particularly strong during winter (April to October) and reverse sign above 22 km during summer (November to March). The mean meridional winds are much weaker with an amplitude of less than about 5 ms^{-1}. The variations in background temperature are most significant in the stratosphere and the tropopause is at a height of about 10 km throughout the whole year.

3.2. Gravity Wave Parameters

The wavelet analysis of the gravity wave field was performed starting at a height of 12000 m MSL using wavelengths $\lambda_i = 450. \cdot 2^{i/8}, i = 0 \ldots 39$. The profiles of u, v, and T were prefiltered with a fifth order Butterworth filter with half-power points at 450 m and 11000 m or the height extent of the radiosonde data, whichever was less. The parameter S_{thresh} was selected as 0.01 m^2s^{-2}. Results here are given as averages per radiosonde flight and function of wavelength or height. In forming these averages the height (and, therefore, wavelength) coverage of the contributing radiosonde flights was taken into account.

Figure 3 shows the average monthly horizontal wind variance $\langle u'^2 + v'^2 \rangle$ as a function of height for upwards and downwards propagating gravity wave packets. The vertical propagation direction of the wave packets was obtained from the Stokes parameter analysis as the sense of rotation of the hodograph, with anti-clockwise rotation with increasing height indicating upwards energy propagation in the Southern hemisphere. The decrease in variance from January 1994 on is probably due to the increased phase fitting length. Note that we here present the gravity wave activity in terms of horizontal wind variance since this variable is directly accessible by measurement and does not depend on other inferred

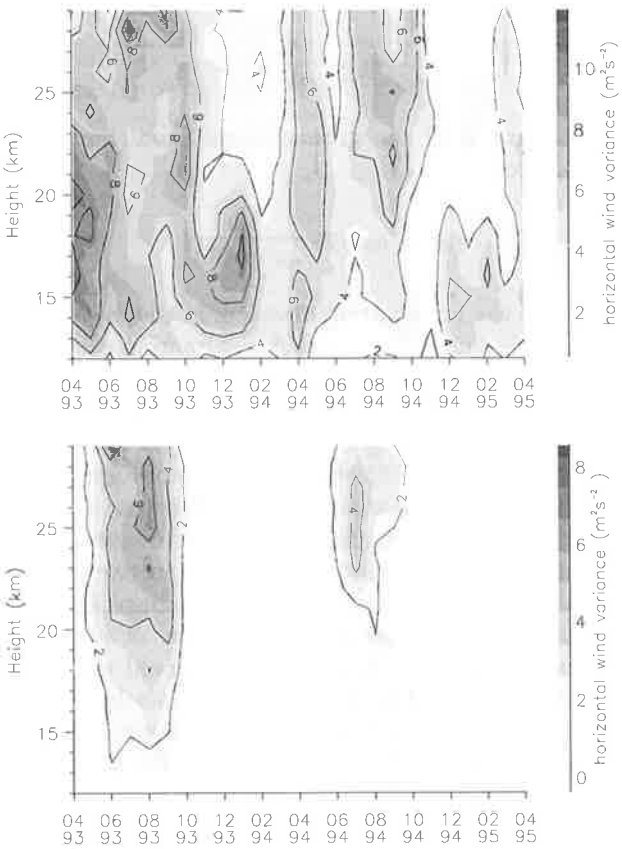

Figure 3. Monthly averaged horizontal wind variance $\langle u'^2 + v'^2 \rangle$ as a function of height and time for upwards (top) and downwards propagating gravity wave packets (bottom).

gravity wave parameters like, for example, wave action does.

In our analysis we will mainly concentrate on the height region from 20 to 28 km, as the waves in this region are important for the wave-mean wind interactions in the middle and upper atmosphere. As will be seen later, waves detected below this region are filtered to a certain extent during their upward propagation. The two phases to be considered are summer (November to March) and winter (April to October). Between 40 and 60 soundings per month reached a height of above 20 km and could be used in our analysis.

Figures 4 to 6 summarize the parameters of the gravity waves detected in the height range 20 to 28 km for upwards propagating gravity waves in summer and upwards and downwards propagating gravity waves in winter, respectively. The statistics for downwards propagating gravity waves during summer are too poor to form reliable parameter estimates. The top panels of Figures 4 to 6 present the horizontal wind variance as a function of intrinsic horizontal propagation direction,

the ground-based horizontal group velocity

$$\mathbf{c_g} = \frac{\partial \omega}{\partial \mathbf{k}_h}, \tag{10}$$

and histograms of the ground-based zonal horizontal phase speed

$$c_{\text{phase,zonal}} = \frac{\omega}{k_h \cos(\Phi)}, \tag{11}$$

where Φ is the propagation direction in the mathematical sense, i.e. in degrees anti-clockwise from east. The group velocity is important for ray-tracing studies to find the origin of the observed wave packets. For each detected wave packet $\mathbf{c_g}$ is represented by a point in the top middle diagram. The bottom panels of Figures 4 to 6 show the horizontal wind variance of the wave field in histogram form as a function of intrinsic frequency and vertical and horizontal wavelength, respectively. The vertical and horizontal wavelengths are binned logarithmically to take the proportionality $\Delta m \propto m$ of the wavelet analysis into account. The observed wave field is clearly dominated by low-frequency (inertio) gravity waves with an average horizontal wavelength of several hundred kilometers. A shift to higher intrinsic frequencies is evident in winter, when large zonal wind speeds occur. The horizontal wind variance peaks at vertical wavelengths around 4 km. Keep in mind, however, the choice of our high wavelength cutoff of 11 km and that the filtering performed by the radiosonde equipment attenuates wavelengths less than about 1 km. The mean values of intrinsic frequency, horizontal and vertical wavelength, and groundbased zonal phase speed are given in Table 1.

3.3. Discussion

3.3.1. Seasonal variation of total gravity wave variance A closer look at the total gravity wave horizontal wind variance and the zonal background wind speed averaged over the height range from 20 to 28 km as a function of time reveals a good correlation between these two variables (Figure 7). Both show a clear annual cycle with maximum values of about 9 m^2s^{-2} and 60 ms^{-1}, respectively, in July/August and minima of about 3 m^2s^{-2} and -5 ms^{-1}, respectively, around January. A similar annual cycle of gravity wave activity has been observed at a multitude of sites in the mid- and highlatitudes in both hemispheres [*Allen and Vincent*, 1995; *Eckermann et al.*, 1994]. Different mechanisms exist to explain this seasonal variability:

Source strength: Changes in wave generation at the source level will lead to variability in wave activity at higher altitudes. Well-known sources of gravity waves in the lower atmosphere are topography [*Smith*, 1985; *McFarlane*, 1987; *Hines*, 1988; *Nastrom and Fritts*, 1992], thunderstorms [*Fovell et al.*, 1992; *Pfister et al.*, 1993; *Alexander et al.*, 1995], fronts [*Fritts and Nastrom*, 1992; *Griffiths and Reeder*, 1996; *Reeder and Griffiths*, 1996], wind shear [*Lalas and Einaudi*, 1976; *Chimonas and Grant*, 1984; *Fritts*, 1982] and geostrophic adjustment [*Schubert et al.*, 1980; *Uccellini and Koch*, 1987; *Duffy*, 1990; *Fritts and Luo*, 1992; *Luo and Fritts*, 1993; *O'Sullivan and Dunkerton*, 1995]. While topography, convection and wind shear are believed to generate mainly high-frequency waves [*Fritts and Luo*, 1992], the most energetic gravity waves in our case study are those with frequencies close to the inertial frequency f. This is in good agreement with many other observations [*Vincent*, 1984; *Sato*, 1994; *Nastrom et al.*, 1997]. Even though the predominance of inertia-gravity waves might be an observational selection effect of the radiosonde equipment [*Alexander*, 1998], the observed waves could have been generated by geostrophic adjustment and frontogenesis, both of which excite waves with near-inertial frequencies [*Fritts and Luo*, 1992; *Griffiths and Reeder*, 1996; *O'Sullivan and Dunkerton*, 1995]. In the simulations of *Griffiths and Reeder* [1996] the inertio-gravity waves generated by the frontogenesis had vertical wavelengths between 2 and 10 km and horizontal wavelengths of several hundred kilometers, in good agreement with our observations. Evidence supporting geostrophic adjustment as a generation mechanism for stratospheric waves over Macquarie Island was given by *Guest et al.* [2000], who could ray-trace gravity waves observed during a campaign in October 1994 backwards in time to their origins near the polar jet.

Background atmosphere: If we assume no explicit dependence of the background atmosphere on horizontal position x and y and time t, then the horizontal wavenumbers k and l and the ground-based frequency

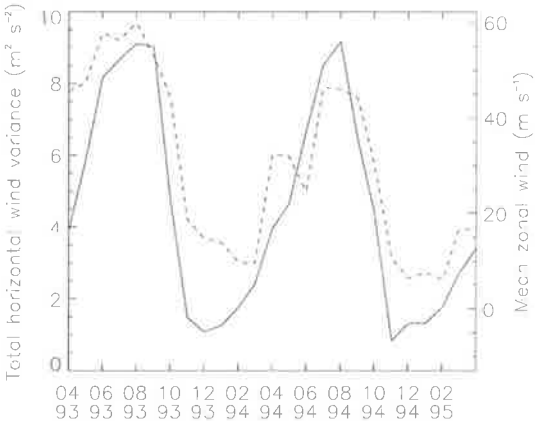

Figure 7. Total horizontal gravity wave wind variance (dashed) and zonal background wind speed (solid) averaged over the height range from 20 to 28 km as a function of time.

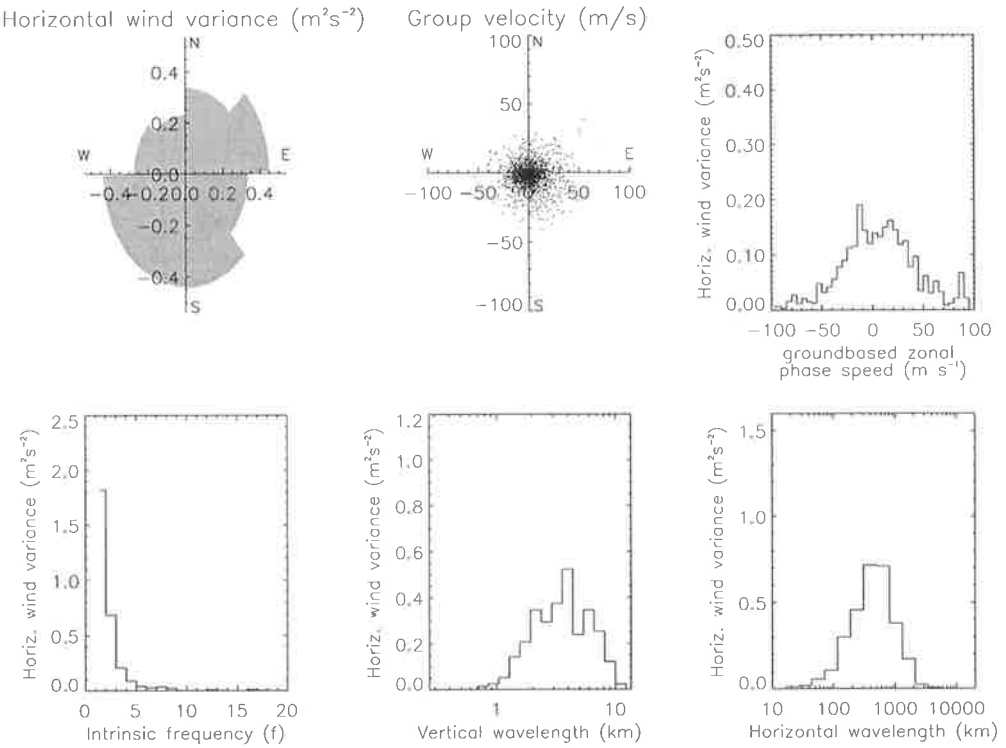

Figure 4. Parameters of upwards propagating gravity waves in the height range 20 to 28 km during summer.

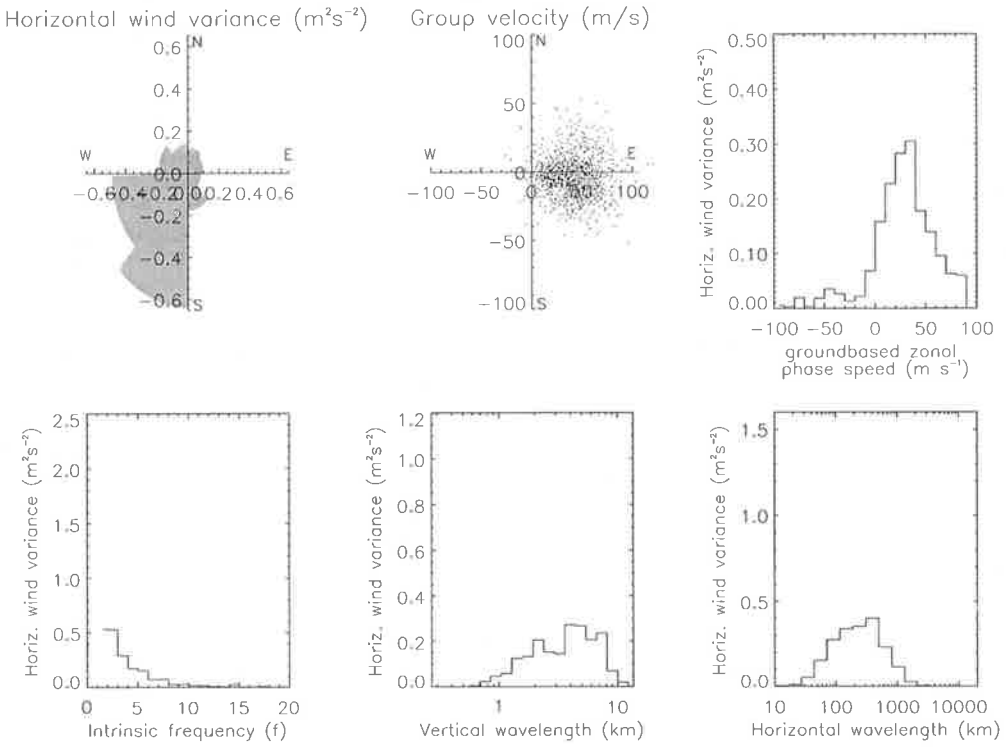

Figure 5. Parameters of downwards propagating gravity waves in the height range 20 to 28 km during winter.

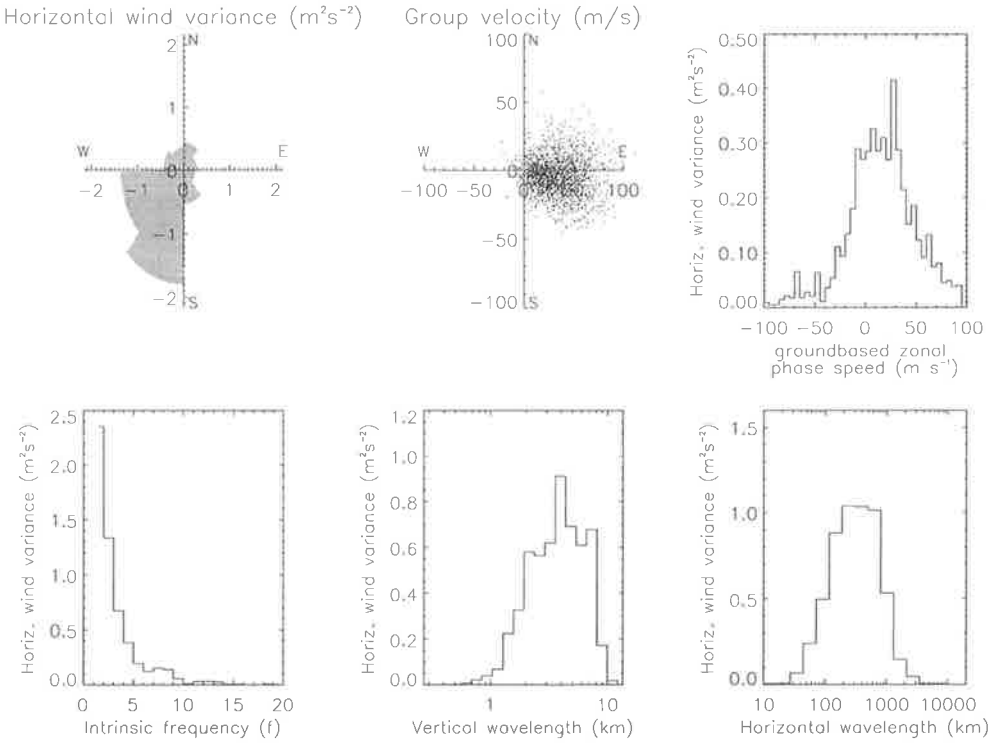

Figure 6. Parameters of upwards propagating gravity waves in the height range 20 to 28 km during winter.

ω are constant along the ray of each wave packet. The intrinsic frequency $\hat{\omega}$ as a function of height is then

$$\hat{\omega}(z) = \omega - u(z)k - v(z)l \tag{12}$$

and the vertical wavenumber $m(z)$ is given via the dispersion relation. In summer $\frac{du}{dz} < 0$ and waves propagating westwards ($k < 0$) are Doppler-shifted to lower intrinsic frequencies as they reach higher levels. Their vertical wavelength, therefore, decreases with height. If their intrinsic frequencies drops below the inertial frequency f these waves will be critically filtered. In winter, on the other hand, $\frac{du}{dz} > 0$ and westwards propagating waves are Doppler-shifted to higher intrinsic frequencies and wavelengths. If their intrinsic frequency reaches the turning frequency these waves will be reflected. Due to the limited bandwidth of our analysis methods, however, waves will be shifted out of the observable vertical wavelength range before they encounter critical or turning levels. Nevertheless, the effect of critical level filtering can be observed in the horizontal wind variance for upwards propagating waves during summer at a height of approximately 20 km, where the zonal wind reverses sign (Figure 3 top). Observations of similar modulation of gravity wave variance by the background wind were made by *Whiteway and Duck* [1996, 1999].

The wind variance of a wave packet will change even if it is shifted within the observable vertical wavelength range. In the absence of dissipation, the amplitude of a wave packet along its ray is determined by the conservation of wave action flux [*Lighthill*, 1978]

$$A_f = c_{g,z}\frac{E}{\hat{\omega}} = \text{const.}, \tag{13}$$

where $c_{g,z}$ is the vertical group velocity and E the total energy density,

$$E = \frac{1}{2}\rho(\overline{u'^2} + \overline{v'^2} + \overline{w'^2} + N^2\overline{\zeta'^2}). \tag{14}$$

Here ζ' is the wave-induced vertical displacement of the air parcel from its equilibrium. Due to the density decreasing exponentially with height, the horizontal perturbation velocity of a wave with constant intrinsic frequency grows exponentially in amplitude. If the intrinsic frequency is increasing with height, however, the (horizontal) wave amplitude will grow less than exponentially; if it is decreasing with height, it will grow more than exponentially. *Eckermann* [1995a] used this effect of background winds on vertical wavenumber spectra to explain the occurrence of attenuated spectra in several experimental observations. He was also able to model seasonal changes in wave activity due to variability in background temperature and, hence, density [*Eckermann*, 1995b]. Similarly, *Alexander* [1998] could explain the variations in gravity wave activity at midlatitudes with effects of the background atmosphere on a constant source spectrum.

Table 1. Mean values of gravity wave parameters

		$\langle c_{\text{phase,zonal}} \rangle$	$\langle \hat{\omega} \rangle$	$2\pi/\langle m \rangle$	$2\pi/\langle k_h \rangle$
winter	upwards	15.3 m/s	3.1 f	4.2 km	431 km
	downwards	27.1 m/s	3.7 f	4.1 km	319 km
summer	upwards	6.4 m/s	2.3 f	3.9 km	547 km

The observed seasonal dependence of gravity wave activity is, therefore, not necessarily indicative of source variability and might be largely explained by the propagation of a constant source spectrum through a variable background atmosphere.

3.3.2. Seasonal variation of downwards propagating gravity wave variance As mentioned above, increased wind speed will shift the intrinsic frequency of gravity waves propagating against the wind to larger values. Such a shift of the intrinsic frequency distribution to higher values is evident in winter from Figures 4 to 6. If the wind speed and, hence, the frequency shift is large enough some waves will reach their turning frequencies and be reflected. Figure 8 reveals a good correlation between the absolute background wind speed and the horizontal wind variance of the downwards propagating waves as a function of time. For background wind speeds of about 50 ms^{-1} during the stratospheric winter jet, the horizontal wind variance reaches values of up to 4 m^2s^{-2}, while the wave activity almost ceases during summer, when the atmosphere in the analyzed height range is basically at rest.

Allen [1996] found a similar increase in the fraction of clockwise rotating wind component during winter, when strong mean winds prevail in the stratosphere over Macquarie Island. Following *Eckermann et al.* [1994], Allen, however, attributed this increase to a change in frequency distribution rather than in ratio of downwards to upwards propagating gravity wave energy. He argued that the intrinsic frequency of an upwards propagating, zonally aligned gravity wave is Doppler-shifted by the zonal mean winds. This Doppler-shifting to higher frequencies reduces the axial ratio of the hodograph ellipse and results in an increased fraction of clockwise rotation. Even though the wave packet is upwards propagating, rotary spectral analysis would regard that fraction of its horizontal wind variance as downwards propagating. In our analysis, however, the total horizontal wind variance is counted as either upwards or downwards propagating, depending on the anti-clockwise or clockwise sense of rotation of the hodograph, i.e. the sign of the Stokes parameter Q. Therefore, the argument of *Eckermann et al.* [1994] can no longer be applied and we believe that in our case we really deal with downwards propagating gravity waves. It is important to note that wave reflection can occur at frequencies much lower than the buoyancy frequency N if the density height terms are retained in the dispersion relation (A7), i.e. if the Boussinesq approximation is not applied. Figure 9 shows the turning frequency as a function of horizontal wavelength for a density scale height of 6500 m and a buoyancy frequency of 0.02 $\frac{\text{rad}}{\text{s}}$ at Macquarie Island for a compressible (dashed) and incompressible (solid) atmosphere. The turning frequency at horizontal wavelengths of several hundred km as observed in this study is reduced to as little as one tenth of the buoyancy frequency N. The local buoyancy frequency encountered by a wave propagating through the atmosphere can be substantially reduced compared to the mean background value by waves of large vertical wavelength. These large vertical wavelength waves can act as a background atmosphere for waves of smaller vertical wavelength, in a manner similar to that described by *Hines* [1991]. The observed variation in

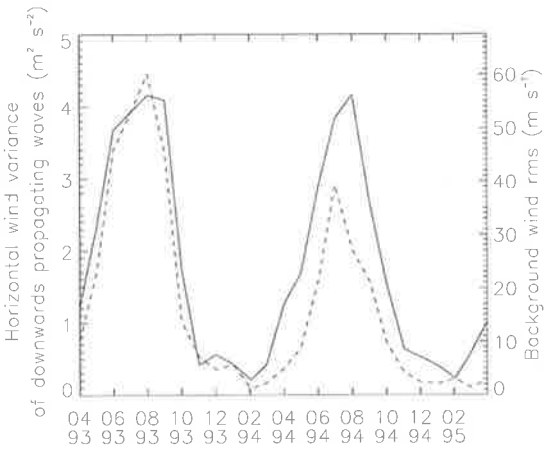

Figure 8. Horizontal wind variance of downwards propagating gravity waves (dashed) and absolute background wind speed (solid) as functions of time.

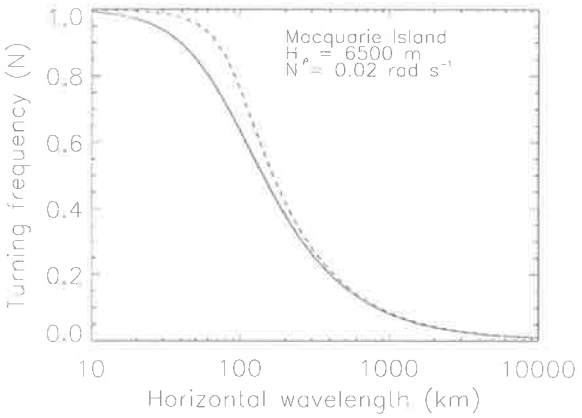

Figure 9. Turning frequency as a function of horizontal wavelength for a density scale height of 6500 m and a buoyancy frequency of $0.02\frac{rad}{s}$ at Macquarie Island for a compressible (dashed, c_s = 300 m/s) and incompressible (solid) atmosphere.

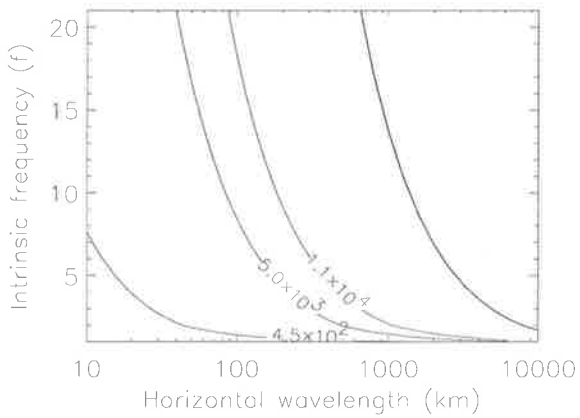

Figure 10. Contour plot of vertical wavelength as a function of horizontal wavelength and intrinsic frequency. The numbers on the contour lines are the vertical wavelength in meters. The thick line corresponds to the turning frequency.

wind variance of downwards propagating waves might thus be explained by reflection of waves from levels of high background wind speed and low local buoyancy frequency. Generation of downwards propagating waves by geostrophic adjustment of the stratospheric jet could also explain our data.

3.3.3. Preponderance of low-frequency gravity waves As seen above, inclusion of the density height terms in the dispersion relation can significantly reduce the range of intrinsic frequencies over which wave propagation is possible. If we furthermore consider the imposed wavelength cutoff at a vertical wavelength of 11000 m, the maximum observable intrinsic frequency as a function of horizontal wavelength is again drastically reduced (Figure 10). The preponderance of inertio gravity waves in our data could, therefore, be an observational selection effect. On the other hand, it could be understood if the main generation mechanisms are frontogenesis and geostrophic adjustment, as indicated above.

Topography, however, is another possible generation mechanism at Macquarie Island, that may generate high frequency waves: When the air stream is deflected by topographical obstacles gravity waves with horizontal wavelengths similar to the scale of the obstacles can be generated. Due to their small horizontal wavelengths these waves can be Doppler-shifted to large intrinsic frequencies when they propagate to regions of large background wind speed. Evidence for the generation of gravity waves by topography is given by *Mitchell et al.* [1990], who report the common occurrence of lee-wave clouds in satellite images of Macquarie Island, which can extend hundreds of kilometers to the east of the island under favourable conditions. *Schoeberl* [1985] calculated the dominant horizontal wavelength of the gravity wave spectrum forced by a bell shaped mountain ridge of equivalent mountain half width a as $2\pi a$. Considering the prevailing eastwards winds at ground level at Macquarie Island and a half width of the island between 1 and 2 km, the dominant horizontal wavelength lies between about 6 and 13 km. The minimum horizontal wavelength of zonally aligned, stationary (i.e. $\omega = 0$) gravity waves that can propagate through a gradually changing background atmosphere is given by (12) with $\omega = l = 0$, i.e.

$$\lambda_{h,min} = 2\pi u/N, \tag{15}$$

resulting in a minimum horizontal wavelength of mountain waves in the lower stratosphere over Macquarie Island of around 15 km. A significant portion of the generated mountain waves is, therefore, likely to be trapped in the troposphere and unlikely to contribute to our studies.

3.3.4. Propagation directions
The variance-weighted intrinsic propagation direction of the observed gravity wave packets is predominantly south-southwest-wards during winter and nearly isotropic during summer, as illustrated in Figures 4 to 6. In interpreting these observations, one has to take the effects of the background atmosphere into account. For the strong zonal winds in winter zonally propagating gravity waves experience large shifts in intrinsic frequency and vertical wavenumber and can be shifted into and out of the observable vertical wavenumber range. Thus, we anticipate some anisotropy in the zonal direction even for an isotropic source spectrum. Due to the low prevailing meridional winds it is hard to explain the meridional

anisotropy by conditions of the background atmosphere or as an observational selection effect. The observed anisotropy, however, does not imply anisotropic gravity wave generation, but could also be due to a latitudinally confined source located north of Macquarie Island.

3.3.5. Wave amplitudes and saturation Gravity waves will only affect the background flow or lead to mixing of constituents in the atmosphere if wave dissipation occurs. Dynamical and convective instability are thought to be the main dissipation processes [*Fritts and Rastogi*, 1985], although other mechanisms do exist (molecular diffusion, radiative damping, nonlinear interactions). Convective and dynamic instability lead to breaking of a wave if its amplitude exceeds a certain threshold. Due to the transverse shear in the velocity field of low-frequency gravity waves the wave amplitude required for dynamic instability falls well below that necessary for convective instability as $\frac{f}{\hat{\omega}} \to 1$ [*Fritts and Rastogi*, 1985]. The threshold amplitude for dynamical instability is [*Fritts*, 1989]

$$u'_{\parallel,\mathrm{sat}} = \frac{2\sqrt{1-\frac{f^2}{\hat{\omega}^2}}}{1+\sqrt{1-\frac{f^2}{\hat{\omega}^2}}} c_{\mathrm{phase,intrinsic}}. \qquad (16)$$

Due to the existence of threshold amplitudes these saturation mechanisms are nonlinear, and the knowledge of actual wave amplitudes is important when the effect of gravity waves on the background atmosphere is to be assessed. Figure 11 shows a contour plot of normalized horizontal wind variance as a function of perturbation amplitude $u'_{\parallel}$ and saturation amplitude $u'_{\parallel,\mathrm{sat}}$ for gravity waves observed at Macquarie Island during summer and winter between heights of 20 and 28 km. Only soundings after February 1994 were considered to ensure identical filtering of the radiosonde data. In both summer and winter, the vast majority of the observed waves have perturbation amplitudes less than the saturation amplitude computed according to Equation 16. The amplitudes of these waves are, therefore, either too small to reach the threshold for dynamic instability within the analyzed height range, or have already been dissipated. It is interesting to note, however, that the observed increase in gravity wave variance in winter coincides with an extension of the amplitude distribution to larger values.

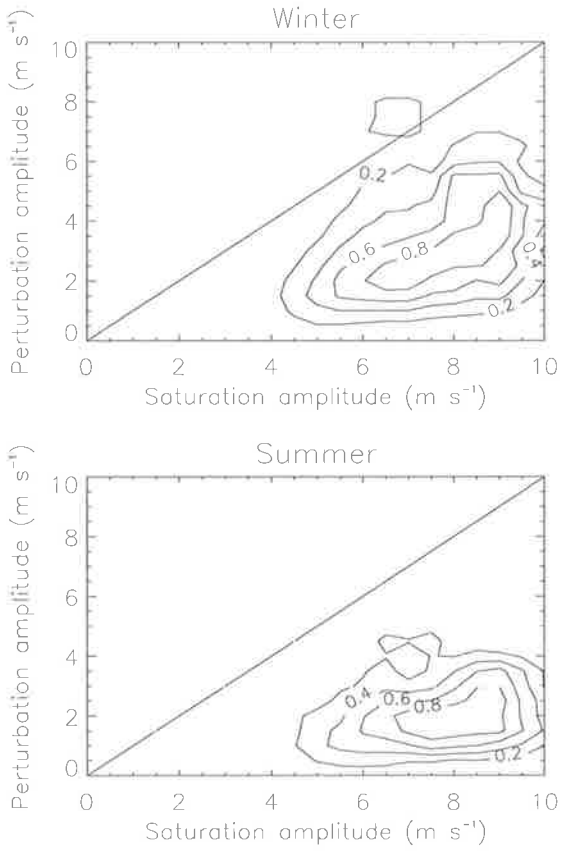

Figure 11. Normalized horizontal wind variance as function of perturbation amplitude $u'_{\parallel}$ and saturation amplitude $u'_{\parallel,\mathrm{sat}}$ for summer and winter between heights of 20 and 28 km.

4. Summary and conclusion

We presented a method to extract gravity wave packets from vertical profiles of horizontal wind and temperature. By using wavelet analysis we are able to separate the wave field in height and wavelength and, therefore, to reduce the presence of multiple waves in the hodograph analysis. Furthermore, we get information about the height extent of the wave packets. The Morlet wavelet was chosen to decompose the wave field into basis functions that are similar to the assumed physical gravity wave packets. This allows a simple reconstruction of the actual wave packet amplitude, an important issue when non-linear saturation effects are considered.

Application of the method to twice-daily radiosonde soundings of the lower stratosphere over Macquarie Island revealed a strong seasonal cycle in the total and downwards propagating gravity wave variance with a maximum in winter. This maximum in gravity wave variance coincides with a shift of the wave amplitude distribution to larger values. The variance-weighted intrinsic propagation direction during winter is predominantly south-southwest-wards, while it is nearly isotropic during summer. The observed wave field was found to be dominated by low frequency inertia gravity waves.

In the interpretation of these findings attention was paid to the limited vertical wavelength range observable with the radiosonde technique [*Alexander*, 1998]. Doppler-shifting of waves into and out of this wavelength band can lead to significant changes in the observed wave field and complicates the analysis. The

usefulness of the presented observations is, therefore, mainly in conjunction with modeling studies. In the present paper, the wave characteristics were presented in terms of variables that are directly accessible by measurements, i.e. vertical wavelength and wind variance. A disadvantage of this approach is the fact, that these variables undergo changes as the wave packet is Doppler-shifted by changes in the background wind with height, and, therefore, depend on the detection level of the wave packet.

In a subsequent paper [*Zink and Vincent*, this issue], we express the wave characteristics by invariants under the propagation of the wave packet through a steady-state atmosphere, and use these parameters to assess the effect of the observed wave field on the lower and middle atmosphere by ray tracing studies.

Appendix: Dispersion and polarization relations

Ignoring gradients in the background flow $\mathbf{u}$ by setting $\mathbf{u}(z) = (u_0, v_0, 0)$ the linearized momentum, continuity, and ideal gas equations for a compressible, inviscid atmosphere become

$$\begin{aligned} \frac{\mathrm{D}u'}{\mathrm{D}t} - fv' &= -\frac{1}{\rho_o}\frac{\partial p'}{\partial x} \\ \frac{\mathrm{D}v'}{\mathrm{D}t} + fu' &= -\frac{1}{\rho_o}\frac{\partial p'}{\partial y} \\ \frac{\mathrm{D}w'}{\mathrm{D}t} &= -\frac{1}{\rho_o}\frac{\partial p'}{\partial z} - \frac{\rho'}{\rho_o}g \end{aligned} \tag{A1}$$

$$\frac{\mathrm{D}\rho'}{\mathrm{D}t} + w'\frac{\partial \rho_o}{\partial z} + \rho_o \mathrm{div}\mathbf{u}' = 0 \tag{A2}$$

$$\frac{\mathrm{D}p'}{\mathrm{D}t} + w'\frac{\partial p_o}{\partial z} - c_s^2\left(\frac{\mathrm{D}\rho'}{\mathrm{D}t} + w'\frac{\partial \rho_o}{\partial z}\right) = 0 \tag{A3}$$

$\frac{\mathrm{D}}{\mathrm{D}t} = \frac{\partial}{\partial t} + \mathbf{u}\nabla$ is the total (Lagrangian) derivative and $\mathbf{u}' = (u', v', w')$, p', and ρ' are the perturbation velocities, pressure, and density, respectively. p_o and ρ_o designate background pressure and density, respectively, which are assumed to only vary with height. f is the Coriolis parameter, g the gravitational acceleration, and c_s the speed of sound.

Substituting solutions of the form

$$\begin{pmatrix} u' \\ v' \\ w' \end{pmatrix} = \rho_o^{-1/2}\begin{pmatrix} \hat{u} \\ \hat{v} \\ \hat{w} \end{pmatrix} \exp i(\mathbf{kx} - \omega t) \tag{A4}$$

$$\begin{pmatrix} p' \\ \rho' \end{pmatrix} = \rho_o^{+1/2}\begin{pmatrix} \hat{p} \\ \hat{\rho} \end{pmatrix} \exp i(\mathbf{kx} - \omega t), \tag{A5}$$

where $\mathbf{k} = (k, l, m)$ and $\mathbf{x} = (x, y, z)$, and expressing the intrinsic frequency in a reference frame following the background flow as

$$\hat{\omega} = \omega - \mathbf{ku}, \tag{A6}$$

yields the non-hydrostatic dispersion relation

$$m^2 = \frac{N^2 - \hat{\omega}^2}{\hat{\omega}^2 - f^2}(k^2 + l^2) - \frac{1}{4H_\rho^2} + \frac{\hat{\omega}^2}{c_s^2}. \tag{A7}$$

Here

$$N^2 = -\frac{g}{\rho_o}\frac{\partial \rho_o}{\partial z} - \frac{g^2}{c_s^2} \tag{A8}$$

is the buoyancy or Brunt-Vaisala frequency and

$$H_\rho = \frac{1}{\rho_o}\frac{\partial \rho_o}{\partial z} \tag{A9}$$

the density scale height. The dispersion relation Equation A7 also includes an acoustic branch. For an incompressible atmosphere, acoustic waves can be excluded by letting $c_s \to \infty$. Further omission of the second term in Equation A7 results in the Boussinesq approximation, a short wavelength approximation valid for $m \gg \frac{1}{2H_\rho}$. This is the approximation used throughout this paper if not mentioned otherwise.

The polarization relations are simplified in a coordinate system aligned with the propagation direction of the wave. Let $u'_\parallel$ and $v'_\perp$ designate the horizontal perturbation velocities parallel and perpendicular to the wave vector. The relevant polarization equations in the Boussinesq approximation then become

$$v'_\perp = -i\frac{f}{\hat{\omega}}u'_\parallel \tag{A10}$$

$$w' = -\frac{k_h}{m}u'_\parallel \tag{A11}$$

$$\hat{T}' = \frac{T'}{T_o} = i\frac{N^2}{g\hat{\omega}}\frac{k_h}{m}u'_\parallel, \tag{A12}$$

where T' and T_o are the perturbation and background temperature, respectively, and k_h is the horizontal wave number.

Acknowledgments. The authors would like to thank Joan Alexander for corrections and comments to an earlier version of this manuscript. We acknowledge the provision of the radiosonde data by the Australian Bureau of Meteorology.

References

Alexander, M. J., Interpretations of observed climatological patterns in stratospheric gravity wave variance, *Journal of Geophysical Research*, *103*, 8627–8640, 1998.

Alexander, M. J., and L. Pfister, Gravity wave momentum flux in the lower stratosphere over convection, *Geophysical Research Letters*, *22*, 2029–2032, 1995.

Alexander, M. J., J. R. Holton, and D. R. Durran, The gravity wave response above deep convection in a squall line simulation, *Journal of the Atmospheric Sciences*, *52*, 2212–2226, 1995.

Allen, S. J., Gravity wave motions in the troposphere and lower stratosphere, Ph.D. thesis, University of Adelaide, South Australia, 1996.

Allen, S. J., and R. A. Vincent, Gravity wave activity in the lower atmosphere: Seasonal and latitudinal variations, *Journal of Geophysical Research*, *100*, 1327–1350, 1995.

Chen, K. Y., I. J. Fu, S. Y. Su, and C. H. Liu, Wavelet analysis on transient behavior of wind fluctuations observed by MST radar, *Radio Science*, *30*, 1111–1123, 1995.

Chimonas, G., and J. R. Grant, Shear excitation of gravity waves. Part II: Upscale scattering from Kelvin-Helmholtz waves, *Journal of the Atmospheric Sciences*, *41*, 2278–2288, 1984.

Cho, J. Y. N., Inertio-gravity wave parameter estimation from cross-spectral analysis, *Journal of Geophysical Research*, *100*, 18,727–18,737, 1995.

Crohn, P. W., The geology and geomorphology of Macquarie Island with special emphasis on heavy metal trace element distribution, *ANARE Research notes*, *39*, 1986.

Duffy, D. G., Geostrophic adjustment in a baroclinic atmosphere, *Journal of the Atmospheric Sciences*, *47*, 457–473, 1990.

Dunkerton, T. J., Theory of the mesopause semiannual oscillation, *Journal of the Atmospheric Sciences*, *39*, 2681–2690, 1982.

Eckermann, S. D., Effect of background winds on vertical wavenumber spectra of atmospheric gravity waves, *Journal of Geophysical Research*, *100*, 14,097–14,112, 1995a.

Eckermann, S. D., On the observed morphology of gravity-wave and equatorial-wave variance in the stratosphere, *Journal of Atmospheric and Solar-Terrestrial Physics*, *57*, 105–134, 1995b.

Eckermann, S. D., Hodographic analysis of gravity waves: Relationships among Stokes parameters, rotary spectra and cross-spectral methods, *Journal of Geophysical Research*, *101*, 19,169–19,174, 1996.

Eckermann, S. D., and W. K. Hocking, Effect of superposition on measurements of atmospheric gravity waves: A cautionary note and some reinterpretations, *Journal of Geophysical Research*, *94*, 6333–6339, 1989.

Eckermann, S. D., and R. A. Vincent, Falling sphere observations of anisotropic gravity wave motions in the upper stratosphere over Australia, *Pure Appl. Geophys.*, *130*, 509–532, 1989.

Eckermann, S. D., I. Hirota, and W. K. Hocking, Gravity wave and equatorial wave morphology of the stratosphere derived from long-term rocket soundings, *Q. J. R. Meteorol. Soc.*, *121*, 149–186, 1994.

Farge, M., Wavelet transforms and their applications to turbulence, *Annu. Rev. Fluid Mech.*, *24*, 395–457, 1992.

Fovell, R., D. Durran, and J. R. Holton, Numerical simulations of convectively generated stratospheric gravity waves, *Journal of the Atmospheric Sciences*, *49*, 1427–1442, 1992.

Fritts, D. C., Shear excitation of atmospheric gravity waves, *Journal of the Atmospheric Sciences*, *39*, 1936–1952, 1982.

Fritts, D. C., A review of gravity wave saturation processes, effects, and variability in the middle atmosphere, *Pure and Applied Geophysics*, *130*, 343–371, 1989.

Fritts, D. C., and Z. Luo, Gravity wave excitation by geostrophic adjustment of the jet stream. Part I: Two-dimensional forcing, *Journal of the Atmospheric Sciences*, *49*, 681–697, 1992.

Fritts, D. C., and G. D. Nastrom, Sources of mesoscale variability of gravity waves. Part II: Frontal, convective, and jet stream excitation, *Journal of the Atmospheric Sciences*, *49*, 681–697, 1992.

Fritts, D. C., and P. K. Rastogi, Convective and dynamical instabilities due to gravity wave motions in the lower and middle atmosphere: Theory and observations, *Radio Science*, *20*, 1247–1277, 1985.

Fritts, D. C., and T. E. VanZandt, Spectral estimates of gravity wave energy and momentum fluxes. Part I: Energy dissipation, acceleration and constraints, *Journal of the Atmospheric Sciences*, *50*, 3685–3694, 1993.

Fritts, D. C., T. Tsuda, T. E. VanZandt, S. A. Smith, T. Sato, S. Fukao, and S. Kato, Studies of velocity fluctuations in the lower atmosphere using the MU radar,II,Momentum fluxes and energy densities, *Journal of the Atmospheric Sciences*, *47*, 51–66, 1990.

Garcia, R. R., and S. Solomon, The effect of breaking gravity waves on the dynamics and chemical composition of the mesosphere and lower thermosphere, *Journal of Geophysical Research*, *90*, 3850–3860, 1985.

Gardner, C. S., and N. F. Gardner, Measurement distortion in aircraft, space shuttle, and balloon observations of atmospheric density and temperature perturbation spectra, *Journal of Geophysical Research*, *98*, 1023–1033, 1993.

Gonella, J., A rotary-component method for analysing meteorological and oceanographic vector time series, *Deep Sea Research*, *19*, 833–846, 1972.

Griffiths, M., and M. J. Reeder, Stratospheric inertia-gravity waves generated in a numerical model of frontogenesis. I: Model solutions, *Q. J. R. Meteorol. Soc.*, *122*, 1153–1174, 1996.

Guest, F. M., M. J. Reeder, C. J. Marks, and D. J. Karoly, Inertia-gravity waves observed in the lower stratosphere over Macquarie Island, *Journal of the Atmospheric Sciences*, *57*, 737–752, 2000.

Hamilton, K., and R. A. Vincent, High-resolution radiosonde data offer new prospects for research, *EOS*, *76*, 497, 1995.

Hines, C. O., A modeling of atmospheric gravity waves and wave drag generated by isotropic and anisotropic terrain, *Journal of the Atmospheric Sciences*, *45*, 309–322, 1988.

Hines, C. O., The saturation of gravity waves in the middle atmosphere. Part II: Development of Doppler-spread theory, *Journal of the Atmospheric Sciences*, *48*, 1360–1379, 1991.

Hines, C. O., Doppler-spread parametrization of gravity-wave momentum deposition in the middle atmosphere. Part 1: Basic formulation, *Journal of Atmospheric and Solar-Terrestrial Physics*, *59*, 371–386, 1997.

Holton, J. R., The role of gravity wave induced drag and diffusion in the momentum budget of the mesosphere, *Journal of the Atmospheric Sciences*, *39*, 791–799, 1982.

Kumar, P., and E. Foufoula-Georgiou, Wavelet analysis for geophysical applications, *Reviews of Geophysics*, pp. 385–412, 1997.

Lalas, D. P., and F. Einaudi, On characteristics of gravity waves generated by atmospheric shear layers, *Journal of the Atmospheric Sciences*, *33*, 1248–1259, 1976.

Lighthill, J., *Waves in Fluids*, Cambridge University Press, New York, 1978.

Lindzen, R. S., Turbulence and stress owing to gravity wave and tidal breakdown, *Journal of Geophysical Research*, *86*, 9707–9714, 1981.

Luo, Z., and D. C. Fritts, Gravity-wave excitation by geostrophic adjustment of the jet stream. Part II: Three-dimensional forcing, *Journal of the Atmospheric Sciences*, *50*, 104–115, 1993.

McFarlane, N. A., The effect of orographically excited gravity wave drag on the general circulation of the lower stratosphere and troposphere, *Journal of the Atmospheric Sciences*, *44*, 1775–1800, 1987.

Meyers, S. D., B. G. Kelly, and J. J. OBrien, An introduction to wavelet analysis in oceanography and meteorology: With application to the dispersion of Yanai waves, *Monthly Weather Review*, *121*, 2858–2866, 1993.

Mitchell, R. M., R. P. Cechet, P. J. Turner, and C. C. Elsum, Observation and interpretation of wave clouds over Macquarie Island, *Q. J. R. Meteorol. Soc.*, *116*, 741–752, 1990.

Nastrom, G. D., and D. C. Fritts, Sources of mesoscale variability of gravity waves. Part I: Topographic excitation, *Journal of the Atmospheric Sciences*, *49*, 101–110, 1992.

Nastrom, G. D., T. E. VanZandt, and J. M. Warnock, Vertical wavenumber spectra of wind and temperature from high-resolution balloon soundings in the lower atmosphere over Illinois, *Journal of Geophysical Research*, *102(D6)*, 6685–6701, 1997.

O'Sullivan, D., and T. J. Dunkerton, Generation of inertia-gravity waves in a simulated life cycle of baroclinic instability, *Journal of the Atmospheric Sciences*, *52*, 3695–3716, 1995.

Pfister, L. W., S. Scott, M. Loewenstein, S. Bowen, and M. Legg, Mesoscale disturbances in the tropical atmosphere excited by convection: Observations and effects on the stratospheric momentum budget, *Journal of the Atmospheric Sciences*, *50*, 1058–1075, 1993.

Reeder, M. J., and M. Griffiths, Stratospheric inertia-gravity waves generated in a numerical model of frontogenesis. II: Wave sources, generation mechanisms and momentum fluxes, *Q. J. R. Meteorol. Soc.*, *122*, 1175–1195, 1996.

Sato, K., A statistical study of the structure, saturation and sources of inertio-gravity waves in the lower stratosphere observed with the MU radar, *Journal of Atmospheric and Solar-Terrestrial Physics*, *56*, 755–774, 1994.

Sato, K., and M. Yamada, Vertical structure of atmospheric gravity waves revealed by the wavelet analysis, *Journal of Geophysical Research*, *99*, 20,623–20,631, 1994.

Schoeberl, M. R., The penetration of mountain waves into the middle atmosphere, *Journal of the Atmospheric Sciences*, *42*, 2856–2864, 1985.

Schubert, W., J. J. Hack, P. L. SilvaDias, and S. R. Fulton, Geostrophic adjustment of an axisymmetric vortex, *Journal of the Atmospheric Sciences*, *37*, 1464–1484, 1980.

Shimomai, T., M. D. Yamanaka, and S. Fukao, Application of wavelet analysis to wind disturbances observed with MST radar techniques, *Journal of Atmospheric and Solar-Terrestrial Physics*, *58*, 683–696, 1996.

Smith, R. B., On severe downslope winds, *Journal of the Atmospheric Sciences*, *42*, 2597–2603, 1985.

Streten, N. A., The climate of Macquarie Island and its role in atmospheric monitoring, *Pap. Proc. R. Soc. Tasm.*, *122*, 91–106, 1988.

Uccellini, L. W., and S. E. Koch, The synoptic setting and possible energy sources for mesoscale wave disturbances, *Monthly Weather Review*, *115*, 721–729, 1987.

Vincent, R. A., Gravity-wave motions in the mesosphere, *Journal of Atmospheric and Solar-Terrestrial Physics*, *46*, 119–128, 1984.

Vincent, R. A., and D. C. Fritts, A climatology of gravity wave motions in the mesopause region at Adelaide, Australia, *Journal of the Atmospheric Sciences*, *44*, 748–760, 1987.

Vincent, R. A., and I. M. Reid, HF Doppler measurements of mesospheric gravity wave momentum fluxes, *Journal of the Atmospheric Sciences*, *40*, 1321–1333, 1983.

Vincent, R. A., S. J. Allen, and S. D. Eckermann, Gravity-wave parameters in the lower stratosphere, in *Gravity wave processes: their parametrization in global climate models*, edited by K. Hamilton, pp. 7–25, Springer-Verlag, Heidelberg, 1997.

Warner, C. D., and M. E. McIntyre, Toward an ultra-simple spectral gravity wave parameterization for general circulation models, *Earth, Planets and Space*, *51*, 475–484, 1999.

Whiteway, J. A., and T. J. Duck, Evidence for critical level filtering of atmospheric gravity waves, *Geophysical Research Letters*, *23*, 145–148, 1996.

Whiteway, J. A., and T. J. Duck, Enhanced Arctic stratospheric gravity wave activity above a tropospheric jet, *Geophysical Research Letters*, *26*, 2453–2456, 1999.

F. Zink and R. A. Vincent, Department of Physics and Mathematical Physics, University of Adelaide, Adelaide 5005, Australia (e-mail: fzink@physics.adelaide.edu.au; rvincent@physics.adelaide.edu.au)

This preprint was prepared with AGU's LaTeX macros v5.01, with the extension package 'AGU++' by P. W. Daly, version 1.6b from 1999/08/19.

Appendix C

Wavelet analysis of stratospheric gravity wave packets over Macquarie Island, II: Intermittency and mean-flow accelerations

This is a preprint of a paper submitted to the *Journal of Geophysical Research.*

Submitted to *J. Geophys. Res.*,

Wavelet analysis of stratospheric gravity wave packets over Macquarie Island, II: Intermittency and mean-flow accelerations

Florian Zink and Robert A. Vincent

Department of Physics and Mathematical Physics, University of Adelaide, Adelaide, South Australia

Abstract. We calculate the mean-flow accelerations due to gravity wave packets observed in the lower stratosphere over Macquarie Island (55°S, 159°E) between February 1994 and April 1995. The parameters of the wave packets were extracted from twice-daily radiosonde soundings using a wavelet-based analysis method introduced in *Zink and Vincent* [this issue]. The deduced wave parameters are used to directly compute momentum flux profiles in the lower stratosphere, and the shortcomings of this approach to assess mean-flow accelerations are discussed. We then use the observed wave packets as an input spectrum in a linear ray tracing model. The vertical extent of the detected wave packets allows us to define an expression for wave intermittency, which enables us to compute zonal accelerations in the strato- and mesosphere.

1. Introduction

Gravity waves can transport energy and momentum from the troposphere to the middle and upper atmosphere (see *Fritts* [1984] for a review) and influence large-scale temperature and circulation patterns [*Geller*, 1983]. Using the gravity wave parametrization of *Lindzen* [1981] the importance of wave drag and diffusion in the middle atmosphere was demonstrated in numerical simulations [*Holton*, 1982, 1983; *Dunkerton*, 1982; *Garcia and Solomon*, 1985]. For low-frequency gravity waves both the vertical flux of horizontal momentum and the horizontal transport of heat are important to describe the wave mean-flow interactions. Both contributions are contained in the so-called Eliassen-Palm flux, which can be expressed as $\rho\overline{u'w'}\delta_-$, where $\delta_- = 1 - \frac{f^2}{\hat{\omega}^2}$ [*Fritts and Vincent*, 1987]. The resulting zonal acceleration of the mean background flow can then be expressed as

$$\langle A_{zonal} \rangle = -\frac{1}{\rho}\frac{\partial}{\partial z}\langle \rho\overline{u'w'}\delta_- \rangle, \qquad (1)$$

where $\langle\rangle$ denotes temporal average. Profiles of momentum flux can either be computed directly from measurements at the respective height levels, or they can be inferred from modelling studies where a given gravity wave source spectrum is propagated through the atmosphere.

In a companion paper [*Zink and Vincent*, this issue], referred to as *ZV1*, we introduced an analysis technique to detect gravity wave packets in high-resolution radiosonde soundings. Wave packets in horizontal wind velocity were detected using the wavelet transform and the wave parameters extracted by Stokes parameter analysis. Application of the technique to twice-daily soundings at Macquarie Island (55°S, 159°E) for a period of two years allowed us to deduce the characteristics of gravity wave packets in the lower stratosphere. Parameters such as horizontal and vertical wavenumbers, intrinsic frequency, packet amplitude and vertical extension were computed for wave packets observed in the height region between 15 and 30 km for summer (November to March) and winter (April to October). These parameters are important to initialize gravity wave parametrization schemes [*Lindzen*, 1981; *Fritts and VanZandt*, 1993; *Hines*, 1997; *Warner and McIntyre*, 1999], which are used in numerical models to take unresolved wave effects into account. In our discussion, special emphasis was put on the observational filter inherent in our radiosonde measurements [*Alexander*, 1998]. The method can only observe waves with vertical wavelengths between about 1.2 km and 11 km. Waves with wavelengths outside this region are either strongly attenuated by smoothing inherent in the radiosonde data processing or they are difficult to distinguish from variations in the background atmosphere.

In this paper, we use the inferred parameters to assess the effect the observed waves have on the mean-flow in the lower and middle atmosphere. As the signal processing parameters of the radiosonde equipment were

altered in January 1994, only soundings after that date were included in our analysis. In Section 2 we compute the momentum flux profile from the gravity parameters of each observed wave packet and discuss the shortcomings of such profiles for the assessment of wave mean-flow interactions. To overcome some of these problems, we derive an expression for wave intermittency in Section 3 and apply it to deduce the effects of the observed gravity waves on the background atmosphere in a linear ray tracing model. We conclude the paper with a summary in Section 4. Notations and gravity wave polarisation and dispersion relations are the same as applied in *ZV1*.

2. Calculation of momentum flux profiles

Different observational techniques have been used to estimate momentum fluxes in the lower atmosphere. *Lilly and Kennedy* [1973] and *Alexander and Pfister* [1995] used aircraft-mounted systems to measure momentum fluxes associated with orographically and convectively generated gravity waves, respectively. *Vincent and Reid* [1983] developed a radar method to infer momentum fluxes from symmetric-beam Doppler measurements, which has been applied in the lower and middle atmosphere [*Fritts et al.*, 1990; *Sato*, 1994; *Murayama et al.*, 1994; *Worthington and Thomas*, 1996; *Reid and Vincent*, 1987; *Tsuda et al.*, 1990]. Furthermore, different authors have used radiosonde data for the estimation of momentum fluxes. *Shutts et al.* [1988] calculated the momentum flux of a single gravity wave from fluctuations in balloon ascent rate and horizontal perturbation velocities. *Mobbs and Rees* [1989] made use of the same variables to compute momentum flux profiles over the whole sounding range. The estimation of the vertical perturbation velocity from fluctuations in balloon ascent rate, however, are only reliable for large-amplitude waves. Smaller fluctuations can be due to measurement errors of radiosonde altitude or changed drag coefficients of the balloon. It can, therefore, be advantageous to calculate the vertical perturbation velocity from observed temperature fluctuations, which are measurable with a much higher accuracy. If the intrinsic frequency of the contributing waves is known, the momentum flux can be expressed using the polarization relations as

$$\rho\overline{u'w'} = -\rho\frac{\hat{\omega}g}{N^2}\overline{u'\hat{T}'_{+90}}. \qquad (2)$$

Here $\hat{T}'_{+90}$ is the 90 degree phase-shifted (i.e. Hilbert transformed) normalized temperature fluctuation $\hat{T}'$ and the overbar denotes spatial average. *Sato and Dunkerton* [1997] analyzed ten years of twice daily radiosonde data at Singapore. They calculated quadrature spectra from time series of horizontal wind speeds and temperature and used (2) to compute the corresponding momentum fluxes. Since the mean wind in the considered height range was weak, they ignored the Doppler shift between intrinsic and ground-based frequency and used the ground-based frequency in their computations. *Vincent et al.* [1997] and *Allen* [1996] fitted observed mean spectra to the gravity wave spectrum parametrization of *Fritts and VanZandt* [1993] and integrated over the model spectrum to find an intrinsic mean frequency $\overline{\hat{\omega}}$, which was then used in (2) to compute the momentum flux from measured values of $\overline{u'\hat{T}'_{+90}}$. Their method, therefore, assumes similar propagation characteristics for all waves independent of frequency, even though mainly low frequency waves were resolved.

The wavelet analysis developed in *ZV1* provides all required gravity wave parameters to compute the momentum flux of each detected wave packet. We computed the height profiles of momentum flux by assuming a Gaussian shape of the wave packets with a full width half maximum as determined by the wavelet analysis. We used (2) to compute the momentum flux from values of $\overline{u'\hat{T}'_{+90}}$ calculated from the perturbation amplitudes of the detected wave packets. The density at the height of the wave packet was obtained from monthly averaged temperature profiles using the hydrostatic approximation, i.e.

$$\rho(z) = \rho(z_o)\exp^{-\int_{z_o}^{z}\frac{\mathrm{d}z'}{H_\rho(z')}}, \qquad (3)$$

where

$$H_\rho = \frac{1}{\frac{g}{RT} + \frac{1}{T}\frac{\mathrm{d}T}{\mathrm{d}z}} \qquad (4)$$

is the density scale height.

Figure 1 shows contour plots of monthly averages of $\overline{\rho u'w'\delta_-}$ and $\overline{\rho v'w'\delta_-}$ calculated for all detected waves with intrinsic frequencies less than 10 f. This cutoff was chosen as the majority of the detected waves have frequencies less than 10 f, and the determination of intrinsic frequencies from hodograph analysis is prone to large uncertainties for high intrinsic frequencies. The mean values of the momentum fluxes at heights of 20 and 28 km are given in Table 1 for summer and winter.

The shape of the momentum flux profiles agrees well with *Allen* [1996], although our values are up to an order of magnitude smaller than the ones reported by *Allen* [1996] and *Vincent et al.* [1997]. This, however, can be explained by the restriction of our analysis to waves with intrinsic frequencies less than 10 f, while *Allen* [1996] and *Vincent et al.* [1997] used the full spectrum of waves in their calculations.

In comparison with other experimental observations and in assessing the importance of the observed gravity waves for the mean circulation, the limited frequency range and our vertical wavelength bandwidth of about 1.2 to 11 km have to be kept in mind. For the same reason an estimation of mean flow acceleration from these momentum flux profiles is prone to

Table 1. Mean values of momentum fluxes for winter and summer at heights of 20 and 28 km.

		$\langle\overline{u'w'}\delta_-\rangle$ (m^2s^{-2})	$\langle\overline{v'w'}\delta_-\rangle$ (m^2s^{-2})	$\langle\rho\overline{u'w'}\delta_-\rangle$ (Nm^{-2})	$\langle\rho\overline{v'w'}\delta_-\rangle$ (Nm^{-2})
winter	20 km	$-1.3 \cdot 10^{-2}$	$-1.2 \cdot 10^{-2}$	$-1.0 \cdot 10^{-3}$	$-9.3 \cdot 10^{-4}$
	28 km	$-1.6 \cdot 10^{-2}$	$-1.8 \cdot 10^{-2}$	$-3.7 \cdot 10^{-4}$	$-4.1 \cdot 10^{-4}$
summer	20 km	$-6.6 \cdot 10^{-4}$	$-1.2 \cdot 10^{-3}$	$-5.6 \cdot 10^{-5}$	$-9.9 \cdot 10^{-5}$
	28 km	$2.1 \cdot 10^{-3}$	$-1.8 \cdot 10^{-3}$	$5.1 \cdot 10^{-5}$	$-4.5 \cdot 10^{-5}$

large errors: Consider a wave packet propagating dissipationless through the background atmosphere. Due to changes in background wind the vertical wavenumber of the wave packet will change along its path. If the vertical wavenumber is within the observable range for certain height regions and out of this range for other height regions, the momentum flux profile from radiosonde observations will show artificial variations with height, leading to errors in the calculated accelerations of the background wind.

One can circumvent this difficulty if ray tracing techniques are applied. After extracting the wave parameters in a height region where the wave packet is observable, the parameters of the wave packet can be calculated for the whole height range of interest. It is then possible to compute the momentum flux even for those height regions, where the vertical wavenumber of the wave packet is not within the observable range, avoiding variations in the momentum flux estimates due to the observational filter. Ray tracing, furthermore, enables us to propagate the gravity wave spectrum to higher regions of the atmosphere which are inaccessible to direct measurements with radiosondes.

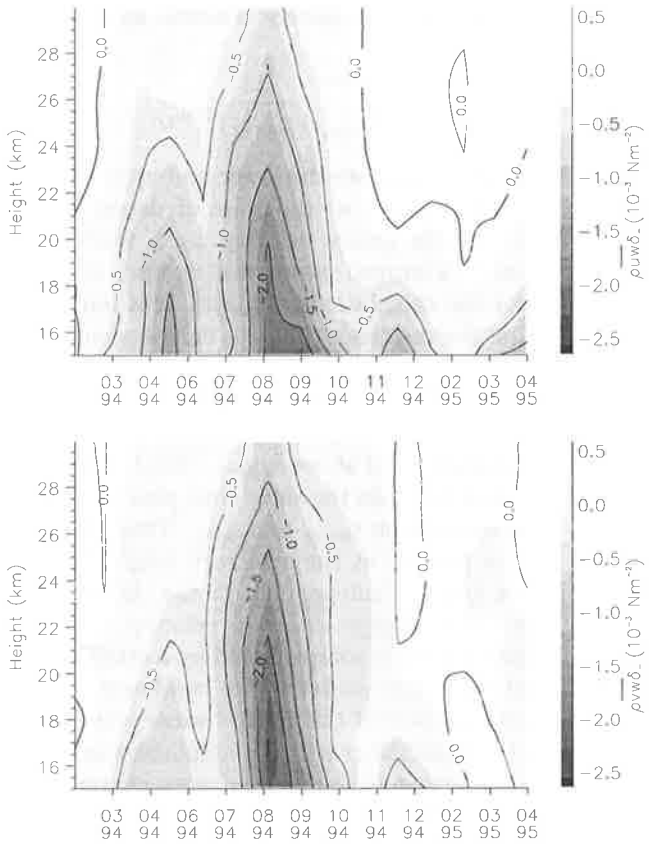

Figure 1. Contour plots of monthly averages of $\rho\overline{u'w'}\delta_-$ (top) and $\rho\overline{v'w'}\delta_-$ (bottom) for waves with intrinsic frequencies less than 10 f.

3. Mean-flow accelerations and intermittency

3.1. A linear ray-tracing model

For our modelling studies we applied a simple linear ray tracing model similar to *Eckermann* [1992], *Marks and Eckermann* [1995], *Alexander* [1996] and *Warner and McIntyre* [1996]. If one assumes no explicit dependence of the background atmosphere on horizontal position x and y and time t, then the horizontal wavenumbers k and l and the ground-based frequency ω of a wave packet are constant along its ray. The intrinsic frequency $\hat{\omega}$ as a function of height is then given by

$$\hat{\omega}(z) = \omega - u(z)k - v(z)l \tag{5}$$

and the vertical wavenumber $m(z)$ can be obtained from the dispersion relation.

The integration along the ray path is taken from the source level until a turning or critical level is encountered, i.e. $m \to 0$ or $\hat{\omega} \to f$, respectively. In the absence of dissipation, the amplitude of the wave packet along the ray is determined by the conservation of wave action flux [*Lighthill*, 1978], which, in a single-column model, can be written as

$$A_f = \frac{c_{g,z}E}{\hat{\omega}} = \text{const.}, \tag{6}$$

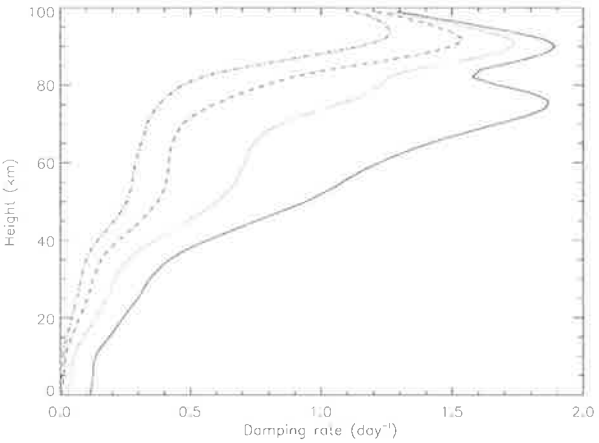

Figure 2. Radiative damping rates for the CIRA atmosphere in June at 50° S for vertical wavelengths of 2 (solid), 5 (dotted), 10 (dashed), and 20 (dot-dashed) km.

where $c_{g,z}$ is the vertical group velocity and E the total energy density. Using the polarization equations in the Boussinesq approximation this can be expressed as

$$A_f = \frac{1}{2m}\rho \hat{u'_{\|}}^2 (1 - \frac{f^2}{\hat{\omega}^2}) = \text{const.}, \tag{7}$$

where $\hat{u'_{\|}}$ is the peak perturbation amplitude parallel to the intrinsic propagation direction of the wave packet. The assumption of a single-column model is justified by our lack of knowledge about the fine scale geography of wave sources [*Warner and McIntyre*, 1996]. Equation 7 is used to calculate the amplitude of the wave packet from one level to the next when dissipation is negligible. Radiative damping, however, can severely attenuate the amplitude of slowly propagating gravity waves. We, therefore, included this dissipative process in our model using the parameterization of *Zhu* [1993]. His scheme allows the calculation of the scale-dependent radiative damping rate τ_{rad} as a function of altitude for a given temperature profile. Radiative damping attenuates the amplitude of a wave packet by a factor $\exp(-\tau_{\text{rad}}(z)\frac{\Delta z}{c_{g,z}(z)})$ during its propagation through a height interval Δz at height z. Figure 2 shows examples of damping rates for the CIRA atmosphere in June at 50° S.

If the resulting amplitude exceeds the critical amplitude for dynamical instability (Equation 16 in *ZV1*), it is thresholded to this value. This corresponds to a dissipation mechanism that acts instantaneously once the critical amplitude is reached and stops as soon as the amplitude is restored to a subcritical value. The existence of a threshold amplitude for instability renders the saturation mechanism non-linear. Hence, it is important to use actual wave packet amplitudes, and not averages over space or time.

3.2. Intermittency and gravity wave source spectrum

While the non-linear saturation mechanism requires the knowledge of actual wave packet amplitudes to correctly identify the heights where saturation becomes important, the mean zonal acceleration (1) depends on the temporally averaged momentum flux. The observation of wave packets in the radiosonde data indicates a degree of intermittency in the gravity wave production, that is, the wave packets will only be present for a certain amount of time at each height level. Hence, a correction factor has to be applied to the momentum flux profile of each wave packet to obtain the required temporal average. Due to the lack of information about wave intermittency, this correction factor was chosen arbitrarily in previous modelling studies to give reasonable magnitudes of acceleration at the required levels in the atmosphere [*Alexander and Rosenlof*, 1996; *Hamilton*, 1997]. The use of wavelet analysis, however, gives us information about the vertical extent of the gravity wave packets and can shed some light on the gravity wave intermittency.

We define the residence time τ of a wave packet as the time it takes to completely traverse an arbitrary height level

$$\tau = \int_{z_{\text{lower}}}^{z_{\text{upper}}} \frac{\mathrm{d}z}{c_{g,z}(z)}, \tag{8}$$

where z_{lower} and z_{upper} are the lower and upper boundary of the wave packet at the time of detection and $c_{g,z}(z)$ the vertical group velocity as a function of height. Monthly averaged values of $u(z)$, $v(z)$, and $T(z)$ were used for the calculation of $c_{g,z}(z)$. It is important to realize that the residence time τ is independent of the chosen height level: Consider an upwards propagating wave packet extending from z_{lower} to z_{upper}. It will take the upper end of the wave packet a certain time to reach an arbitrary height level above z_{upper}. The lower end of the wave packet will take the same time plus the time it takes to propagate from z_{lower} to z_{upper}. Thus, the wave packet will be present at the arbitrary height level for the residence time τ, independent of the choice of the height level. Any change in group velocity $c_{g,z}$ along the propagation path is compensated by a stretching or shrinking of the wave packet. The residence time is, therefore, an invariant of the gravity wave propagation and equals the time the gravity wave source was turned on for the generation of the observed wave packet. Note that our definition of the residence time differs from that in *Alexander* [1998] who defined the residence time as the ratio of a *constant* height interval to vertical group velocity. Her residence time is, therefore, a function of height, as she did not take the shrinking and stretching of the wave packet into account.

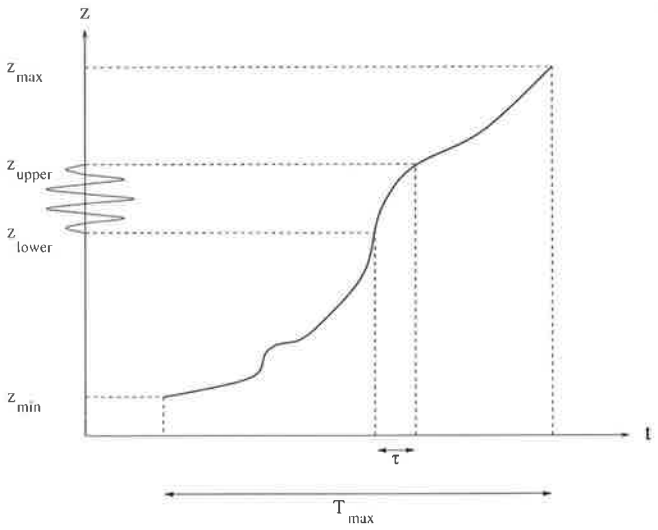

Figure 3. Trajectory of a wave packet observed between z_{lower} and z_{upper}. The residence time τ is the time the gravity wave source had to be switched on to produce the observed wave packet. If the wave packet extended over the whole observed height interval $[z_{\min}, z_{\max}]$ the gravity wave source would have had to be active for the whole time $T_{\max}$.

We can then define the intermittency of the wave packet as

$$\epsilon = \frac{\tau}{T_{\max}}, \tag{9}$$

where $T_{\max}$ is the residence time of a hypothetical wave packet extending over all those height regions where it could have been observed with the applied analysis method. The intermittency, therefore, equals the fraction of time during the time interval $T_{\max}$ the source had to be active to generate the observed gravity wave packet. $T_{\max}$ can be calculated as

$$T_{\max} = \int_{z_{min}}^{z_{max}'} \frac{\mathrm{d}z}{c_{g,z}(z)}, \tag{10}$$

where the prime indicates integration over only those height intervals where the vertical wavenumber $m(z)$ is within the observable range. The method is illustrated in Figure 3.

The horizontal wavenumber vector $\mathbf{k_h}$, the ground-based frequency ω, the wave action flux A_f, and the wave intermittency τ, all invariants of the dissipationless wave propagation through a horizontally isotropic steady-state atmosphere, fully characterize the wave packet and its effect on the atmosphere in our model. The applied observation method, however, cannot provide information about the full $(\mathbf{k_h}, \omega)$ spectrum. As indicated above, the radiosonde technique can only observe gravity waves with vertical wavelengths between about 1.2 km and 11 km. Due to this observational

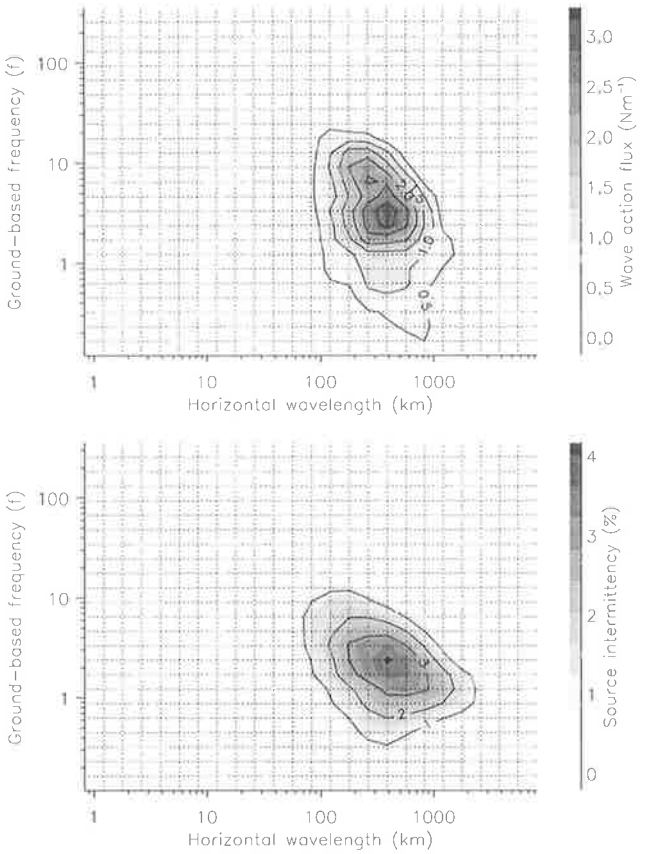

Figure 4. Contour plot of average wave action flux (top) and source intermittency (bottom) as a function of horizontal wavelength and ground-based frequency for summer. The dashed lines show the intervals over which the data have been binned.

filter, only certain parts of the $(\mathbf{k_h}, \omega)$ spectrum are observable at each height. Changes in background wind with height Doppler-shift different parts of the $(\mathbf{k_h}, \omega)$ spectrum into the observable wavenumber range, so that different parts of the spectrum can be observed at different heights. Because of the invariance of $\mathbf{k_h}$, ω, A_f, and τ, however, these wave parameters are independent of height and a larger part of the gravity wave spectrum can be reconstructed. By using different observation techniques together, one can obtain more detailed information about the spectrum.

Figures 4 and 5 illustrate the source spectra reconstructed from our observations for summer and winter, respectively. This source spectra corresponds to the spectra that, when input at a height of 15 km, will reproduce the observed characteristics of the gravity wave field. For the reasons given above, it is not necessarily the spectrum emitted by a physical source somewhere in the lower atmosphere. To obtain better statistics, all information about wave propagation directions was discarded in our spectra and only the magnitudes of the

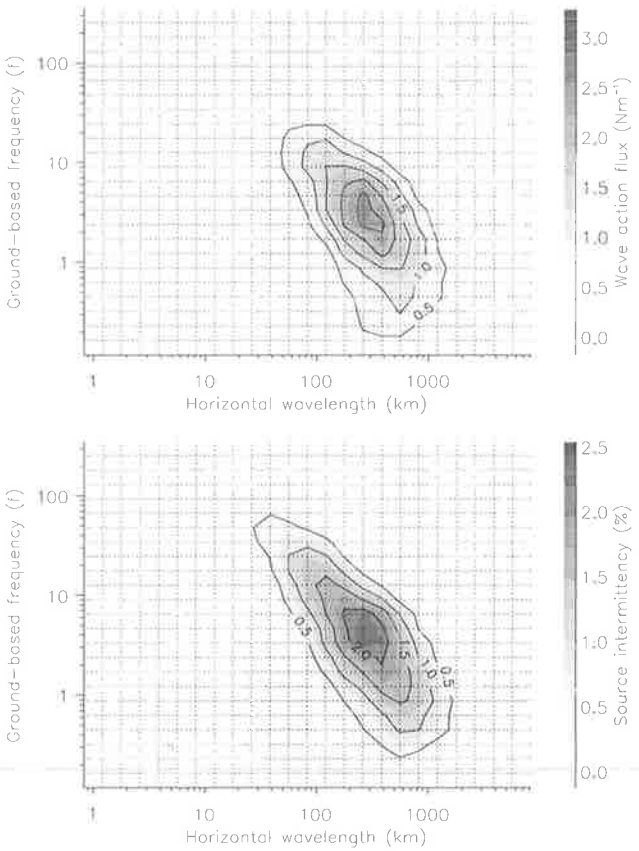

Figure 5. Same as Figure 4 but for winter.

horizontal wavenumber vector $\mathbf{k_h}$ and the ground-based frequency ω were utilized. The figures show slightly smoothed contour plots of time-averaged wave action flux

$$\overline{A_f}(k_h,\omega) = \frac{1}{N}\sum_{i=1}^{N} \|A_f(k_h,\omega,i)\| \frac{\tau(k_h,\omega,i)}{T_{\max}(k_h,\omega,i)} \quad (11)$$

and source intermittency

$$\overline{\epsilon}(k_h,\omega) = \frac{1}{N}\sum_{i=1}^{N} \frac{\tau(k_h,\omega,i)}{T_{\max}(k_h,\omega,i)}, \quad (12)$$

where i is an index to the different radiosonde soundings. The analysed height range was from 15 km to the maximum height of the soundings, often reaching up to 30 km. The horizontal wavenumber k_h and the ground-based frequency ω were binned logarithmically into 25 bins for the ranges $k_h = \frac{2\pi}{10^7\,\mathrm{m}} \ldots \frac{2\pi}{10^3\,\mathrm{m}}$ and $\omega = 0.1f \ldots 300f$, respectively. For a better comparison of source strength between the two seasons, the average source strength is shown as a one-dimensional function of horizontal wavelength and ground-based frequency, respectively, in Figure 6. It is evident that the total wave action flux in the observed vertical wavenumber

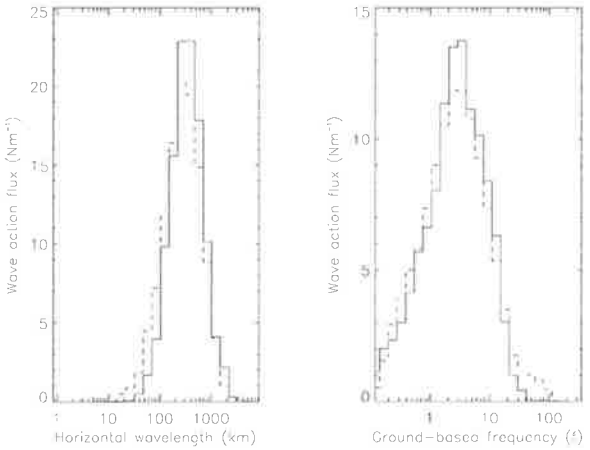

Figure 6. Average wave action flux as a function of horizontal wavelength and ground-based frequency for winter (dashed) and summer (solid).

range is very similar in magnitude for winter and summer. This corroborates the argument that the differences in horizontal wind variance as presented in *ZV1*, Figure 7, can be largely due to seasonal changes in the background atmosphere. It is also noteworthy, that, while the gravity wave field was shown in *ZV1* to be clearly dominated by low intrinsic frequency, inertio gravity waves, the Doppler-shifting by the background wind leads to tails in the ground-based frequency distribution to both low and large frequencies. Figure 7 shows the average wave action flux as a function of intrinsic horizontal propagation direction for winter and summer. In both cases the observed wave action flux is distributed anisotropically. This observed anisotropy does not necessarily imply an anisotropic wave field, but may again be due to the observational filter of the radiosonde method. If the dominant background wind is confined to certain azimuths, then only certain regions of the $(\mathbf{k_h},\omega)$ spectrum contribute to our observations, and what might be an isotropic wave field, can appear anisotropic in observations.

3.3. Mean-flow accelerations

In our model we raytraced all upwards propagating gravity wave packets detected above 15 km for each month of the year to a maximum height of 100 km. As a starting level we chose the lowest height above $z_{\mathrm{start}} = 15$ km from where a propagation of a wave packet to its level of detection was possible in the given background atmosphere (Figure 8). The wave action flux of the wave packet at the starting level was adjusted to reach agreement between model and observation at the detection level and to compensate for any radiaton damping effects. We used a height resolution of 500 m and no interaction of the packets was allowed. As back-

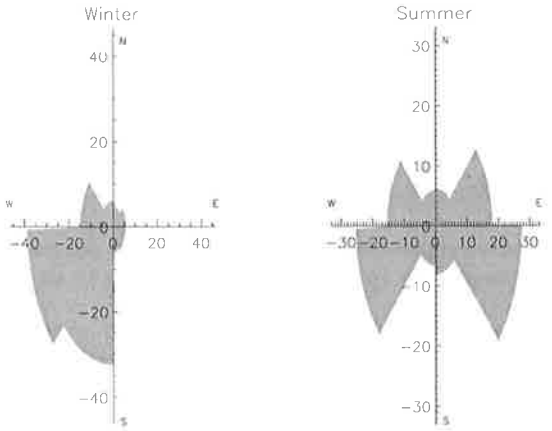

Figure 7. Average wave action flux as a function of intrinsic horizontal propagation direction for winter and summer. Units are Nm^{-1}.

ground atmosphere we used the COSPAR International Reference Atmosphere (CIRA) 1986 temperature and zonal winds of the respective month linearly interpolated to the required latitude of 55° S. A contour plot of the zonal wind profiles is given in Figure 9. The acceleration was calculated using (1) with

$$\langle \rho u' w' \delta_- \rangle = \epsilon k A_f \tag{13}$$

computed for each wave packet.

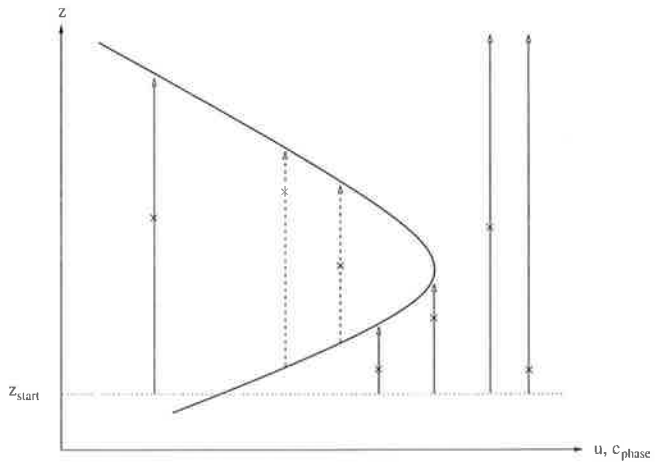

Figure 8. The starting level for each wave packet was chosen as the lowest height above z_{start} from where a propagation of the wave packet to its level of detection (cross) was possible. Wave propagation from a uniform starting level z_{start} could not reproduce the effects of waves observed above a possible critical level (dashed lines).

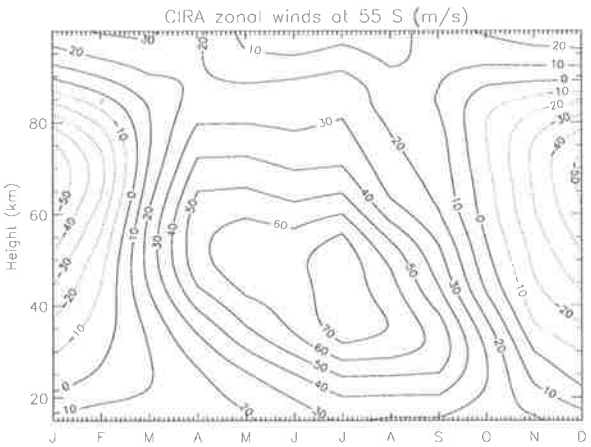

Figure 9. CIRA zonal winds linearly interpolated to 55° S.

Figure 10 shows a contour plot of the inferred zonal accelerations in the mesosphere. The accelerations are most significant at regions of high wind shear, at around 85 km during summer and between 60 and 80 km during winter. The magnitude of the wave drag in winter seems to be about two to three times higher than the average drag expected both from observations and theory [*Fritts and Vincent*, 1987; *Fritts and Yuan*, 1989; *Holton*, 1983]. The accelerations deduced from our model, however, are based on the data from a single station only and might deviate from a zonal average over all longitudes.

In contrast to the decelarative effect of the waves in the mesosphere, our model reveals an accelerative effect in the middle stratosphere (Figure 11). This is in agreement with calculations of *Alexander and Rosenlof* [1996] who used global measurements of temperature, wind, and chemical constituents to estimate the zonal mean forcing by unresolved waves in the stratosphere.

It is important to realize, that the analysis of the radiosonde data might be biased towards low intrinsic frequency waves, as these waves usually have larger amplitudes than their high frequency counterparts and are, thus, easier to detect. Waves of high intrinsic frequency, while smaller in amplitude, might still outweigh the effect of the observed low frequency waves. Nevertheless, our computations show, that waves with low intrinsic frequency in the stratosphere can have a profound impact on the circulation in the middle atmosphere, at least in our simple linear model.

4. Summary and conclusion

We used the wave parameters of gravity wave packets detected in the lower stratosphere over Macquarie Island to assess the influence of the observed gravity wave

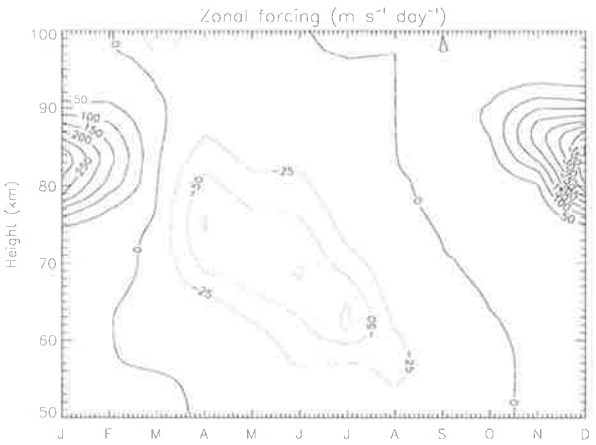

Figure 10. Inferred zonal accelerations in the mesosphere. Solid contour lines correspond to eastward acceleration.

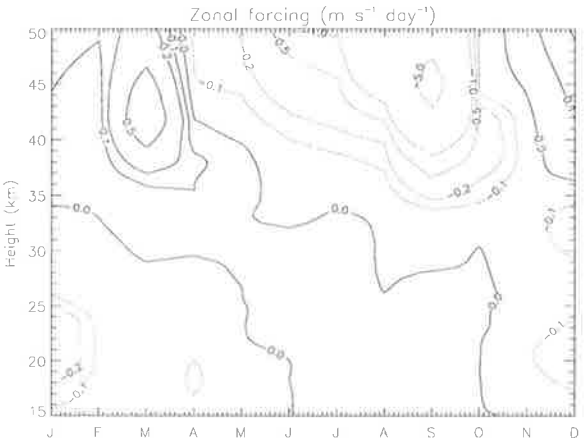

Figure 11. As Figure 10, but for the stratosphere.

field on the mean-flow. While a direct computation of a vertical momentum flux profile corresponding to the wave packets observed at the respective heights is possible, the observational filter of the radiosonde technique, together with the Doppler-shifting of the wave packets due to a height variable background atmosphere, prohibit the determination of mean-flow accelerations from these profiles.

To overcome this problem, we input the detected waves in a linear ray tracing model from a common source level. The calculation of a momentum flux profile is then possible even at those heights, where the wave packets would be outside the observationally accessible vertical wavenumber range. The definition of a wave source intermittency then allows the calculation of a temporally averaged momentum flux profile for each detected wave packet.

The inferred mean-flow decelerations in the mesosphere were shown to be up to a factor of 2 to 3 times higher than measurements and theory would predict. In the lower stratosphere, the waves lead to an acceleration of the mean-flow in accordance with theoretical predictions.

Acknowledgments. The authors would like to thank Joan Alexander for corrections and comments to an earlier version of this manuscript. We acknowledge the provision of the radiosonde data by the Australian Bureau of Meteorology.

References

Alexander, M. J., A simulated spectrum of convectively generated gravity waves: Propagation from the tropopause to the mesopause and effects on the middle atmosphere, *Journal of Geophysical Research*, *101*, 1571–1588, 1996.

Alexander, M. J., Interpretations of observed climatological patterns in stratospheric gravity wave variance, *Journal of Geophysical Research*, *103*, 8627–8640, 1998.

Alexander, M. J., and L. Pfister, Gravity wave momentum flux in the lower stratosphere over convection, *Geophysical Research Letters*, *22*, 2029–2032, 1995.

Alexander, M. J., and K. H. Rosenlof, Nonstationary gravity wave forcing of the stratospheric zonal mean wind, *Journal of Geophysical Research*, *101*, 23,465–23,474, 1996.

Allen, S. J., Gravity wave motions in the troposphere and lower stratosphere, Ph.D. thesis, University of Adelaide, South Australia, 1996.

Dunkerton, T. J., Theory of the mesopause semiannual oscillation, *Journal of the Atmospheric Sciences*, *39*, 2681–2690, 1982.

Eckermann, S. D., Ray-tracing simulation of the global propagation of inertia gravity waves through the zonally averaged middle atmosphere, *Journal of Geophysical Research*, *97*, 15,849–15,866, 1992.

Fritts, D. C., Gravity wave saturation in the middle atmosphere: A review of theory and observations, *Reviews of Geophysics and Space Physics*, *22*, 275–308, 1984.

Fritts, D. C., and T. E. VanZandt, Spectral estimates of gravity wave energy and momentum fluxes. Part I: Energy dissipation, acceleration and constraints, *Journal of the Atmospheric Sciences*, *50*, 3685–3694, 1993.

Fritts, D. C., and R. A. Vincent, Mesospheric momentum flux studies at Adelaide, Australia: Observations and a gravity wave-tidal interaction model, *Journal of the Atmospheric Sciences*, *44*, 605–619, 1987.

Fritts, D. C., and L. Yuan, Measurement of momentum fluxes near the summer mesopause at Poker Flat, Alaska, *Journal of the Atmospheric Sciences*, *46*, 2569–2579, 1989.

Fritts, D. C., T. Tsuda, T. E. VanZandt, S. A. Smith, T. Sato, S. Fukao, and S. Kato, Studies of velocity fluctuations in the lower atmosphere using the MU radar,II,Momentum fluxes and energy densities, *Journal of the Atmospheric Sciences*, *47*, 51–66, 1990.

Garcia, R. R., and S. Solomon, The effect of breaking gravity waves on the dynamics and chemical composition of the mesosphere and lower thermosphere, *Journal of Geophysical Research*, *90*, 3850–3860, 1985.

Geller, M. A., Dynamics of the middle atmosphere, *Space Science Reviews*, *34*, 359–375, 1983.

Hamilton, K., The role of parameterized drag in a troposphere-stratosphere-mesosphere general circulation model, in *Gravity wave processes: their parametrization in global climate models*, edited by K. Hamilton, pp. 337–350, Springer-Verlag, Heidelberg, 1997.

Hines, C. O., Doppler-spread parametrization of gravity-wave momentum deposition in the middle atmosphere. Part 1: Basic formulation, *Journal of Atmospheric and Solar-Terrestrial Physics*, *59*, 371–386, 1997.

Holton, J. R., The role of gravity wave induced drag and diffusion in the momentum budget of the mesosphere, *Journal of the Atmospheric Sciences*, *39*, 791–799, 1982.

Holton, J. R., The influence of gravity wave breaking on the general circulation of the middle atmosphere, *Journal of the Atmospheric Sciences*, *40*, 2497–2507, 1983.

Lighthill, J., *Waves in Fluids*, Cambridge University Press, New York, 1978.

Lilly, D. K., and P. J. Kennedy, Observations of a stationary mountain wave and its associated momentum flux and energy dissipation, *Journal of the Atmospheric Sciences*, *30*, 1135–1152, 1973.

Lindzen, R. S., Turbulence and stress owing to gravity wave and tidal breakdown, *Journal of Geophysical Research*, *86*, 9707–9714, 1981.

Marks, C. J., and S. D. Eckermann, A three-dimensional nonhydrostatic ray-tracing model for gravity waves: Formulation and preliminary results for the middle atmosphere, *Journal of the Atmospheric Sciences*, *52*, 1959–1984, 1995.

Mobbs, S. D., and J. M. Rees, Studies of atmospheric internal gravity waves at Halley station,Antarctica, using radiosondes, *Antarctic Science*, *1*, 65–75, 1989.

Murayama, Y., T. Tsuda, and S. Fukao, Seasonal variation of gravity wave activity in the lower atmosphere observed with the MU radar, *Journal of Geophysical Research*, *99*, 23,057–23,069, 1994.

Reid, I. M., and R. A. Vincent, Measurements of mesospheric gravity wave momentum fluxes and mean flow accelerations at Adelaide,Australia, *Journal of Atmospheric and Solar-Terrestrial Physics*, *49*, 443–460, 1987.

Sato, K., A statistical study of the structure, saturation and sources of inertio-gravity waves in the lower stratosphere observed with the MU radar, *Journal of Atmospheric and Solar-Terrestrial Physics*, *56*, 755–774, 1994.

Sato, K., and T. J. Dunkerton, Estimates of momentum flux associated with equatorial Kelvin and gravity waves, *Journal of Geophysical Research*, *102*, 26,247–26,261, 1997.

Shutts, G. J., M. Kitchen, and P. H. Hoare, A large amplitude gravity wave in the lower stratosphere detected by radiosonde, *Q. J. R. Meteorol. Soc.*, *114*, 579–594, 1988.

Tsuda, T. S., S. Kato, T. Yokoi, T. Inoue, M. Yamamoto, T. E. VanZandt, S. Fukao, and T. Sato, Gravity waves in the mesosphere observed with the middle and upper atmosphere radar, *Radio Science*, *25*, 1005–1018, 1990.

Vincent, R. A., and I. M. Reid, HF Doppler measurements of mesospheric gravity wave momentum fluxes, *Journal of the Atmospheric Sciences*, *40*, 1321–1333, 1983.

Vincent, R. A., S. J. Allen, and S. D. Eckermann, Gravity-wave parameters in the lower stratosphere, in *Gravity wave processes: their parametrization in global climate models*, edited by K. Hamilton, pp. 7–25, Springer-Verlag, Heidelberg, 1997.

Warner, C. D., and M. E. McIntyre, On the propagation and dissipation of gravity wave spectra through a realistic middle atmosphere, *Journal of the Atmospheric Sciences*, *53*, 3213–3225, 1996.

Warner, C. D., and M. E. McIntyre, Toward an ultra-simple spectral gravity wave parameterization for general circulation models, *Earth, Planets and Space*, *51*, 475–484, 1999.

Worthington, R. M., and L. Thomas, The measurement of gravity wave momentum flux in the lower atmosphere using VHF radar, *Radio Science*, *31*, 1501–1517, 1996.

Zhu, X., Radiative damping revisited: Parameterization of damping rate in the middle atmosphere, *Journal of the Atmospheric Sciences*, *50*, 3008–3021, 1993.

F. Zink and R. A. Vincent, Department of Physics and Mathematical Physics, University of Adelaide, Adelaide 5005, Australia. (e-mail: fzink@physics.adelaide.edu.au; rvincent@physics.adelaide.edu.au)

This preprint was prepared with AGU's LaTeX macros v5.01, with the extension package 'AGU++' by P. W. Daly, version 1.6b from 1999/08/19.

References

Alexander, M. J. (1996), 'A simulated spectrum of convectively generated gravity waves: Propagation from the tropopause to the mesopause and effects on the middle atmosphere', *Journal of Geophysical Research* **101**(D1), 1571–1588.

Alexander, M. J. (1998), 'Interpretations of observed climatological patterns in stratospheric gravity wave variance', *Journal of Geophysical Research* **103**(D8), 8627–8640.

Alexander, M. J. & Pfister, L. (1995), 'Gravity wave momentum flux in the lower stratosphere over convection', *Geophysical Research Letters* **22**, 2029–2032.

Alexander, M. J. & Rosenlof, K. H. (1996), 'Nonstationary gravity wave forcing of the stratospheric zonal mean wind', *Journal of Geophysical Research* **101**(D18), 23465–23474.

Alexander, M. J., Holton, J. R. & Durran, D. R. (1995), 'The gravity wave response above deep convection in a squall line simulation', *Journal of the Atmospheric Sciences* **52**, 2212–2226.

Allen, S. J. (1996), Gravity wave motions in the troposphere and lower stratosphere, PhD thesis, University of Adelaide, South Australia.

Allen, S. J. & Vincent, R. A. (1995), 'Gravity wave activity in the lower atmosphere: Seasonal and latitudinal variations', *Journal of Geophysical Research* **100**, 1327–1350.

Andrews, D. G. & McIntyre, M. E. (1976), 'Planetary waves in horizontal and vertical shear: The generalized Eliassen-Palm relation and the mean zonal acceleration', *Journal of the Atmospheric Sciences* **33**, 2031–2048.

Andrews, D. G. & McIntyre, M. E. (1978*a*), 'Generalized Eliassen-Palm and Charney-Drazin theorems for waves on axisymmetric mean flows in compressible atmospheres', *Journal of the Atmospheric Sciences* **35**, 175–185.

Andrews, D. G. & McIntyre, M. E. (1978*b*), 'On wave-action and its relatives', *Journal of Fluid Mechanics* **89**, 647–664.

Angevine, W. M. & MacPherson, J. I. (1995), 'Comparison of wind profiler and aircraft wind measurements at Chebogue Point, Nova Scotia', *Journal of Atmospheric and Oceanic Technology* **12**, 421–426.

Atlas, D., Srivastava, R. C. & Sloss, P. W. (1969), 'Wind shear and reflectivity gradient effects on Doppler radar spectra, II', *Journal of Applied Meteorology* **8**, 384–388.

Bacmeister, J. T., Eckermann, S. D., Newman, P. A., Lait, L., Chan, K. R., Loewenstein, M., Profitt, M. H. & Gary, B. L. (1996), 'Stratospheric horizontal wavenumber spectra of winds, potential temperature and atmospheric tracers observed by high-altitude aircraft', *Journal of Geophysical Research* **101**, 9441–9470.

Balsley, B. B. & Ecklund, W. L. (1972), 'A portable coaxial collinear antenna', *IEEE Trans. Antennas Propagat.* **AP-20**, 513–516.

Barat, J. (1982), 'Some characteristics of clear-air turbulence in the middle stratosphere', *Journal of the Atmospheric Sciences* **39**, 2553–2564.

Barat, J. (1983), 'The fine structure of the stratospheric flow revealed by differential sounding', *Journal of Geophysical Research* **88**, 5219–5228.

Barat, J. & Bertin, F. (1984*a*), 'On the contamination of stratospheric turbulence measurements by wind shear', *Journal of the Atmospheric Sciences* **41**, 819–827.

Barat, J. & Bertin, F. (1984*b*), 'Simultaneous measurements of temperature and wind velocity fluctuations within CAT: Analysis of the estimate of dissipation rate by remote sensing techniques', *Journal of the Atmospheric Sciences* **41**, 1613–1619.

Batchelor, G. K. (1953), *The theory of homogeneous turbulence*, Cambridge University Press.

Bertin, F., Barat, J. & Wilson, R. (1997), 'Energy dissipation rates, eddy diffusivity, and the Prandtl number: An in situ experimental approach and its consequences on radar estimates of turbulent parameters', *Radio Science* **32**, 791–804.

Boer, G. J., McFarlane, N. A., Laprise, R., Henderson, J. D. & Blanchet, J. P. (1984), 'The Canadian climate centre spectral atmospheric general circulation model', *Atmos. Ocean* **22**, 397–429.

Boisse, J. C., Klaus, V. & Aubagnac, J. P. (1999), 'A wavelet transform technique for removing airplane echoes from ST radar signals', *Journal of Atmospheric and Oceanic Technology* **16**, 334–346.

Booker, J. R. & Bretherton, F. P. (1967), 'The critical layer for internal gravity waves in a shear flow', *Journal of Fluid Mechanics* **27**, 513–539.

Born, M. & Wolf, E. (1970), *Principles of optics*, Pergamon Press, Sydney.

Bretherton, F. P. (1966), 'The propagation of groups of internal gravity waves in a shear flow', *Q. J. R. Meteorol. Soc.* **92**, 466–480.

Bretherton, F. P. (1969*a*), 'On the mean motion induced by internal gravity waves', *Journal of Fluid Mechanics* **36**, 785–803.

Bretherton, F. P. (1969*b*), 'Waves and turbulence in stably stratified fluids', *Radio Science* **4**, 1279–1287.

Bretherton, F. P. & Garrett, C. J. R. (1969), 'Wavetrains in inhomogeneous moving media', *Proceedings of the Royal Society of London, Series A* **302**, 529–554.

Briggs, B. H. (1984), The analysis of spaced sensor records by correlation techniques, *in* R. A. Vincent, ed., 'Handbook for MAP', Vol. 13, SCOSTEP Secretariat, University of Illinois, pp. 166–186.

Briggs, B. H. (1993), 'Observations of atmospheric dynamics using radar techniques', *Australian Journal of Physics* **46**, 127–147.

Browning, K. A. & Watkins, C. D. (1970), 'Observation of clear air turbulence by high power radar', *Nature* **227**, 260–263.

Cadet, D. & Teitelbaum, H. (1979), 'Observational evidence of internal gravity waves in the tropical stratosphere', *Journal of the Atmospheric Sciences* **36**, 892–907.

Cervera, M. A. & Reid, I. M. (1995), 'Comparison of simultaneous wind measurements using colocated VHF meteor radar and MF spaced antenna radar systems', *Radio Science* **30**, 1245–1261.

Chan, K. R., Scott, S. G., Bowen, S. W., Gaines, S. E., Danielsen, E. F. & Pfister, L. (1991), 'Horizontal wind fluctuations in the stratosphere during large-scale cyclogenesis', *Journal of Geophysical Research* **96**, 17425–17432.

Chen, K. Y., Fu, I. J., Su, S. Y. & Liu, C. H. (1995), 'Wavelet analysis on transient behavior of wind fluctuations observed by MST radar', *Radio Science* **30**, 1111–1123.

Chen, W. Y. (1974), 'Energy dissipation rates of free atmospheric turbulence', *Journal of the Atmospheric Sciences* **31**, 2222–2225.

Chimonas, G. (1970), 'The extension of the Miles-Howard theorem to compressible fluids', *Journal of Fluid Mechanics* **43**, 833–836.

Chimonas, G. & Grant, J. R. (1984), 'Shear excitation of gravity waves. Part II: Upscale scattering from Kelvin-Helmholtz waves', *Journal of the Atmospheric Sciences* **41**, 2278–2288.

Cho, J. Y. N. (1995), 'Inertio-gravity wave parameter estimation from cross-spectral analysis', *Journal of Geophysical Research* **100**(D9), 18727–18737.

Cohen, L. (1995), *Time-frequency analysis*, Prentice-Hall, Englewood Cliffs, N. J.

Cohn, S. A. (1995), 'Radar measurements of eddy dissipation rate in the troposphere: A comparison of techniques', *Journal of Atmospheric and Oceanic Technology* **12**, 85–95.

Cornish, C. R. & Larsen, M. F. (1989), 'Observations of low-frequency inertia-gravity waves in the lower stratosphere over Arecibo', *Journal of the Atmospheric Sciences* **46**, 2428–2439.

Cornman, L. B., Goodrich, R. K., Morse, C. S. & Ecklund, W. L. (1998), 'A fuzzy logic method for improved moment estimation from Doppler spectra', *Journal of Atmospheric and Oceanic Technology* **15**, 1287–1305.

Crane, R. K. (1980), 'A review of radar observations of turbulence in the lower stratosphere', *Radio Science* **15**, 177–193.

Crohn, P. W. (1986), 'The geology and geomorphology of Macquarie Island with special emphasis on heavy metal trace element distribution', *ANARE Research notes.*

Davis, P. & Peltier, W. (1976), 'Resonant parallel shear instability in the stably stratified planetary boundary layer', *Journal of the Atmospheric Sciences* **33**, 1287–1300.

Dewan, E. M. (1994), 'The saturated-cascade model for atmospheric gravity wave spectra, and the wavelength-period (W-P) relations', *Geophysical Research Letters* **21**, 817–820.

Dewan, E. M. & Good, R. E. (1986), 'Saturation and the 'universal' spectrum for vertical profiles of horizontal scalar winds in the atmosphere', *Journal of Geophysical Research* **91**(D2), 2742–2748.

Doviak, R. J. & Zirnic, D. S. (1984), *Doppler radar and weather observations*, Academic Press.

Duffy, D. G. (1990), 'Geostrophic adjustment in a baroclinic atmosphere', *Journal of the Atmospheric Sciences* **47**, 457–473.

Dunkerton, T. J. (1982), 'Theory of the mesopause semiannual oscillation', *Journal of the Atmospheric Sciences* **39**, 2681–2690.

Eaton, F. D., Peterson, W. A., Hines, J. R., Peterman, K. R., Good, R. E., Beland, R. R. & Brown, J. H. (1988), 'Comparisons of VHF radar, optical, and temperature fluctuation measurements of C_n^2, r_0 and θ_0', *Theoretical and Applied Climatology* **39**, 17–29.

Eckermann, S. D. (1992), 'Ray-tracing simulation of the global propagation of inertia gravity waves through the zonally averaged middle atmosphere', *Journal of Geophysical Research* **97**, 15849–15866.

Eckermann, S. D. (1995*a*), 'Effect of background winds on vertical wavenumber spectra of atmospheric gravity waves', *Journal of Geophysical Research* **100**, 14097–14112.

Eckermann, S. D. (1995*b*), 'On the observed morphology of gravity-wave and equatorial-wave variance in the stratosphere', *Journal of Atmospheric and Solar-Terrestrial Physics* **57**, 105–134.

Eckermann, S. D. (1996), 'Hodographic analysis of gravity waves: Relationships among Stokes parameters, rotary spectra and cross-spectral methods', *Journal of Geophysical Research* **101**(D14), 19169–19174.

Eckermann, S. D. & Hocking, W. K. (1989), 'Effect of superposition on measurements of atmospheric gravity waves: A cautionary note and some reinterpretations', *Journal of Geophysical Research* **94**, 6333–6339.

Eckermann, S. D. & Vincent, R. A. (1989), 'Falling sphere observations of anisotropic gravity wave motions in the upper stratosphere over Australia', *Pure Appl. Geophys.* **130**(2/3), 509–532.

Eckermann, S. D. & Vincent, R. A. (1993), 'VHF radar observations of gravity wave production by cold fronts over southern australia', *Journal of the Atmospheric Sciences* **50**, 785–806.

Eckermann, S. D., Hirota, I. & Hocking, W. K. (1994), 'Gravity wave and equatorial wave morphology of the stratosphere derived from long-term rocket soundings', *Q. J. R. Meteorol. Soc.* **121**, 149–186.

Einaudi, F. & Hines, C. O. (1970), 'WKB approximation in application to acoustic-gravity waves', *Canadian Journal of Physics* **48**, 1458–1471.

Eliassen, A. & Palm, E. (1961), 'On the transfer of energy in stationary mountain waves', *Geofys. Publik.* **22**, 1–23.

Ericksen, C. C. (1982), 'Observations of internal wave reflection off sloping bottoms', *Journal of Geophysical Research* **87**, 525–538.

Farge, M. (1992), 'Wavelet transforms and their applications to turbulence', *Annu. Rev. Fluid Mech.* **24**, 395–457.

Farley, D. T. (1983), Coherent integration, *in* S. Bowhill & B. Edwards, eds, 'Handbook for MAP', Vol. 9, SCOSTEP Secretariat, University of Illinois, pp. 507–508.

Fovell, R., Durran, D. & Holton, J. R. (1992), 'Numerical simulations of convectively generated stratospheric gravity waves', *Journal of the Atmospheric Sciences* **49**, 1427–1442.

Frisch, A. S. & Clifford, S. F. (1974), 'A study of convection capped by a stable layer using Doppler radar and acoustic echo sounders', *Journal of the Atmospheric Sciences* **31**, 1622–1628.

Frisch, A. S. & Strauch, R. G. (1976), 'Doppler radar measurements of turbulent kinetic eddy dissipation rates in a northeastern Colorado convective storm', *Journal of Applied Meteorology* **15**, 1012–1017.

Fritts, D. C. (1982), 'Shear excitation of atmospheric gravity waves', *Journal of the Atmospheric Sciences* **39**, 1936–1952.

Fritts, D. C. (1984*a*), 'Gravity wave saturation in the middle atmosphere: A review of theory and observations', *Reviews of Geophysics and Space Physics* **22**, 275–308.

Fritts, D. C. (1984*b*), 'Shear excitation of atmospheric gravity waves.Part II: Nonlinear radiation from a free shear layer', *Journal of the Atmospheric Sciences* **41**, 524–537.

Fritts, D. C. (1989), 'A review of gravity wave saturation processes, effects, and variability in the middle atmosphere', *Pure and Applied Geophysics* **130**, 343–371.

Fritts, D. C. & Luo, Z. (1992), 'Gravity wave excitation by geostrophic adjustment of the jet stream. Part I: Two-dimensional forcing', *Journal of the Atmospheric Sciences* **49**(8), 681–697.

Fritts, D. C. & Nastrom, G. D. (1992), 'Sources of mesoscale variability of gravity waves. Part II: Frontal, convective, and jet stream excitation', *Journal of the Atmospheric Sciences* **49**, 681–697.

Fritts, D. C. & Rastogi, P. K. (1985), 'Convective and dynamical instabilities due to gravity wave motions in the lower and middle atmosphere: Theory and observations', *Radio Science* **20**, 1247–1277.

Fritts, D. C. & VanZandt, T. E. (1993), 'Spectral estimates of gravity wave energy and momentum fluxes. Part I: Energy dissipation, acceleration and constraints', *Journal of the Atmospheric Sciences* **50**(22), 3685–3694.

Fritts, D. C. & Vincent, R. A. (1987), 'Mesospheric momentum flux studies at Adelaide, Australia: Observations and a gravity wave-tidal interaction model', *Journal of the Atmospheric Sciences* **44**, 605–619.

Fritts, D. C. & Yuan, L. (1989), 'Measurement of momentum fluxes near the summer mesopause at Poker Flat, Alaska', *Journal of the Atmospheric Sciences* **46**, 2569–2579.

Fritts, D. C., Tsuda, T., VanZandt, T. E., Smith, S. A., Sato, T., Fukao, S. & Kato, S. (1990), 'Studies of velocity fluctuations in the lower atmosphere using the MU radar,II,Momentum fluxes and energy densities', *Journal of the Atmospheric Sciences* **47**, 51–66.

Fukao, S., Sato, T., Yamasaki, N., Harper, R. M. & Kato, S. (1982), 'Winds measured by a UHF Doppler radar and rawinsondes: Comparisons made on twenty-six days (August - September 1977) at Arecibo, Puerto Rico', *Journal of Applied Meteorology* **21**, 1357–1363.

Fukao, S., Yamanaka, M. D., Ao, N., Hocking, W. K., Sato, T., Yamamoto, M., Nakamura, T., Tsuda, T. & Kato, S. (1994), 'Seasonal variability of vertical eddy diffusivity in the middle atmosphere, 1.Three-year observations by the middle and upper atmosphere radar', *Journal of Geophysical Research* **99**(D9), 18973–18987.

Gage, K. S. & Balsley, B. B. (1978), 'Doppler radar probing of the clear atmosphere', *Bulletin of the American Meteorological Society* **59**, 1074–1093.

Gage, K. S. & Balsley, B. B. (1980), 'On the scattering and reflection mechanisms contributing to clear air radar echoes from the troposphere, stratosphere, and mesosphere.', *Radio Science* **15**, 243–257.

Gage, K. S. & VanZandt, T. E. (1983), The simulation of intermittent clear air turbulence by a Monte Carlo technique, *in* 'Sixth Symposium on Turbulence and Diffusion', American Meteorological Society, Boston, Massachusetts, pp. 85–88.

Garcia, R. R. & Solomon, S. (1985), 'The effect of breaking gravity waves on the dynamics and chemical composition of the mesosphere and lower thermosphere', *Journal of Geophysical Research* **90**, 3850–3860.

Gardner, C. S. (1994), 'Diffusive filtering theory of gravity wave spectra in the atmosphere', *Journal of Geophysical Research* **99**, 20601–20622.

Gardner, C. S. & Gardner, N. F. (1993), 'Measurement distortion in aircraft, space shuttle, and balloon observations of atmospheric density and temperature perturbation spectra', *Journal of Geophysical Research* **98**, 1023–1033.

Geller, M. A. (1983), 'Dynamics of the middle atmosphere', *Space Science Reviews* **34**, 359–375.

Gill, A. E. (1982), *Atmosphere-Ocean Dynamics*, Academic Press, New York.

Gille, J. C., Lyjak, L. V. & Smith, A. K. (1987), 'The global residual mean circulation in the middle atmosphere for the northern winter period', *Journal of the Atmospheric Sciences* **44**, 1437–1452.

Gonella, J. (1972), 'A rotary-component method for analysing meteorological and oceanographic vector time series', *Deep Sea Research* **19**, 833–846.

Gossard, E. E. (1998), 'Measurement of clear-air gradients and turbulence properties with radar wind profilers', *Journal of Atmospheric and Oceanic Technology* **15**, 321–342.

Gossard, E. E. & Hooke, W. H. (1975), *Waves in the Atmosphere*, Elsevier, New York.

Griffiths, M. & Reeder, M. J. (1996), 'Stratospheric inertia-gravity waves generated in a numerical model of frontogenesis. I: Model solutions', *Q. J. R. Meteorol. Soc.* **122**, 1153–1174.

Guest, F. M., Reeder, M. J., Marks, C. J. & Karoly, D. J. (2000), 'Inertia-gravity waves observed in the lower stratosphere over Macquarie Island', *Journal of the Atmospheric Sciences* **57**, 737–752.

Hamilton, K. (1997), The role of parameterized drag in a troposphere-stratosphere-mesosphere general circulation model, *in* K. Hamilton, ed., 'Gravity wave processes: their parametrization in global climate models', Springer-Verlag, Heidelberg, pp. 337–350.

Hamilton, K. & Vincent, R. A. (1995), 'High-resolution radiosonde data offer new prospects for research', *EOS* **76**, 497.

Hasselmann, K. (1967), 'A criterion for non-linear wave instability', *Journal of Fluid Mechanics* **30**, 737–739.

Hecht, E. (1987), *Optics*, Addison-Wesley Publishing Company, Sydney.

Hecht, J. H., Walterscheid, R. L. & Ross, M. N. (1994), 'First measurements of the two-dimensional horizontal wavenumber spectrum from CCD images of the nightglow', *Journal of Geophysical Research* **99**, 11449 11460.

Hermawan, E. & Tsuda, T. (1999), 'Estimation of turbulence energy dissipation rate and vertical eddy diffusivity with the MU radar RASS', *Journal of Atmospheric and Solar-Terrestrial Physics* **61**, 1123–1130.

Hildebrand, P. H. & Sekhon, R. S. (1974), 'Objective determination of the noise level in Doppler spectra', *Journal of Applied Meteorology* **13**, 808–811.

Hill, R. J. & Clifford, S. F. (1978), 'Modified spectrum of atmospheric temperature fluctuations and its application to optical propagation', *Journal of the Optical Society of America* **68**, 892–899.

Hines, C. O. (1960), 'Internal atmospheric gravity waves at ionospheric heights', *Canadian Journal of Physics* **38**, 1441–1481.

Hines, C. O. (1971), 'Generalizations of the Richardson criterion for the onset of turbulence', *Q. J. R. Meteorol. Soc.* **97**, 429–439.

Hines, C. O. (1972), 'Momentum deposition by atmospheric waves and its effect on thermospheric circulation', *Space Research* **12**, 1157–1161.

Hines, C. O. (1988*a*), 'Generation of turbulence by atmospheric gravity waves', *Journal of the Atmospheric Sciences* **45**, 1269–1278.

Hines, C. O. (1988*b*), 'A modeling of atmospheric gravity waves and wave drag generated by isotropic and anisotropic terrain', *Journal of the Atmospheric Sciences* **45**, 309–322.

Hines, C. O. (1988*c*), 'Tropopausal mountain waves over Arecibo: A case study', *Journal of the Atmospheric Sciences* **46**, 476–488.

Hines, C. O. (1991*a*), 'The saturation of gravity waves in the middle atmosphere. Part I: Critique of linear instability theory', *Journal of the Atmospheric Sciences* **48**, 1348–1359.

Hines, C. O. (1991*b*), 'The saturation of gravity waves in the middle atmosphere. Part II: Development of Doppler-spread theory', *Journal of the Atmospheric Sciences* **48**, 1360–1379.

Hines, C. O. (1993), 'Pseudosaturation of gravity waves in the middle atmosphere: An interpretation of certain lidar observations', *Journal of Atmospheric and Solar-Terrestrial Physics* **55**, 441–445.

Hines, C. O. (1997), 'Doppler-spread parametrization of gravity-wave momentum deposition in the middle atmosphere. Part 1: Basic formulation', *Journal of Atmospheric and Solar-Terrestrial Physics* **59**, 371–386.

Hirota, I. & Niki, T. (1986), 'Inertia-gravity waves in the troposphere and stratosphere observed by the MU radar', *Journal of the Meteorological Society of Japan* **64**, 995–999.

Hobbs, B. G. (1998), Measurements of tropospheric scatter with a new multi-beam, multi-receiver VHF Doppler radar, PhD thesis, University of Adelaide, Adelaide, South Australia.

Hocking, W. K. (1983), 'On the extraction of atmospheric turbulence parameters from radar backscatter Doppler spectra - I. Theory', *Journal of Atmospheric and Solar-Terrestrial Physics* **45**, 89–102.

Hocking, W. K. (1985), 'Measurement of turbulent energy dissipation rates in the middle atmosphere by radar techniques: A review', *Radio Science* **20**, 1403–1422.

Hocking, W. K. (1986), 'Observation and measurement of turbulence in the middle atmosphere with a VHF radar', *Journal of Atmospheric and Solar-Terrestrial Physics* **48**, 655–670.

Hocking, W. K. (1988), 'Two years of continuous measurements of turbulence parameters in the upper mesosphere and lower thermosphere with a 2-MHz radar', *Journal of Geophysical Research* **93**, 2475–2491.

Hocking, W. K. & Mu, P. K. L. (1997), 'Upper and middle tropospheric kinetic energy dissipation rates from measurements of $\overline{C_n^2}$ - review of theories, in-situ investigations, and experimental studies using the Buckland Park atmospheric radar in Australia', *Journal of Atmospheric and Solar-Terrestrial Physics* **59**, 1779–1803.

Hocking, W. K., Fukao, S., Tsuda, T., Yamamoto, M., Sato, T. & Kato, S. (1990), 'Aspect sensitivity of stratospheric VHF radio wave scatterers, particularly above 15-km altitude', *Radio Science* **25**, 613–627.

Hocking, W. K., May, P. & Roettger, J. (1989), 'Interpretation, reliability and accuracies of parameters deduced by the spaced antenna method in middle atmosphere applications', *Pure and Applied Geophysics* **130**, 571–604.

Hodges Jr., R. R. (1967), 'Generation of turbulence in the upper atmosphere by internal gravity waves', *Journal of Geophysical Research* **72**, 3455–3458.

Hodges Jr., R. R. (1969), 'Eddy diffusion coefficients due to instabilities in internal gravity waves', *Journal of Geophysical Research* **74**, 4087–4090.

Holdsworth, D. A. & Reid, I. M. (1995*a*), 'A simple model of atmospheric radar backscatter: Description and application to the full correlation analysis of spaced antenna sensor data', *Radio Science* **30**, 1263–1280.

Holdsworth, D. A. & Reid, I. M. (1995*b*), 'Spaced antenna analysis of atmospheric radar backscatter model data', *Radio Science* **30**, 1417–1433.

Holton, J. R. (1982), 'The role of gravity wave induced drag and diffusion in the momentum budget of the mesosphere', *Journal of the Atmospheric Sciences* **39**, 791–799.

Holton, J. R. (1983), 'The influence of gravity wave breaking on the general circulation of the middle atmosphere', *Journal of the Atmospheric Sciences* **40**, 2497–2507.

Holton, J. R. & Wehrbein, W. M. (1980), 'A numerical model of the zonal mean circulation of the middle atmosphere', *Pure and Applied Geophysics* **118**, 284–306.

Holton, J. R. & Zhu, X. (1984), 'A further study of gravity wave induced drag and diffusion in the mesosphere', *Journal of the Atmospheric Sciences* **41**, 2653–2662.

Holton, J. R., Haynes, P. H., McIntyre, M. E., Douglass, A. R., Rood, R. B. & Pfister, L. (1995), 'Stratosphere-Troposphere exchange', *Reviews of Geophysics* **33**, 403–439.

Hooper, D. A. & Thomas, L. (1998), 'Complimentary criteria for identifying regions of intense atmospheric turbulence using lower VHF radar', *Journal of Atmospheric and Solar-Terrestrial Physics* **60**, 49–61.

Houghton, J. T. (1978), 'The stratosphere and mesosphere', *Q. J. R. Meteorol. Soc.* **104**, 1–29.

Howard, L. (1961), 'Note on a paper by John W. Miles', *Journal of Fluid Mechanics* **10**, 509–512.

Jordan, J. R., Lataitis, R. J. & Carter, D. A. (1997), 'Removing ground and intermittent clutter contamination from wind profiler signals using wavelet transforms', *Journal of Atmospheric and Oceanic Technology* **14**, 1280–1297.

Judasz, T. J., Ecklund, W. L. & Balsley, B. B. (1987), 'The coaxial collinear antenna:Current distribution from the cylindrical antenna equation', *IEEE Trans. Antennas Propagat.* **AP-35**, 327–331.

Jumper, G. Y., Beland, R. R. & Tracy, P. (1999), Investigating sources of error in balloon-borne optical turbulence measurements, Technical Report AIAA 99-3618, American Institute of Aeronautics and Astronautics.

Kaimal, J. C., Wyngaard, J. C., Izumi, Y. & Cote, O. R. (1972), 'Spectral characteristics of surface layer turbulence', *Q. J. R. Meteorol. Soc.* **98**, 563–589.

Kellogg, W. W. (1956), 'Diffusion of smoke in the stratosphere', *Journal of Meteorology* **13**, 241–250.

Koch, S. E. & Dorian, P. B. (1988), 'A mesoscale gravity wave event observed during CCOPE. Part III: Wave environment and probable source mechanisms', *Monthly Weather Review* **116**, 2570–2592.

Koscielny, A. J., Doviak, R. J. & Rabin, R. (1984), 'An evaluation of the accuracy of some radar wind profiling techniques', *Journal of Atmospheric and Oceanic Technology* **1**, 309–320.

Kumar, P. & Foufoula-Georgiou, E. (1997), 'Wavelet analysis for geophysical applications', *Reviews of Geophysics* pp. 385–412.

Kunze, E. (1985), 'Near-inertial wave propagation in geostrophic shear', *Journal of Physical Oceanography* **15**, 544–565.

Lalas, D. P. & Einaudi, F. (1976), 'On characteristics of gravity waves generated by atmospheric shear layers', *Journal of the Atmospheric Sciences* **33**, 1248–1259.

LeBlond, P. H. & Mysak, L. A. (1978), *Waves in the ocean*, Elsevier, New York.

Leovy, C. B. (1964), 'Simple models of thermally driven mesospheric circulation', *Journal of the Atmospheric Sciences* **21**, 327–341.

Lighthill, J. (1978), *Waves in Fluids*, Cambridge University Press, New York.

Lilly, D. K. & Kennedy, P. J. (1973), 'Observations of a stationary mountain wave and its associated momentum flux and energy dissipation', *Journal of the Atmospheric Sciences* **30**, 1135–1152.

Lilly, D. K., Waco, D. E. & Adelfang, S. I. (1974), 'Stratospheric mixing estimates from high-altitude turbulence measurements', *Journal of Applied Meteorology* **13**, 488–493.

Lindzen, R. S. (1974), 'Stability of a Helmholtz velocity profile in a continuously stratified infinite Boussinesq fluid - Applications to clear air turbulence', *Journal of the Atmospheric Sciences* **31**, 1507–1514.

Lindzen, R. S. (1981), 'Turbulence and stress owing to gravity wave and tidal breakdown', *Journal of Geophysical Research* **86**, 9707–9714.

London, J. (1980), Radiative energy sources and sinks in the stratosphere and mesosphere, *in* A. C. Aiken, ed., 'Atmospheric Ozone', Proc. NATO Adv. Study Inst., pp. 703–721.

Luce, H., Crochet, M., Dalaudier, F. & Sidi, C. (1997), 'An improved interpretation of VHF oblique radar echoes by a direct balloon C_n^2 estimation using a horizontal pair of sensors', *Radio Science* **32**, 1261–1268.

Luce, H., Dalaudier, F., Crochet, M. & Sidi, C. (1996), 'Direct comparison between in situ VHF oblique radar measurements of refractive index spectra: A new successful attempt', *Radio Science* **31**, 1487–1500.

Ludlam, F. H. (1967), 'Characteristics of billow clouds and their relation to clear-air turbulence', *Q. J. R. Meteorol. Soc.* **93**, 419–435.

Luo, Z. & Fritts, D. C. (1993), 'Gravity-wave excitation by geostrophic adjustment of the jet stream. Part II: Three-dimensional forcing', *Journal of the Atmospheric Sciences* **50**(1), 104–115.

Maekawa, Y., Fukao, S., Sato, T., Kato, S. & Woodman, R. F. (1984), 'Internal inertia-gravity waves in the tropical lower stratosphere observed by the Arecibo radar', *Journal of the Atmospheric Sciences* **41**, 2539–2545.

Marks, C. J. & Eckermann, S. D. (1995), 'A three-dimensional nonhydrostatic ray-tracing model for gravity waves: Formulation and preliminary results for the middle atmosphere', *Journal of the Atmospheric Sciences* **52**, 1959–1984.

Mastrantonio, G., Einaudi, F., Fua, D. & Lalas, D. (1976), 'Generation of gravity waves by jet streams in the atmosphere', *Journal of the Atmospheric Sciences* **33**, 1730–1738.

Matsuno, T. (1982), 'A quasi one-dimensional model of the middle atmosphere circulation interacting with internal gravity waves', *Journal of the Meteorological Society of Japan* **60**, 215–226.

May, P. T. (1988), 'Statistical errors in the determination of wind velocities by the spaced antenna technique', *Journal of Atmospheric and Solar-Terrestrial Physics* **50**, 21–32.

May, P. T. (1993), 'Comparison of wind-profiler and radiosonde measurements in the tropics', *Journal of Atmospheric and Oceanic Technology* **10**, 122–127.

May, P. T. & Strauch, R. G. (1998), 'Reducing the effect of ground clutter on wind profiler velocity measurements', *Journal of Atmospheric and Oceanic Technology* **15**, 579–586.

McComas, C. H. & Bretherton, F. P. (1977), 'Resonant interaction of oceanic internal waves', *Journal of Geophysical Research* **82**, 1397–1412.

McFarlane, N. A. (1987), 'The effect of orographically excited gravity wave drag on the general circulation of the lower stratosphere and troposphere', *Journal of the Atmospheric Sciences* **44**, 1775–1800.

McIntyre, M. E. (1981), 'On the 'wave momentum' myth', *Journal of Fluid Mechanics* **106**, 331–347.

Medvedev, A. S. & Klaassen, G. P. (1995), 'Vertical evolution of gravity wave spectra and the parameterization of associated wave drag', *Journal of Geophysical Research* **100**, 25841–25853.

Merritt, D. A. (1995), 'A statistical averaging method for wind profiler Doppler spectra', *Journal of Atmospheric and Oceanic Technology* **12**, 985–995.

Meyers, S. D., Kelly, B. G. & OBrien, J. J. (1993), 'An introduction to wavelet analysis in oceanography and meteorology: With application to the dispersion of Yanai waves', *Monthly Weather Review* **121**, 2858–2866.

Miles, J. W. (1961), 'On the stability of heterogeneous shear flows', *Journal of Fluid Mechanics* **10**, 496–508.

Mitchell, R. M., Cechet, R. P., Turner, P. J. & Elsum, C. C. (1990), 'Observation and interpretation of wave clouds over Macquarie Island', *Q. J. R. Meteorol. Soc.* **116**, 741–752.

Mobbs, S. D. & Rees, J. M. (1989), 'Studies of atmospheric internal gravity waves at Halley station,Antarctica, using radiosondes', *Antarctic Science* **1**, 65–75.

Murayama, Y., Tsuda, T. & Fukao, S. (1994), 'Seasonal variation of gravity wave activity in the lower atmosphere observed with the MU radar', *Journal of Geophysical Research* **99**, 23057–23069.

Murphy, D. J., Hocking, W. K. & Fritts, D. C. (1994), 'An assessment of the effect of gravity waves on the width of radar Doppler spectra', *Journal of Atmospheric and Solar-Terrestrial Physics* **56**, 17–29.

Nastrom, G. D. (1997), 'Doppler radar spectral width broadening due to beamwidth and wind shear', *Annales Geophysicae* **15**, 786–796.

Nastrom, G. D. & Eaton, F. D. (1997), 'Turbulence eddy dissipation rates from radar observations at 5-20 km at White Sands Missile Range, New Mexico', *Journal of Geophysical Research* **102**(D16), 19495–19505.

Nastrom, G. D. & Fritts, D. C. (1992), 'Sources of mesoscale variability of gravity waves. Part I: Topographic excitation', *Journal of the Atmospheric Sciences* **49**, 101–110.

Nastrom, G. D., VanZandt, T. E. & Warnock, J. M. (1997), 'Vertical wavenumber spectra of wind and temperature from high-resolution balloon soundings in the lower atmosphere over Illinois', *Journal of Geophysical Research* **102(D6)**, 6685–6701.

Newland, D. E. (1993), 'Harmonic wavelet analysis', *Proc. R. Soc. Lond. A* **443**, 203–225.

O'Sullivan, D. & Dunkerton, T. J. (1995), 'Generation of inertia-gravity waves in a simulated life cycle of baroclinic instability', *Journal of the Atmospheric Sciences* **52**, 3695–3716.

Ottersten, H. (1969), 'Atmospheric structure and radar backscattering in clear air', *Radio Science* **4**, 1179–1193.

Palmer, T. N., Shutts, G. J. & Swinbank, R. (1986), 'Alleviation of a systematic westerly bias in general circulation and numerical weather prediction models through an orographic gravity wave drag parameterization', *Q. J. R. Meteorol. Soc.* **112**, 1001–1039.

Pepler, S. J., Vaughan, G. & Hooper, D. A. (1998), 'Detection of turbulence around jet streams using a VHF radar', *Q. J. R. Meteorol. Soc.* **124**, 447–462.

Pfister, L. W., Scott, S., Loewenstein, M., Bowen, S. & Legg, M. (1993), 'Mesoscale disturbances in the tropical atmosphere excited by convection: Observations and effects on the stratospheric momentum budget', *Journal of the Atmospheric Sciences* **50**, 1058–1075.

Puri, K., Dietachmayer, G. S., Mills, G. A., Davidson, N. E., Bowen, R. A. & Logan, L. W. (1998), 'The new BMRC Limited Area Prediction System, LAPS', *Aust. Meteor. Mag.* **47**, 203–223.

Rastogi, P. K. (1983), A note on the use of coherent integration in periodogramm analysis of MST radar signals, *in* S. Bowhill & B. Edwards, eds, 'Handbook for MAP', Vol. 9, SCOSTEP Secretariat, University of Illinois, pp. 509–512.

Rastogi, P. K. (1989), Spectral and correlation analysis with applications to middle-atmosphere radars, *in* S. Fukao, ed., 'Handbook for MAP', Vol. 30, SCOSTEP Secretariat, University of Illinois, pp. 184–227.

Rastogi, P. K. (1990), 'Signal processing and data analysis in middle atmosphere radar', *Radio Science* **25**, 1071–1086.

Reeder, M. J. & Griffiths, M. (1996), 'Stratospheric inertia-gravity waves generated in a numerical model of frontogenesis. II: Wave sources, generation mechanisms and momentum fluxes', *Q. J. R. Meteorol. Soc.* **122**, 1175–1195.

Reid, I. M. (1988), 'MF Doppler and spaced antenna measurements of upper middle atmosphere winds', *Journal of Atmospheric and Solar-Terrestrial Physics* **50**, 117–134.

Reid, I. M. & Vincent, R. A. (1987), 'Measurements of mesospheric gravity wave momentum fluxes and mean flow accelerations at Adelaide,Australia', *Journal of Atmospheric and Solar-Terrestrial Physics* **49**, 443–460.

Reiter, E. R. & Burns, A. (1966), 'The structure of clear-air turbulence derived from TOPCAT aircraft measurements', *Journal of the Atmospheric Sciences* pp. 206–212.

Roettger, J. (1980), 'Reflection and scattering of VHF radar signals from atmospheric refractivity structures', *Radio Science* **15**, 259–276.

Roettger, J. (1984), The MST radar technique, *in* R. A. Vincent, ed., 'Handbook for MAP', Vol. 13, SCOSTEP Secretariat, University of Illinois, pp. 187–232.

Roettger, J. & Larsen, M. F. (1990), UHF/VHF radar techniques for atmospheric research and wind profiler applications, *in* D. Atlas, ed., 'Radar in Meteorology', American Meteorological Society, pp. 253–281.

Roper, R. G. (1996), 'Rocket vapor trail releases revisited: Turbulence and the scale of gravity waves', *Journal of Geophysical Research* **101**, 7013–7017.

Sato, K. (1989), 'An inertial gravity wave associated with a synoptic-scale pressure trough observed by the MU radar', *Journal of the Meteorological Society of Japan* **67**, 325–334.

Sato, K. (1993), 'Small-scale wind disturbances observed by the MU radar during the passage of Typhoon Kelly', *Journal of the Atmospheric Sciences* **50**, 518–537.

Sato, K. (1994), 'A statistical study of the structure, saturation and sources of inertio-gravity waves in the lower stratosphere observed with the MU radar', *Journal of Atmospheric and Solar-Terrestrial Physics* **56**, 755–774.

Sato, K. & Dunkerton, T. J. (1997), 'Estimates of momentum flux associated with equatorial Kelvin and gravity waves', *Journal of Geophysical Research* **102**(D22), 26247–26261.

Sato, K. & Yamada, M. (1994), 'Vertical structure of atmospheric gravity waves revealed by the wavelet analysis', *Journal of Geophysical Research* **99**(D10), 20,623–20,631.

Sato, T. & Woodman, R. F. (1982*a*), 'Fine altitude resolution observations of stratospheric turbulent layers by the Arecibo 430 MHz radar', *Journal of the Atmospheric Sciences* **39**, 2553–2564.

Sato, T. & Woodman, R. F. (1982*b*), 'Fine altitude resolution radar observations of upper tropospheric and lower stratospheric winds and waves', *Journal of the Atmospheric Sciences* **39**, 2539–2545.

Schoeberl, M. R. (1985), 'The penetration of mountain waves into the middle atmosphere', *Journal of the Atmospheric Sciences* **42**, 2856–2864.

Schoeberl, M. R. & Strobel, D. F. (1978), 'The zonally averaged circulation of the middle atmosphere', *Journal of the Atmospheric Sciences* **35**, 577–591.

Schoeberl, M. R., Strobel, D. F. & Apruzese, J. P. (1983), 'A numerical model of gravity wave breaking and stress in the middle atmosphere', *Journal of Geophysical Research* **88**, 5249–5259.

Schubert, W., Hack, J. J., SilvaDias, P. L. & Fulton, S. R. (1980), 'Geostrophic adjustment of an axisymmetric vortex', *Journal of the Atmospheric Sciences* **37**, 1464–1484.

Senft, D. C. & Gardner, C. S. (1991), 'Seasonal variability of gravity wave activity and spectra in the mesopause region at Urbana', *Journal of Geophysical Research* **96**, 17229–17264.

Shimomai, T., Yamanaka, M. D. & Fukao, S. (1996), 'Application of wavelet analysis to wind disturbances observed with MST radar techniques', *Journal of Atmospheric and Solar-Terrestrial Physics* **58**, 683–696.

Shine, K. (1989), 'Sources and sinks of zonal momentum in the middle atmosphere diagnosed using the diabatic circulation', *Q. J. R. Meteorol. Soc.* **115**, 265–292.

Shutts, G. J., Kitchen, M. & Hoare, P. H. (1988), 'A large amplitude gravity wave in the lower stratosphere detected by radiosonde', *Q. J. R. Meteorol. Soc.* **114**, 579–594.

Sloss, P. W. & Atlas, D. (1968), 'Wind shear and reflectivity gradient effects on Doppler radar spectra', *Journal of the Atmospheric Sciences* **25**, 1080–1089.

Smith, R. B. (1985), 'On severe downslope winds', *Journal of the Atmospheric Sciences* **42**, 2597–2603.

Smith, S. A., Fritts, D. C. & VanZandt, T. E. (1987), 'Evidence for a saturated spectrum of atmospheric gravity waves', *Journal of the Atmospheric Sciences* **44**, 1404–1410.

Srivastava, R. C. & Atlas, D. (1974), 'Effect of finite radar pulse volume on turbulence measurements', *Journal of Applied Meteorology* **13**, 472–480.

Streten, N. A. (1988), 'The climate of Macquarie Island and its role in atmospheric monitoring', *Pap. Proc. R. Soc. Tasm.* **122**, 91–106.

Sutherland, B. & Peltier, W. (1994), 'Turbulence transition and internal wave generation in density stratified jets', *Phys. Fluids Ser. A* **6**, 1267–1284.

Sutherland, B. & Peltier, W. (1995), 'Internal gravity wave emission into the middle atmosphere from a model tropospheric jet', *Journal of the Atmospheric Sciences* **52**, 3214–3235.

Sykes, R. I. & Lewellen, W. S. (1982), 'A numerical study of breaking Kelvin Helmholtz billows using a Reynolds stress turbulence closure model', *Journal of the Atmospheric Sciences* **39**, 1506–1520.

Tanaka, H. (1986), 'A slowly varying model of the lower stratospheric zonal wind minimum induced by mesoscale mountain wave breakdown', *Journal of the Atmospheric Sciences* **43**, 1881–1892.

Tatarskii, V. I. (1961), *Wave propagation in a turbulent medium*, McGraw-Hill.

Thomas, L., Astin, I. & Worthington, R. M. (1997), 'A statistical study of underestimates of wind speeds by VHF radar', *Annales Geophysicae* **15**, 805–812.

Thomas, L., Prichard, I. T. & Astin, I. (1992), 'Radar observations of an inertia-gravity wave in the troposphere and lower stratosphere', *Annales Geophysicae* **10**, 690–697.

Thomas, L., Worthington, R. M. & McDonald, A. J. (1999), 'Inertia-gravity waves in the troposphere and lower stratosphere associated with a jet stream exit region', *Annales Geophysicae* **17**, 115–121.

Thompson, R. O. R. Y. (1978), 'Observation of inertial waves in the stratosphere', *Q. J. R. Meteorol. Soc.* **104**, 691–698.

Thrane, E. V., Blix, T., Hoppe, U. P., Luebken, F. J., Hillert, W., Lehmacher, G. & Fritts, D. C. (1994), 'A study of small-scale waves and turbulence in the mesosphere using simultaneous in situ observations of neutral gas and plasma fluctuations', *Journal of Atmospheric and Solar-Terrestrial Physics* **56**, 1797–1808.

Tsuda, T. (1989), Data acqusition and processing, *in* S. Fukao, ed., 'Handbook for MAP', Vol. 30, SCOSTEP Secretariat, University of Illinois, pp. 151–189.

Tsuda, T. S., Kato, S., Yokoi, T., Inoue, T., Yamamoto, M., VanZandt, T. E., Fukao, S. & Sato, T. (1990), 'Gravity waves in the mesosphere observed with the middle and upper atmosphere radar', *Radio Science* **25**, 1005–1018.

Uccellini, L. W. & Koch, S. E. (1987), 'The synoptic setting and possible energy sources for mesoscale wave disturbances', *Monthly Weather Review* **115**, 721–729.

VanBaelen, J. S., Tsuda, T., Richmond, A. D., Avery, S. K., Kato, S., Fukao, S. & Yamamoto, M. (1990), 'Comparison of VHF Doppler beam swinging and spaced antenna observations with the MU radar: First results', *Radio Science* **25**, 629–640.

VanZandt, T. E. (1982), 'A universal spectrum of buoyancy waves in the atmosphere', *Geophysical Research Letters* **9**, 575–578.

VanZandt, T. E. (1985), Gravity waves, Spectral description of mesoscale variations, *in* K. Labitzke, J. J. Barnett & B. Edwards, eds, 'Handbook for MAP', Vol. 16, SCOSTEP Secretariat, University of Illinois, pp. 149–156.

VanZandt, T. E., Green, J. L., Gage, K. S. & Clark, W. L. (1978), 'Vertical profiles of refractivity turbulence structure constant: Comparisons of observations by the Sunset Radar with a new theoretical model', *Radio Science* **13**, 819–829.

Vincent, R. A. (1984), 'Gravity-wave motions in the mesosphere', *Journal of Atmospheric and Solar-Terrestrial Physics* **46**, 119–128.

Vincent, R. A. & Fritts, D. C. (1987), 'A climatology of gravity wave motions in the mesopause region at Adelaide, Australia', *Journal of the Atmospheric Sciences* **44**, 748–760.

Vincent, R. A. & Reid, I. M. (1983), 'HF Doppler measurements of mesospheric gravity wave momentum fluxes', *Journal of the Atmospheric Sciences* **40**, 1321–1333.

Vincent, R. A. & Roettger, J. (1980), 'Spaced antenna VHF radar observations of tropospheric velocities and irregularities', *Radio Science* **15**, 319–335.

Vincent, R. A., Allen, S. J. & Eckermann, S. D. (1997), Gravity-wave parameters in the lower stratosphere, *in* K. Hamilton, ed., 'Gravity wave processes: their parametrization in global climate models', Springer-Verlag, Heidelberg, pp. 7–25.

Vincent, R. A., May, P. T., Hocking, W. K., Elford, W. G., Candy, B. H. & Briggs, B. H. (1987), 'First results with the Adelaide VHF radar: Spaced antenna studies of tropospheric winds', *Journal of Atmospheric and Solar-Terrestrial Physics* **49**, 353–366.

Vincent, R. A., Stubbs, T. J., Pearson, P. H. O., Lloyd, K. H. & Low, C. H. (1977), 'A comparison of partial reflection drifts with winds determined by rocket techniques - I', *Journal of Atmospheric and Solar-Terrestrial Physics* **39**, 813–821.

Warner, C. D. & McIntyre, M. E. (1996), 'On the propagation and dissipation of gravity wave spectra through a realistic middle atmosphere', *Journal of the Atmospheric Sciences* **53**, 3213–3225.

Warner, C. D. & McIntyre, M. E. (1999), 'Toward an ultra-simple spectral gravity wave parameterization for general circulation models', *Earth, Planets and Space* **51**, 475–484.

Weber, B. L. & Wuertz, D. A. (1990), 'Comparison of rawinsonde and wind profiler radar measurements', *Journal of Atmospheric and Oceanic Technology* **7**, 157–174.

Weinstock, J. (1978), 'On the theory of turbulence in the buoyancy subrange of stably stratified flows', *Journal of the Atmospheric Sciences* pp. 634–649.

Weinstock, J. (1981), 'Using radar to estimate dissipation rates in thin layers of turbulence', *Radio Science* **16**, 1401–1406.

Weinstock, J. (1990), 'Saturated and unsaturated spectra of gravity wavws and scale dependend diffusion', *Journal of the Atmospheric Sciences* **47**, 2211–2225.

Welch, P. D. (1967), 'The use of Fast Fourier Transform for the estimation of power spectra: A method based on time averaging over short, modified periodograms', *IEEE Trans. Audio and Electroacoust.* **AU-15**, 70–73.

Whiteway, J. A. & Carswell, A. I. (1994), 'Rayleigh lidar observations of thermal structure and gravity wave activity in the high Arctic during a stratospheric warming', *Journal of the Atmospheric Sciences* **51**, 3122–3136.

Whiteway, J. A. & Duck, T. J. (1996), 'Evidence for critical level filtering of atmospheric gravity waves', *Geophysical Research Letters* **23**, 145–148.

Whiteway, J. A. & Duck, T. J. (1999), 'Enhanced Arctic stratospheric gravity wave activity above a tropospheric jet', *Geophysical Research Letters* **26**, 2453–2456.

WMO (1998), *Stratospheric processes and their role in climate: Implementation plan*, number 105 *in* 'World Climate Research Program', World Meteorological Organization, Geneva, Switzerland.

Worthington, R. M. & Thomas, L. (1996), 'The measurement of gravity wave momentum flux in the lower atmosphere using VHF radar', *Radio Science* **31**, 1501–1517.

Wu, Y. F. & Widdel, H. U. (1991), 'Further study of a saturated gravity wave spectrum in the mesosphere', *Journal of Geophysical Research* **96**, 9263–9272.

Yamanaka, M. D., Fukao, S., Matsumoto, H., Sato, T., Tsuda, T. & Kato, S. (1989), 'Internal gravity wave selection in the upper troposphere and lower stratosphere observed by the MU radar: Preliminary results', *Pure and Applied Geophysics* **130**, 481–495.

Zhu, X. (1993), 'Radiative damping revisited: Parameterization of damping rate in the middle atmosphere', *Journal of the Atmospheric Sciences* **50**, 3008–3021.

Zhu, X. (1994), 'A new theory of the saturated gravity wave spectrum for the middle atmosphere', *Journal of the Atmospheric Sciences* **51**, 3615–3626.

Zrnic, D. S. (1975), 'Simulation of weatherlike Doppler spectra and signals', *Journal of Applied Meteorology* **14**, 619–620.